Alma Mater Studiorum – Università di Bologna

DOTTORATO DI RICERCA IN
CHIMICA

Ciclo XXXI

Settore Concorsuale: 03/B1
Settore Scientifico Disciplinare: CHIM/03

Synthesis, Characterization and Reactivity of New Heterometallic Rhodium Carbonyl Nanoclusters

Tesi presentata da: **Silvia Ruggieri**

Coordinatore Dottorato
Prof. Aldo Roda

Supervisore
Prof. Cristina Femoni

Co-Supervisore
Prof. Maria Carmela Iapalucci

Esame Finale Anno 2019

A Lorenzo

Synthesis, Characterization and Reactivity of New Heterometallic Rh Carbonyl Nanoclusters

Content

CHAPTER I

General Introduction

I.I. What are Clusters made of?

The most widely accepted definition of metal clusters dates back to 1966, when F. A. Cotton described such compounds as "those containing a finite group of metal atoms which are held together entirely, mainly, or at least to a significant extent, by bonds directly between the metal atoms even though some non-metal atoms may be associated intimately with the cluster". [1] When the expression "metal atom cluster" was introduced, the number of known compounds which could satisfy this definition was small, but over the past fifty years, the growth in the field has been exponential. Indeed, several types of metal clusters are now known, which may be classified on the basis of the metals, their oxidation state and the ligands (if present) employed to stabilize the metal cage. Herein, we will focus on a particular class of metal clusters, namely transition-metal carbonyl clusters. These compounds are low-valence transition-metal clusters stabilized by carbon monoxide. This ligand is indeed particularly suitable in stabilizing the low oxidation states that metals have in such compounds since it is involved in a σ-donation (it gives two electrons to the empty orbitals of the metal) behaving as a Lewis base, and at the same time it accepts electronic density from the metal on its empty anti-bonding orbitals through a π-back-donation, this way behaving as a Lewis acid. Furthermore, carbon monoxide is a small ligand with not relevant steric hindrance, which is able to coordinate metal through terminal, edge-bridged and face-bridged bonds.

I.II. The birth of Metal Carbonyl Chemistry

Walter Otto Hieber (1895-1976) is considered the *Father of Metal Carbonyl Chemistry*. His work resulted in an impressive number of publications, which documents his extraordinary contribution. [2, 3] When Hieber carried out his first reaction on $Fe(CO)_5$, there were not so many known carbonyl compounds (among them we can name $Ni(CO)_4$ [4] and $Pt(CO)_2Cl_2$ [5]), but they were enough to rationalize their chemistry, and he classified these species as organometallics complexes.

He studied the "*Reaktionen und Derivate des Eisencarbonyls*" observing for instance that the carbon monoxide in $Fe(CO)_5$ could be replaced by a chelated base as ethylenediamine. [6] The products were described as amine-substituted iron carbonyls, in contrast with their real anionic nature. Indeed, some of those were low nuclearity "clusters" such as $[Fe_2(CO)_8]^{2-}$, $[Fe_3(CO)_{11}]^{2-}$ and $[Fe_4(CO)_{13}]^{2-}$. Their anionic nature was unravelled by osmotic and molar conductivity measurements. Although the descriptions of these compounds were not correct at the time, the possibility that carbon monoxide could be displaced by other ligands was an idea of great significance.

I.III. Metal Carbonyl Clusters and the Milano's School

Over the last thirty years of the twentieth century, following Walter Hieber's retirement, the metal carbonyl history had been recording the chemical contribution of many research groups, some of which were only meteors. Conversely, systematic studies were started by the research group of Brian Frederick Johnson and Jack Lewis in Cambridge (UK), and by Paolo Chini in Milan. There was no conflict between the two groups on their research topics, thanks to the different synthetic strategies and employed metals. Indeed, the Milan's group synthesized anionic nickel, platinum, cobalt and rhodium clusters, while in Cambridge osmium and ruthenium were the main core elements of neutral carbonyl clusters.

Despite his premature death, Paolo Chini played a key role in the development of high-nuclearity metal carbonyl clusters. For instance, he recognized the possibility

of modulating the cluster's nuclearity by changing the redox state setting. He developed the *redox condensation* strategy for the reactions where the cluster is formed through the comproportionation of the reagents with different redox potentials. This method was actually firstly exploited by Hieber in 1965. [7] He was also interested in the development and improvement of methods for the synthesis of large carbonyl clusters with thermal degradation. Today these methods are still the main approaches exploited in the synthesis of high nuclearity homo- and heterometallic clusters. [8]

In some cases, the synthesis of clusters can take a completely different reaction path from the expected one. It is exactly what happened to Chini, when he tried to synthesize a bimetallic Co-Cr cluster by reacting $Co_2(CO)_8$ and $Cr(CO)_6$, in line with the reaction that had led to the obtainment of $HFeCo_3(CO)_{12}$. [9] However, this reaction led to the homometallic $[Co_6(CO)_{15}]^{2-}$ cluster, whose structure is based on an octahedral metal cage (Figure 1.1). [10]

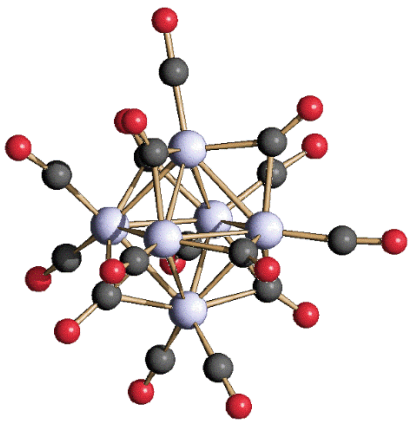

Figure 1.1. Molecular structure of $[Co_6(CO)_{15}]^{2-}$ cluster. Co atoms are depicted in light grey, C atoms are in grey, O atoms are in red.

The characterization of this hexanuclear cobalt species marked the historical beginning of the high nuclearity metal carbonyl clusters.

I.IV. Clusters as atomically precise compounds

Since ancient times, the desire to synthesize materials with well-defined properties let to the obtainment of new compounds by taking mixtures of elements to generate intermetallic species and alloys. In many cases, there is an enhancement in specific properties upon alloying, due to synergic effects that have led to widespread applications in electronics, engineering and catalysis.

Heterometallic nanoclusters are particularly interesting thanks to the combination of intermetallic materials and nanometric dimensions, which gives them a certain flexibility. Indeed, it is possible to modify their chemical and physical properties by tuning not only the size of the clusters (which is possible for homometallic clusters too), but also their composition and the atomic ordering. [11] Heterometallic nanoclusters show different properties from the corresponding bulk alloys because of the finite size effects and of the stabilizing role of the carbonyl ligands. Because of the intrinsically associated combinations of the metal components, bimetallic carbonyl clusters may be valuable precursors for the preparation of atomically precise metal nanoparticles.

The synthesis of metal nanoparticles has significantly taken off in the last two decades. [12] In 1994, an innovative paper on this subject was published by Brust et al., [13] reporting a straightforward synthesis of thiolate-protected gold nanoparticles. However, as the physical and chemical properties of nanoparticles are size-dependent, the possibility of synthesize and identify them at a molecular level remains of crucial importance. Extraordinary progresses have been made in the field of thiolate-, [14] or *p*-MBA, [15] or PA-protected [16] gold and silver [17] nanoclusters (*p*-MBA = *p*-mercaptobenzoic acid; PA = phenylalkynyl), which led to atomically precise species. However, the preparation of molecular nanoparticles in general can follow different approaches, for instance they can be obtained as carbonyl-protected metal clusters.

Within this field, metal carbonyl clusters have been of great importance, as documented by the characterization of countless both homoleptic and heteroleptic species. Over the years, also thanks to the advances in the single-crystal X-ray

diffraction devices, the nuclearity of metal carbonyl clusters has increased at a point that their dimensions have reached a nanometric level. The most outstanding example is represented by Dahl's $(\mu_{12}\text{-Pt})Pd_{164-x}Pt_x(CO)_{72}(PPh_3)_{20}$ ($x \approx 7$) heteroleptic cluster, [18] (Figure 1.2) with dimensions of about 3 nm.

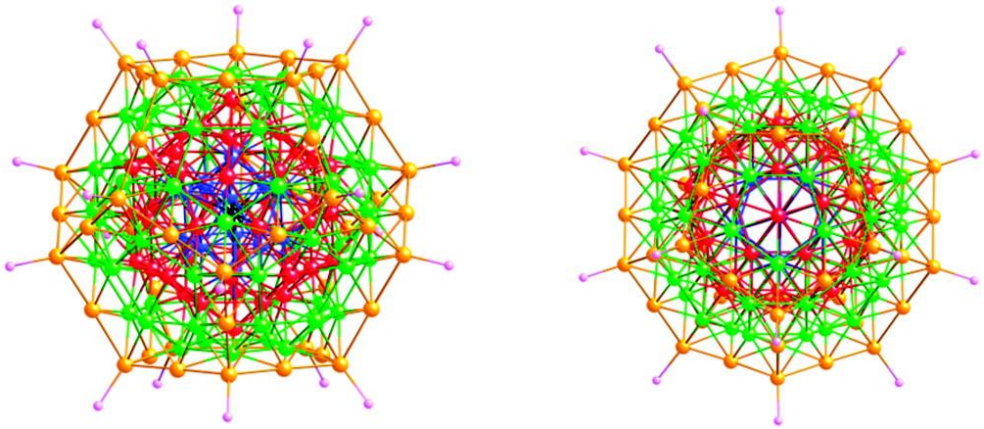

Figure 1.2. Metal skeleton of $(\mu_{12}\text{-Pt})Pd_{164-x}Pt_x(CO)_{72}(PPh_3)_{20}$ ($x \approx 7$) cluster. On the left is represented the side view showing the four-shell geometry of the cluster, while on the right the top one. The central blue cage is a Pt_xPd_{12-x} ($x \approx 1.2$) icosahedron centred by a Pt atom; the red cage is a ν_2 icosahedral Pt_xPd_{42-x} cage ($x \approx 3.5$); the green cage is a 60-atom semi-regular icosahedron of Pt_xPd_{60-x}, ($x \approx 2.2$); the yellow cage is a 50-atom ν_2 pentagonal dodecahedral Pd_{50} one.

Large homoleptic species in the range of around 2 nm size can also be found in the literature, among which $[Pt_{38}(CO)_{44}]^{2-}$, [19] $[H_{6-n}Ni_{38}Pt_6(CO)_{44}]^{n-}$ (n = 6-4) [20, 21] and $[Ni_{32}Pt_{24}(CO)_{56}]^{6-}$ (Figure 1.3). [22]

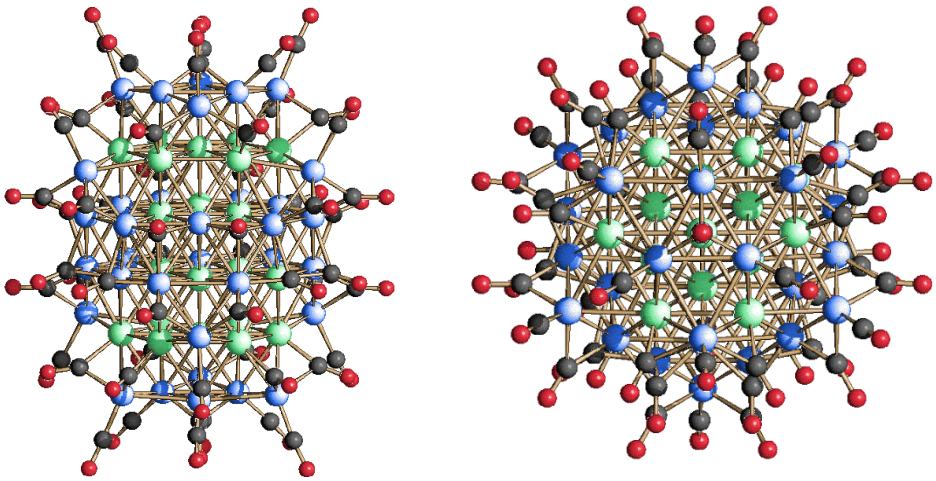

Figure 1.3. Molecular structure of $[Ni_{32}Pt_{24}(CO)_{56}]^{6-}$ cluster. On the left is represented the side view of the cluster, while on the right the top one. Ni atoms are depicted in blue, Pt atoms are depicted in green, C atoms are in grey and O atoms are in red.

One of the most important features of carbonyl clusters is that, regardless of the size, they can be prepared as atomically precise species, therefore they can offer useful insights in comprehending the structures of metal nanoparticles. [23] For instance, the structural icosahedral pattern found in large gold nanoparticles is also present in some Au-Fe carbonyl compounds. [24]

The possibility of preparing carbonyl nanoclusters following standard procedures, such as redox condensation, and the fact that they can be characterized at a molecular level, make such compounds valuable candidates for the study of the chemical and structural properties of nanoparticles in general.

Moreover, when they have dimensions of about 2 nm, not only they can be considered as possible precursors for nanocatalysts, [25] but they can also be identified as ultrafine metal nanoparticles (UMNPs). These have been attracting growing attention lately, as they possess an even higher density of active catalytic sites than their larger nanometric equivalents. [26] Finally, carbonyl clusters' well-defined morphology could in principle contribute to the studies on the shape-dependence performance of catalysts. [27] Indeed, homo-and heterometallic

carbonyl clusters may represent effective precursors for applications in homogeneous and heterogeneous catalysis. [28]

1 F. A. Cotton, *Q. Rev. Chem. Soc.* **1966**, *20*, 389.

2 W. O. Hieber, *Angew. Chem.* **1961**, *73*, 364.

3 W. O. Hieber, *Angew. Chem.* **1952**, *64*, 465.

4 L. Mond, C. Langer, F. Quincke, *J. Chem. Soc.* **1890**, *57*, 749.

5 P. Schützenberger, *J. Chem. Soc.* **1871**, *24*, 1009.

6 W. O. Hieber, F. Sonnekalb, *Ber. Dtsch. Chem. Ges.* **1928**, *61*, 558.

7 W. O. Hieber, E. H. Schubert, *Z. Anorg. Allg. Chem.* **1965**, *32*, 338.

8 P. Chini, *J. Organomet. Chem.* **1980**, *200*, 37.

9 P. Chini, L. Colli, M. Peraldo, *Gazz. Chim. Ital.* **1960**, *90*, 1005.

10 V. G. Albano, P. Chini, V. Scatturin, *Chem. Commun.* **1968**, *15*(2), 163.

11 D. Collini, C. Femoni, M. C. Iapalucci, G. Longoni, P. Zanello, *Perspectives in Organometallic Chemistry* C. G. Screttas and B. R. Steele Eds., The Royal Society of Chemistry **2003**, *287*, 183.

12 C. Femoni, M. C. Iapalucci, S. Ruggieri, S. Zacchini, *Acc. Chem. Res.* **2018**, *51*, 2748.

13 M. Brust, M. Walker, D. Bethell, D. J. Schiffrin, R. Whyman, *Chem. Soc., Chem. Commun*. **1994**, 801.

14 M. W. Heaven, A. Dass, P. S. White, K. M. Holt, R. W. Murray, *J. Am. Chem. Soc.* **2008**, *130*, 3754.

15 P. D. Jadzinsky, G. Calero, C. J. Ackerson, D. A. Bushnell, R. D. Kornberg, *Science* **2007**, *318*, 430.

16 C. Zeng, Y. Chen, K. Kirschbaum, K. J. Lambright, R. Jin, *Science* **2016**, *354*, 1580.

17 A. Desireddy, B. E. Conn, J. Guo, B. Yoon, R. N. Barnett, B. M. Monahan, K. Kirschbaum, W. P. Griffith, R. L. Whetten, U. Landman, T. P. Bigioni, *Nature* **2013**, *501*, 399.

18 E. G. Mednikov, M. C. Jewell, L. F. Dahl, *J. Am. Chem. Soc.* **2007**, *129*, 11619.

19 A. Ceriotti, N. Masciocchi, P. Macchi, G. Longoni, *Angew. Chem. Int. Ed.* **1999**, *38*, 3724.

20 A. Ceriotti, F. Demartin, G. Longoni, M. Manassero, M. Marchionna, G. Piva, M. Sansoni, *Angew. Chem., Int. Ed. Engl.* **1985**, *24*, 697.

21 N. De Silva, L. F. Dahl, *Inorg. Chem.* **2006**, *45*, 8814.

22 C. Femoni, M. C. Iapalucci, G. Longoni, P. H. Svensson, *Chem. Commun.* **2004**, 2274.

23 G. Hogarth, S. E. Kabir, E. Nordlander, *Dalton Trans.* **2010**, *39*, 6153.

24 C. Femoni, M. C. Iapalucci, G. Longoni, C. Tiozzo, S. Zacchini, *Angew. Chem. Int. Ed.* **2008**, *47*, 6666.

25 Q.-L. Zhu, Q. Xu, *Chem.* **2016**, *1*, 220.

26 R. Jin, *Nanotechnol. Rev.* **2012**, *1*, 31.

27 Y. Li, Q. Liu, W. Shen, *Dalton Trans.* **2011**, *40*, 5811.

28 P. Serna, B. C. Gates, *J. Am. Chem. Soc.* **2011**, *133*, 4714.

CHAPTER II

Rhodium Carbonyl Clusters

II.I. General remarks

During my Ph.D. we focused our attention on the investigation of heterometallic Rh clusters. Rhodium possesses the ability to form polynuclear carbonyl compounds with large numbers of metal atoms arranged in an extensive variety of polyhedra, thanks to the high energy of Rh-Rh and Rh-CO bonds. [1] The chemistry of homo-metallic rhodium carbonyl clusters has been widely investigated over the last four decades. Indeed, high Rh-Rh and Rh-CO bond energies allow large homometallic carbonyl clusters to be prepared, such as $[Rh_{22}(CO)_{37}]^{4-}$, [2] $[H_{8-n}Rh_{22}(CO)_{35}]^{n-}$ (n = 4, 5), [3] $Rh_{26}(CO)_{29}(CH_3CN)_{11}$ and $[Rh_{33}(CO)_{47}]^{5-}$, [4] the highest nuclearity one known to date (Figure 2.1). Notably, the latter two species possess an icosahedral-based geometry.

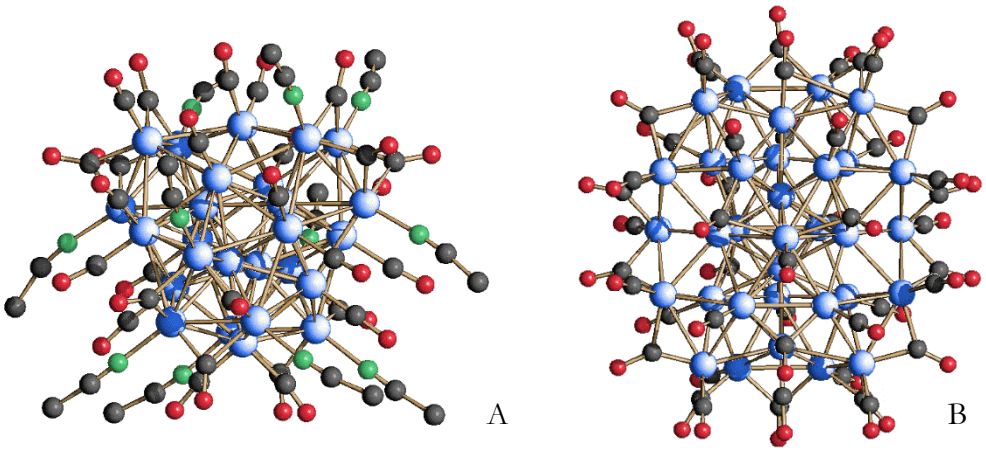

Figure 2.1. Molecular structure of $Rh_{26}(CO)_{29}(CH_3CN)_{11}$ (A) and of $[Rh_{33}(CO)_{47}]^{5-}$ (B). Rh atoms are depicted in blue, N atoms are depicted in green, C atoms are in grey and O atoms are in red.

In the following table we report the average Rh-Rh bond lengths for the two homometallic Rh clusters represented in Figure 2.1. As expected, the shortest contacts are those among the interstitial atoms, followed by those of the interstitial atoms with the peripheral Rh metals. The longest contacts are among the external atoms.

Involved atoms	Bond lengths (average, Å) in $Rh_{26}(CO)_{29}(CH_3CN)_{11}$	Bond lengths (average, Å) in $[Rh_{33}(CO)_{47}]^{5-}$
Rh_{out}-Rh_{out}	2.897	2.816
Rh_{in}- Rh_{in}	2.543	2.485
Rh_{out}-Rh_{in}	2.691	2.687

Table 2.1. Average Rh-Rh bond lengths in the $Rh_{26}(CO)_{29}(CH_3CN)_{11}$ and $[Rh_{33}(CO)_{47}]^{5-}$ clusters. Rh_{out}: external atoms; Rh_{in}: interstitial atoms.

In general heteroatoms can impart extra stability to the cluster compounds and the capability of rhodium species to interstitially host light p elements, such as C and N, gave rise to the fruitful chemistry of carbide and nitride Rh clusters. Among them we can mention $[Rh_{15}C_2(CO)_{24}X_2]^{3-}$ (X = Cl, Br, I) [5] and $[Rh_{28}N_4(CO)_{41}H_x]^{4-}$ [6] (Figure 2.2).

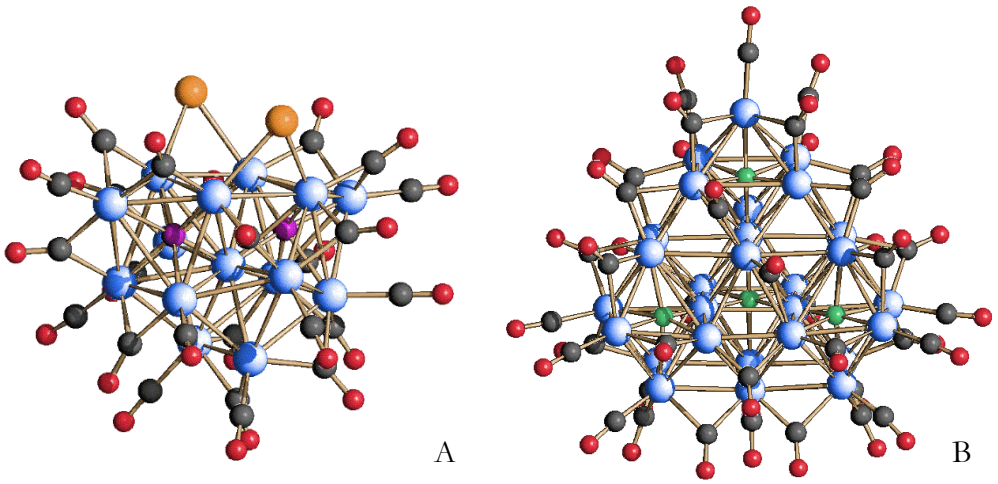

Figure 2.2. Molecular structure of $[Rh_{15}C_2(CO)_{24}X_2]^{3-}$ (A) and of $[Rh_{28}N_4(CO)_{41}H_x]^{4-}$ (B). Rh atoms are depicted in blue, N atoms are depicted in green, interstitial C atoms are depicted in magenta, X atoms are in orange, C atoms are in grey and O atoms are in red.

However, when moving to the third-row p elements only a few examples are reported, such as $[Rh_9P(CO)_{21}]^{2-}$, [7] $[Rh_{10}P(CO)_{22}]^{3-}$, [8] $[Rh_{10}S(CO)_{22}]^{2-}$ [9] and $[Rh_{17}S_2(CO)_{32}]^{3-}$. [10] Similarly, with heavier and bulkier post-transition elements there are just a few species known so far, among which $[Rh_9(\mu_8\text{-As})(CO)_{21}]^{2-}$, $[Rh_{10}(\mu_8\text{-As})(CO)_{22}]^{3-}$ [11] (Figure 2.3 (A)), $[Rh_{12}Sb(CO)_{27}]^{3-}$. [12] and the more recent $[Rh_{12}Sn(CO)_{27}]^{4-}$ [13] (Figure 2.3 (B)). The two aforementioned Rh-As clusters, prepared under high pressure of CO (250 atm) and at high temperature (140-160 °C), adopt As-centred square-antiprismatic frameworks that are mono- and bi-capped, respectively. Of the latter two species, only the second one was synthesized in mild conditions.

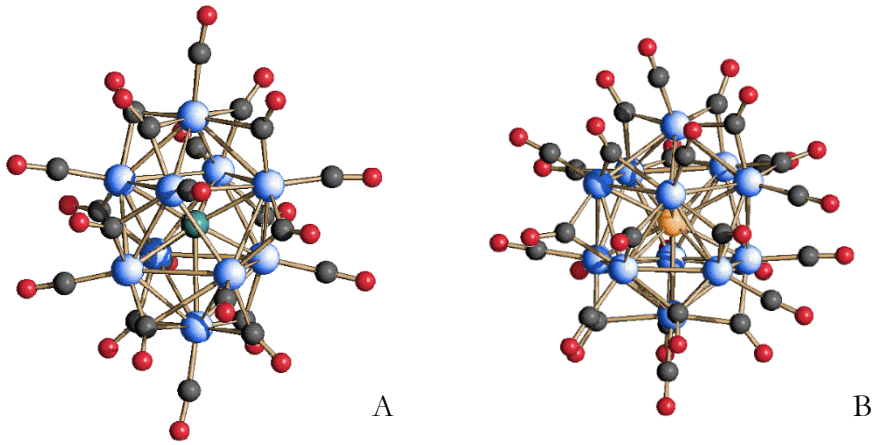

Figure 2.3. Molecular structure of $[Rh_{10}As(CO)_{22}]^{3-}$ (A) and of $[Rh_{12}Sn(CO)_{27}]^{4-}$ (B). Rh atoms are depicted in blue, As atom is depicted in light blue, Sn atom is depicted in orange, C atoms are in grey and O atoms are in red.

II.II. Aim of the Project

The aim of my work was to widen the chemistry of heterometallic Rh clusters with post-transition elements, and find milder and general procedures to synthesize high-nuclearity species. More specifically, I focused my attention on the study of the Rh-Bi, Rh-Ge and Rh-Sb systems, then I extended this investigation to the Rh-Au species, considering the lack of Au-embedded heterometallic Rh clusters in the literature. As discussed in the previous chapter, the interest in preparing such compounds is not only related to base chemistry but it is relevant in the field of atomically-precise nanoparticles, whose synthesis is still a current challenge within the scientific community. Moreover, Rh carbonyl clusters doped with different metals may represent effective precursors for applications in homogeneous and heterogeneous catalysis. Over my Ph.D. period, I actually tested some Rh clusters in the steam reforming process (SR) carried out at low temperature to verify their stability in the reaction conditions and evaluate their performance with respect to more conventional Rh-based catalysts. Finally, a fallout of my work project consisted in the analysis of the cytotoxicity of some heterometallic Rh clusters, which had never been performed before.

Before my Ph.D., the only Rh-E system (E = post-transition element) investigated by our research group had been the Rh-Sn one. The strategy which led to the synthesis of the icosahedral Rh-Sn compound was the redox condensation method, first reported by Hieber and Schubert, [14] but effectively coined and developed by Chini. [15] Indeed, $[Rh_{12}Sn(CO)_{27}]^{4-}$ is the product of the reaction between $[Rh_7(CO)_{16}]^{3-}$ cluster precursor and a salt of Sn^{2+} under nitrogen atmosphere; the Rh oxidation state is less negative in the icosahedral species than in the reagent and Sn, encapsulated in the metal cage, is reduced to a zero formal state.

Moreover, from the $[Rh_{12}Sn(CO)_{27}]^{4-}$ derivative, the coordinatively and electronically unsaturated $[Rh_{12}Sn(CO)_{26}]^{4-}$ and $[Rh_{12}Sn(CO)_{25}]^{4-}$ were obtained. [16] Not only they could be relevant in the field of CO-releasing molecules (CORMs), but they represented the first examples of icosahedral clusters with less than 170 CVEs, likely thanks to the extra stability imparted by the interstitial heteroatom.

The difference in the number of CO ligands is accompanied by a shortening in the bond lengths within the metal cage. One of the reasons could be that the carbonyl arrangement changes when their number decreases. More specifically, when going from $[Rh_{12}Sn(CO)_{27}]^{4-}$ to $[Rh_{12}Sn(CO)_{25}]^{4-}$ the ratio between terminal and bridging CO decreases. As reported in Table 2.2, the negligible difference between the average Rh-Rh and Rh-Sn bond lengths when $[Rh_{12}Sn(CO)_{27}]^{4-}$ and $[Rh_{12}Sn(CO)_{26}]^{4-}$ are considered, becomes relevant if we compare the former with the most unsaturated $[Rh_{12}Sn(CO)_{25}]^{4-}$ species. The contribution of the interstitial atom in the stability of metal clusters was mentioned when referring to multivalence, [17] and it could be evoked also in these cases as we have three stable species with a different number of valence electrons.

Bond lengths	$[Rh_{12}Sn(CO)_{27}]^{4-}$ (170 CVEs)	$[Rh_{12}Sn(CO)_{26}]^{4-}$ (168 CVEs)	$[Rh_{12}Sn(CO)_{25}]^{4-}$ (166 CVEs)
Rh-Rh average (Å)	2.977 (first isomer)	2.976 (first isomer)	2.944
	2.979 (second isomer)	2.977 (second isomer)	
Rh-Sn average (Å)	2.830 (first isomer)	2.829 (first isomer)	2.798
	2.830 (second isomer)	2.830 (second isomer)	

Table 2.2. Rh-Rh and Rh-Sn average bond lengths in the $[Rh_{12}Sn(CO)_{27\text{-}26\text{-}25}]^{4-}$ clusters.

As for the electron counting in deltahedral clusters, it derives from the borane chemistry analogy, as suggested by Wade and Mingos within the Polyhedral Skeleton Electron Pair Theory (PSEPT). [18] For instance, a closo-borane features N + (N + 1) filled molecular orbitals (where N = number of boron atoms), of which N molecular orbitals (MOs) for the localized B−H bonds and N + 1 for the delocalized MOs to sustain the boron cage. When the counting is moved to a transition metal, this has five additional atomic orbitals (the d orbitals), taking the whole to 5N + N + N + 1 = 7N + 1 cluster valence molecular orbitals (CVMOs). According to this rule, an icosahedral carbonyl metal cluster (N = 12) should exhibit 85 CVMOs and 170 cluster valence electrons (CVEs). Note that, according to the inclusion principle formulated by D. M. P. Mingos, [19] interstitial heteroatoms can be considered as an internal source of electrons; therefore, their valence electrons should be included in the CVEs counting.

II.III. Preliminary steps

In order to synthesize and characterize new Rh-E species we decided to exploit the same redox condensation method applied in the Rh-Sn system by starting from the $[Rh_7(CO)_{16}]^{3-}$ cluster precursor.

Therefore, the first necessary step in our reactions, irrespective of the chosen heteroatom, was the synthesis of the cluster precursor $[Rh_7(CO)_{16}]^{3-}$ which derives, in turn, from $Rh_4(CO)_{12}$; their structures are reported in Figure 2.4.

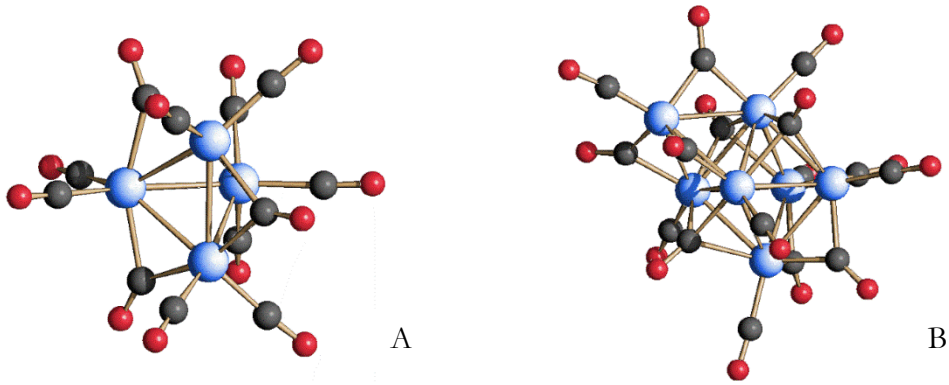

Figure 2.4. Molecular structures of $Rh_4(CO)_{12}$ (A) and of $[Rh_7(CO)_{16}]^{3-}$ (B). Rh atoms are depicted in blue, C atoms are in grey and O atoms are in red.

As reported in the literature, [20] the tetrahedral neutral species $Rh_4(CO)_{12}$ is obtained by the reaction of the mononuclear complex of Rh(III) $[RhCl_6]^{3-}$ with powdered Cu metal, followed by further reduction of the Rh(I) complex $[Rh(CO)_2Cl_2]^-$ by carbon monoxide, according to the following equations.

$$[RhCl_6]^{3-} + 2Cu + 2CO \rightarrow [Rh(CO)_2Cl_2]^- + 2CuCl + 2Cl^- \quad (1)$$

$$4[Rh(CO)_2Cl_2]^- + 6CO + 2H_2O \rightarrow Rh_4(CO)_{12} + 2CO_2 + 4Cl^- + 4HCl \quad (2)$$

The reactions are carried out in water solution because it is necessary a solvent enable to solubilize carbon monoxide. It is important that the solution remains always saturated with CO, in order to avoid the formation of metallic rhodium.

Moreover, the pH plays a really important role in the second step of the reaction; indeed, it is necessary to control it by using a buffer such as a solution of disodium citrate, in order to have a pH of ca. 4. In fact, at a lower pH the reduction of $[Rh(CO)_2Cl_2]^-$ is too slow, while at a higher one $Rh_6(CO)_{16}$ is formed. The reaction needs 24 hours to being completed.

Once obtained the tetrahedral neutral species, this is reacted with a strong excess of KOH under carbon monoxide in methanol, in order to synthesize the anionic $[Rh_7(CO)_{16}]^{3-}$ cluster as described in the following equation. [21]

$$7Rh_4(CO)_{12} + 12OH^- \rightarrow 4[Rh_7(CO)_{16}]^{3-} + 14CO + 6CO_2 + 6H_2O \quad (3)$$

As K^+ salt, the $[Rh_7(CO)_{16}]^{3-}$ anion is soluble in all solvents. In order to achieve a certain degree of product separation when it is used as a reactant, it is necessary to carry out the metathesis of the alkaline cation with an ammonium salt.

At this point, it is possible to use $[Rh_7(CO)_{16}]^{3-}$ as starting material in the strategic approach of the redox condensation in the buildup of Rh carbonyl clusters. Indeed, rhodium is in a negative oxidation state, so quite susceptible of oxidation even at room temperature. Moreover, it is able to provide the necessary CO ligands for the reactions to occur, avoiding the need of working under high pressures of carbon monoxide. During the condensation reaction with halides of the target heteroatom E, $[Rh_7(CO)_{16}]^{3-}$ is oxidized to less negative oxidation states, and the heteroatom is formally reduced to zero when inserts in the cluster.

1 A. K. Hughes, K. Wade, *Coord. Chem. Rev.* **2000**, *197*, 191.

2 S. Martinengo, G. Ciani, A. Sironi, *J. Am. Chem. Soc.* **1980**, *102*, 7564.

3 D. Collini, F. Fabrizi De Biani, D. S. Dolznikov, C. Femoni, M. C. Iapalucci, G. Longoni, C. Tiozzo, S. Zacchini, P. Zanello, *Inorg. Chem.* **2011**, *50*, 2790.

4 D. S. Dolzhnikov, M. C. Iapalucci, G. Longoni, C. Tiozzo, S. Zacchini, C. Femoni, *Inorg. Chem.* **2012**, *51*, 11214.

5 A. Fumagalli, S. Martinengo, G. Bernasconi, L. Noziglia, V. G. Albano, M. Monari, C. Castellari, *Organomet.* **2000**, *19*, 5149.

6 A. Fumagalli, S. Martinengo, G. Bernasconi, G. Ciani, D. M. Proserpio, A. Sironi, *J. Am. Chem. Soc.* **1997**, *119*, 1450.

7 J. L. Vidal, W. E. Walker, R. L. Pruett, R. C. Schoening, *Inorg. Chem.* **1979**, *18*, 129.

8 J. L. Vidal, W. E. Walker, R. C. Schoening, *Inorg. Chem.* **1981**, *20*, 238.

9 G. Ciani, L. Garlaschelli, A. Sironi, S. Martinengo, *J. Chem. Soc. Chem. Commun* **1981**, 563.

10 J. L. Vidal, R. A. Fiato, L. A. Cosby, R. L. Pruett, *Inorg. Chem.* **1978**, *17*, 2574.

11 J. L. Vidal, *Inorg. Chem.* **1981**, *20*, 243.

12 J. L. Vidal, *J. Organomet. Chem.* **1981**, *213*, 351.

13 C. Femoni, M. C. Iapalucci, G. Longoni, C. Tiozzo, S. Zacchini, B. T. Heaton, J. A. Iggo, *Dalton Trans.* **2007**, *35*, 3914.

14 W. O. Hieber, E. H. Schubert, *Z. Anorg. Allg. Chem.* **1965**, *338*, 32.

15 P. Chini, *J. Organomet. Chem.* **1980**, *200*, 37.

16 C. Femoni, M. C. Iapalucci, G. Longoni, C. Tiozzo, S. Zacchini, B. T. Heaton, J. A. Iggo, P. Zanello, S. Fedi, M. V. Garland, C. Li, *Dalton Trans.* **2009**, 2217.

17 G. Longoni, C. Femoni, M. C. Iapalucci, P. Zanello, in *Metal Clusters in Chemistry*, P. Braunstein, L. A. Oro, P. R. Raithby (Eds.), Wiley-VCH, Weinheim **1999**, 1137.

18 D. M. P. Mingos, *Acc. Chem. Res.* **1984**, *17*, 311.

19 J. F. Halet, D. G. Evans, D. M. P. Mingos, *J. Am. Chem. Soc.* **1988**, *110*, 87.

20 S. Martinengo, P. Chini, G. Giordano, *J. Organomet. Chem.* **1971**, *27*, 389.

21 S. Martinengo, P. Chini, *Gazz. Chim. It.* **1972**, *102*, 344.

CHAPTER III

New Rhodium-Bismuth Carbonyl Clusters

To widen the chemistry of rhodium compounds containing post-transition elements, we started by investigating the chemistry of heterometallic Rh−Bi carbonyl clusters. Notably, Bi is an active heterogeneous catalyst in oxidation reaction, [1] and bismuth nanoparticles mixed with other active metals can be prepared and employed in such reactions by using Bi containing metal compounds as precursors. [2]

In the field of heterometallic carbonyl clusters, bismuth has received growing attention over the past thirty years, and several scattered examples of transition-metal carbonyl compounds containing bismuth are known in the literature, albeit none with rhodium, before our study. Among them it is worth mentioning $BiIr_3(CO)_9$, [3] $[Bi_4Fe_4(CO)_{13}]^{2-}$, [4] $[Co_{14}Bi_8(CO)_{20}]^{2-}$, [5] $[Ni_x@Bi_6Ni_6(CO)_8]^{4-}$, [6] $Ir_5Bi_3(CO)_{10}$, [2] $[Bi_{12}Ni_7(CO)_4]^{4-}$ [7] and $Bi_3Ir_6(CO)_{13}$. [8]

Their structures vary from (capped) tetrahedral, to (capped) octahedral, to centred cubic, and to icosahedral geometries. In all those species Bi contributes to the polyhedron forming the cluster framework, alongside the metal atoms, and it is never lodged inside the cavities. Their syntheses largely differ, as they were prepared in various pressure (from atmospheric to 400 bar) and temperature (from room to 160 °C) conditions and starting from completely different reactants. Furthermore, the $[Co_4Bi_2(CO)_{11}]^-$ cluster [9] shows redox properties. [10]

Since rhodium clusters lodging or simply coordinating bismuth atoms where not reported in the literature, we decided to investigate this field in order to expand the heterometallic Rh clusters family.

General results

The following sections illustrate the investigation of the reactions of $[Rh_7(CO)_{16}][NEt_4]_3$ precursor cluster with $BiCl_3$ in different stoichiometric ratios, which led to several heterometallic nanoclusters. The choice of the $[NEt_4]^+$ counter-ion was dictated by the different solubility that this cation imparts to the various final products, making them separable by extraction in solvents of increasing polarity.

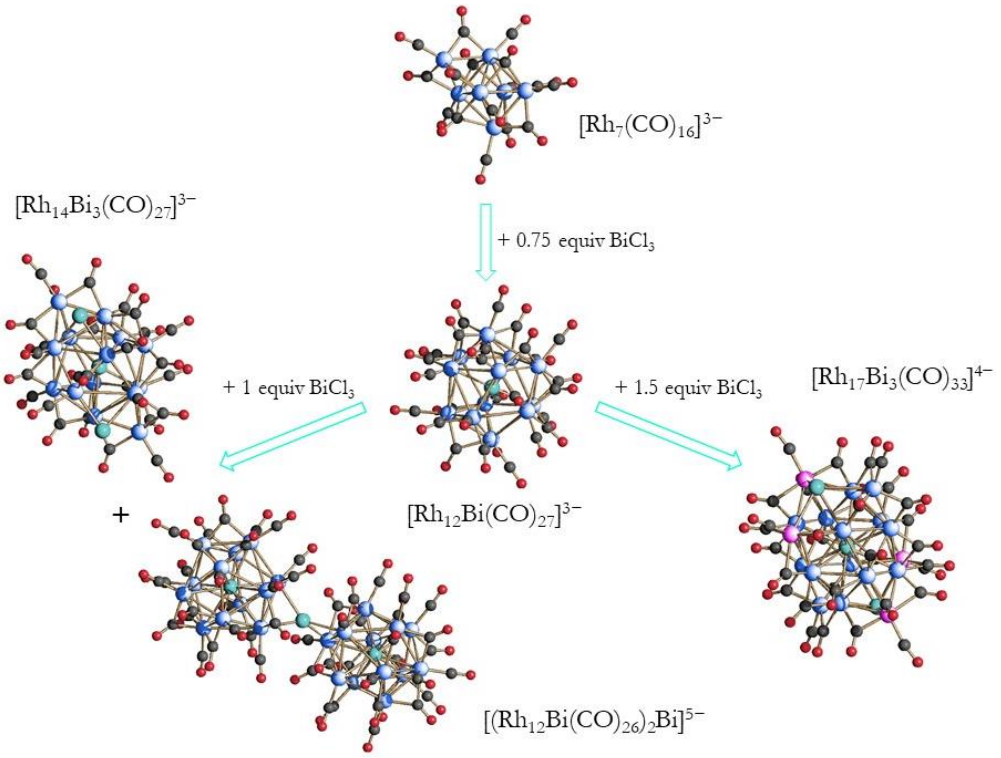

Figure 3.1. Reaction scheme of Rh-Bi system. Rh atoms are depicted in blue, Rh atoms with 75% occupation factor are depicted in magenta, Bi atoms are depicted in light blue, C atoms are in grey and O atoms are in red.

III.I. Reactivity of $[Rh_7(CO)_{16}]^{3-}$ with $BiCl_3$

The first system we studied during my Ph.D. was the Rh-Bi one. [11] In particular we decided to investigate the reactivity of $[Rh_7(CO)_{16}][NEt_4]_3$ with $BiCl_3$ in different reaction conditions, in line with what had been previously done by the same research group on the Rh-Sn system. [12, 13]

First of all, we tested the reactivity of the homometallic cluster precursor with a Bi^{3+} salt under nitrogen atmosphere and at room temperature. As $BiCl_3$ is only sparingly soluble in CH_3CN and actually forms a suspension, after the first reactions we always prepared the $BiCl_3$ suspension in the desired quantity and completely added it to the cluster solution. By checking the reaction path through infrared spectroscopy, it was possible to identify the stoichiometric ratio which led to the full conversion of the $[Rh_7(CO)_{16}]^{3-}$ cluster into a mixture of unknown species. Indeed, after the addition of 0.75 equivalents of $BiCl_3$, the final IR spectrum recorded in solution showed no residual presence of $[Rh_7(CO)_{16}]^{3-}$, whose carbonyl absorption peaks are at 1955(vs), 1939(sh), 1815(m), 1770(ms) and 1742(m) cm^{-1}. In fact, the spectroscopic signals of the starting material were replaced by the characteristic carbonyl absorptions of the $[Rh(CO)_2Cl_2]^-$ complex at 2067(s) and 1991(s) cm^{-1}, which represented an expected by-product, plus other peaks of an unknown species with a main absorption at 1992 cm^{-1}.

The work-up of the mother solution consisted in drying it under vacuum, washing the solid residue with water in order to eliminate all the residual ammonium salts, and then with ethanol and THF (tetrahydrofuran) to eliminate the aforementioned by-product. The unknown species was extracted with acetonitrile and di-isopropyl ether was slowly layered on top of the solution. The obtained crystals were of good enough quality to be analysed through X-ray diffraction and allowed us to identify the compound as $[Rh_{12}Bi(CO)_{27}][NEt_4]_3$. The cluster was also crystallized with $[NMe_4]^+$ as counter-ion, resulting in the $[Rh_{12}Bi(CO)_{27}][NMe_4]_3 \cdot 2(CH_3)_2CO$ solvate salt.

The formation of $[Rh_{12}Bi(CO)_{27}]^{3-}$ is in accord with the following equation:

$$4[Rh_7(CO)_{16}]^{3-} + 3BiCl_3 \rightarrow 2[Rh_{12}Bi(CO)_{27}]^{3-} + 3Cl^- + 3[Rh(CO)_2Cl_2]^- + Bi + Rh + 4CO \quad (1)$$

If we consider the total reaction shown in eq. (1), it is clear that the formation of metallic species (Rh and Bi in this case) is expected in these kinds of reactions. As a matter of fact, some residual dark precipitate, not soluble in any solvent, remained at the end of the work-up. Rh is oxidized to various oxidation states by Bi, which, in turn, is reduced to zero. More specifically, in the starting material Rh atoms are all formally in a −3/7 oxidation state and they are oxidized to +1 (in $[Rh(CO)_2Cl_2]^-$), zero (in metallic Rh), and −3/12 (in the cluster product). On the other side Bi is reduced from +3 to zero both in the heterometallic cluster and in the metal state. This redox behaviour is consistent with what can be expected by relating the standard reduction potentials of the $[Rh_7(CO)_{16}]^{3-}/[Rh_7(CO)_{16}]^{2-}$ and Bi^{3+}/Bi couples (−0.04 measured in CH_3CN and 0.308 V in water, respectively). More in details, it was experimentally established in the past [14] that whenever $[Rh_7(CO)_{16}]^{3-}$ is treated with aquo-complexes featuring $E°(M^{n+}/M) <$ ca. −0.20 V, the Rh cluster is oxidized to an homometallic species with the concurred reduction of H^+ to H_2, whose presence is justified by the intrinsic Brønsted acidity of the metal salt. Conversely, when the standard potential of the couple M^{n+}/M is higher than −0.20 V, irrespective of the pKa of the salt, it is M^{n+} that oxides the starting $[Rh_7(CO)_{16}]^{3-}$ and that, in turn, is formally reduced to M(0) and becomes part of the heterometallic cluster product. The synthesis of $[Rh_{12}Bi(CO)_{27}]^{3-}$ is in line with the above findings.

III.II. Molecular structure of the $[Rh_{12}Bi(CO)_{27}]^{3-}$ cluster

The molecular structure of $[Rh_{12}Bi(CO)_{27}]^{3-}$ (1) is illustrated in Figure 3.2. $[Rh_{12}Bi(CO)_{27}][NEt_4]_3$ crystallized in the centric monoclinic *C2/c* space group with Z = 4; the asymmetric unit contains half a cluster, with the Bi atom laying on a twofold axis, and one and a half molecule of cation. The clusters and the cations are arranged in an ionic fashion in the solid state, with no voids left for solvent

molecules. The molecular structure of $[Rh_{12}Bi(CO)_{27}]^{3-}$ consists of an icosahedral metal skeleton of Rh atoms centred by the unique Bi.

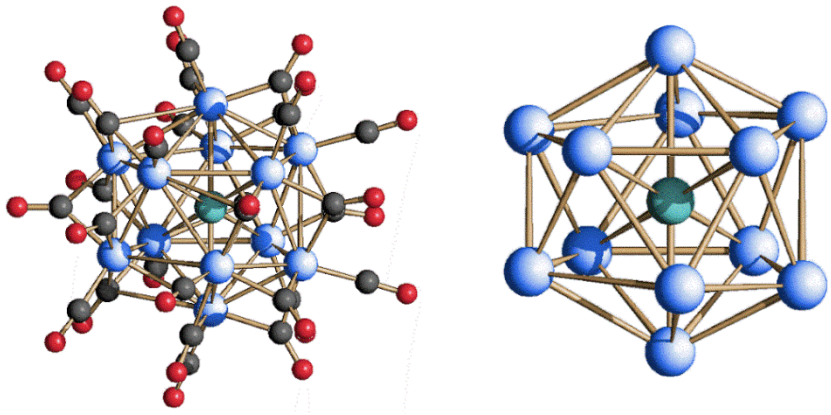

Figure 3.2. Molecular structure of $[Rh_{12}Bi(CO)_{27}]^{3-}$ (left) and its metal skeleton (right). Rh atoms are depicted in blue, Bi atoms are depicted in light blue, C atoms are in grey and O atoms are in red.

Bi(1)-Rh(3)#1	2.7358(4)
Bi(1)-Rh(3)	2.7358(4)
Bi(1)-Rh(6)	2.7556(4)
Bi(1)-Rh(6)#1	2.7556(4)
Bi(1)-Rh(5)#1	2.7575(4)
Bi(1)-Rh(5)	2.7575(4)
Bi(1)-Rh(7)	2.9595(4)
Bi(1)-Rh(7)#1	2.9595(4)
Bi(1)-Rh(4)#1	2.9692(4)
Bi(1)-Rh(4)	2.9692(4)
Bi(1)-Rh(2)#1	2.9780(4)
Bi(1)-Rh(2)	2.9781(4)
Rh(2)-Rh(7)	2.8117(5)
Rh(2)-Rh(5)	2.8857(5)
Rh(2)-Rh(3)	2.8981(5)
Rh(2)-Rh(3)#1	3.0794(5)

Rh(3)-Rh(5)#1	3.0648(5)
Rh(3)-Rh(6)#1	3.0710(6)
Rh(3)-Rh(7)	2.8926(5)
Rh(3)-Rh(2)#1	3.0794(5)
Rh(4)-Rh(4)#1	2.8182(7)
Rh(4)-Rh(6)#1	2.8918(5)
Rh(4)-Rh(6)	2.8918(5)
Rh(4)-Rh(5)#1	3.0766(5)
Rh(5)-Rh(7)	2.8938(5)
Rh(5)-Rh(3)#1	3.0647(5)
Rh(5)-Rh(6)	3.0662(5)
Rh(5)-Rh(4)#1	3.0766(5)
Rh(6)-Rh(4)#1	2.8916(5)
Rh(6)-Rh(7)#1	3.0694(5)
Rh(6)-Rh(3)#1	3.0710(6)
Rh(7)-Rh(6)#1	3.0693(5)

Table 3.1. Most relevant bond lengths for $[Rh_{12}Bi(CO)_{27}][NEt_4]_3$

As inferred from the bond lengths the metal polyhedron is to some extent distorted, with an average Rh−Rh distance of 2.9832 Å, but having the shortest bonding contact at 2.8119(6) Å and the longest at 3.0792(6) Å. Furthermore, there are three extra, longer Rh−Rh distances at 3.388(6) and 3.470(6) Å. The Rh−Bi bond lengths span between 2.7358(4) and 2.9781(4) Å, with an average value of 2.8593 Å.

The metal frame of the icosahedral Rh-Bi compound is stabilized by 27 carbonyl ligands, of which 12 are terminally bonded (one for each vertex) and 15 are edge-bridged. This ligand distribution is shared with the analogous $[Rh_{12}Sb(CO)_{27}]^{3-}$ derivative and one isomer of $[Rh_{12}Sn(CO)_{27}]^{4-}$, while the second isomer presents 13 terminal and 14 edge-bridging COs. Notably, in all the above clusters there are no edge-bridging carbonyls connecting Rh atoms separated by bond distances greater than 3 Å.

The size of the $[Rh_{12}Bi(CO)_{27}]^{3-}$ cluster places it in the nanometric regime, in fact its maximum dimension, measured from the outermost oxygen atoms of the carbonyl ligands and including twice the oxygen van der Waals radius, is 1.4 nm.

The icosahedral arrangement is not new for clusters of such nuclearity [15] and well beyond, and it is observed not only with Rh but also in Ni, Pd, Au, and Ag clusters. Among them it is worth mentioning $[Ni_{12}M(CO)_{22}]^{2-}$ (M = Ge, Sn), [16] $Pd_{145}(CO)_x(PEt_3)_{30}$, [17] and the most recent $Pd_{55}L_{12}(CO)_{20}$, [18] $[M(AuPMe_3)_{11}(AuCl)]^{3+}$ (M = Pt, Pd, Ni), [19] $[Au_{25}(SCH_2CH_2Ph)_{18}]^{-}$, [20] $Au_{38}(SC_2H_4Ph)_{24}$, [21] $[Au_{60}Se_2(Ph_3P)_{10}(SeR)_{15}]^{+}$, [22] and $[Ag_{44}(p\text{-}MBA)_{30}]^{4-}$ (p- MBA = p-mercaptobenzoic acid). [23] Notably, the latter is the only one having an empty icosahedral core.

As stated earlier, the Rh-Bi carbonyl cluster has been also structurally characterized with $[NMe_4]^{+}$ counter-ion, but its geometrical parameters do not significantly differ from the ones with $[NEt_4]^{+}$ in the lattice.

Bi(1)-Rh(2)	2.7412(12)
Bi(1)-Rh(5)	2.7435(12)
Bi(1)-Rh(3)	2.7567(12)
Bi(1)-Rh(6)	2.7567(12)
Bi(1)-Rh(4)	2.7608(12)
Bi(1)-Rh(8)	2.7610(12)
Bi(1)-Rh(13)	2.9500(12)
Bi(1)-Rh(11)	2.9701(12)
Bi(1)-Rh(9)	2.9706(12)
Bi(1)-Rh(12)	2.9764(12)
Bi(1)-Rh(7)	2.9833(12)
Bi(1)-Rh(10)	2.9864(12)
Rh(2)-Rh(11)	2.8904(15)
Rh(2)-Rh(7)	2.8931(15)
Rh(2)-Rh(8)	3.0597(15)
Rh(2)-Rh(6)	3.0605(15)
Rh(2)-Rh(12)	3.0869(16)
Rh(3)-Rh(9)	2.8853(16)
Rh(3)-Rh(10)	2.8998(16)
Rh(3)-Rh(4)	3.0522(16)
Rh(3)-Rh(13)	3.0937(16)
Rh(3)-Rh(5)	3.1027(15)
Rh(4)-Rh(7)	2.8797(15)
Rh(4)-Rh(11)	2.9016(16)
Rh(4)-Rh(5)	3.0633(16)
Rh(4)-Rh(9)	3.0950(15)
Rh(5)-Rh(13)	2.8877(16)
Rh(5)-Rh(12)	2.8904(16)
Rh(5)-Rh(7)	3.0842(16)
Rh(6)-Rh(10)	2.8910(15)
Rh(6)-Rh(9)	2.9011(16)
Rh(6)-Rh(8)	3.0432(16)
Rh(6)-Rh(11)	3.0966(15)
Rh(7)-Rh(11)	2.8013(15)
Rh(8)-Rh(12)	2.8801(15)
Rh(8)-Rh(13)	2.9093(17)
Rh(8)-Rh(10)	3.1239(15)
Rh(9)-Rh(10)	2.8074(15)
Rh(12)-Rh(13)	2.8043(15)

Table 3.2. Most relevant bond lengths for $[Rh_{12}Bi(CO)_{27}][NMe_4]_3$

III.III. IR and ESI-MS characterization and electron counting of the $[Rh_{12}Bi(CO)_{27}]^{3-}$ cluster

$[Rh_{12}Bi(CO)_{27}]^{3-}$, with both $[NEt_4]^+$ and $[NMe_4]^+$ counter-ions, is soluble in acetone and acetonitrile and stable, but not soluble, in water.

Its IR spectrum recorded in CH_3CN shows ν_{CO} absorptions at 1992(s), 1857(m), 1829(m), and 1774(sh) cm^{-1}. $[Rh_{12}Bi(CO)_{27}][NEt_4]_3$ was also characterized by ESI-MS, and the spectrum reveals minor fragmentations in the experimental conditions, mainly due to CO loss. Actually, the loss of ligands is essential to correctly assign the negative charge to the cluster within the peaks, which is hardly

ever the original one. As a matter of fact, in the ESI-MS analysis the cluster compound was detected as bi- and trianion, holding up to three counter-ion molecules. The main peaks at 705, 855, 1095, 1146, and 1240 m/z can be assigned to $\{[Rh_{12}Bi(CO)_{24}]\}^{3-}$, $\{[Rh_{12}Bi(CO)_{26}][NEt_4]_3\}^{3-}$, $\{[Rh_{12}Bi(CO)_{22}][NEt_4]\}^{2-}$, $\{[Rh_{12}Bi(CO)_{21}][NEt_4]_2\}^{2-}$, and $\{[Rh_{12}Bi(CO)_{23}][NEt_4]_3\}^{2-}$ ions. The other peaks are associated with their derived species but with different number of CO ligands (Figure 3.3 and Table 3.3).

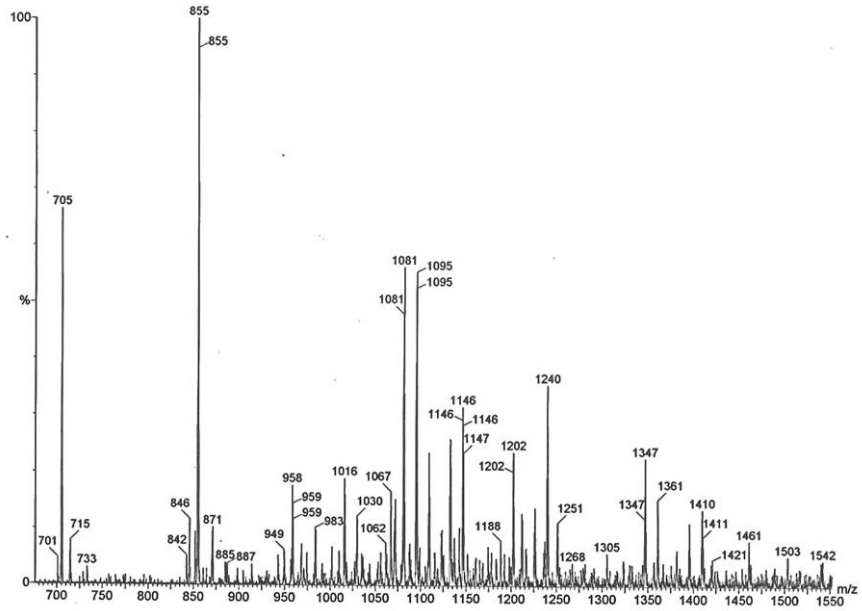

Figure 3.3. ESI-MS spectrum of $[Rh_{12}Bi(CO)_{27}][NEt_4]_3$ recorded in CH_3CN solution.

Signals or groups of signals (m/z)	Corresponding Ions
1240	$\{[Rh_{12}Bi(CO)_{23}][NEt_4]_3\}^{2-}$
1202-1188-1174-1160-1146-1132	$\{[Rh_{12}Bi(CO)_{25\text{-}24\text{-}23\text{-}22\text{-}21\text{-}20}][NEt_4]_2\}^{2-}$
1123-1109-1095-1081-1067	$\{[Rh_{12}Bi(CO)_{24\text{-}23\text{-}22\text{-}21\text{-}20}][NEt_4]\}^{2-}$
1030-1016-1002	$[Rh_{12}Bi(CO)_{22\text{-}21\text{-}20}]^{2-}$
855-846	$\{[Rh_{12}Bi(CO)_{26\text{-}25}][NEt_4]_3\}^{3-}$
733-715-705	$[Rh_{12}Bi(CO)_{27\text{-}25\text{-}24}]^{3-}$

Table 3.3. ESI-MS signal assignments for $[Rh_{12}Bi(CO)_{27}][NEt_4]_3$.

As for the electron counting, the $[Rh_{12}Bi(CO)_{27}]^{3-}$ cluster perfectly conforms to previously described rules (Chapter II) and presents 170 CVEs, given by the 9 × 12 rhodium atoms (108), the 2 × 27 carbonyl ligands (54), the interstitial Bi atom (5), and the negative charge (3).

III.IV. Reactivity of $[Rh_{12}Bi(CO)_{27}]^{3-}$ under CO atmosphere and at high temperature

Once having completely characterized the icosahedral species, we tested its stability under CO atmosphere as, in some cases, due to the high Rh-CO bond energy, the excess of carbonyl ligands may lead to different species. [24] However, the cluster proved to be completely stable even for a prolonged period of time (up to one week), as inferred by IR spectroscopy. It is not possible to assume the same about its stability at high temperature. Indeed, by refluxing a $[Rh_{12}Bi(CO)_{27}]^{3-}$ acetone solution under N_2 atmosphere we recorded a progressive lowering of the ν_{CO} absorptions of the terminal carbonyls from 1992 to ~1980 cm^{-1}, coherent with a possible loss of some CO ligands and the formation of an unsaturated species. The fact that under CO atmosphere the new unknown cluster returned to the parent compound sustained our conclusion. This behaviour is reminiscent of that of the $[Rh_{12}Sn(CO)_{27}]^{4-}$ cluster, from which the isostructural, unsaturated $[Rh_{12}Sn(CO)_{26}]^{4-}$ and $[Rh_{12}Sn(CO)_{25}]^{4-}$ [25] can be thermally prepared, as previously mentioned in Chapter II.

Unfortunately, any attempt to obtain suitable crystals for X-ray diffraction studies failed. In the end, we tested the reactivity of the icosahedral Rh-Bi species with further addition of $BiCl_3$ and the results are presented in the following section.

III.V. Reactivity of $[Rh_{12}Bi(CO)_{27}]^{3-}$ with $BiCl_3$

Since we had obtained the $[Rh_{12}Bi(CO)_{27}]^{3-}$ cluster in good yield, we employed it as starting material and made it react with further amounts of $BiCl_3$, to check the possibility to synthesize higher nuclearity Rh-Bi cluster compounds.

The first $Rh_{12}Bi$:Bi^{3+} stoichiometric ratio which led to new Rh-Bi clusters is 1:1. As for the synthesis of the icosahedral Rh-Bi cluster, the $BiCl_3$ suspension was prepared in the desired quantity and completely added to the cluster solution. At the end of the reaction, the characteristic ν_{CO} absorptions of the starting cluster were totally replaced by others not related to any known species. After the usual work-up, all attempts to crystallize the unknown species failed. Therefore, after repeating the whole reaction, the final mixture was dried under vacuum and dissolved in DMF (N,N-dimethylformamide) in order to perform a metathesis from $[NEt_4]^+$ to $[NMe_4]^+$. At this point, the precipitate was dried and washed with ethanol and THF to completely extract the $[Rh(CO)_2Cl_2]^-$ complex. Thus, in acetone and acetonitrile it was possible to isolate two different new species, later identified as $[(Rh_{12}Bi(CO)_{26})_2Bi]^{5-}$ and $[Rh_{14}Bi_3(CO)_{27}]^{3-}$, respectively.

More specifically, the former dimeric species was crystallized by layering hexane on the acetone solution and characterized as $[(Rh_{12}Bi(CO)_{26})_2Bi][NEt_4][NMe_4]_4 \cdot 4(CH_3)_2CO$, indicating an incomplete metathesis of the $[NEt_4]^+$ cation. Moreover, the extraction in acetonitrile, layered with di-isopropyl ether, gave black crystals of $[Rh_{14}Bi_3(CO)_{27}][NMe_4]_3 \cdot 3CH_3CN$.

Considering the experimental results, we can confidently assume that the total reaction occurred according to the following equation (2):

$$4[Rh_{12}Bi(CO)_{27}]^{3-} + 3BiCl_3 \rightarrow [Rh_{14}Bi_3(CO)_{27}]^{3-} + [(Rh_{12}Bi(CO)_{26})_2Bi]^{5-} + Cl^- + 4[Rh(CO)_2Cl_2]^- + Bi + 6Rh + 21CO \quad (2)$$

It is interesting to note how this reaction may be carried out irrespective of the atmosphere, that is either under carbon monoxide or nitrogen. On paper, 0.75 equivalents of $BiCl_3$ were enough to obtain the two Rh-Bi clusters; however, in order to observe the complete disappearance of the starting icosahedral species, it was necessary to add 1 whole equivalent of Bi^{3+} salt.

Furthermore, after having isolated and crystallized these two new cluster compounds, we kept on the investigation of the reactivity of the icosahedral Rh-Bi

cluster with further amount of Bi^{3+} salt to verify how far this strategy of obtaining new species could be applied. By monitoring the reaction path via IR spectroscopy, after the addition of 1.5 equivalents of $BiCl_3$ to $[Rh_{12}Bi(CO)_{27}]^{3-}$ it was possible to see the ν_{CO} absorptions of the above described new compounds disappearing, in favour of another species with unknown signals. The ordinary work-up was carried out on the mother solution, and beside large quantities of $[Rh(CO)_2Cl_2]^-$, the new $[Rh_{17}Bi_3(CO)_{33}]^{4-}$ was isolated in acetone. It represents the highest nuclearity Rh-Bi carbonyl cluster known to date.

The new cluster was crystallized by layering hexane on the solution, as salt of tetraethylammonium. Also in this case, it was equally possible to carry out the reaction under either N_2 or CO.

Beyond a stoichiometric ratio between $Rh_{12}Bi$ and Bi^{3+} of 1:1.7, the reaction results in a degradation into Rh(I) complexes.

III.VI. Molecular structure of the $[(Rh_{12}Bi(CO)_{26})_2Bi]^{5-}$ cluster

The molecular structure of $[(Rh_{12}Bi(CO)_{26})_2Bi]^{5-}$ (2) is illustrated in Figure 3.4.

It consists of two icosahedral $\{Rh_{12}Bi(CO)_{26}\}$ units connected via a Bi atom and rotated by ~90° one with respect to the other, as Bi shows a pseudo tetrahedral coordination. The 26 carbonyl ligands of each unit are divided into two groups: 12 are terminally bonded, and 14 are edge-bridged. The overall, delocalized charge of the cluster is −5, counterbalanced by four $[NMe_4]^+$ and one $[NEt_4]^+$ cations. In the unit cell there are also positionally disordered acetone molecules, four per cluster. As $[(Rh_{12}Bi(CO)_{26})_2Bi][NEt_4][NMe_4]_4 \cdot 4(CH_3)_2CO$ crystallized in the tetragonal *P*-4n2 space group, with Z = 2; the asymmetric unit contains half a $\{Rh_{12}Bi(CO)_{26}\}$ unit plus the bridging Bi atom (with both Bi atoms lying on a fourfold axis), one $[NMe_4]^+$ cation and a quarter of the $[NEt_4]^+$ one, and finally one acetone molecule.

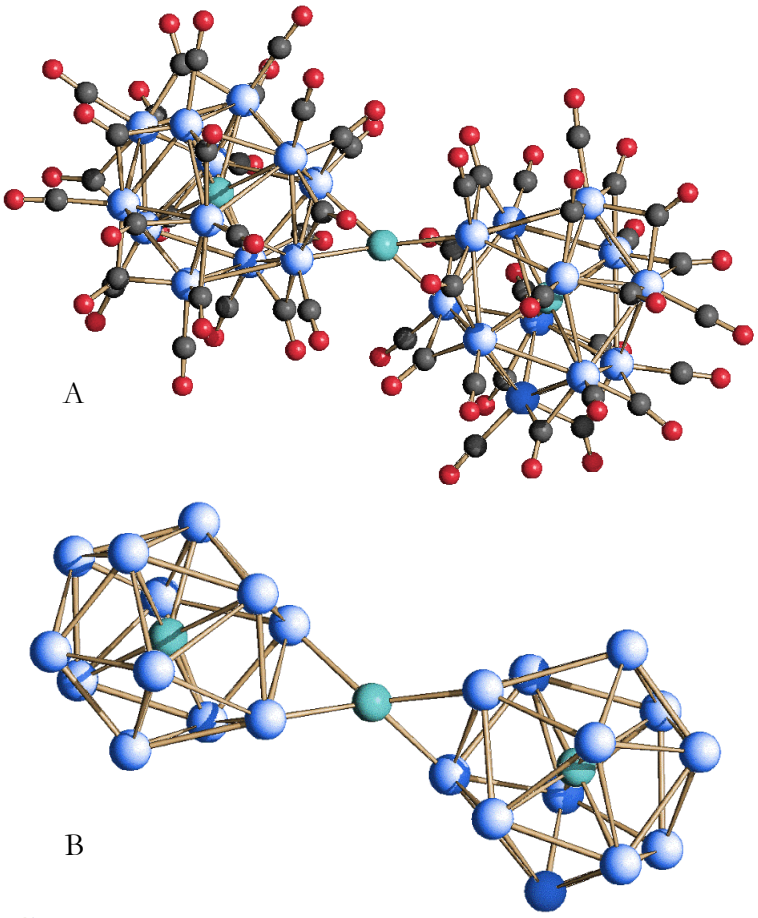

Figure 3.4. Molecular structure of $[(Rh_{12}Bi(CO)_{26})_2Bi]^{5-}$ (A) and its metal skeleton (B). Rh atoms are depicted in blue, Bi atoms are depicted in light blue, C atoms are in grey and O atoms are in red.

The molecular structure of the single $\{Rh_{12}Bi(CO)_{26}\}$ unit coincides with the one of $[Rh_{12}Bi(CO)_{27}]^{3-}$, both in terms of geometry and metal contacts. The Rh−Rh bond lengths vary from 2.8050(17) to 3.188(3) Å, with an average of 2.9703 Å, only slightly shorter than in the icosahedral compound. The Rh−Bi bond distances within the icosahedra vary from 2.7258(10) to 2.9697(11) Å, with an average of 2.8521 Å (similarly to $[Rh_{12}Bi(CO)_{27}]^{3-}$), while those involving the bridging Bi atom are all equivalent and much shorter, 2.6678(10) Å. With respect to the starting cluster, the missing CO ligand in the $\{Rh_{12}Bi(CO)_{26}\}$ monomeric unit is replaced

by the coordination with the bridging Bi atom. The minimum and maximum sizes of the dimeric cluster, measured from the outermost oxygen atoms of the carbonyl ligands and including twice the oxygen van der Waals radius, are 1.3 and 2.3 nm, respectively.

Bi(1)-Rh(3)#1	2.6678(10)	Rh(3)-Rh(7)	3.0956(15)
Bi(1)-Rh(3)#2	2.6678(10)	Rh(4)-Rh(6)	2.8520(17)
Bi(1)-Rh(3)#3	2.6678(10)	Rh(4)-Rh(8)#3	2.8693(16)
Bi(1)-Rh(3)	2.6679(10)	Rh(4)-Rh(7)	3.0345(17)
Bi(2)-Rh(5)#3	2.7258(11)	Rh(4)-Rh(5)#3	3.0389(14)
Bi(2)-Rh(5)	2.7259(11)	Rh(4)-Rh(6)#3	3.1062(16)
Bi(2)-Rh(7)#3	2.7318(11)	Rh(5)-Rh(3)#3	2.9103(14)
Bi(2)-Rh(7)	2.7318(11)	Rh(5)-Rh(7)#3	3.0233(15)
Bi(2)-Rh(4)	2.7833(11)	Rh(5)-Rh(4)#3	3.0390(14)
Bi(2)-Rh(4)#3	2.7834(11)	Rh(5)-Rh(8)	3.1604(16)
Bi(2)-Rh(6)	2.9360(13)	Rh(6)-Rh(8)#3	2.8050(17)
Bi(2)-Rh(6)#3	2.9360(13)	Rh(6)-Rh(7)#3	2.9015(16)
Bi(2)-Rh(8)#3	2.9660(11)	Rh(6)-Rh(4)#3	3.1062(16)
Bi(2)-Rh(8)	2.9661(12)	Rh(6)-Rh(6)#3	3.188(3)
Bi(2)-Rh(3)	2.9697(11)	Rh(7)-Rh(8)	2.8687(16)
Bi(2)-Rh(3)#3	2.9697(11)	Rh(7)-Rh(6)#3	2.9016(16)
Rh(3)-Rh(5)	2.8937(14)	Rh(7)-Rh(5)#3	3.0233(15)
Rh(3)-Rh(5)#3	2.9103(14)	Rh(8)-Rh(6)#3	2.8050(17)
Rh(3)-Rh(3)#3	2.966(2)	Rh(8)-Rh(4)#3	2.8694(16)

Table 3.4. Most relevant bond lengths for $[(Rh_{12}Bi(CO)_{26})_2Bi][NEt_4][NMe_4]_4 \cdot 4(CH_3)_2CO$.

III.VII. IR and ESI-MS characterization and electron counting of the $[(Rh_{12}Bi(CO)_{26})_2Bi]^{5-}$ cluster

$[(Rh_{12}Bi(CO)_{26})_2Bi][NEt_4][NMe_4]_4$ is soluble in acetone, acetonitrile and DMF and stable, but not soluble, in water.

Its IR spectrum recorded in CH_3CN shows ν_{CO} absorptions at 1991(s), 1865(m), 1829(ms), and 1828(m) cm^{-1}.

$[(Rh_{12}Bi(CO)_{26})_2Bi][NEt_4][NMe_4]_4$ was also characterized by ESI-MS. The molecular-ion signal is not present, indicating some instability in the experimental conditions; however, signals due to its partial fragmentation are well-observed. Indeed, ESI-MS analysis displays signals at 1190, 1095, and 1072 m/z (accompanied by satellite ones due to CO losses) attributable to the $\{[Rh_{12}Bi(CO)_{26}]Bi\}^{2-}$, $\{[Rh_{12}Bi(CO)_{22}]NEt_4\}^{2-}$ and $[Rh_{12}Bi(CO)_{25}]^{2-}$ ions, respectively.

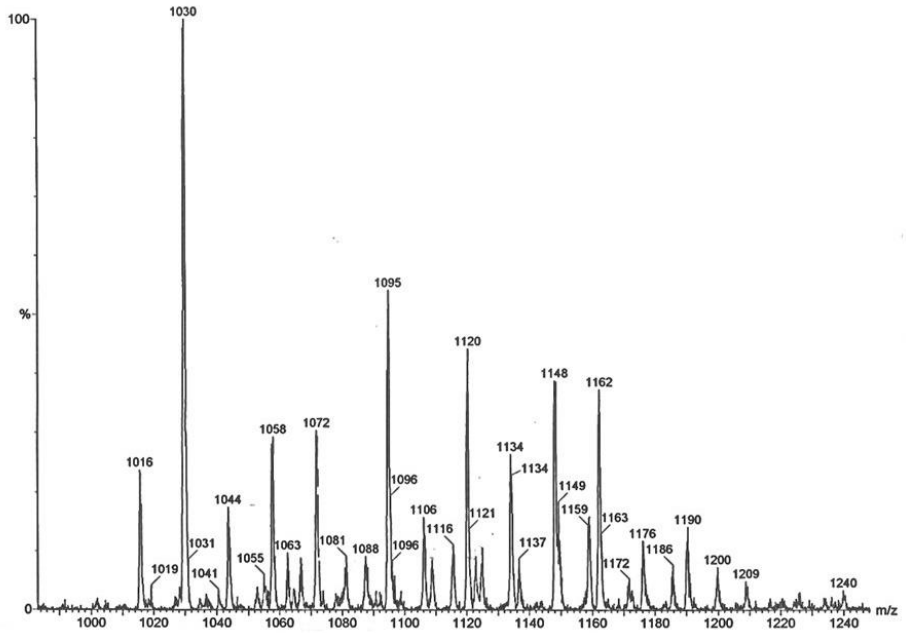

Figure 3.5. ESI-MS spectrum of $[(Rh_{12}Bi(CO)_{26})_2Bi][NEt_4][NMe_4]_4$ recorded in CH_3CN solution.

Signals or groups of signals (m/z)	Corresponding Ions
1190-1176-1162-1148-1134-1120-1106	$\{[Rh_{12}Bi(CO)_{26\text{-}25\text{-}24\text{-}23\text{-}22\text{-}21\text{-}20}]Bi\}^{2-}$
1137-1095	$\{[Rh_{12}Bi(CO)_{25\text{-}22}]NEt_4\}^{2-}$
1072-1058-1044-1030-1016	$[Rh_{12}Bi(CO)_{25\text{-}24\text{-}23\text{-}22\text{-}21}]^{2-}$

Table 3.5. ESI-MS signal assignments for $[(Rh_{12}Bi(CO)_{26})_2Bi][NEt_4][NMe_4]_4$.

As for the electron counting, because the dimer consists of two icosahedra that do not share any face or vertex, we expect it to have 340 CVEs in total. [26] Each $[Rh_{12}Bi(CO)_{26}]$ unit possesses 165 CVEs, and then 5 + 5 electrons must be added: 5 from the bridging Bi atom and 5 from the negative charge. The dimeric species again conforms to the Polyhedral Skeleton Electron Pair Theory (PSEPT).

III.VIII. Molecular structure of the $[Rh_{14}Bi_3(CO)_{27}]^{3-}$ cluster

$[Rh_{14}Bi_3(CO)_{27}][NMe_4]_3 \cdot 3CH_3CN$ is based on an icosahedral geometry with the addition of two Bi-Rh capping fragments on two different sides of the polyhedron. The metal frame is stabilized by 27 carbonyl ligands, of which 12 are terminally bonded, and 15 are edge-bridged. The molecular structure of $[Rh_{14}Bi_3(CO)_{27}]^{3-}$ (3), as well as the metal skeleton, are represented in Figure 3.6.

This cluster compound crystallized in the orthorhombic $Pna2_1$ space group, with Z = 8 and the asymmetric unit contains six cations, six acetonitrile solvent molecules, and two clusters, which only marginally differ in terms of bond lengths. The main icosahedral core is slightly less compact with respect to both Rh-Bi clusters above described, being the average Rh−Bi distances of 2.872 and 2.869 Å for the two clusters in the asymmetric unit. Significantly shorter are the bond lengths involving the two Bi capping atoms: the Rh−Bi average are 2.784 and 2.724 Å for the first cluster, and 2.783 and 2.731 Å for the second one. The Rh−Rh distances within the icosahedral unit vary from 2.754(4) to 3.117(4) Å, for the first cluster, and from 2.761(4) to 3.170(5) for the second one (average values of 2.968 and 2.962 Å, respectively, slightly shorter than in 1 and 2). The Rh−Rh distances of the capping rhodium atoms are shorter, being their average 2.749 and 2.743 Å for the two independent clusters. Four longer nonbonding Rh−Rh distances are observed where the capping Bi−Rh fragments lay, up to 3.404 Å in the first cluster and 3.442 Å in the second one.

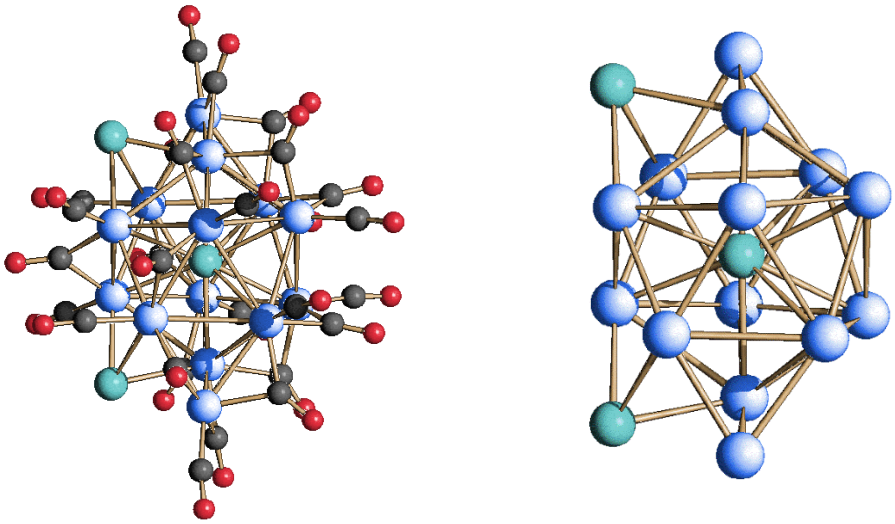

Figure 3.6. Molecular structure of $[Rh_{14}Bi_3(CO)_{27}]^{3-}$ (left) and its metal skeleton (right). Rh atoms are depicted in blue, Bi atoms are depicted in light blue, C atoms are in grey and O atoms are in red.

The maximum size of the $[Rh_{14}Bi_3(CO)_{27}]^{3-}$ cluster, measured from the outermost oxygen atoms of the carbonyl ligands and including twice the oxygen van der Waals radius, is 1.7 nm.

The $[Rh_{14}Bi_3(CO)_{27}]^{3-}$ anion differs from all the other Rh-Bi clusters here reported because it shows a very interesting packing in the solid state. As a matter of fact, due to exceptionally short intermolecular Bi−Bi interactions of 3.591(2) Å and 3.774(2) Å involving the two Bi capping atoms in each cluster, the network results in infinite zigzag chains spaced by cations and solvent molecules, making $[Rh_{14}Bi_3(CO)_{27}]^{3-}$ a molecular wire in the solid state (Figure 3.7).

Bi(1)-Rh(14)	2.781(4)
Bi(1)-Rh(13)	2.812(4)
Bi(1)-Rh(7)	2.831(4)
Bi(1)-Rh(12)	2.833(3)
Bi(1)-Rh(6)	2.844(4)
Bi(1)-Rh(5)	2.849(3)
Bi(1)-Rh(4)	2.863(4)
Bi(1)-Rh(11)	2.869(4)
Bi(1)-Rh(8)	2.895(3)
Bi(1)-Rh(10)	2.899(4)
Bi(1)-Rh(9)	2.975(3)
Bi(1)-Rh(15)	3.008(4)
Bi(2)-Rh(14)	2.657(3)
Bi(2)-Rh(5)	2.744(4)
Bi(2)-Rh(9)	2.769(4)
Bi(2)-Rh(17)	2.965(4)
Bi(3)-Rh(13)	2.656(3)
Bi(3)-Rh(12)	2.741(4)
Bi(3)-Rh(15)	2.775(4)
Bi(3)-Rh(16)	2.972(4)
Bi(3)-Bi(22)	3.591(2)
Rh(4)-Rh(17)	2.778(5)
Rh(4)-Rh(6)	2.875(4)
Rh(4)-Rh(7)	2.998(5)
Rh(4)-Rh(9)	3.076(5)
Rh(4)-Rh(5)	3.093(4)
Rh(4)-Rh(8)	3.177(5)

Rh(5)-Rh(17)	2.693(5)
Rh(5)-Rh(10)	2.757(5)
Rh(5)-Rh(6)	2.859(5)
Rh(5)-Rh(14)	3.111(5)
Rh(6)-Rh(7)	2.997(4)
Rh(6)-Rh(11)	2.999(5)
Rh(6)-Rh(10)	3.028(5)
Rh(7)-Rh(12)	2.857(5)
Rh(7)-Rh(11)	2.872(4)
Rh(7)-Rh(8)	3.022(5)
Rh(8)-Rh(12)	2.754(4)
Rh(8)-Rh(9)	2.937(4)
Rh(8)-Rh(13)	2.941(4)
Rh(9)-Rh(17)	2.770(5)
Rh(9)-Rh(13)	2.827(4)
Rh(10)-Rh(15)	2.936(5)
Rh(10)-Rh(14)	2.949(5)
Rh(10)-Rh(11)	3.166(5)
Rh(11)-Rh(16)	2.798(5)
Rh(11)-Rh(15)	3.088(5)
Rh(11)-Rh(12)	3.090(4)
Rh(12)-Rh(16)	2.689(4)
Rh(12)-Rh(13)	3.117(4)
Rh(13)-Rh(14)	2.780(4)
Rh(14)-Rh(15)	2.852(4)
Rh(15)-Rh(16)	2.763(5)

Table 3.6. Most relevant bond lengths for the first isomer of $[Rh_{14}Bi_3(CO)_{27}][NMe_4]_3 \cdot 3CH_3CN$.

Bi(21)-Rh(25)	2.773(4)	Rh(25)-Rh(30)	2.930(5)
Bi(21)-Rh(26)	2.814(4)	Rh(25)-Rh(29)	3.102(5)
Bi(21)-Rh(28)	2.832(3)	Rh(26)-Rh(27)	2.947(5)
Bi(21)-Rh(34)	2.834(4)	Rh(26)-Rh(32)	3.139(5)
Bi(21)-Rh(32)	2.840(3)	Rh(27)-Rh(32)	2.762(4)
Bi(21)-Rh(36)	2.840(3)	Rh(27)-Rh(34)	3.037(4)
Bi(21)-Rh(35)	2.851(3)	Rh(27)-Rh(28)	3.153(4)
Bi(21)-Rh(29)	2.859(3)	Rh(28)-Rh(37)	2.789(5)
Bi(21)-Rh(30)	2.897(3)	Rh(28)-Rh(35)	2.863(4)
Bi(21)-Rh(27)	2.898(3)	Rh(28)-Rh(34)	3.002(4)
Bi(21)-Rh(31)	2.989(4)	Rh(28)-Rh(29)	3.054(4)
Bi(21)-Rh(24)	2.998(3)	Rh(29)-Rh(37)	2.677(4)
Bi(22)-Rh(25)	2.646(3)	Rh(29)-Rh(30)	2.761(4)
Bi(22)-Rh(29)	2.756(4)	Rh(29)-Rh(35)	2.862(5)
Bi(22)-Rh(24)	2.772(3)	Rh(30)-Rh(31)	2.901(5)
Bi(22)-Rh(37)	2.957(4)	Rh(30)-Rh(35)	3.042(5)
Bi(23)-Rh(26)	2.658(3)	Rh(30)-Rh(36)	3.170(5)
Bi(23)-Rh(32)	2.752(4)	Rh(31)-Rh(33)	2.758(5)
Bi(23)-Rh(31)	2.782(4)	Rh(31)-Rh(36)	3.056(5)
Bi(23)-Rh(33)	2.925(4)	Rh(32)-Rh(33)	2.677(5)
Rh(24)-Rh(37)	2.776(4)	Rh(32)-Rh(34)	2.851(5)
Rh(24)-Rh(26)	2.848(4)	Rh(32)-Rh(36)	3.071(4)
Rh(24)-Rh(27)	2.932(4)	Rh(33)-Rh(36)	2.778(5)
Rh(24)-Rh(28)	3.036(5)	Rh(34)-Rh(36)	2.858(4)
Rh(25)-Rh(26)	2.785(4)	Rh(34)-Rh(35)	2.993(4)
Rh(25)-Rh(31)	2.842(4)	Rh(35)-Rh(36)	3.007(4)

Table 3.7. Most relevant bond lengths for the second isomer of $[Rh_{14}Bi_3(CO)_{27}][NMe_4]_3 \cdot 3CH_3CN$.

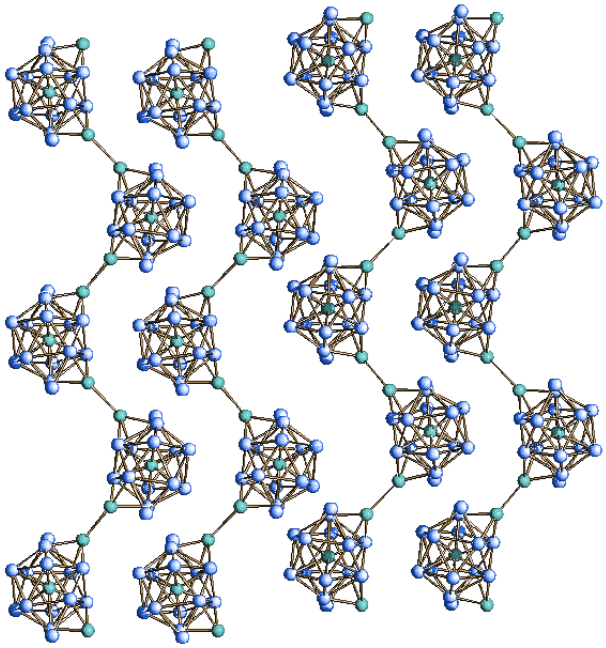

Figure 3.7. Molecular packing of $[Rh_{14}Bi_3(CO)_{27}]^{3-}$ in the solid state along the *c* axis, showing infinite zigzag chains. Rh atoms are depicted in blue, Bi atoms are depicted in light blue. Carbonyl groups, cations, and solvent molecules have been omitted for sake of clarity.

III.IX. IR and ESI-MS characterization and electron counting of the $[Rh_{14}Bi_3(CO)_{27}]^{3-}$ cluster

$[Rh_{14}Bi_3(CO)_{27}][NMe_4]_3$ is soluble in acetonitrile and DMF and stable, but not soluble, in water.

Its IR spectrum recorded in CH_3CN shows ν_{CO} absorptions at 1989(s), 1865(m), 1896(s) and 1863(ms) cm^{-1}. $[Rh_{14}Bi_3(CO)_{27}]^{3-}$ was also characterized by ESI-MS. The positive-ion region shows the presence of some residual $[NEt_4]^+$ in solution. Notably, its compact structure makes it more stable in the experimental conditions (except for some CO loss) than the dimeric Rh-Bi cluster above discussed, and the signal at 1566 m/z is attributable to the $[Rh_{14}Bi_3(CO)_{26}][NEt_4]_2[NMe_4]\}^{2-}$ molecular ion. The ESI-MS spectrum presents also main signals at 1341, 1072, 922, and 851

m/z, due to the $[Rh_{14}Bi_3(CO)_{22}]^{2-}$, $\{[Rh_{14}Bi_3(CO)_{27}][NEt_4]_3\}^{3-}$, $[Rh_{14}Bi_3(CO)_{25}]^{3-}$, and $[Rh_{14}Bi_2(CO)_{25}]^{3-}$ ions, respectively. In the end, it is also possible to find traces of the highest nuclearity Rh-Bi cluster to date as $\{[Rh_{17}Bi_3(CO)_{32}][NEt_4]\}^{3-}$ at 1134 m/z.

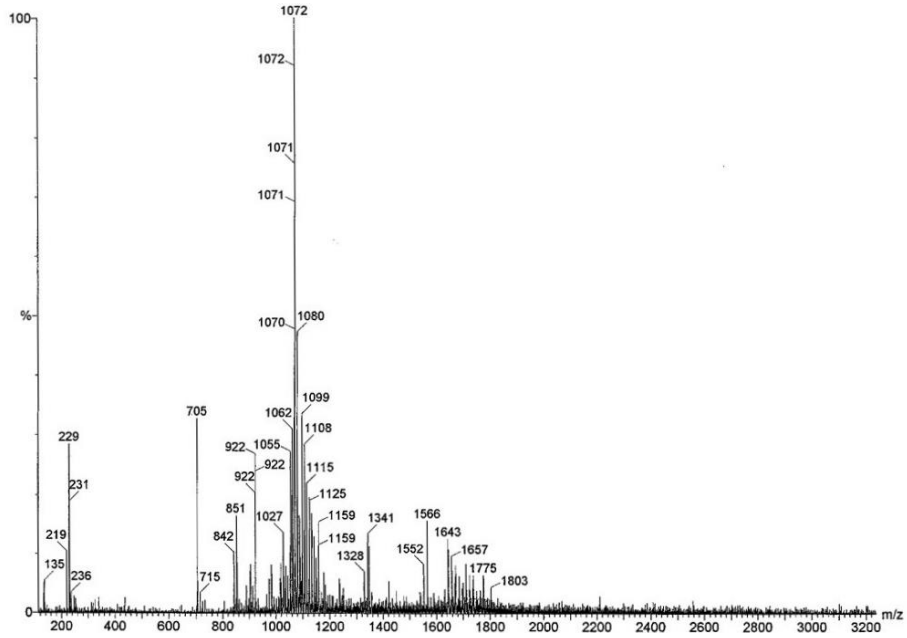

Figure 3.8. ESI-MS spectrum of $[Rh_{14}Bi_3(CO)_{27}][NMe_4]_3$ recorded in CH_3CN solution.

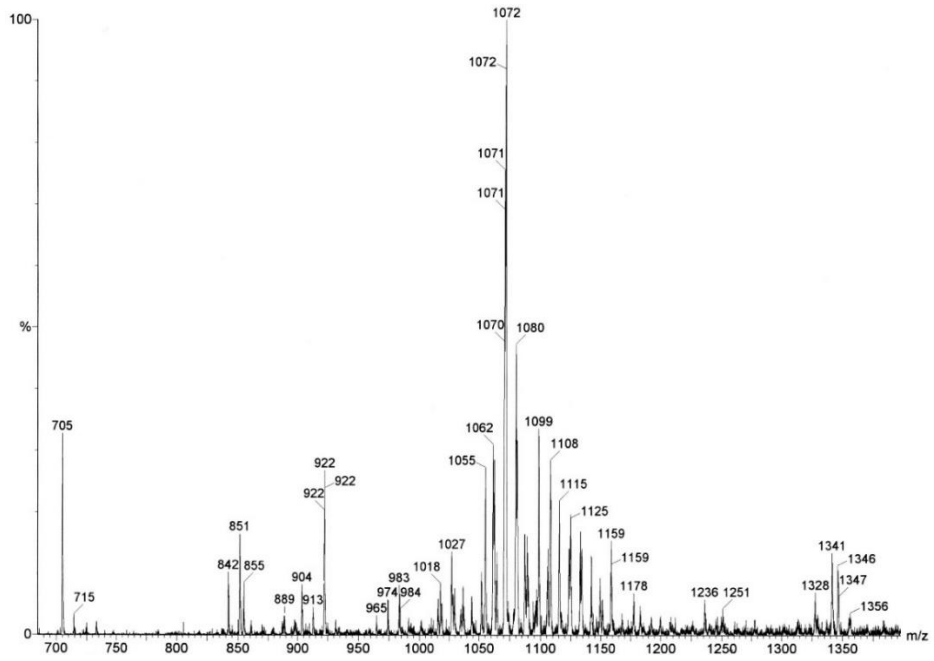

Figure 3.9. Close-up of the ESI-MS spectrum of $[Rh_{14}Bi_3(CO)_{27}][NMe_4]_3$ recorded in CH_3CN solution.

Signals or groups of signals (m/z)	Corresponding Ions
1566	$\{[Rh_{14}Bi_3(CO)_{26}][NEt_4]_2[NMe_4]\}^{2-}$
1341-1328	$[Rh_{14}Bi_3(CO)_{22-21}]^{2-}$
1134-1125-1115	$\{[Rh_{17}Bi_3(CO)_{32-31-30}][NEt_4]\}^{3-}$
1072-1062-1053-1044	$\{[Rh_{14}Bi_3(CO)_{27-26-25-24}][NEt_4]_3\}^{3-}$
922-913-904	$[Rh_{14}Bi_3(CO)_{25-24-23}]^{3-}$
851-842	$[Rh_{14}Bi_2(CO)_{25}]^{3-}$
715-705	$[Rh_{12}Bi(CO)_{25-24}]^{3-}$

Table 3.8. ESI-MS signal assignments for $[Rh_{14}Bi_3(CO)_{27}][NMe_4]_3 \cdot 3CH_3CN$.

In the case of $[Rh_{14}Bi_3(CO)_{27}]^{3-}$, the electron counting rule would predict 194 CVEs, being an icosahedron (170 CVEs) capped by two metal atoms (2 × 12 CVEs). The same electron counting is obtained when considering this cluster as a condensed polyhedral molecule formed by the fusion of one icosahedron (170 CVEs) with two surface tetrahedral fragments (60 × 2 CVEs), sharing one

triangular face each (−48 × 2 CVEs). Indeed, the total electron counting is the following: 9 × 14 (Rh atoms) + 2 × 27 (CO ligands) + 5 (interstitial Bi atom) + 3 × 2 (surface Bi atoms) + 3 (negative charge), giving a total of 194 CVEs.

III.X. Molecular structure of the $[(Rh_{17}Bi_3(CO)_{33}]^{4-}$ cluster

The molecular structure of $[Rh_{17}Bi_3(CO)_{33}]^{4-}$ (4) is represented in Figure 3.10.

The cluster crystallized in the orthorhombic *C*mca space group with Z = 4, and its asymmetric unit contains one-quarter of the cluster and one cation molecule. The metal skeleton is again based on a Bi-centred icosahedron of Rh atoms symmetrically decorated by two Rh−Bi−Rh_x fragments (x = 3/2), presenting a Rh atom in the asymmetric unit with a partial occupation factor of 75%. As a result, there are three Rh atoms disordered over four positions. Reasonably, this partial occupation factor has a repercussion on the entire cluster, so five of the eight independent carbonyl groups were split in two positions, and the overall structural model presents numerous distance and anisotropic displacement parameter (ADP) restraints. The icosahedral kernel shows Bi−Rh and Rh−Rh bond lengths similar to the previously discussed Rh-Bi clusters, being their average 2.9025 and 2.9215 Å, respectively. There are also six longer Rh−Rh distances of 3.488 and 3.490 Å. Conversely, the Rh−Rh and Rh−Bi bond distances on the icosahedral surface are significantly shorter (average values 2.7153 and 2.7944 Å) than those in the core. Notably, the Bi−Rh bond lengths involving the disordered Rh atoms are sensibly longer, having an average value of 3.0113 Å.

Finally, the metal frame of $[Rh_{17}Bi_3(CO)_{33}]^{4-}$ is stabilized by 33 carbonyl ligands, of which, notably, only five are terminally bonded, while the remaining 28 are edge-bridged.

The maximum size of the $[Rh_{17}Bi_3(CO)_{33}]^{4-}$ cluster, measured from the outermost oxygen atoms of the carbonyl ligands and including twice the oxygen van der Waals radius, is 1.8 nm.

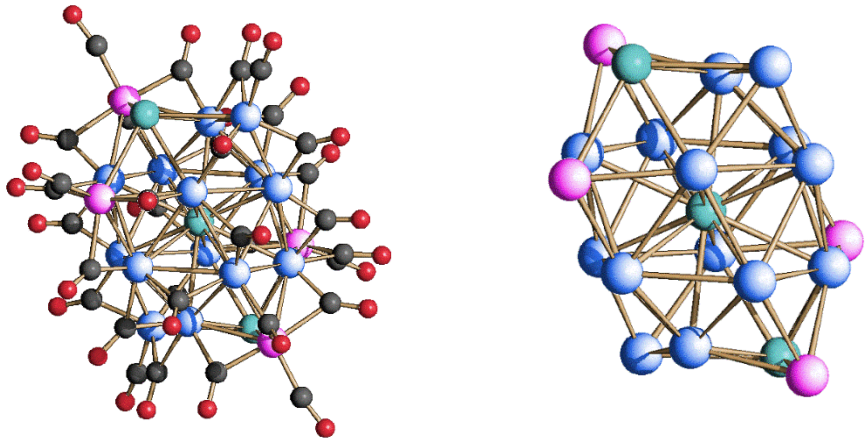

Figure 3.10. Molecular structure of $[Rh_{17}Bi_3(CO)_{33}]^{4-}$ (left) and its metal skeleton (right). Rh atoms are depicted in blue, Rh atoms with 75% occupation factor are depicted in magenta, Bi atoms are depicted in light blue, C atoms are in grey and O atoms are in red.

Bi(1)-Rh(4)	2.8022(15)
Bi(1)-Rh(4)#1	2.8022(15)
Bi(1)-Rh(6)	2.8257(13)
Bi(1)-Rh(6)#1	2.8257(13)
Bi(1)-Rh(6)#2	2.8257(13)
Bi(1)-Rh(6)#3	2.8257(13)
Bi(1)-Rh(7)#1	2.9763(17)
Bi(1)-Rh(7)	2.9763(17)
Bi(1)-Rh(3)	2.9924(10)
Bi(1)-Rh(3)#1	2.9924(10)
Bi(1)-Rh(3)#2	2.9924(10)
Bi(1)-Rh(3)#3	2.9924(10)
Bi(2)-Rh(7)#1	2.794(2)
Bi(2)-Rh(3)#2	2.7946(13)
Bi(2)-Rh(3)	2.7947(13)
Bi(2)-Rh(8)#2	2.988(2)
Bi(2)-Rh(8)	2.988(2)
Bi(2)-Rh(5)	3.058(2)

Rh(3)-Rh(8)	2.756(2)
Rh(3)-Rh(5)	2.7603(17)
Rh(3)-Rh(6)	2.8274(16)
Rh(3)-Rh(6)#3	3.0014(16)
Rh(3)-Rh(4)	3.0084(17)
Rh(4)-Rh(5)	2.714(2)
Rh(4)-Rh(7)	2.791(2)
Rh(4)-Rh(6)#2	2.9636(17)
Rh(5)-Rh(3)#2	2.7603(17)
Rh(6)-Rh(8)#3	2.694(2)
Rh(6)-Rh(6)#3	2.925(3)
Rh(6)-Rh(3)#3	3.0013(16)
Rh(6)-Rh(7)	3.0151(18)
Rh(7)-Rh(8)#1	2.686(2)
Rh(7)-Rh(8)#3	2.686(2)
Rh(7)-Bi(2)#1	2.794(2)
Rh(8)-Rh(7)#1	2.686(2)
Rh(8)-Rh(6)#3	2.694(2)

Table 3.9. Most relevant bond lengths for $[Rh_{17}Bi_3(CO)_{33}][NEt_4]_3$.

III.XI. IR and ESI-MS characterization and electron counting of the $[Rh_{17}Bi_3(CO)_{33}]^{4-}$ cluster

$[Rh_{17}Bi_3(CO)_{33}][NEt_4]_4$ is soluble in acetone, acetonitrile and DMF and stable, but not soluble, in water.

Its IR spectrum recorded in CH_3CN shows ν_{CO} absorptions at 2002(sh), 1996(s), 1990(sh), 1872(ms) and 1870(ms) cm^{-1}.

$[Rh_{17}Bi_3(CO)_{33}]^{4-}$ was also characterized by ESI-MS analysis. The spectrum shows characteristic signals at 1673, 1566, 1134, and 1091 m/z, assigned to the $\{[Rh_{17}Bi_3(CO)_{30}][NEt_4]\}^{2-}$, $[Rh_{17}Bi_3(CO)_{27}]^{2-}$, $\{[Rh_{17}Bi_3(CO)_{32}][NEt_4]\}^{3-}$ and $[Rh_{17}Bi_3(CO)_{32}]^{3-}$ ions, respectively.

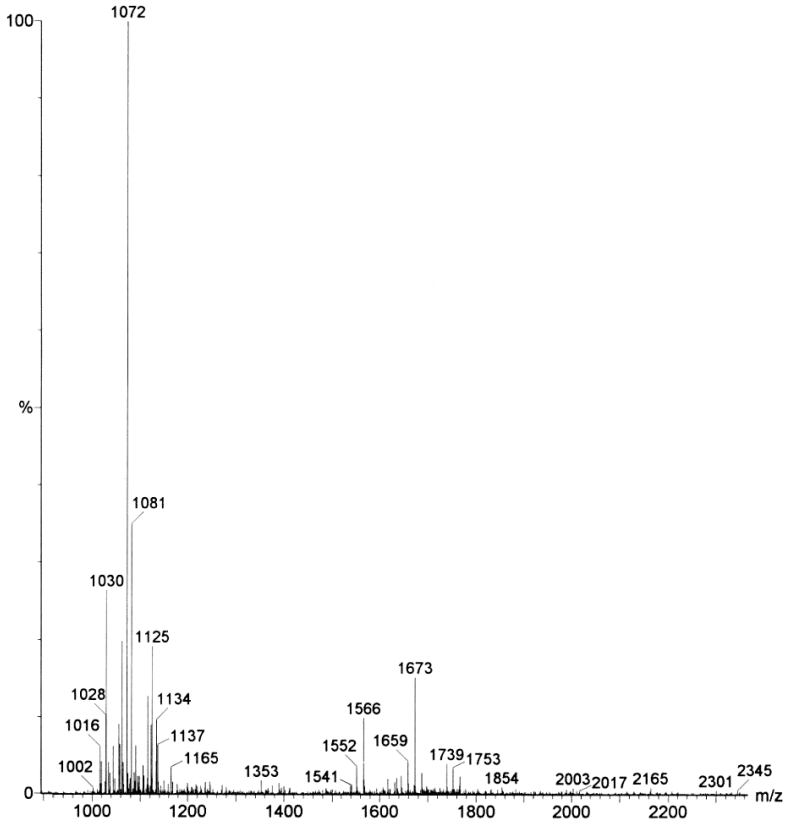

Figure 3.11. ESI-MS spectrum of $[Rh_{17}Bi_3(CO)_{33}][NEt_4]_3$ recorded in CH_3CN solution.

Signals or groups of signals (m/z)	Corresponding Ions
1673-1659	$\{[Rh_{17}Bi_3(CO)_{30\text{-}29}][NEt_4]\}^{2-}$
1566-1552	$[Rh_{17}Bi_3(CO)_{27\text{-}26}]^{2-}$
1134-1125-1116	$\{[Rh_{17}Bi_3(CO)_{32\text{-}31\text{-}30}][NEt_4]\}^{3-}$
1091-1081-1072-1063	$[Rh_{17}Bi_3(CO)_{32\text{-}31\text{-}30\text{-}29}]^{3-}$
1044-1030-1016	$[Rh_{12}Bi(CO)_{23\text{-}22\text{-}21}]^{2-}$

Table 3.10. ESI-MS signal assignments for $[Rh_{17}Bi_3(CO)_{33}][NEt_4]_3$.

$[Rh_{17}Bi_3(CO)_{33}]^{4-}$ is the only Rh-Bi species that does not follow the electron counting rule. In fact, as it can be seen as an icosahedron capped by five metal atoms, 230 CVEs are expected. The same number of valence electrons is obtained when using the condensed polyhedral formalism. However, the actual whole electron counting gives 234 CVEs: 9 × 17 (Rh atoms) + 2 × 33 (CO ligands) + 5 (interstitial Bi atom) + 3 × 2 (surface Bi atoms) + 4 (negative charge). This deviation from the rule is not unprecedented for clusters of similar nuclearity. [27] For instance, bimetallic Rh−Ni carbonyl clusters sharing the same nuclearity and metal architecture but with different numbers of valence electrons are known. [28] Notably, the PSEPT approach is not suitable for gold clusters, even those closer to $[B_{12}H_{12}]^{2-}$ with 12 ligands like $[Pd@Au_{12}(PR_3)_8Cl_4]$ [29] and $[M@(AuPMe_3)_{11}(AuCl)]^{3+}$ (M = Pt, Pd, Ni), for which alternative models can be applied. [30, 31]

Crystallographic data for Rh-Bi carbonyl clusters

Compound	**1**$[NEt_4]_3$	**1**$[NMe_4]_3 \cdot 2(CH_3)_2CO$	**2**$[NEt_4][NMe_4]_4 4(CH_3)_2CO$	**3**$[NMe_4]_3 3CH_3CN$	**4**$[NEt_4]_4$
Formula	$C_{51}H_{60}BiN_3O_{27}Rh_{12}$	$C_{45}H_{48}BiN_3O_{29}Rh_{12}$	$C_{88}H_{92}BiN_5O_{56}Rh_{24}$	$C_{45}H_{45}Bi_3N_6O_{27}Rh_{14}$	$C_{65}H_{80}Bi_3N_4O_{33}Rh_{17}$
Fw	2590.92	2538.76	5212.45	3169.55	3821.74
Crystal system	Monoclinic	Monoclinic	Tetragonal	Orthorhombic	Orthorhombic
Space group	*C*2/*c*	*P*2(1)/*c*	*P*-4n2	*Pna*2$_1$	*C*mca
***a* (Å)**	20.0343(4)	12.5792(7)	17.4735(13)	38.119(5)	24.6007(14)
***b* (Å)**	22.6293(5)	22.5805(12)	17.4735(13)	16.966(2)	23.7403(13)
***c* (Å)**	15.8131(3)	24.8173(13)	22.3715(17)	22.150(3)	15.3839(9)
***α* (deg)**	90	90	90	90	90
***β* (deg)**	102.6850(10)	104.4950(10)	90	90	90
***γ* (deg)**	90	90	90	90	90
Cell volume (Å^3)	6994.1(2)	6824.8(6)	6830.5(9)	14325(3)	8984.6(9)
Z	4	4	2	8	4
D (g/cm^3)	2.461	2.471	2.534	2.939	2.825
μ (mm^{-1})	5.333	5.464	6.739	10.544	8.957
F (000)	4904	4776	4864	11616	7104
***θ* limits (deg)**	1.377-24.999	1.24-25.00	1.48-25.000	1.31-24.000	1.656-25.000
Index ranges	-23≤ *h* ≤23, -26≤ *k* ≤26, -18≤ *l* ≤18	-14≤ *h* ≤14, -26≤ *k* ≤26, -29≤ *l* ≤29	-20≤ *h* ≤20, -20≤ *k* ≤20, -26≤ *l* ≤26	-43≤ *h* ≤43, -19≤ *k* ≤19, -25≤ *l* ≤25	-29≤ *h* ≤29, -28≤ *k* ≤28, -18≤ *l* ≤18
Reflections collected	46309	65094	62807	122815	41787
Independent reflections	6141 [R(int) = 0.0509]	12008 [R(int) = 0.1754]	6014 [R(int) = 0.0626]	22470 [R(int) = 0.2462]	4077 [R(int) = 0.0587]
Completeness to *θ* max	100.0%	100.0%	99.9%	100.0%	100.0%
Data/restraints/ parameters	6141/0/432	12008/120/811	6014/528/457	22470/1686/1711	4077/661/487
Goodness-of-fit	1.073	0.979	1.067	0.993	1.042
R_1 (I > 2σ(I))	0.0271	0.0535	0.0517	0.0733	0.0536
wR_2 (all data)	0.0698	0.0957	0.1263	0.1621	0.1522
Largest diff. peak and hole, e Å^{-3}	1.625 and -0.882	1.128 and -0.870	2.142 and -0.857	1.792 and -1.681	1.827 and -1.909

Table 3.11. Crystallographic data for clusters 1, 2, 3 and 4.

1 R. K. Grasselli, *Catal. Today* **2014**, *238*, 10.

2 R. D. Adams, M. Chen, G. Elpitiya, M. E. Potter, R. Raja, *ACS Catal.* **2013**, *3*, 3106.

3 W. Kruppa, D. Bläser, R. Boese, G. Schmid, *Z. Naturforsch., B: J. Chem. Sci.* **1982**, *37*, 209.

4 K. H. Whitmire, M. R. Churchill, J. C. Fettinger, *J. Am. Chem. Soc.* **1985**, *107*, 1056.

5 K. H. Whitmire, J. R. Eveland, J. Chem. Soc., Chem. Commun. 1994, 1335.

6 J. M. Goicoechea, M. W. Hull, S. C. Sevov, J. Am. Chem. Soc. 2007, 129, 7885.

7 L. G. Perla, S. C. Sevov, *Inorg. Chem.* **2015**, *54*, 8401.

8 R. D. Adams, G. Elpitiya, *J. Organomet. Chem.* **2016**, *812*, 115.

9 S. Martinengo, G. Ciani, *Chem*. Commun. 1987, 1589.

10 T. A. Albright, K. A. Yee, J.-Y. Saillard, S. Kahlal, J.-F. Halet, J.S. Leigh, K.H. Whitmire, *Inorg. Chem.* **1991**, *30*, 1179.

11 C. Femoni, G. Bussoli, I. Ciabatti, M. Ermini, M. Hayatifar, M. C. Iapalucci, S. Ruggieri, S. Zacchini, *Inorg. Chem.* **2017**, *56*, 6343.

12 C. Femoni, M. C. Iapalucci, G. Longoni, C. Tiozzo, S. Zacchini, B. T. Heaton, J. A. Iggo, *Dalton Trans.* **2007**, *35*, 3914.

13 C. Femoni, M. C. Iapalucci, G. Longoni, C. Tiozzo, S. Zacchini, B. T. Heaton, J. A. Iggo, P. Zanello, S. Fedi, M. V. Garland, C. Li, *Dalton Trans.* **2009**, 2217.

14 D. Collini, F. F. De Biani, S. Fedi, C. Femoni, F. Kaswalder, M. C. Iapalucci, G. Longoni, C. Tiozzo, S. Zacchini, P. Zanello, *Inorg. Chem.* **2007**, *46*, 7971.

15 H. Zhang, B. K. Teo, *Inorg. Chim. Acta* **1997**, *265*, 213.

16 A. Ceriotti, F. Demartin, B. T. Heaton, P. Ingallina, G. Longoni, M. Manassero, M. Marchionna, N. Masciocchi, *J. Chem. Soc., Chem. Commun.* **1989**, 786.

17 N. T. Tran, D. R. Powell, L. F. Dahl, *Angew. Chem., Int. Ed.* **2000**, *39*, 4121.

18 J. D. Erickson, E. G. Mednikov, S. A. Ivanov, L. F. Dahl, *J. Am. Chem. Soc.* **2016**, *138*, 1502.

19 A. Puls, P. Jerabek, W. Kurashige, M. Förster, M. Molon, T. Bollermann, M. Winter, C. Gemel, Y. Negishi, G. Frenking, R. A. Fischer, *Angew. Chem., Int. Ed.* **2014**, *53*, 4327.

20 M. Zhu, E. Lanni, N. Garg, M. E. Bier, R. Jin, *J. Am. Chem. Soc.* **2008**, *130*, 1138.

21 H. Qian, W. T. Eckenhoff, Y. Zhu, T. Pintauer, R. Jin, *J. Am. Chem. Soc.* **2010**, *132*, 8280.

22 Y. Song, F. Fu, J. Zhang, J. Chai, X. Kang, P. Li, S. Li, H. Zhou, M. Zhu, *Angew. Chem., Int. Ed.* **2015**, *54*, 8430.

23 A. Desireddy, B. E. Conn, J. Guo, B. Yoon, R. N. Barnett, B. M. Monahan, K. Kirschbaum, W. P. Griffith, R. L. Whetten, U. Landman, T. P. Bigioni, *Nature* **2013**, *501*, 399.

24 P. Chini, S. Martinengo, *Inorg. Chim. Acta* **1969**, *3(C)*, 299.

25 C. Femoni, M. C. Iapalucci, G. Longoni, C. Tiozzo, S. Zacchini, B. T. Heaton, J. A. Iggo, P. Zanello, S. Fedi, M. V. Garland, C. Li, *Dalton Trans.* **2009**, 2217.

26 D. M. P. Mingos, *Pure Appl. Chem.* **1991**, *63*, 807.

27 C. Femoni, F. Kaswalder, M. C. Iapalucci, G. Longoni, S. Zacchini, Coord. Chem. Rev. **2006**, *250*, 1580.

28 D. Collini, C. Femoni, M. C. Iapalucci, G. Longoni, P. H. Svensson, P. Zanello, *Angew. Chem., Int. Ed.* **2002**, *41*, 3685.

29 M. Laupp, J. Sträle, *Z. Naturforsch.* **1995**, *50b*, 1369.

30 P. Pyykkö, *J. Organomet. Chem.* **2006**, *691*, 4336.

31 H. Häkkinen, *Chem. Soc. Rev.* **2008**, *37*, 1847.

CHAPTER IV

New Rhodium-Germanium Carbonyl Clusters

In order to keep on the investigation of heterometallic Rh carbonyl clusters, we focused our attention on the possibility of obtaining species with germanium encapsulated in the metal cage.

The chemistry of transition metal carbonyl clusters decorated by organogermanium ligands is well documented. There are many reported Ge-containing carbonyl species with more than two metal atoms, including $[Ru_3\{\mu\text{-}Ge(NCH_2CMe_3)_2C_6H_4\}_3(CO)_9]$, [1] $Ir_4(CO)_8(GePh_3)_2(\mu\text{-}GePh_2)_4$, [2] and $Ru_6(CO)_{12}(\mu_3\text{-}Ge^tBu)_4(H)_2$, [3] but only a few with Rh, namely $Rh_3(CO)_5(GePh_3)(\mu\text{-}GePh_2)_3(\mu_3\text{-}GePh)(\mu\text{-}H)$, and $Rh_8(CO)_{12}(\mu_4\text{-}GePh)_6$. [4] However, to the best of our knowledge, there were no examples of Rh clusters with fully encapsulated Ge atoms before our investigation. The only transition metal carbonyl cluster with an interstitial germanium atom was the icosahedral $[Ge@Ni_{12}(CO)_{22}]^{2-}$ dianion. [5] Conversely, many germanium Zintl ions that host interstitial transition metals in polyhedral cages are known, as in $[Ru@Ge_{12}]^{3-}$, [6] $[Fe@Ge_{10}]^{3-}$, [7] $[Co@Ge_{10}]^{3-}$, [8] $[Pd_2@Ge_{18}]^{4-}$ [9] and $[Ni_3@Ge_{18}]^{4-}$. [10] They can also be decorated by transition metal fragments giving rise, for instance, to $[Ge_{12}\{FeCp(CO)_2\}_8\{FeCp(CO)\}_2]$ [11] and $[Ge_{10}Mn(CO)_4]^{3-}$. [12] Finally, germanium clusters can be found fused with other metal units as in $[Ge_{18}Pd_3(SnPr_3)_6]^{2-}$ [13] and $[Ge_{18}Au_3]^{5-}$, [14] or combined with them to create new architectures, as in $[Ni_6Ge_{13}(CO)_5]^{4-}$. [15]

General results

The following sections show the study of the reactivity of $[Rh_7(CO)_{16}][NEt_4]_3$ cluster precursor with $GeBr_2$ in different stoichiometric ratios and under different atmospheres, [16, 17] which led to the synthesis of four new nanoclusters.

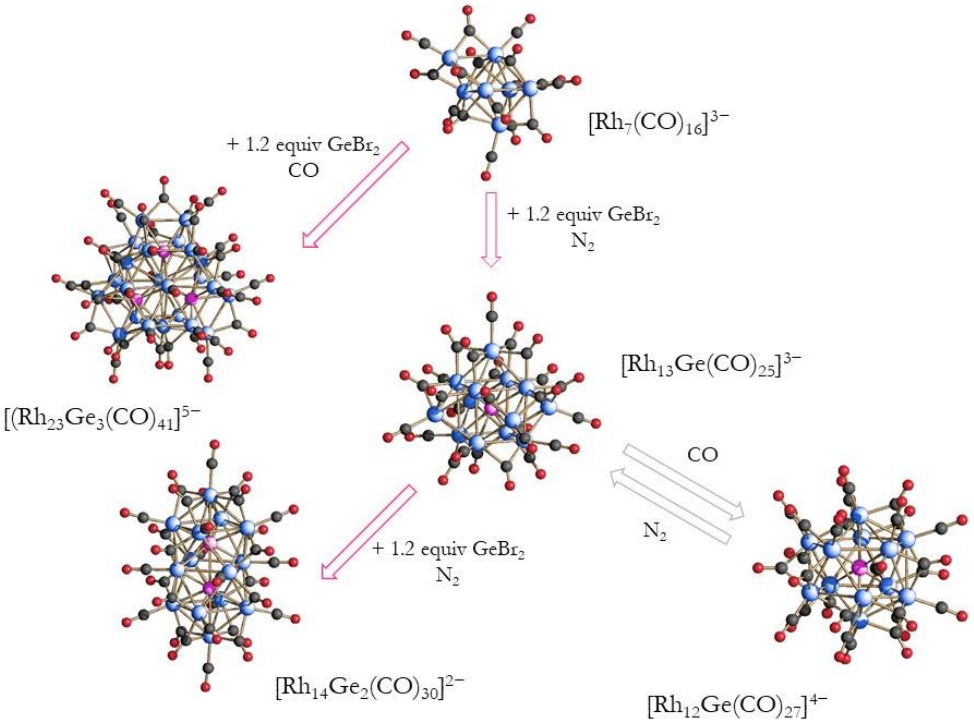

Figure 4.1 Reaction scheme of Rh-Ge system. Rh atoms are depicted in blue, Ge atoms are depicted in magenta, C atoms are in grey and O atoms are in red.

IV.I. Reactivity of $[Rh_7(CO)_{16}]^{3-}$ with $GeBr_2$ under N_2 atmosphere

The first reaction we investigated in Rh-Ge system is the one between the cluster precursor $[Rh_7(CO)_{16}][NEt_4]_3$ and 0.75 equivalents of $GeBr_2$ in acetonitrile, in line with what had been previously done for Rh-Bi system. Indeed, our first target was represented by an hypothetic icosahedral $Rh_{12}Ge$ cluster. However, it was clear from the beginning that this system had a different behaviour from Rh-Bi and Rh-Sn ones. In fact, the reaction did not lead to the expected product, but to the already known $[Rh_7(CO)_{16}Br]^{2-}$ cluster, previously obtained via a different route. [18] Therefore, we increased the amount of the Ge^{2+} salt and only when we reached the Rh_7:Ge^{2+} stoichiometric ratio of 1:1.2 we obtained a mixture which, analysed by IR spectroscopy, presented the complete disappearance of the ν_{CO} absorptions of both the cluster precursor and $[Rh_7(CO)_{16}Br]^{2-}$.

The work-up of the mother solution was conducted by drying it under vacuum, washing the solid residue with water in order to eliminate all the residual salts, and then with ethanol and THF to eliminate the $[Rh(CO)_2Br_2]^-$ complex. In acetone we extracted a new species and by layering hexane onto the solution it was possible to crystallize it and identify it as $[Rh_{13}Ge(CO)_{25}]^{3-}$. Surprisingly, this cluster was not the expected icosahedral equivalent of the Rh-Bi system as its molecular structure is based on a *bcc* lattice (see later) with the Ge atom hosted in the cubic cavity. Considering the different sizes of the icosahedral and the cubic Rh cages, this significant structural difference from the $[Rh_{12}E(CO)_{27}]^{n-}$ family of clusters may be due to the smaller radius of germanium compared with those of the Sn and Bi atoms. [19]

The reaction which led to the formation of this heterometallic cluster can be written as follow:

$$2[Rh_7(CO)_{16}]^{3-} + 2GeBr_2 \rightarrow [Rh_{13}Ge(CO)_{25}]^{3-} + 2Br^- + [Rh(CO)_2Br_2]^- + Ge + 5CO \quad (1)$$

However, a slight excess of $GeBr_2$ is needed for the complete conversion of the starting material in favour of $[Rh_{13}Ge(CO)_{25}]^{3-}$.

The new $[Rh_{13}Ge(CO)_{25}]^{3-}$ heterometallic cluster had been initially mistaken for the isostructural $[HRh_{14}(CO)_{25}]^{3-}$ [20] homometallic compound, that could not have been discarded as a possible reaction product. In fact, $[HRh_{14}(CO)_{25}]^{3-}$ is one of the reaction products when $[Rh_7(CO)_{16}]^{3-}$ reacts with $GeCl_4$, which we utilized at the beginning of our study but that we abandoned due to the predominant formation of $[Rh(CO)_2Cl_2]^-$.

Thus, it was necessary to characterize $[Rh_{13}Ge(CO)_{25}]^{3-}$ with ancillary techniques in order to unravel, without any doubt, its heterometallic nature (see section IV.III).

IV.II. Molecular structure of the $[Rh_{13}Ge(CO)_{25}]^{3-}$ cluster

The cluster compound crystallized in the tetragonal *P*4/ncc space group with Z = 4 as $[Rh_{13}Ge(CO)_{25}][NEt_4]_3 \cdot [NEt_4]Br$.

The molecular structure of $[Rh_{13}Ge(CO)_{25}]^{3-}$ (1) is illustrated in Figure 4.2.

It consists of a slightly-irregular penta-capped cube of rhodium atoms centred by the unique Ge, and stabilized by 25 carbonyl groups, of which 9 are terminal and 16 edge bridging. The sole uncapped cubic face shows the shortest Rh-Rh distance (2.7597(8) Å), while all the other distances within the cube are significantly longer, going from 2.9335(8) to 2.9638(8) Å (average 2.9486 Å). The bonding interactions between the capping atoms and the cube vertexes are somewhat intermediate, varying from 2.7576(8) to 2.8273(10) Å (average 2.8071 Å). The eight Ge-Rh bonds range from 2.4549(9) to 2.5565 (10) Å, with an average value of 2.5057 Å, and are in line with those reported for similar compounds. All Rh-Rh bond lengths in this heterometallic cluster are slightly shorter but comparable with those found in the parent $[HRh_{14}(CO)_{25}]^{3-}$ homometallic species. The difference is likely due to the larger radius of Rh than Ge and the presence of an additional interstitial hydride in the latter, which further swells the cluster.

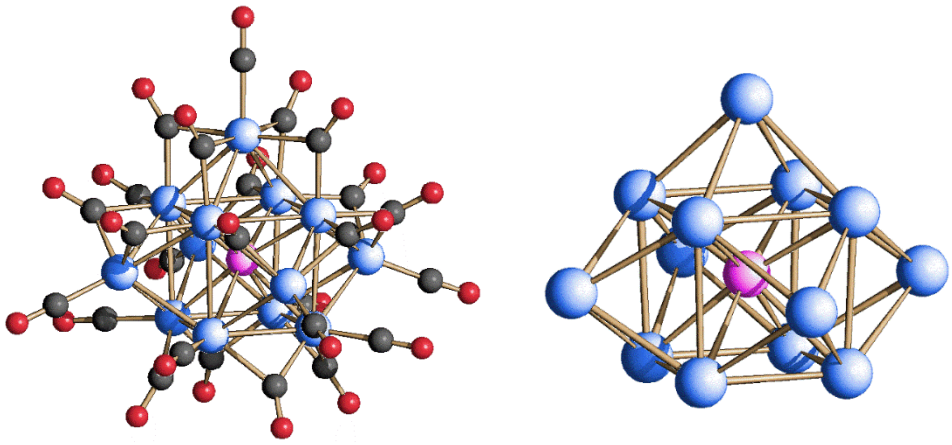

Figure 4.2. Molecular structure of $[Rh_{13}Ge(CO)_{25}]^{3-}$ (left) and its metal skeleton (right). Rh atoms are depicted in blue, Ge atoms are depicted in magenta, C atoms are in grey and O atoms are in red.

Rh(1)-Ge(5)	2.5565(10)
Rh(2)-Ge(5)	2.4548(9)
Ge(5)-Rh(2)#1	2.4549(9)
Ge(5)-Rh(2)#3	2.4549(9)
Ge(5)-Rh(2)#2	2.4549(9)
Ge(5)-Rh(1)#1	2.5565(10)
Ge(5)-Rh(1)#3	2.5565(10)
Ge(5)-Rh(1)#2	2.5565(10)
Rh(1)-Rh(1)#1	2.7597(8)
Rh(1)-Rh(1)#2	2.7597(8)
Rh(1)-Rh(4)#3	2.8191(8)
Rh(1)-Rh(4)#1	2.8261(8)
Rh(1)-Rh(2)#1	2.9335(8)

Rh(2)-Rh(4)#1	2.7576(8)
Rh(2)-Rh(4)	2.7632(8)
Rh(2)-Rh(3)	2.8273(10)
Rh(2)-Rh(1)#2	2.9335(8)
Rh(2)-Rh(2)#2	2.9638(8)
Rh(2)-Rh(2)#1	2.9638(8)
Rh(3)-Rh(2)#3	2.8273(10)
Rh(3)-Rh(2)#2	2.8273(10)
Rh(3)-Rh(2)#1	2.8273(10)
Rh(4)-Rh(2)#2	2.7576(8)
Rh(4)-Rh(1)#3	2.8192(8)
Rh(4)-Rh(1)#2	2.8261(8)

Table 4.1. Most relevant bond lengths for $[Rh_{13}Ge(CO)_{25}]^{3-}$.

The maximum size of the $[Rh_{13}Ge(CO)_{25}]^{3-}$ cluster, measured from the outermost oxygen atoms of the carbonyl ligands and including twice the oxygen van der Waals radius, is 1.5 nm.

In the literature there are other reported heterometallic Rh clusters based on this same cubic structure, such as $[NiRh_{13}(CO)_{25}]^{5-}$, $[Ni_2Rh_{12}(CO)_{25}]^{4-}$ and $[Ni_5Rh_9(CO)_{25}]^{3-}$. [21] Remarkably, despite their different CVEs, all of them and $[Rh_{13}Ge(CO)_{25}]^{3-}$, as well as the homometallic $[H_xRh_{14}(CO)_{25}]^{(4-x)-}$ (x = 0, 1) clusters, are coordinated by the same number of carbonyl ligands.

IV.III. IR and ESI-MS characterization and electron counting of the $[Rh_{13}Ge(CO)_{25}]^{3-}$ cluster

$[Rh_{13}Ge(CO)_{25}]^{3-}$ as salt of $[NEt_4]^+$ is soluble in acetone, acetonitrile and DMF and stable, but not soluble, in water.

Its IR spectrum recorded in CH_3CN shows ν_{CO} absorptions at 1987(vs), 1885(mw) and 1834(ms) cm^{-1}. Conversely, the absorptions signals of the known homometallic $[HRh_{14}(CO)_{25}]^{3-}$ cluster are at 1989(vs) and 1839(ms) cm^{-1}. Still, despite their different shapes, those IR spectra have frequencies quite close in values and, again, could not alone sustain a definite identification. Providentially, the ESI-MS analysis unambiguously confirmed the identity of the heterometallic cluster and ruled out the homometallic one, as the two spectra are completely different.

As a matter of fact, the spectrum of $[Rh_{13}Ge(CO)_{25}]^{3-}$ (Figure 4.3) exhibits a peak at 694 m/z, due to the $[Rh_{13}Ge(CO)_{24}]^{3-}$ trianion, a less intense group of peaks from 1056 to 984 m/z due to the $[Rh_{13}Ge(CO)_{25}]^{2-}$ dianion (accompanied by successive CO loss), and a peak at 1106 m/z of the $\{[Rh_{13}Ge(CO)_{24}][NEt_4]\}^{2-}$ ion. Other minor peaks due to cluster fragmentation are also present. The spectrum of $[HRh_{14}(CO)_{25}]^{3-}$ (Figure 4.4), on the contrary, displays three main peaks at 1200 ($\{[HRh_{14}(CO)_{25}][NEt_4]_2\}^{2-}$), 1135 ($\{[HRh_{14}(CO)_{25}][NEt_4]\}^{2-}$) and 1070-1056 ($[HRh_{14}(CO)_{25/24}]^{2-}$) m/z, with no signs of cluster breaking in the experimental conditions.

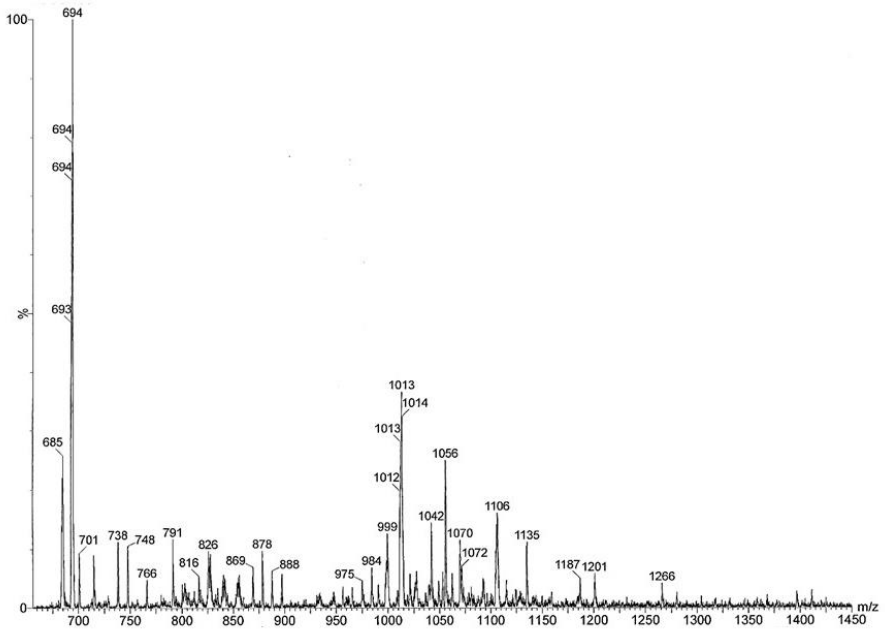

Figure 4.3. ESI-MS spectrum of $[Rh_{13}Ge(CO)_{25}][NEt_4]_3 \cdot [NEt_4]Br$ recorded in CH_3CN solution.

Peaks or groups of peaks (m/z)	Corresponding Ions
1106	$\{[Rh_{13}Ge(CO)_{24}][NEt_4]\}^{2-}$
1056-1042-1013-999-984	$[Rh_{13}Ge(CO)_{25\text{-}24\text{-}22\text{-}21\text{-}20}]^{2-}$
694-685	$[Rh_{13}Ge(CO)_{24\text{-}23}]^{3-}$

Table 4.2. ESI-MS signal assignments for $[Rh_{13}Ge(CO)_{25}][NEt_4]_3 \cdot [NEt_4]Br$.

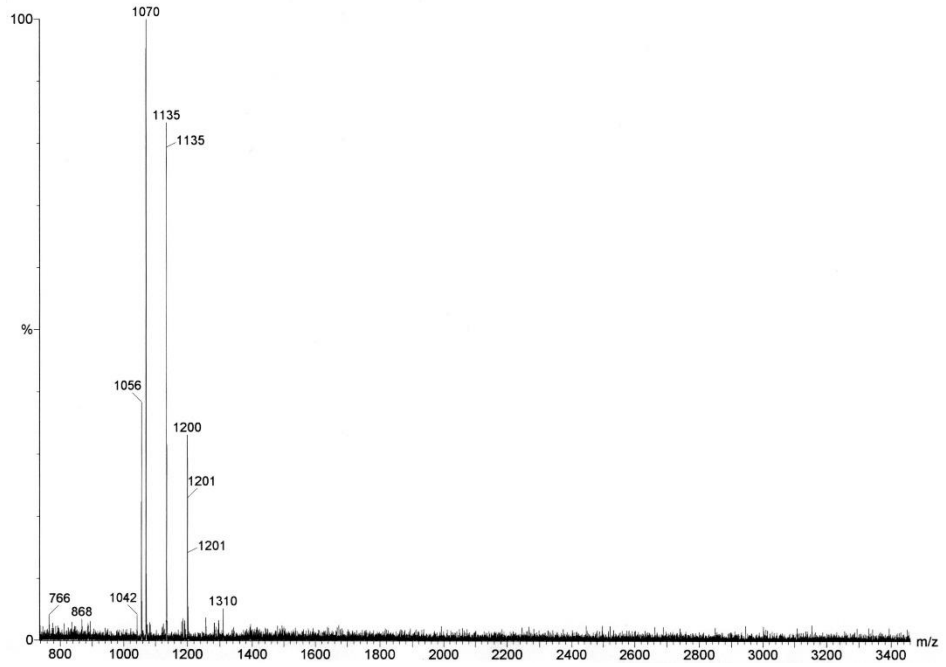

Figure 4.4. ESI-MS spectrum of $[HRh_{14}(CO)_{25}][NEt_4]_3$ recorded in CH_3CN solution.

Peaks or groups of peaks (m/z)	Corresponding Ions
1070-1057	$[HRh_{14}(CO)_{25-24}]^{2-}$
1135	$\{[HRh_{14}(CO)_{25}][NEt_4]\}^{2-}$
1200	$\{[HRh_{14}(CO)_{25}][NEt_4]_2\}^{2-}$

Table 4.3. ESI-MS signal assignments for $[HRh_{14}(CO)_{25}][NEt_4]_3$.

As for the electron counting, the $[Rh_{13}Ge(CO)_{25}]^{3-}$ should possess 180 CVEs being a penta-capped cube; however, this cluster only presents 174 CVEs, given by the 9 × 13 rhodium atoms (117), the 2 × 25 carbonyl ligands (50), the interstitial Ge atom (4), and the negative charge (3). It could be interesting to make a comparison among the electron counting of this cluster and that of the other previously mentioned species based on the same geometry. The first one that we are going to take into consideration is the homometallic $[HRh_{14}(CO)_{25}]^{3-}$ cluster, which is

conform to the Polyhedral Skeleton Electron Pair Theory; indeed, it possesses 180 CVEs given by the 9 × 14 rhodium atoms (126), the 2 × 25 carbonyl ligands (50), the H atom (1) and the negative charge (3). Note that the non-hydride $[Rh_{14}(CO)_{25}]^{4-}$ congener has the same number of CVEs.

Conversely, a major number of CVEs is present in $[NiRh_{13}(CO)_{25}]^{5-}$ (182), given by the nickel atom (10), the 9 × 13 rhodium atoms (117), the 2 × 25 carbonyl ligands (50) and the negative charge (5). The same number of CVEs is present in $[Ni_2Rh_{12}(CO)_{25}]^{4-}$, because of the 10 × 2 nickel atoms (20), the 9 × 12 rhodium atoms (108), the 2 × 25 carbonyl ligands (50) and the negative charge (4). Finally, the $[Ni_5Rh_9(CO)_{25}]^{3-}$ species presents 184 CVEs given by the 10 × 5 nickel atoms (50), the 9 × 9 rhodium atoms (81), the 2 × 25 carbonyl ligands (50) and the negative charge (3).

We can affirm that even if all these clusters are based on the same metal structure and possess the same number of carbonyl ligands, the role of the interstitial atom seems to have a significant impact on the number of their CVEs. Notably, this is at its lowest when the cubic cage is centred by the post-transition Ge element in $[Rh_{13}Ge(CO)_{25}]^{3-}$ (174 CVEs), it has an intermediate value when the interstitial atom is Rh (180 CVEs) in $[H_xRh_{14}(CO)_{25}]^{(4-x)-}$ (x = 0, 1), and higher values are observed when the cubic cage hosts Ni. Among $[NiRh_{13}(CO)_{25}]^{5-}$, $[Ni_2Rh_{12}(CO)_{25}]^{4-}$ (both with 182 CVEs) and $[Ni_5Rh_9(CO)_{25}]^{3-}$ (184 CVEs), the highest value is achieved by the latter, which presents several peripheral Ni atoms.

IV.IV. Reactivity of $[Rh_{13}Ge(CO)_{25}]^{3-}$ with $GeBr_2$ under N_2 atmosphere

Once $[Rh_{13}Ge(CO)_{25}]^{3-}$ had been characterized, we decided to test its reactivity with further amount of $GeBr_2$ under nitrogen atmosphere, to verify the possibility of obtaining higher nuclearity Rh-Ge clusters, similarly with what had been done for the Rh-Bi system. To observe the complete disappearance of ν_{CO} absorptions of the Rh-Ge cluster precursor it was necessary to reach the final $Rh_{13}Ge:Ge^{2+}$ stoichiometric ratio of 1:1.2. During the work-up, after the elimination of the usual

$[Rh(CO)_2Br_2]^-$ complex, the new $[Rh_{14}Ge_2(CO)_{30}]^{2-}$ cluster was extracted in acetone and crystallized by layering hexane on top of the acetone solution.

It is possible to obtain $[Rh_{14}Ge_2(CO)_{30}]^{2-}$ also by directly reacting $[Rh_7(CO)_{16}]^{3-}$ with 1.9 equivalents of $GeBr_2$ under N_2 atmosphere, therefore the $[Rh_{13}Ge(CO)_{25}]^{3-}$ cluster can be considered as a reaction intermediate. Beyond a stoichiometric ratio between $Rh_{13}Ge$ and Ge^{2+} of 1:1.5, the reaction results in a degradation into Rh(I) complexes.

IV.V. Molecular structure of the $[Rh_{14}Ge_2(CO)_{30}]^{2-}$ cluster

The cluster compound crystallized in the triclinic *P*-1 space group with Z = 4 as $[Rh_{14}Ge_2(CO)_{30}][NEt_4]_2$.

The molecular structure of $[Rh_{14}Ge_2(CO)_{30}]^{2-}$ (2) is illustrated in Figure 4.5.

It consists of two mono-capped square antiprisms fused via one face, and inside each anti-prismatic cavity lays one germanium atom.

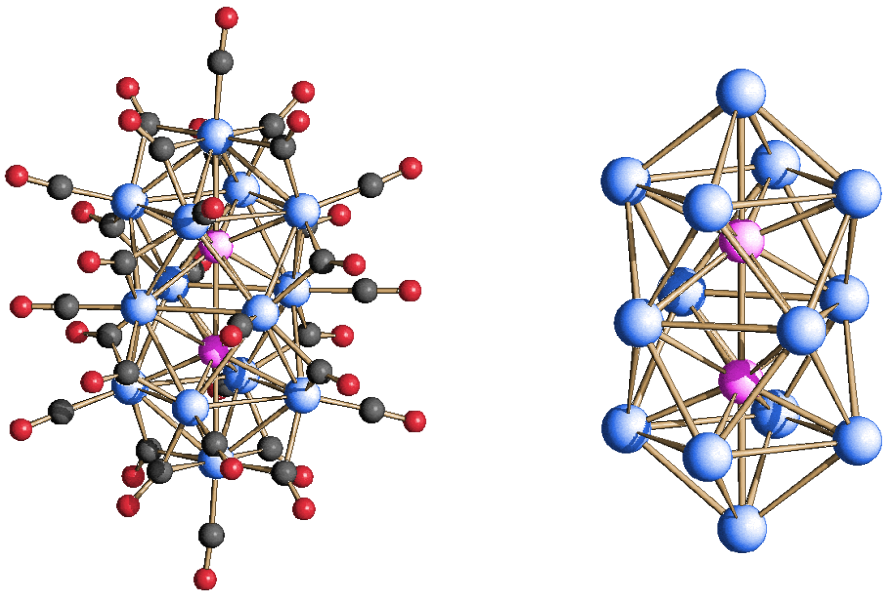

Figure 4.5. Molecular structure of $[Rh_{14}Ge_2(CO)_{30}]^{2-}$ (left) and its metal skeleton (right). Rh atoms are depicted in blue, Ge atoms are depicted in magenta, C atoms are in grey and O atoms are in red.

The anti-prismatic cage size is similar to the cubic one of $[Rh_{13}Ge(CO)_{25}]^{3-}$, demonstrating that the (small) Ge atom prefers not to be hosted in larger Rh cavities, such as an icosahedron.

Rh(1)-Ge(8)	2.4796(19)	Rh(2)-Rh(5)	2.8823(17)
Rh(2)-Ge(8)	2.4711(19)	Rh(2)-Rh(7)#1	2.8854(15)
Rh(3)-Ge(8)	2.4862(19)	Rh(2)-Rh(6)#1	2.9820(16)
Rh(4)-Ge(8)	2.4829(18)	Rh(2)-Rh(3)	3.1694(17)
Rh(5)-Ge(8)	2.8119(18)	Rh(3)-Rh(5)	2.8668(16)
Rh(6)-Ge(8)#1	2.6009(19)	Rh(3)-Rh(6)	2.8946(16)
Rh(6)-Ge(8)	2.6166(18)	Rh(3)-Rh(7)#1	2.9660(16)
Rh(7)-Ge(8)#1	2.6097(19)	Rh(4)-Rh(5)	2.8740(17)
Rh(7)-Ge(8)	2.6114(19)	Rh(4)-Rh(6)#1	2.8785(16)
Ge(8)-Rh(6)#1	2.6009(19)	Rh(4)-Rh(7)	2.9625(15)
Ge(8)-Rh(7)#1	2.6097(19)	Rh(6)-Rh(4)#1	2.8785(16)
Ge(8)-Ge(8)#1	2.678(3)	Rh(6)-Rh(2)#1	2.9820(16)
Rh(1)-Rh(5)	2.8790(16)	Rh(6)-Rh(7)#1	3.1415(17)
Rh(1)-Rh(7)	2.8811(16)	Rh(6)-Rh(7)	3.1938(16)
Rh(1)-Rh(6)	2.9724(16)	Rh(7)-Rh(2)#1	2.8854(15)
Rh(1)-Rh(4)	3.1913(17)	Rh(7)-Rh(3)#1	2.9659(16)
Rh(1)-Rh(3)	3.1975(17)	Rh(7)-Rh(6)#1	3.1415(17)

Table 4.4. Most relevant bond lengths for $[Rh_{14}Ge_2(CO)_{30}]^{2-}$.

The Ge-Rh bond lengths may be divided into three categories depending on the involved Rh atoms: those of the inner square, the outer square faces, and finally the apical atoms. The former bond lengths are the shortest, having an average value of 2.4800 Å (from 2.4711(19) to 2.4862(19) Å), the latter are the longest ones (both 2.8119(18) Å), and those involving the outer square faces show intermediate bond lengths of 2.6182 Å (from 2.6009(19) to 2.6166(18) Å). These bond lengths are comparable with those found in $[Rh_{13}Ge(CO)_{25}]^{3-}$.

As for the Rh-Rh bond contacts, they span from 2.8740(17) to 3.1975(17) Å, with an average value of 2.9851 Å, slightly longer than those observed in

$[Rh_{13}Ge(CO)_{25}]^{3-}$ cluster. Finally, there is a bond distance of 2.678(3) between the two Ge atoms, comparable with those reported in the literature for Ge cluster compounds. [22]

The metal frame is stabilized by 30 carbonyl ligands, 14 of which are terminal and the remaining 16 are edge bridging.

The maximum size of the $[Rh_{14}Ge_2(CO)_{30}]^{2-}$ cluster, measured from the outermost oxygen atoms of the carbonyl ligands and including twice the oxygen van der Waals radius, is 1.7 nm.

IV.VI. IR and ESI-MS characterization and electron counting of the $[Rh_{14}Ge_2(CO)_{30}]^{2-}$ cluster

$[Rh_{14}Ge_2(CO)_{30}]^{2-}$ as salt of $[NEt_4]^+$ is soluble in acetone, acetonitrile and DMF and stable, but not soluble, in water.

The IR spectrum, recorded in acetonitrile, displays main peaks at 2012(vs) and 1837(ms) cm^{-1}.

The ESI-MS analysis, performed on the same solution of the IR one, shows that under the experimental conditions significant loss of Rh(CO) fragments occurs. The peak at 1185 m/z can be attributed to the integer $[Rh_{14}Ge_2(CO)_{28}]^{2-}$, while the others at 1134, 869, 757 and 627 m/z are due to the fragmented $[Rh_{13}Ge_2(CO)_{28}]^{2-}$, $\{[Rh_9Ge(CO)_{17}][NEt_4]_2\}^{2-}$, $[Rh_{13}Ge_2(CO)_{28}]^{3-}$ and $[Rh_{11}Ge(CO)_{24}]^{3-}$ ions, respectively.

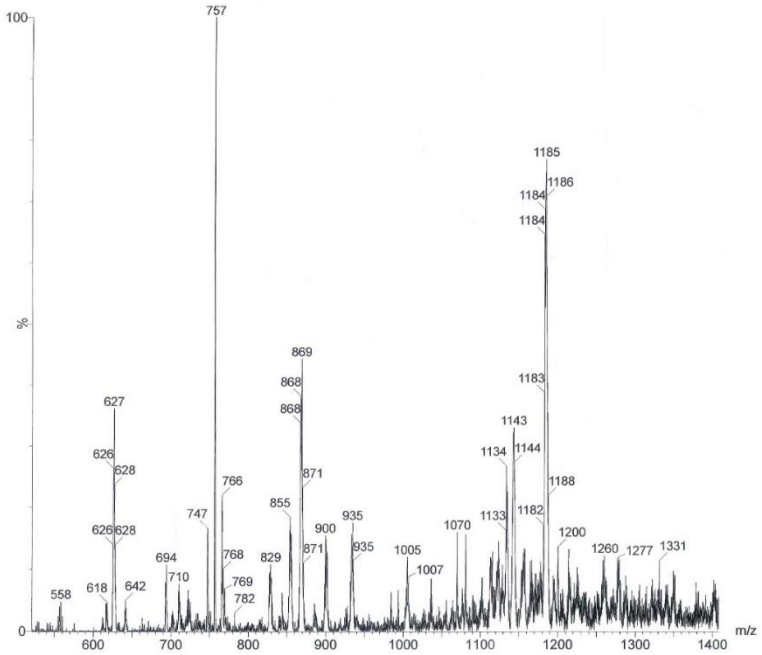

Figure 4.6. ESI-MS spectrum of $[Rh_{14}Ge_2(CO)_{30}][NEt_4]_2$ recorded in CH_3CN solution.

Peaks or groups of peaks (m/z)	Corresponding Ions
1185-1143	$[Rh_{14}Ge_2(CO)_{28\text{-}25}]^{2-}$
1134	$[Rh_{13}Ge_2(CO)_{28}]^{2-}$
869-855	$\{[Rh_9Ge(CO)_{17\text{-}16}][NEt_4]_2\}^{2-}$
766-757-747	$[Rh_{13}Ge_2(CO)_{29\text{-}28\text{-}27}]^{3-}$
627-618	$[Rh_{11}Ge(CO)_{24\text{-}23}]^{3-}$

Table 4.5. ESI-MS signal assignments for $[Rh_{14}Ge_2(CO)_{30}][NEt_4]_2$.

As for the electron counting, $[Rh_{14}Ge_2(CO)_{30}]^{2-}$ should possess 196 CVEs as it can be seen as two capped square antiprisms (2 × 130) fused through a base (−64). As a matter of fact, this cluster presents 196 CVEs, given by the 9 × 14 rhodium atoms (126), the 2 × 30 carbonyl ligands (60), the 4 × 2 interstitial Ge atoms (8), and the negative charge (2). We find the same electron counting in $[Ni_{14}P_2(CO)_{22}]^{2-}$ [23] where the 196 CVEs are given by the 10 × 14 nickel atoms (140), the 2 × 22

carbonyl ligands (44), the 5 × 2 interstitial P atoms (10), and the negative charge (2). These two clusters are indeed based on the same metal structure, but the major number of electrons in nickel skeleton involves a minor number of ligands to stabilize the entire compound. The $[Ni_{14}P_2(CO)_{22}]^{2-}$ species was synthesised through the redox condensation method by working in similar conditions of those that led to $[Ni_{11}P(CO)_{18}]^{3-}$ and $[H_{6-n}Ni_{31}P_4(CO)_{39}]^{n-}$. [24]

IV.VII. Reactivity of $[Rh_{13}Ge(CO)_{25}]^{3-}$ under CO atmosphere

Since $[Rh_{13}Ge(CO)_{25}]^{3-}$ could be obtained in good yields, we tested its stability under CO atmosphere and the result was completely different if compared to the Rh-Bi system. Indeed, when an acetonitrile solution of $[Rh_{13}Ge(CO)_{25}][NEt_4]_3 \cdot [NEt_4]Br$ was placed under vacuum for a few minutes, purged with CO and then left to stand overnight under stirring, the resulting solution presented different ν_{CO} absorptions from the ones of the starting cluster. In fact, they shifted from 1987(vs), 1884(w) and 1834(ms) cm^{-1} to 1997(vs), 1989(s), 1850(sh), 1823(ms) and 1756(sh) cm^{-1}. Without further work-up, by layering di-isopropyl ether on the top of the resulting acetonitrile solution, we obtained crystals which allowed us to identify the new compound as $[Rh_{12}Ge(CO)_{27}][NEt_4]_4$. Notably, the cubic $[Rh_{13}Ge(CO)_{25}]^{3-}$ tri-anion rearranged to give rise to an icosahedral species, which widens the $[Rh_{12}E(CO)_{27}]^{n-}$ family of clusters. This transformation under CO is reversible, i.e. if the CO is removed and replaced by N_2, icosahedral $[Rh_{12}Ge(CO)_{27}]^{4-}$ reverts to the parent compound $[Rh_{13}Ge(CO)_{25}]^{3-}$. Considering all the experimental evidences we can quite confidently assume that the starting cluster reacts with CO according to the following equation:

$$[Rh_{13}Ge(CO)_{25}]^{3-} + 2Br^- + 4CO \leftrightarrows [Rh_{12}Ge(CO)_{27}]^{4-} + [Rh(CO)_2Br_2]^- \quad (2)$$

The disproportion of $[Rh_{13}Ge(CO)_{25}]^{3-}$ into the Rh(I) complex and the more reduced heterometallic cluster $[Rh_{12}Ge(CO)_{27}]^{4-}$ is apparently only induced by CO,

and it is likely to be the result of the energetic balance of the Rh-CO, Rh-Rh and Rh-Ge interactions. Conversely, the $[Rh_{14}Ge_2(CO)_{30}]^{2-}$ cluster does not undergo to any change when put under CO atmosphere.

The icosahedral arrangement is actually quite common in both homo- and bimetallic clusters of the coinage metals [25] and in homometallic Pd clusters, which display a distinct propensity for condensed, fused or interpenetrating centred icosahedral frameworks. [26]

IV.VIII. Molecular structure of the $[Rh_{12}Ge(CO)_{27}]^{4-}$ cluster

The cluster compound crystallized in the triclinic *P*-1 space group with Z = 4 as $[Rh_{12}Ge(CO)_{27}][NEt_4]_4 \cdot 2CH_3CN$. The molecular structure of the $[Rh_{12}Ge(CO)_{27}]^{4-}$ (3) anion is illustrated in Figure 4.7.

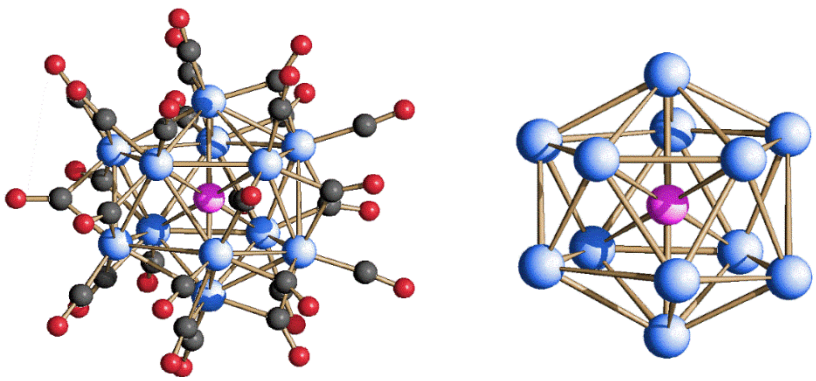

Figure 4.7. Molecular structure of $[Rh_{12}Ge(CO)_{27}]^{4-}$ (left) and its metal skeleton (right). Rh atoms are depicted in blue, Ge atoms are depicted in magenta, C atoms are in grey and O atoms are in red.

The independent unit contains two entire clusters, which are only marginally different in their interatomic distances. The Rh-Ge bond distances are notably longer than those in the cubic congener and span from 2.645(2) to 2.929(2) Å and from 2.647(2) to 2.937(2) Å in the two isomers, with an equal average value of 2.788 Å. The Rh-Rh distances are similar to those in $[Rh_{13}Ge(CO)_{25}]^{3-}$, and vary

from 2.8078(17) to 2.9979(17) Å and from 2.8079(17) to 3.1970(18) Å in the two isomers, with average values of 2.8954 and 2.9057 Å, respectively. Finally, there are Rh-Rh interactions that may be considered as non-bonding in both isomers and which contribute to distance the icosahedral metal frameworks from the ideal polyhedra. These long interactions are in the same positions in both isomers. The metal skeleton of $[Rh_{12}Ge(CO)_{27}]^{4-}$ is stabilized by 27 carbonyl ligands, 12 of which are terminally bonded and the remaining 15 are edge bridging.

Ge(1)-Rh(10)	2,645(2)	Rh(3)-Rh(12)	2,8650(18)
Ge(1)-Rh(9)	2,656(2)	Rh(3)-Rh(6)	2,9158(17)
Ge(1)-Rh(5)	2,6666(19)	Rh(3)-Rh(9)	2,9493(18)
Ge(1)-Rh(3)	2,6677(19)	Rh(3)-Rh(11)	2,9677(18)
Ge(1)-Rh(4)	2,6751(19)	Rh(4)-Rh(8)	2,8392(18)
Ge(1)-Rh(6)	2,6924(19)	Rh(4)-Rh(10)	2,9320(18)
Ge(1)-Rh(2)	2,882(2)	Rh(4)-Rh(5)	2,9452(17)
Ge(1)-Rh(8)	2,893(2)	Rh(5)-Rh(12)	2,8435(18)
Ge(1)-Rh(12)	2,907(2)	Rh(5)-Rh(7)	2,8763(17)
Ge(1)-Rh(7)	2,918(2)	Rh(5)-Rh(10)	2,9372(17)
Ge(1)-Rh(1)	2,922(2)	Rh(6)-Rh(11)	2,8675(18)
Ge(1)-Rh(11)	2,929(2)	Rh(6)-Rh(9)	2,9505(18)
Rh(1)-Rh(8)	2,8244(17)	Rh(6)-Rh(8)	2,9979(17)
Rh(1)-Rh(9)	2,8429(17)	Rh(7)-Rh(12)	2,8208(18)
Rh(1)-Rh(4)	2,8633(18)	Rh(7)-Rh(10)	2,9715(18)
Rh(1)-Rh(5)	2,9657(18)	Rh(8)-Rh(9)	2,8573(18)
Rh(2)-Rh(11)	2,8078(17)	Rh(9)-Rh(12)	2,9512(18)
Rh(2)-Rh(10)	2,8506(17)	Rh(10)-Rh(11)	2,8595(18)
Rh(2)-Rh(6)	2,8544(18)	Rh(1)-Rh(12)	3.301
Rh(2)-Rh(4)	2,9764(18)	Rh(2)-Rh(8)	3.250
Rh(3)-Rh(7)	2,8438(18)	Rh(7)-Rh(11)	3.307

Table 4.6. Most relevant bond lengths for $[Rh_{12}Ge(CO)_{27}]^{4-}$ (first isomer).

Ge(2)-Rh(23)	2,647(2)	Rh(23)-Rh(24)	2,9280(17)
Ge(2)-Rh(27)	2,647(2)	Rh(23)-Rh(31)	2,9474(18)
Ge(2)-Rh(31)	2,6499(19)	Rh(23)-Rh(28)	2,9708(17)
Ge(2)-Rh(22)	2,6647(19)	Rh(24)-Rh(25)	2,8560(18)
Ge(2)-Rh(26)	2,6849(19)	Rh(24)-Rh(29)	2,8576(18)
Ge(2)-Rh(24)	2,706(2)	Rh(24)-Rh(31)	2,9321(18)
Ge(2)-Rh(28)	2,898(2)	Rh(24)-Rh(32)	2,9963(18)
Ge(2)-Rh(32)	2,899(2)	Rh(25)-Rh(29)	2,8120(17)
Ge(2)-Rh(30)	2,899(2)	Rh(25)-Rh(27)	2,8684(17)
Ge(2)-Rh(21)	2,909(2)	Rh(25)-Rh(26)	2,9842(17)
Ge(2)-Rh(25)	2,915(2)	Rh(25)-Rh(32)	3,1970(18)
Ge(2)-Rh(29)	2,937(2)	Rh(26)-Rh(32)	2,8435(18)
Rh(21)-Rh(32)	2,8079(17)	Rh(26)-Rh(27)	2,9225(18)
Rh(21)-Rh(23)	2,8303(17)	Rh(27)-Rh(29)	2,8360(17)
Rh(21)-Rh(26)	2,8727(17)	Rh(27)-Rh(30)	2,9573(17)
Rh(21)-Rh(22)	2,9784(18)	Rh(28)-Rh(30)	2,8072(18)
Rh(22)-Rh(30)	2,8397(18)	Rh(28)-Rh(31)	2,8419(17)
Rh(22)-Rh(28)	2,8514(18)	Rh(29)-Rh(31)	2,9888(17)
Rh(22)-Rh(26)	2,9296(18)	Rh(30)-Rh(31)	2,8562(18)
Rh(22)-Rh(27)	2,9755(17)	Rh(21)-Rh(28)	3,321
Rh(23)-Rh(32)	2,8716(17)	Rh(29)-Rh(30)	3,366

Table 4.7. Most relevant bond lengths for $[Rh_{12}Ge(CO)_{27}]^{4-}$ (second isomer).

The Rh-Rh bond distances are comparable with those found in the $[Rh_{12}E(CO)_{27}]^{n-}$ family of clusters (E = Sn, Sb and Bi), and the Ge-Rh clusters are in line with the smaller dimension of Ge with respect to the other heteroatoms, as inferred from the data collected in Table 4.8. For comparison, the longer Rh-Rh bonding interactions have been included in calculating the average values, as they are a shared feature in all clusters.

Bond lengths	**$[Rh_{12}Ge(CO)_{27}]^{4-}$**	$[Rh_{12}Sn(CO)_{27}]^{4-}$	$[Rh_{12}Sb(CO)_{27}]^{3-}$	$[Rh_{12}Bi(CO)_{27}]^{3-}$
Rh-Rh average (Å)	**2.9345** **(first isomer)**	2.977 **(first isomer)**	2.9821	3.0237
	2.9349 **(second isomer)**	2.979 **(second isomer)**		
Rh-E average (Å)	**2.788**	2.830	2.8227	2.8593
	2.788	2.830		

Table 4.8. Rh-Rh and Rh-E average bond lengths in the $[Rh_{12}E(CO)_{27}]^{n-}$ family of clusters.

The maximum size of the icosahedral $[Rh_{12}Ge(CO)_{27}]^{4-}$ cluster, measured from the outermost oxygen atoms of the carbonyl ligands and including twice the oxygen van der Waals radius, is 1.4 nm.

The metal cage of $[Rh_{12}Ge(CO)_{27}]^{4-}$ completely differs from that of $[Rh_{13}Ge(CO)_{25}]^{3-}$ as the Ge atom is hosted inside an icosahedral cavity of Rh atoms, which is larger than the cubic one.

The geometry of a cavity limits the size of the atoms that can be encapsulated. Table 4.9 [27] shows the expected ratio between the radii of the interstitial atom (r_{int}) and the metal one (r_{met}) , calculated on pure geometrical bases.

Cavity	$\mathbf{r}_{int}/\mathbf{r}_{met}$
Tetrahedral	0.23
Octahedral	0.41
Trigonal prismatic	0.53
Square anti-prismatic	0.65
Cubic	0.73
Icosahedral	0.90
Cuboctahedral	1.00

Table 4.9. Ratios $\mathbf{r}_{int}/\mathbf{r}_{met}$ in different geometric cavities.

If we compare the above theoretical values with those obtained by considering the clusters described so far, we can observe that the expected geometry may be different from the actually adopted one.

In the following table we report the ratios between the covalent radius of E (Sn, Bi, Ge and Sb) and the one of Rh (these ratios can be also calculated by using the metallic radii of elements, which are overall longer).

Elements	$\mathbf{r}_E$:$\mathbf{r}_{Rh}$ ratio (E = Sn, Bi, Ge and Sb)	**Expected cavity**	**Adopted cavity**
Bi/Rh	1.04	Cuboctahedral	Icosahedral
Sn/Rh	0.979	Icosahedral/ Cuboctahedral	Icosahedral
Sb/Rh	0.979	Icosahedral/ Cuboctahedral	Icosahedral
Ge/Rh	0.824	Cubic/Icosahedral	Square anti-prismatic/ Cubic/Icosahedral

Table 4.10. $\mathbf{r}_E/\mathbf{r}_{Rh}$ ratios for the analysed systems with reference to the expected and effectively adopted cavities

According to Table 4.9, in Rh-Bi clusters Bi should be encapsulated in Rh cuboctahedral cavities, but it is actually always found inside icosahedral ones.

As for the Rh-Sn and Rh-Sb systems, the ideal cavity calculated only on geometrical bases is the cuboctahedral one, since the ratio among both the covalent radii of Sn and Sb and the one of Rh is really close to 1.00. However, also in these cases, the effective geometrical cavity is icosahedral. Finally, in Rh-Ge carbonyl clusters, despite the fact that the Ge/Rh ratio would theoretically point towards either a cubic (like in $([Rh_{13}Ge(CO)_{25}]^{3-}$) or an icosahedral cavity ($[Rh_{12}Ge(CO)_{27}]^{4-}$), the Ge atom can be experimentally found also in a square anti-prismatic one ($[Rh_{14}Ge_2(CO)_{30}]^{2-}$).

These deviations from the geometrical predictions are the results of different contributions. Firstly, the structures of the Rh-Bi, Rh-Sb, Rh-Sn and Rh-Ge are

generally distorted, so the cavities are actually larger than in regular polyhedra. Secondly, interstitial atoms can be soft enough to adapt to the cavity dimensions. Finally, and more importantly, the adopted geometry of the metal skeleton also depends on the energetic balance of the Rh-CO, Rh-Rh and Rh-E interactions.
In light of all these considerations, the icosahedral geometry seems to represent the best compromise in the case of Rh-Bi, Rh-Sb and Rh-Sn clusters. As for the Rh-Ge species, due to the smaller Ge dimensions, the icosahedral cavity becomes the preferred one only when, under an excess of CO, it is necessary to maximize the Rh-ligand interactions.

IV.IX. IR and ESI-MS characterization and electron counting of the $[Rh_{12}Ge(CO)_{27}]^{4-}$ cluster

$[Rh_{12}Ge(CO)_{27}]^{4-}$ as salt of $[NEt_4]^+$ is soluble in acetonitrile and DMF and stable, but not soluble, in water.
Its IR spectrum recorded in CH_3CN shows ν_{CO} absorptions at 1997(vs), 1989(vs), 1795(ms) and 1751(mbr) cm^{-1}.
The ESI-MS was performed on the same solution. The spectrum displays two intense groups of peaks starting at 1097 and 1019 m/z, attributable to the $\{[Rh_{12}Ge(CO)_{27\text{-}26\text{-}25\text{-}24\text{-}23}][NEt_4]\}^{2-}$ and $[Rh_{12}Ge(CO)_{26\text{-}25\text{-}24\text{-}23}]^{2-}$ ions, respectively, plus another less intense group of peaks starting at 1163 m/z, due to the $\{[Rh_{12}Ge(CO)_{26\text{-}25\text{-}24\text{-}23}][NEt_4]_2\}^{2-}$ ions.

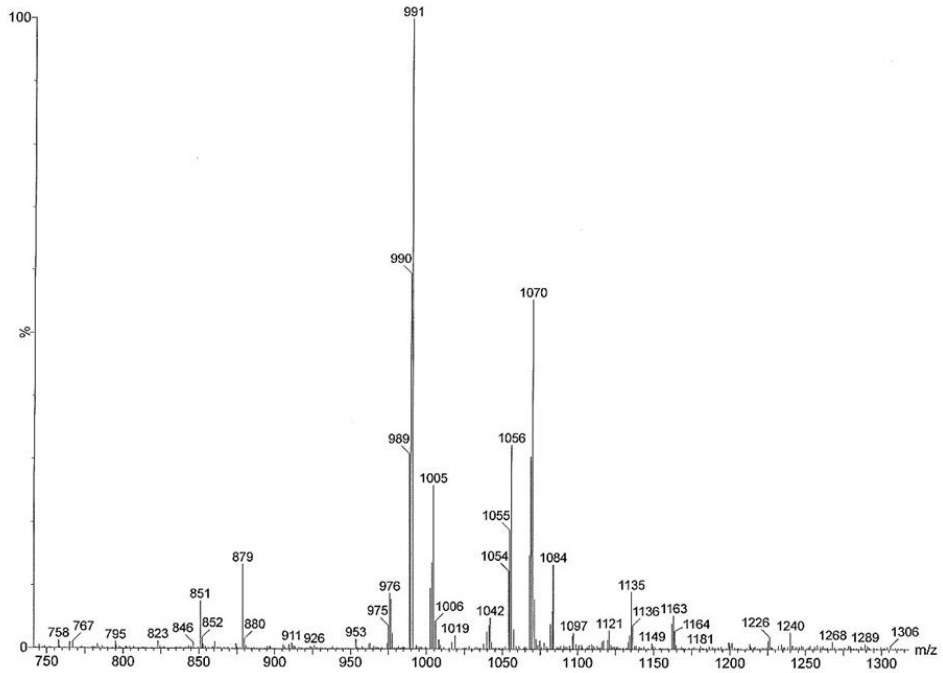

Figure 4.8. ESI-MS spectrum of $[Rh_{12}Ge(CO)_{27}][NEt_4]_4$ recorded in CH_3CN solution.

Peaks or groups of peaks (m/z)	Corresponding Ions
1163-1149-1135-1121	$[Rh_{12}Ge(CO)_{26\text{-}25\text{-}24\text{-}23}]^{2-}$
1097-1084-1070-1056-1042	$\{[Rh_{12}Ge(CO)_{27\text{-}26\text{-}25\text{-}24\text{-}23}][NEt_4]\}^{2-}$
1019-1005-991-976	$[Rh_{12}Ge(CO)_{26\text{-}25\text{-}24\text{-}23}]^{2-}$
879-851	$[Rh_5(CO)_{13\text{-}12}]^-$

Table 4.11. ESI-MS signal assignments for $[Rh_{12}Ge(CO)_{27}][NEt_4]_4$.

As for the electron counting, the $[Rh_{12}Ge(CO)_{27}]^{4-}$ cluster perfectly conforms to the rules based on the Polyhedral Skeleton Electron Pair Theory (PSEPT), as it presents 170 CVEs given by the 9 × 12 rhodium atoms (108), the 2 × 27 carbonyl ligands (54), the interstitial Ge atom (4), and the negative charge (4).

IV.X. Reactivity of $[Rh_7(CO)_{16}]^{3-}$ with $GeBr_2$ under CO atmosphere

Since we had obtained $[Rh_{12}Ge(CO)_{27}]^{4-}$ by reacting the cubic $[Rh_{13}Ge(CO)_{25}]^{3-}$ under CO atmosphere, we considered the possibility of studying the overall reactivity of $[Rh_7(CO)_{16}]^{3-}$ with $GeBr_2$ under CO to verify the direct synthesis of the icosahedral compound. For this reason, we reacted $[Rh_7(CO)_{16}]^{3-}$ with $GeBr_2$ in the same reaction conditions which had led to the cubic cluster previously described, but under CO atmosphere. Nevertheless, this reaction did not lead to the expected icosahedral cluster, but to the highest nuclearity Rh-Ge carbonyl cluster to date: $[Rh_{23}Ge_3(CO)_{41}]^{5-}$. Evidently, the presence of a large excess of CO since the beginning made the reaction take a complete different path, as the formation of $[Rh_{12}Ge(CO)_{27}]^{4-}$ was never detected.

At the end of the reaction, the usual work-up was carried out and after the elimination of the $[Rh(CO)_2Br_2]^-$ complex, the product was extracted in acetonitrile.

This compound crystallized as $[Rh_{23}Ge_3(CO)_{41}][NEt_4]_5 \cdot 6CH_3CN$ by layering di-isopropyl ether on top of the acetonitrile solution.

IV.XI. Molecular structure of the $[Rh_{23}Ge_3(CO)_{41}]^{5-}$ cluster

The $[Rh_{23}Ge_3(CO)_{41}][NEt_4]_5 \cdot 6CH_3CN$ compound crystallized in the monoclinic $P2_1/n$ space group and Z = 4, so the unit cell contains four cluster units, twenty cations and twenty-four acetonitrile molecules, all arranged in an ionic solid fashion. The molecular structure of the $[Rh_{23}Ge_3(CO)_{41}]^{5-}$ (4) anion is illustrated in Figure 4.9.

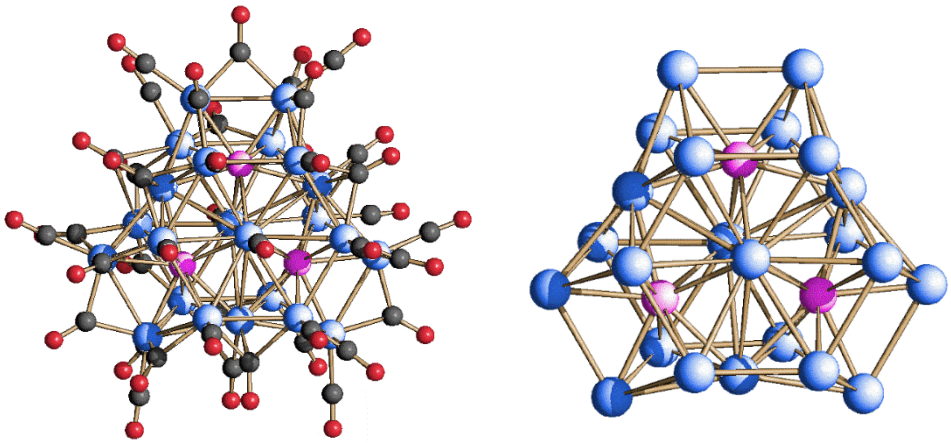

Figure 4.9. Molecular structure of $[Rh_{23}Ge_3(CO)_{41}]^{5-}$ (left) and its metal skeleton (right). Rh atoms are depicted in blue, Ge atoms are depicted in magenta, C atoms are in grey and O atoms are in red.

The molecular structure of $[Rh_{23}Ge_3(CO)_{41}]^{5-}$ consists of three equivalent, $Rh_{10}Ge$ polyhedra fused by one Rh_2 edge and sharing in pairs another Rh atom. Each $Rh_{10}Ge$ unit is a convex solid possessing two square faces and seven triangular ones, with an overall C_{2v} symmetry, and therefore can be identified as a sphenocorona centred by Ge. The cluster overall contains three fully interstitial Ge atoms and two semi-interstitial Rh atoms capped by two hexagonal faces. The metal structure is stabilized by 41 carbonyl ligands, of which 23 terminally bonded to each Rh atom, 15 edge-bridging and 3 face-bridging. The average Rh-Ge bond distance is 2.631 Å, with a minimum value of 2.506(3) Å and a maximum of 2.818(2) Å. As for the Rh-Rh bond lengths, they vary from 2.703(2) to 3.137(2) Å, with an average value of 2.875 Å.

The maximum size of the $[Rh_{23}Ge_3(CO)_{41}]^{5-}$ cluster, measured from the outermost oxygen atoms of the carbonyl ligands and including twice the oxygen van der Waals radius, is 1.7 nm.

Rh(1)-Ge(24)	2.532(2)
Rh(1)-Ge(25)	2.534(2)
Rh(1)-Ge(26)	2.535(2)
Rh(2)-Ge(25)	2.531(3)
Rh(2)-Ge(24)	2.542(2)
Rh(3)-Ge(26)	2.609(2)
Rh(3)-Ge(24)	2.610(2)
Rh(3)-Ge(25)	2.613(2)
Rh(4)-Ge(24)	2.743(2)
Rh(5)-Ge(24)	2.530(2)
Rh(5)-Ge(26)	2.545(2)
Rh(6)-Ge(24)	2.716(2)
Rh(7)-Ge(25)	2.731(2)
Rh(8)-Ge(26)	2.722(2)
Rh(9)-Ge(25)	2.734(2)
Rh(10)-Ge(25)	2.818(2)
Rh(11)-Ge(26)	2.538(2)
Rh(11)-Ge(25)	2.545(3)
Rh(12)-Ge(24)	2.844(2)
Rh(13)-Ge(26)	2.727(2)
Rh(14)-Ge(24)	2.736(2)
Rh(15)-Ge(25)	2.758(2)
Rh(16)-Ge(24)	2.502(2)
Rh(17)-Ge(26)	2.755(3)
Rh(18)-Ge(24)	2.517(2)
Rh(19)-Ge(26)	2.806(3)
Rh(21)-Ge(25)	2.507(3)
Rh(23)-Ge(25)	2.506(3)
Rh(20)-Ge(26)	2.524(3)
Rh(1)-Rh(13)	2.978(2)
Rh(1)-Rh(4)	2.982(2)
Rh(1)-Rh(3)	2.9874(19)
Rh(1)-Rh(8)	2.989(2)
Rh(1)-Rh(9)	2.995(2)

Rh(1)-Rh(6)	2.999(2)
Rh(1)-Rh(7)	3.014(2)
Rh(1)-Rh(2)	3.137(2)
Rh(2)-Rh(7)	2.704(2)
Rh(2)-Rh(4)	2.719(2)
Rh(2)-Rh(10)	2.796(2)
Rh(2)-Rh(14)	2.810(2)
Rh(2)-Rh(18)	2.917(2)
Rh(2)-Rh(21)	2.943(2)
Rh(3)-Rh(14)	2.910(2)
Rh(3)-Rh(15)	2.923(2)
Rh(3)-Rh(17)	2.931(2)
Rh(3)-Rh(10)	2.945(2)
Rh(3)-Rh(12)	2.965(2)
Rh(3)-Rh(19)	2.966(2)
Rh(4)-Rh(6)	2.859(2)
Rh(4)-Rh(18)	2.867(2)
Rh(4)-Rh(7)	2.892(2)
Rh(5)-Rh(6)	2.707(2)
Rh(5)-Rh(8)	2.719(2)
Rh(5)-Rh(12)	2.787(2)
Rh(5)-Rh(17)	2.807(2)
Rh(5)-Rh(20)	2.909(2)
Rh(5)-Rh(16)	2.934(2)
Rh(6)-Rh(8)	2.865(2)
Rh(6)-Rh(16)	2.874(2)
Rh(7)-Rh(9)	2.865(2)
Rh(7)-Rh(21)	2.866(2)
Rh(8)-Rh(20)	2.856(2)
Rh(8)-Rh(13)	2.858(2)
Rh(9)-Rh(11)	2.722(2)
Rh(9)-Rh(13)	2.853(2)
Rh(9)-Rh(23)	2.857(2)
Rh(10)-Rh(14)	2.816(2)

Rh(10)-Rh(15)	2.847(2)	Rh(13)-Rh(22)	2.871(2)
Rh(10)-Rh(21)	2.917(2)	Rh(14)-Rh(18)	2.877(2)
Rh(11)-Rh(13)	2.703(2)	Rh(15)-Rh(19)	2.823(2)
Rh(11)-Rh(19)	2.785(2)	Rh(15)-Rh(23)	2.884(2)
Rh(11)-Rh(15)	2.801(2)	Rh(16)-Rh(18)	2.857(2)
Rh(11)-Rh(23)	2.914(2)	Rh(17)-Rh(19)	2.823(2)
Rh(11)-Rh(22)	2.935(2)	Rh(17)-Rh(20)	2.876(2)
Rh(12)-Rh(17)	2.809(2)	Rh(19)-Rh(22)	2.906(2)
Rh(12)-Rh(14)	2.838(2)	Rh(20)-Rh(22)	2.866(2)
Rh(12)-Rh(16)	2.924(2)	Rh(21)-Rh(23)	2.857(2)

Table 4.12. Most relevant bond lengths for $[Rh_{23}Ge_3(CO)_{41}]^{5-}$.

IV.XII. IR and ESI-MS characterization of the $[Rh_{23}Ge_3(CO)_{41}]^{5-}$ cluster

$[Rh_{23}Ge_3(CO)_{41}]^{5-}$ as salt of $[NEt_4]^+$ is soluble in acetone, in acetonitrile and DMF and stable, but not soluble, in water.

Its IR spectrum in CH_3CN shows peaks at 1991(s) and 1800(ms) cm^{-1}. An ESI-MS analysis in solution was performed, but the cluster heavily breaks in the experimental conditions and gives rise to the $[Rh_{10}Ge(CO)_{20}]^{2-}$ and $[Rh_9Ge(CO)_{19}]^{2-}$ ions, with signals at 831 and 766 m/z, respectively. Only one signal at 1199 m/z, and those deriving from some CO loss, can be attributed to the $[Rh_{23}Ge_3(CO)_{36}]^{3-}$ ion (Figure 4.10).

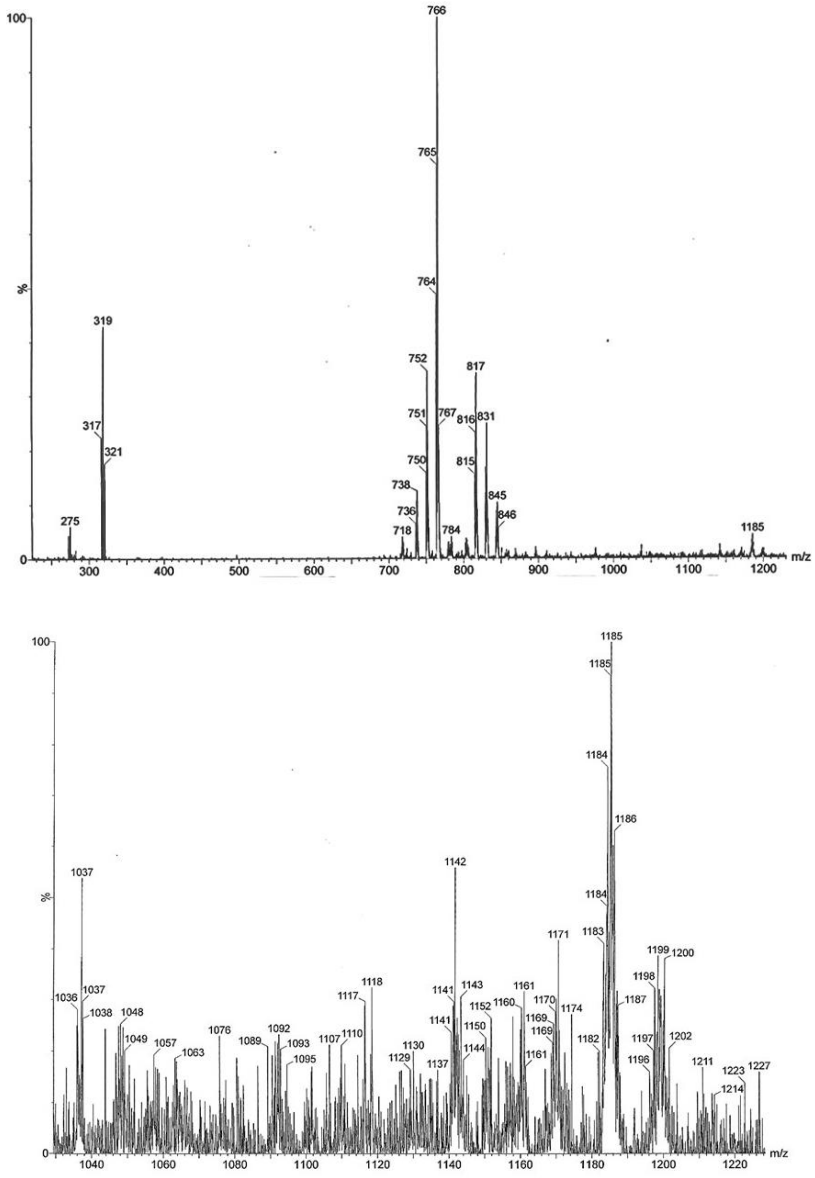

Figure 4.10. ESI-MS spectra of $[Rh_{23}Ge_3(CO)_{41}][NEt_4]_5$ recorded in CH_3CN solution.

Peaks or groups of peaks (m/z)	Corresponding Ions
1198-1188-1171-1161-1152-1142	$[Rh_{23}Ge_3(CO)_{36\text{-}35\text{-}33\text{-}32\text{-}31\text{-}30}]^{3-}$
845-831-817	$[Rh_{10}Ge(CO)_{21\text{-}20\text{-}19}]^{2-}$
766-752-738	$[Rh_9Ge(CO)_{19\text{-}18\text{-}17}]^{2-}$

Table 4.13. ESI-MS signal assignments for $[Rh_{23}Ge_3(CO)_{41}][NEt_4]_5$.

Crystallographic data for Rh-Ge carbonyl clusters

Compound	**1**$[NEt_4]_3 \cdot [NEt_4]Br$	**2**$[NEt_4]_2$	**3**$[NEt_4]_4 \cdot 2CH_3CN$	**4**$[NEt_4]_5 \cdot 6CH_3CN$
Formula	$C_{57}H_{80}BrGeN_4O_{25}Rh_{13}$	$C_{46}H_{40}Ge_2N_2O_{30}Rh_{14}$	$C_{63}H_{86}GeN_6O_{27}Rh_{12}$	$C_{93}H_{118}Ge_3N_{11}O_{41}Rh_{23}$
Fw	2711.57	2686.72	2666.88	4630.68
Crystal system	Tetragonal	Triclinic	Triclinic	Monoclinic
Space group	*P*4/ncc	*P*-1	*P*-1	$P2_1/n$
***a* (Å)**	18.5028(6)	11.4246(4)	13.279(3)	16.781(2)
***b* (Å)**	18.5028(6)	11.5375(4)	26.614(5)	26.848(3)
***c* (Å)**	22.8486(11)	13.4617(5)	27.049(5)	28.168(4)
α (deg)	90	112.059(2)	119.285(3)	90
β (deg)	90	98.082(2)	98.012(4)	92.494(3)
γ (deg)	90	94.045(3)	95.078(4)	90
Cell volume (Å^3)	7822.3(6)	1613.40(10)	8119(3)	12678(3)
Z	4	1	4	4
D (g/cm^3)	2.302	2.765	2.182	2.426
μ (mm^{-1})	3.623	4.474	2.810	3.679
F (000)	5208	1264	5176	8848
θ limits (deg)	1.783-24.998	1.660-24.997	1.521-24.999	1.681-24.999
Index ranges	$-22 \leq h \leq 22$, $-21 \leq k \leq 21$, $-27 \leq l \leq 27$	$-13 \leq h \leq 13$, $-13 \leq k \leq 13$, $-16 \leq l \leq 16$	$-15 \leq h \leq 15$, $-31 \leq k \leq 31$, $-32 \leq l \leq 32$	$-19 \leq h \leq 19$, $-31 \leq k \leq 31$, $-33 \leq l \leq 33$
Reflections collected	89494	23355	76284	138977
Independent reflections	3455 [R(int) = 0.1077]	5690 [R(int) = 0.1320]	27668 [R(int) = 0.0543]	22100 [R(int) = 0.1050]
Completeness to θ max	100.0%	99.9%	99.8%	99.1%
Data/restraints/ parameters	3455/0/231	5690/90/429	27668/658/2029	22100/831/1674
Goodness-of-fit	1.146	0.990	1.088	1.191
R_1 ($I > 2\sigma(I)$)	0.0482	0.0550	0.0726	0.0884
wR_2 (all data)	0.1035	0.1445	0.2114	0.2127
Largest diff. peak and hole, e Å^{-3}	1.383 and -1.338	2.397 and -1.639	2.892 and -2.092	2.409 and -1.855

Table 4.14. Crystallographic data for clusters 1, 2, 3 and 4.

1 J. A. Cabeza, P. Garcia-Alvarez, D. Polo, *Inorg. Chem.* **2011**, *50*, 6195.

2 R. D. Adams, B. Captain, J. L. Smith, Jr., *Inorg. Chem.* **2005**, *44*, 1413.

3 S. Saha, D. Isrow, B. Captain, *J. Organomet. Chem.* **2014**, *751*, 815.

4 R. D. Adams, J. L. Smith, Jr., *Inorg. Chem.* **2005**, *44*, 4276.

5 A. Ceriotti, F. Demartin, B. T. Heaton, P. Ingallina, G. Longoni, M. Manassero, M. Marchionna, N. Masciocchi, *J. Chem. Soc. Chem. Commun.* **1989**, 786.

6 G. Espinoza-Quintero, J. C. A. Duckworth, W. K. Myers, J. E. McGrady, J. M. Goicoechea, *J. Am. Chem. Soc.* **2014**, *136*, 1210.

7 B. Zhou, M. S. Denning, D. L. Kays, J. M. Goicoechea, *J. Am. Chem. Soc.* **2009**, *131*, 2802.

8 J. Q. Wang, S. Stegmaier, T. F. Fässler, *Angew. Chem. Int. Ed.* **2009**, *48*, 1998.

9 J. M. Goicoechea, S. C. Sevov, *J. Am. Chem. Soc.* **2005**, *127*, 7676.

10 J. M. Goicoechea, S. C. Sevov, *Angew. Chem. Int. Ed.* **2005**, *44*, 4026.

11 C. Schenk, F. Henke, A. Schnepf, *Angew. Chem. Int. Ed.* **2013**, *52*, 1834.

12 D. Rios, S. C. Sevov, *Inorg. Chem.* **2010**, *49*, 6396.

13 L. G. Perla, S. C. Sevov, *J. Am. Chem. Soc.* **2016**, *138*, 9795.

14 A. Spiekermann, S. D. Hoffmann, F. Kraus, T. F. Fässler, *Angew. Chem. Int. Ed.* **2007**, *46*, 1638.

15 E. N. Esenturk, J. Fettinger, B. Eichhorn, *Polyhedron* **2006**, *25*, 521.

16 A. Boccalini, P. J. Dyson, C. Femoni, M. C. Iapalucci, S. Ruggieri, S. Zacchini, *Dalton Trans.* **2018**, *47*, 15737.

17 C. Femoni, M. C. Iapalucci, S. Ruggieri, S. Zacchini, *Acc. Chem. Res.* **2018**, *51*, 2748.

18 S. Martinengo, P. Chini, G. Giordano, A. Ceriotti, V. G. Albano, G. Ciani, *J. Organomet. Chem.* **1975**, *88*, 375.

19 L. Pauling, *J. Am. Chem. Soc.* **1947**, *69*, 542.

20 G. Ciani, A. Sironi, S. Martinengo, *J. Organomet. Chem.* **1980**, *192*, C42.

21 D. Collini, C. Femoni, M. C. Iapalucci, G. Longoni, P. H. Svensson, P. Zanello, *Angew. Chem. Int. Ed.* **2002**, *41*, 3685.

22 M. W. Hull, S. C. Sevov, *Angew. Chem. Int. Ed.* **2007**, *46*, 6695.

23 S. Ruggieri, *Bachelor Thesis* **2013**.

24 C. Capacci, I. Ciabatti, C. Femoni, T. Funaioli, M. C. Iapalucci, S. Zacchini, V. Zanotti, *Inorg. Chem.* **2018**, *57*, 1136.

25 C. Zeng, Y. Chen, K. Kirschbaum, K. Appavoo, M. Y. Sfeir, R. Jin, *Sci. Adv.* **2015**, *1*, e1500045.

26 G. Mednikov, L. F. Dahl, *Philos. Trans. R. Soc. London, Ser. A* **2010**, *368*, 1301.

27 P. J. Dyson, J. S. McIndoe, *Transition Metal Carbonyl Clusters*, Gordon and Breach Science Publishers, CRC Press, **2000**, 52.

CHAPTER V

New Rhodium-Antimony Carbonyl Clusters

After having analysed the Rh-Bi and the Rh-Ge systems, we took into consideration the hypothesis of synthesizing new Rh-Sb carbonyl clusters.

The only Rh-Sb carbonyl cluster reported in the literature is $[Rh_{12}Sb(CO)_{27}]^{3-}$, which has been known for over three decades thanks to Vidal and co-workers. [1] It also represents the first example of an E-centred (E = heteroatom) icosahedral rhodium carbonyl cluster. However, its synthesis required high temperature (140-160°C) and elevated CO pressure (400 atm). If it was not possible to find other examples of Rh-Sb clusters in the literature, we cannot assume the same for other metal-antimony clusters. For instance, there are many examples of Ni-Sb carbonyl clusters among which $[Ni_{15}Sb(CO)_{24}]^{2-}$ and $[Ni_{11}Sb_2(CO)_{18}]^{3-}$ [2] (where Sb is interstitially lodged), $[Ni_{10}(SbR)_2(CO)_{18}]^{2-}$ (R = Me, Et, *i*Pr, *t*-Bu, *p*-FC_6H_4) [3] and $[Ni_{13}Sb_2(CO)_{24}]^{n-}$ [4] (where Sb is on the surface), $[Ni_{19}Sb_4(CO)_{26}]^{4-}$ [5] and $[Ni_{31}Sb_4(CO)_{40}]^{6-}$ [6] (where Sb is semi-interstitially lodged). Moreover, we can also find examples of Ru-Sb and Os-Sb clusters, among which $[H_2Ru_6Sb_2(CO)_{20}Ph_4]$, [7] $[H_3Ru_6Sb_2(CO)_{18}Ph_3]$, [8] $[H_2Os_6Sb_2(C_6H_4)(CO)_{17}Ph_2]$, [8] $[Os_3Sb_2(CO)_{10}Ph_4]$ [9] and $[Os_3Sb_2(OC_{10}H_6)(CO)_7Ph_6]$. [10]

We decided to approach also the Rh-Sb system by the usual method of redox condensation (exploited for Rh-Bi and Rh-Ge ones), in order to obtain new compounds by working in mild reaction conditions of pressure and temperature.

General results

The following sections show the study of the reactivity of $[Rh_7(CO)_{16}][NEt_4]_3$ cluster precursor with $SbCl_3$ in different reaction conditions, leading to the obtainment of several new nanoclusters. The different atmospheres are particularly influent in the Rh-Sb system, they are its proper keystone. Therefore, we are going to analyse the different species which can be obtained from the various reactions, by separating the study carried out under CO from the one under N_2.

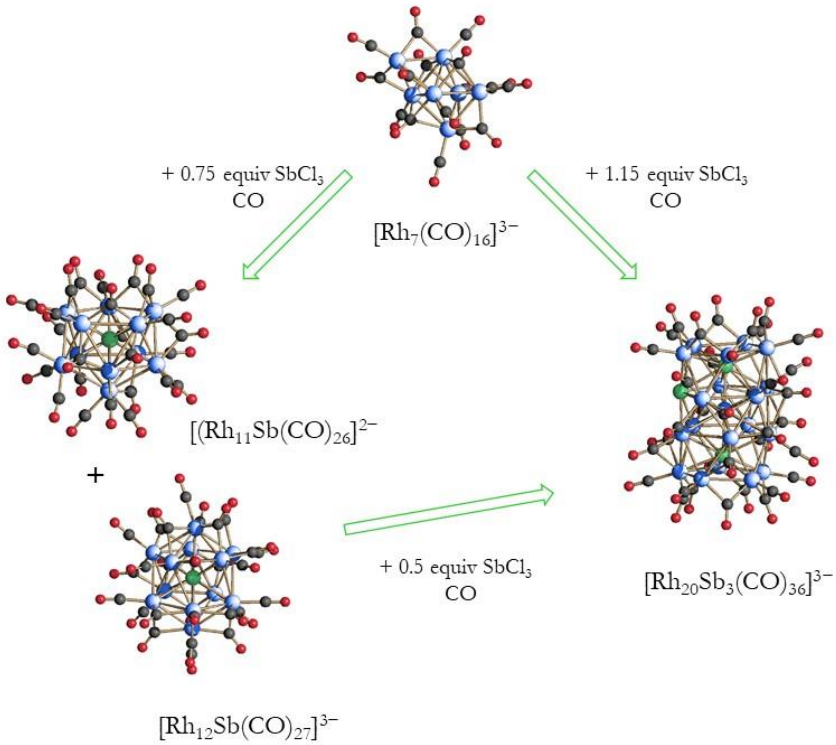

Figure 5.1. Reaction scheme of Rh-Sb system under CO atmosphere. Rh atoms are depicted in blue, Sb atoms are depicted in green, C atoms are in grey and O atoms are in red.

In this system, under CO atmosphere, the first reaction between $[Rh_7(CO)_{16}]^{3-}$ and $SbCl_3$ shown in the scheme leads to the expected icosahedral species together with another similar nuclearity compound.

The reactivity completely changes when the system is studied under N_2 atmosphere (Figure 5.2).

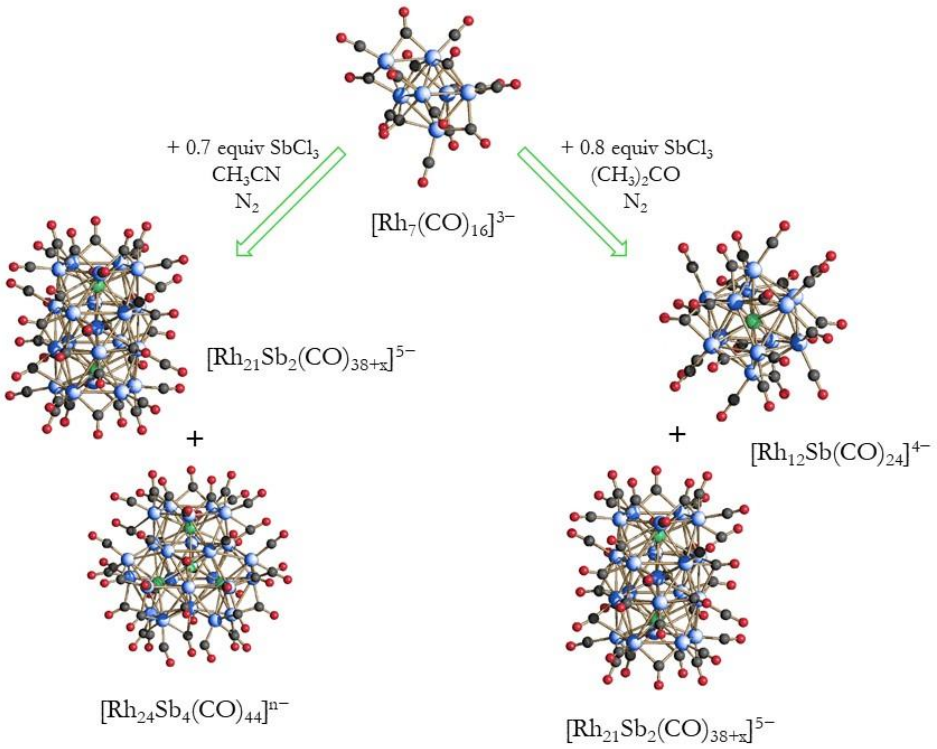

Figure 5.2. Reaction scheme of Rh-Sb system under N_2 atmosphere. Rh atoms are depicted in blue, Sb atoms are depicted in green, C atoms are in grey and O atoms are in red.

In this case, the solvent reaction played a key role in maximizing the formation of the three clusters. It is worth mentioning the obtaining of the coordinatively and electronically unsaturated icosahedral $[Rh_{12}Sb(CO)_{24}]^{4-}$ cluster.

V.I. Reactivity of $[Rh_7(CO)_{16}]^{3-}$ with $SbCl_3$ under CO atmosphere

The first aim we wanted to reach in the study of Rh-Sb system was represented by the synthesis of the icosahedral $[Rh_{12}Sb(CO)_{27}]^{3-}$ by exploiting the usual redox condensation method which, in general, requires milder reaction conditions than those used by Vidal. Since Vidal's group had used very high pressures of CO and H_2 atmospheres to obtain the icosahedral cluster, we thought of testing the reactivity of our $[Rh_7(CO)_{16}]^{3-}$ cluster precursor with a salt of Sb^{3+}, but under CO atmosphere and at room temperature.

After the addition of 0.75 equivalents of $SbCl_3$ to the cluster precursor in acetonitrile, it was possible to observe the complete disappearance of the ν_{CO} absorptions of $[Rh_7(CO)_{16}]^{3-}$ in favour of the ones belonging to the $[Rh(CO)_2Cl_2]^-$ complex and the known $[Rh_{12}Sb(CO)_{27}]^{3-}$. The final mixture was washed with water to eliminate the residual salts and with ethanol to extract the usual $[Rh(CO)_2Cl_2]^-$, while the $[Rh_{12}Sb(CO)_{27}]^{3-}$ anion was isolated in acetone. Its structural characterization was achieved through the X-ray analysis of the single crystals obtained by layering 2-propanol onto the acetone solution.

This way we synthesized the already known icosahedral Rh-Sb cluster, but through a very different reaction path. [11] Indeed, we started from an already reduced Rh compound, the pre-formed $[Rh_7(CO)_{16}]^{3-}$ cluster, as source of both Rh and CO ligands, which we reacted with $SbCl_3$. This way the presence of H_2 became unnecessary and the CO pressure could be reduced to just 1-1.5 atm. Furthermore, no high temperature was needed, as the driving force of the reaction was the spontaneous oxidation of the Rh atoms by the Sb^{3+} species, which occurred at room temperature.

$[Rh_{12}Sb(CO)_{27}]^{3-}$ is the principal product of this reaction, but not the only cluster that was extracted. Indeed, unlike the previously studied systems, we isolated for the first time another species that, in principle, could be considered an intermediate species in the growing path of the $[Rh_{12}Sb(CO)_{27}]^{3-}$ cluster, being structurally based on an incomplete icosahedron. In fact, during the work-up, the THF extraction

allowed us to separate and characterize the new $[Rh_{11}Sb(CO)_{26}][NEt_4]_2$ compound, although in a rather low yield.

After the characterization of these two cluster compounds, we kept on the investigation of the reactivity of $[Rh_7(CO)_{16}]^{3-}$ cluster precursor with further amount of Sb^{3+} salt, in the attempt to synthesize higher nuclearity Rh-Sb clusters.

By reacting $[Rh_7(CO)_{16}]^{3-}$ with 1.15 equivalents of $SbCl_3$, still under CO atmosphere, we obtained a mother solution which presented an IR spectrum where the ν_{CO} absorptions of the above descripted compounds were replaced by those of another species. During the work-up, the new $[Rh_{20}Sb_3(CO)_{36}]^{3-}$ was extracted in acetone and crystallized as salt of $[NEt_4]^+$, by layering hexane onto the acetone solution. The same result was achieved by using $[Rh_{12}Sb(CO)_{27}]^{3-}$ as starting material, by adding 0.5 equivalents of $SbCl_3$ under CO atmosphere. This latter reaction strategy identifies $[Rh_{12}Sb(CO)_{27}]^{3-}$ as a reaction intermediate in the oxidation and condensation pathway which leads to $[Rh_{20}Sb_3(CO)_{36}]^{3-}$ from $[Rh_7(CO)_{16}]^{3-}$. However, it is less convenient than the first one described above because of the major number of reaction steps and of the minor product yield.

By further addition of Sb^{3+} salt to the homometallic cluster precursor, up to a stoichiometric Rh_7:Sb^{3+} ratio of 1:1.5, we only lowered the yield of $[Rh_{20}Sb_3(CO)_{36}]^{3-}$ because of its partial degradation in favour of the formation of $[Rh(CO)_2Cl_2]^-$.

V.II. Molecular structure of the $[Rh_{11}Sb(CO)_{26}]^{2-}$ cluster

The molecular structure of $[Rh_{11}Sb(CO)_{26}]^{2-}$ (1) is illustrated in Figure 5.3.

$[Rh_{11}Sb(CO)_{26}][NEt_4]_2$ crystallized in the monoclinic $P2_1/c$, with Z = 4, so the unit cell contains four cluster units, eight cations and four THF molecules, all arranged in an ionic solid fashion.

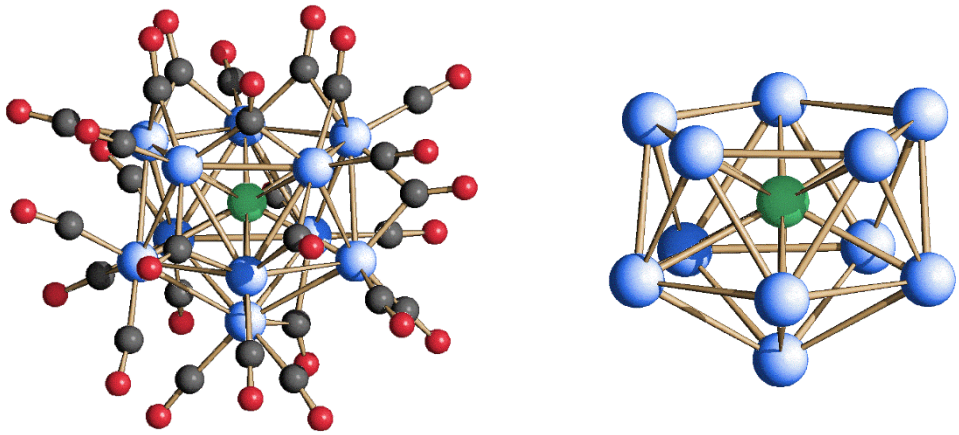

Figure 5.3. Molecular structure of $[Rh_{11}Sb(CO)_{26}]^{2-}$ (left) and its metal skeleton (right). Rh atoms are depicted in blue, Sb atoms are depicted in green, C atoms are in grey and O atoms are in red.

The molecular structure of $[Rh_{11}Sb(CO)_{26}]^{2-}$ consists of an open icosahedron made of eleven Rh atoms and centred by the unique Sb. The metal skeleton is stabilized by 26 carbonyl ligands, of which 15 terminally bonded and 11 edge-bridging.
The Rh-Rh distances vary from 2.8404(4) to 3.1133(4) Å (average 2.9427 Å), while the Rh-Sb bond lengths span from 2.6422(4) to 2.8654(4), with an average of 2.7933 Å. These distances are slightly shorter than those found in the icosahedral species, because of the minor distortion of the skeleton probably due to the lack of one capping Rh atom. As a matter of fact, there are no Rh-Rh bond contacts longer than 3.1133(4) Å, unlike in the other complete icosahedral Rh-Bi, Rh-Ge and Rh-Sb clusters.
The maximum size of the icosahedral $[Rh_{11}Sb(CO)_{26}]^{2-}$ cluster, measured from the outermost oxygen atoms of the carbonyl ligands and including twice the oxygen van der Waals radius, is 1.4 nm.

Sb(12)-Rh(1)	2.8649(4)	Rh(2)-Rh(6)	3.1133(4)
Sb(12)-Rh(2)	2.7898(4)	Rh(2)-Rh(7)	2.8502(4)
Sb(12)-Rh(3)	2.7908(4)	Rh(2)-Rh(10)	2.8404(4)
Sb(12)-Rh(4)	2.7881(4)	Rh(3)-Rh(4)	2.9349(4)
Sb(12)-Rh(5)	2.8272(4)	Rh(3)-Rh(6)	3.0226(4)
Sb(12)-Rh(6)	2.7401(4)	Rh(3)-Rh(10)	2.9466(4)
Sb(12)-Rh(7)	2.8654(4)	Rh(3)-Rh(11)	2.9044(4)
Sb(12)-Rh(8)	2.6422(4)	Rh(4)-Rh(6)	2.8707(4)
Sb(12)-Rh(9)	2.8293(4)	Rh(4)-Rh(9)	2.8746(4)
Sb(12)-Rh(10)	2.8245(4)	Rh(4)-Rh(11)	2.9999(4)
Sb(12)-Rh(11)	2.7639(4)	Rh(5)-Rh(6)	3.0043(4)
Rh(1)-Rh(4)	3.0593(4)	Rh(5)-Rh(7)	2.9732(4)
Rh(1)-Rh(5)	2.9045(4)	Rh(5)-Rh(8)	2.8569(4)
Rh(1)-Rh(6)	2.8754(4)	Rh(7)-Rh(8)	2.8831(4)
Rh(1)-Rh(8)	2.9015(4)	Rh(7)-Rh(10)	2.9225(4)
Rh(1)-Rh(9)	2.9719(4)	Rh(8)-Rh(9)	2.8833(4)
Rh(2)-Rh(3)	3.0683(4)	Rh(9)-Rh(11)	2.9776(4)
Rh(2)-Rh(5)	2.9943(4)	Rh(10)-Rh(11)	2.9348(4)

Table 5.1. Bond lengths for $[Rh_{11}Sb(CO)_{26}]^{2-}$.

V.III. IR and ESI-MS characterization and electron counting of the $[Rh_{11}Sb(CO)_{26}]^{2-}$ cluster

$[Rh_{11}Sb(CO)_{26}]^{2-}$ as salt of $[NEt_4]^+$ is soluble in THF, acetone, acetonitrile and DMF and stable, but not soluble, in water.

Its IR spectrum recorded in CH_3CN shows ν_{CO} absorptions at 2033(vs), 1869(mw) and 1823(mw) cm^{-1}.

The ESI-MS analysis was performed on the same solution of the IR one. The spectrum displays just one intense group of peaks starting at 963 m/z, attributable to the $[Rh_{11}Sb(CO)_{24}]^{2-}$ ion, with significant loss of CO fragments.

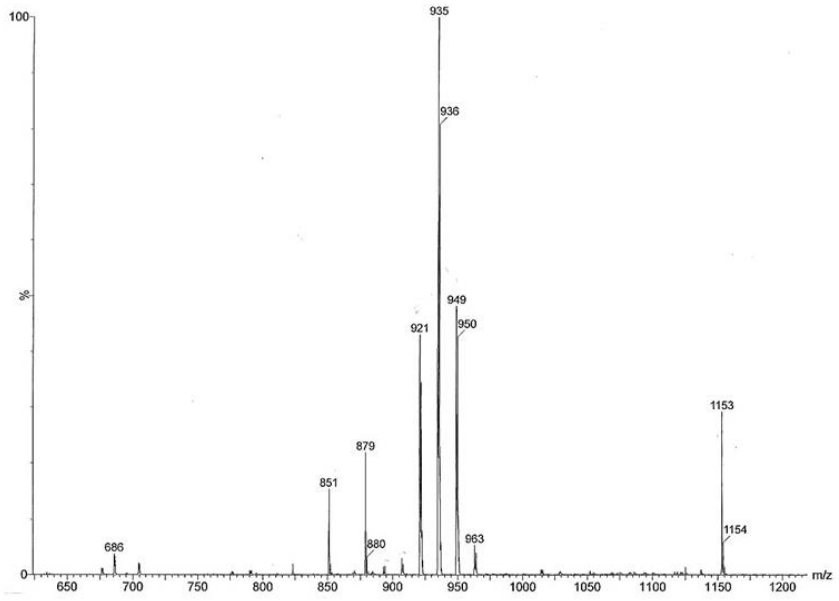

Figure 5.4. ESI-MS spectrum of $[Rh_{11}Sb(CO)_{26}][NEt_4]_2$ recorded in CH_3CN solution.

Peaks or groups of peaks (m/z)	Corresponding Ions
963-949-935-921-879-851	$[Rh_{11}Sb(CO)_{24\text{-}23\text{-}22\text{-}21\text{-}18\text{-}16}]^{2-}$

Table 5.2. ESI-MS signal assignments for $[Rh_{11}Sb(CO)_{26}][NEt_4]_2$.

As for the electron counting, the $[Rh_{11}Sb(CO)_{26}]^{2-}$ cluster presents 158 CVEs, given by the 9 × 11 rhodium atoms (99), the 2 × 26 carbonyl ligands (52), the interstitial Sb atom (5), and the negative charge (2). The CVEs number is in perfect agreement with the PSEPT applied to an icosahedral cluster (170 CVEs) which lacks in one atom (−12 CVEs).

V.IV. Molecular structure of the $[Rh_{12}Sb(CO)_{27}]^{3-}$ cluster

The molecular structure of $[Rh_{12}Sb(CO)_{27}]^{3-}$ (2) is illustrated in Figure 5.5.

The $[Rh_{12}Sb(CO)_{27}][NEt_4]_3$ salt reported by Vidal crystallized in the rhombohedral *R*-3c space group, while we found polymorphic crystals which crystallized in the *C*2/c space group. However, the molecular structure of the trianion is equivalent to the one originally reported, and it consists of a distorted icosahedron made of

Rh atoms centred by the unique Sb, stabilized by 27 carbonyl ligands: 12 terminal (one for each Rh) and 15 edge-bridging COs. The distortion is reflected in the Rh-Rh distances reported in Table 5.3, spanning from 2.8720(14) to 3.3680 (15) Å (average 2.9821 Å), while the Rh-Sb bond lengths vary from 2.7069(12) to 2.9409(13), with an average of 2.8227 Å, analogous to the bond distances found by Vidal. Note that Rh-Rh bonding interactions in the cluster fall within 2.60-3.20 Å range, making the longer distance in the cluster a clear sign of the deviation from an ideal icosahedral geometry. Furthermore, no edge-bridging COs are found on the two longest bond interactions.

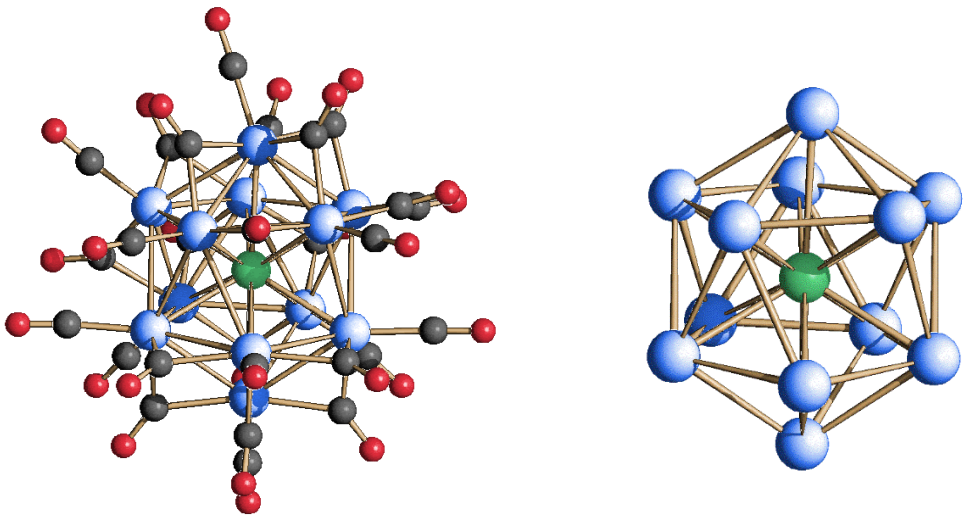

Figure 5.5. Molecular structure of $[Rh_{12}Sb(CO)_{27}]^{3-}$ (left) and its metal skeleton (right). Rh atoms are depicted in blue, Sb atoms are depicted in green, C atoms are in grey and O atoms are in red.

The maximum size of the icosahedral $[Rh_{12}Sb(CO)_{27}]^{3-}$ cluster, measured from the outermost oxygen atoms of the carbonyl ligands and including twice the oxygen van der Waals radius, is 1.4 nm.

Sb(1)-Rh(4)#1	2.7069(12)	Rh(3)-Rh(6)	2.8209(13)
Sb(1)-Rh(4)	2.7070(12)	Rh(3)-Rh(4)	2.8740(14)
Sb(1)-Rh(5)#1	2.7218(12)	Rh(3)-Rh(4)#1	3.0302(14)
Sb(1)-Rh(5)	2.7218(12)	Rh(4)-Rh(6)	2.8791(14)
Sb(1)-Rh(2)#1	2.7238(11)	Rh(4)-Rh(2)#1	3.0002(13)
Sb(1)-Rh(2)	2.7238(11)	Rh(4)-Rh(5)#1	3.0090(15)
Sb(1)-Rh(6)#1	2.9174(10)	Rh(4)-Rh(3)#1	3.0303(14)
Sb(1)-Rh(6)	2.9174(10)	Rh(5)-Rh(7)	2.8694(14)
Sb(1)-Rh(7)	2.9253(14)	Rh(5)-Rh(7)#1	2.8786(14)
Sb(1)-Rh(7)#1	2.9254(14)	Rh(5)-Rh(4)#1	3.0090(14)
Sb(1)-Rh(3)	2.9409(13)	Rh(5)-Rh(6)#1	3.0174(14)
Sb(1)-Rh(3)#1	2.9409(13)	Rh(6)-Rh(5)#1	3.0174(14)
Rh(2)-Rh(6)	2.8720(14)	Rh(7)-Rh(7)#1	2.8262(19)
Rh(2)-Rh(3)	2.8788(13)	Rh(7)-Rh(5)#1	2.8786(14)
Rh(2)-Rh(4)#1	3.0002(13)	Rh(7)-Rh(2)#1	3.0249(14)
Rh(2)-Rh(5)	3.0029(13)	Rh(6)-Rh(7)#1	3.2940(14)
Rh(2)-Rh(7)#1	3.0250(14)	Rh(3)-Rh(3)#1	3.3680(15)

Table 5.3. Most relevant bond lengths for $[Rh_{12}Sb(CO)_{27}]^{3-}$.

V.V. IR and ESI-MS characterization and electron counting of the $[Rh_{12}Sb(CO)_{27}]^{3-}$ cluster

$[Rh_{12}Sb(CO)_{27}]^{3-}$ as salt of $[NEt_4]^+$ is soluble in acetone, acetonitrile and DMF and stable, but not soluble, in water.

Its IR spectrum recorded in CH_3CN shows ν_{CO} absorptions at 2021(sh), 2013(vs) and 1826(m) cm^{-1}.

The ESI-MS analysis was performed on the same solution of the IR one. The spectrum displays many groups of peaks starting at 1159, 1093, 1028 and 704, which can be correlated respectively to $\{[Rh_{12}Sb(CO)_{25}][NEt_4]_2\}^{2-}$, $\{[Rh_{12}Sb(CO)_{25}][NEt_4]\}^{2-}$, $[Rh_{12}Sb(CO)_{25}]^{2-}$ and $[Rh_{12}Sb(CO)_{27}]^{3-}$.

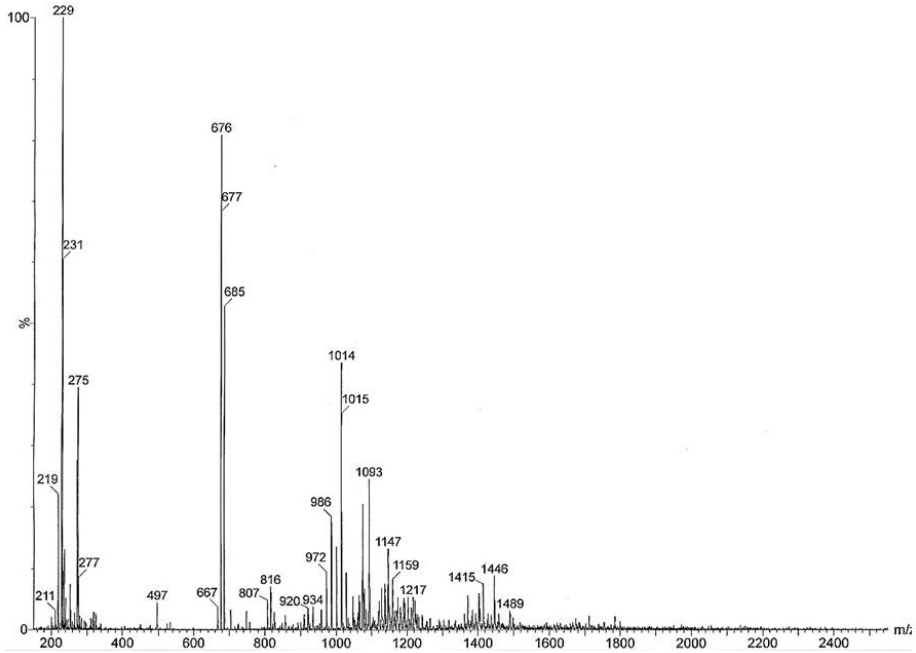

Figure 5.6. ESI-MS spectrum of $[Rh_{12}Sb(CO)_{27}][NEt_4]_3$ recorded in CH_3CN solution.

Peaks or groups of peaks (m/z)	Corresponding Ions
1159	$\{[Rh_{12}Sb(CO)_{25}][NEt_4]_2\}^{2-}$
1093-1065	$\{[Rh_{12}Sb(CO)_{25\text{-}23}][NEt_4]\}^{2-}$
1028-1014-1000-986-972-958	$[Rh_{12}Sb(CO)_{25\text{-}24\text{-}23\text{-}22\text{-}21\text{-}20}]^{2-}$
704-685-676	$[Rh_{12}Sb(CO)_{27\text{-}25\text{-}24}]^{3-}$

Table 5.4. ESI-MS signal assignments for $[Rh_{12}Sb(CO)_{27}][NEt_4]_3$.

As for the electron counting, the $[Rh_{12}Sb(CO)_{27}]^{3-}$ cluster perfectly conforms to previously descripted rules (Chapter II) and presents 170 CVEs, given by the 9 × 12 rhodium atoms (108), the 2 × 27 carbonyl ligands (54), the interstitial Sb atom (5), and the negative charge (3).

V.VI. Molecular structure of the $[Rh_{20}Sb_3(CO)_{36}]^{3-}$ cluster

The molecular structure of $[Rh_{20}Sb_3(CO)_{36}]^{3-}$ (3) is illustrated in Figure 5.7. The $[Rh_{20}Sb_3(CO)_{36}][NEt_4]_3 \cdot 2(CH_3)_2CO$ compound crystallized in the triclinic *P*-1, with Z = 2, so the unit cell contains two cluster units and six cations, all arranged in an ionic solid fashion.

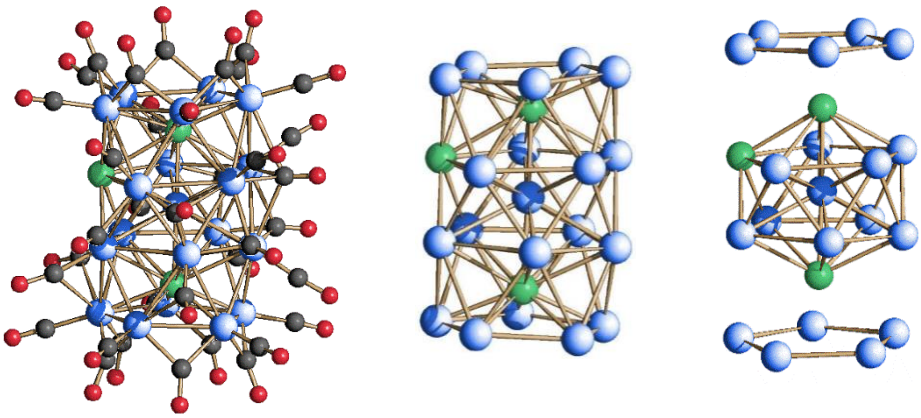

Figure 5.7. Molecular structure of $[Rh_{20}Sb_3(CO)_{36}]^{3-}$ (left), its metal skeleton (centre) and icosahedral unit $Rh_{10}Sb_3$ capped by two pentagonal Rh_5 faces (right). Rh atoms are depicted in blue, Sb atoms are depicted in green, C atoms are in grey and O atoms are in red.

The metal skeleton consists of a Rh-centred $Rh_{10}Sb_3$ icosahedron capped by two pentagonal Rh_5 faces and it is stabilized by 36 carbonyl ligands, of which 19 terminally bonded, 15 edge-bridging and 2 face-bridging.

The Rh-Rh distances present an average contact of 2.893 Å, having the shortest bonding distance at 2.747(4) Å and the longest one at 3.140(4) Å. The Rh-Sb bond lengths involving the interstitial Sb atoms (Sb(1) and Sb(3)) with the inner Rh(7) atom are the shortest, being 2.533(4) Å and 2.570(4) Å, average 2.552 Å. The bond distances with the peripheral Rh atoms are significantly longer as they span from 2.622(3) Å to 3.048(3) Å, with an average of 2.801 Å. Conversely, the Rh-Sb bond

lengths involving the surface Sb atom (Sb(2)) vary from 2.671(3) to 3.074(3) Å, with an average contact of 2.863 Å.

Sb(1)-Rh(7)	2.570(4)
Sb(1)-Rh(22)	2.658(3)
Sb(1)-Rh(19)	2.677(3)
Sb(1)-Rh(12)	2.687(4)
Sb(1)-Rh(23)	2.686(3)
Sb(1)-Rh(18)	2.699(3)
Sb(1)-Rh(4)	2.887(3)
Sb(1)-Rh(9)	2.891(3)
Sb(1)-Rh(14)	2.923(3)
Sb(1)-Rh(16)	2.947(3)
Sb(1)-Rh(8)	2.952(3)
Sb(2)-Rh(4)	2.671(3)
Sb(2)-Rh(9)	2.672(3)
Sb(2)-Rh(7)	2.724(3)
Sb(2)-Rh(17)	2.836(3)
Sb(2)-Rh(10)	2.852(3)
Sb(2)-Sb(3)	3.009(3)
Sb(2)-Rh(5)	3.063(4)
Sb(2)-Rh(15)	3.074(3)
Sb(3)-Rh(7)	2.533(4)
Sb(3)-Rh(21)	2.622(3)
Sb(3)-Rh(11)	2.628(3)
Sb(3)-Rh(13)	2.627(3)
Sb(3)-Rh(17)	2.699(3)
Sb(3)-Rh(10)	2.700(3)
Sb(3)-Rh(20)	2.920(3)
Sb(3)-Rh(6)	2.925(3)
Sb(3)-Rh(5)	3.039(3)
Sb(3)-Rh(15)	3.048(3)
Rh(4)-Rh(5)	2.781(4)
Rh(4)-Rh(22)	2.862(4)

Rh(4)-Rh(7)	2.869(3)
Rh(4)-Rh(19)	2.886(4)
Rh(4)-Rh(9)	3.010(4)
Rh(4)-Rh(8)	3.140(4)
Rh(5)-Rh(8)	2.747(4)
Rh(5)-Rh(7)	2.808(4)
Rh(5)-Rh(11)	2.891(4)
Rh(5)-Rh(17)	2.912(4)
Rh(5)-Rh(6)	3.097(3)
Rh(6)-Rh(8)	2.797(4)
Rh(6)-Rh(7)	2.812(4)
Rh(6)-Rh(16)	2.822(4)
Rh(6)-Rh(20)	2.922(4)
Rh(6)-Rh(13)	2.932(4)
Rh(6)-Rh(11)	2.947(4)
Rh(7)-Rh(20)	2.807(4)
Rh(7)-Rh(15)	2.823(4)
Rh(7)-Rh(8)	2.827(4)
Rh(7)-Rh(14)	2.830(4)
Rh(7)-Rh(16)	2.843(4)
Rh(7)-Rh(9)	2.880(4)
Rh(8)-Rh(18)	2.876(4)
Rh(8)-Rh(22)	2.933(4)
Rh(8)-Rh(16)	2.959(4)
Rh(9)-Rh(15)	2.779(4)
Rh(9)-Rh(19)	2.881(4)
Rh(9)-Rh(12)	2.887(4)
Rh(9)-Rh(14)	3.125(4)
Rh(10)-Rh(17)	2.889(4)
Rh(10)-Rh(15)	2.905(4)
Rh(10)-Rh(21)	2.917(3)

Rh(11)-Rh(17)	2.914(4)	Rh(14)-Rh(16)	2.940(4)
Rh(11)-Rh(13)	2.926(4)	Rh(15)-Rh(21)	2.905(4)
Rh(12)-Rh(23)	2.868(4)	Rh(15)-Rh(20)	3.081(4)
Rh(12)-Rh(14)	2.923(4)	Rh(16)-Rh(20)	2.812(4)
Rh(12)-Rh(19)	2.936(4)	Rh(16)-Rh(23)	2.891(4)
Rh(13)-Rh(21)	2.907(4)	Rh(16)-Rh(18)	2.893(4)
Rh(13)-Rh(20)	2.947(4)	Rh(18)-Rh(22)	2.862(4)
Rh(14)-Rh(15)	2.749(4)	Rh(18)-Rh(23)	2.862(4)
Rh(14)-Rh(20)	2.802(4)	Rh(19)-Rh(22)	2.928(4)
Rh(14)-Rh(23)	2.872(4)	Rh(20)-Rh(21)	2.920(4)

Table 5.5. Most relevant bond lengths for $[Rh_{20}Sb_3(CO)_{36}]^{3-}$.

The maximum size of the $[Rh_{20}Sb_3(CO)_{36}]^{3-}$ cluster, measured from the outermost oxygen atoms of the carbonyl ligands and including twice the oxygen van der Waals radius, is 1.6 nm.

V.VII. IR and ESI-MS characterization and electron counting of the $[Rh_{20}Sb_3(CO)_{36}]^{3-}$ cluster

$[Rh_{20}Sb_3(CO)_{36}]^{3-}$ as salt of $[NEt_4]^+$ is soluble in acetone, acetonitrile and DMF and stable, but not soluble, in water.

Its IR spectrum recorded in CH_3CN shows ν_{CO} absorptions at 2030(vs) and 1833(ms) cm^{-1}.

The ESI-MS analysis was performed on the same solution of the IR one. The spectrum displays many groups of peaks because of the instability of this high nuclearity cluster in the experimental conditions. The only group of peaks attributable at the integer species starts at 1135 m/z. The others are due to the breaking of the metal skeleton.

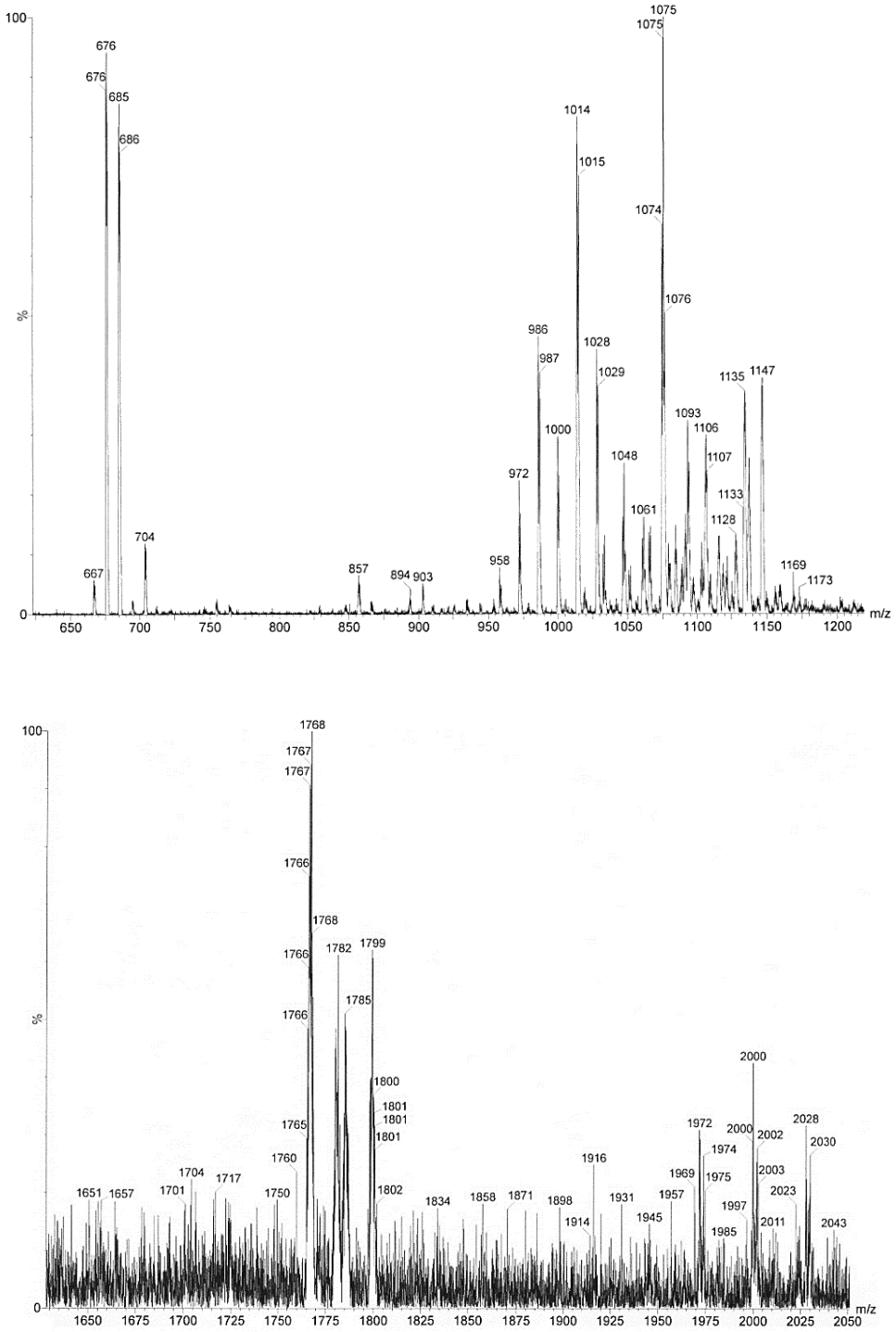

Figure 5.8. ESI-MS spectra of $[Rh_{20}Sb_3(CO)_{36}][NEt_4]_3$ recorded in CH_3CN solution.

Signals or groups of signals (m/z)	Corresponding Ions
2028-2000-1972-1945-1916	$\{[Rh_{10}Sb_3(CO)_{18\text{-}17\text{-}16\text{-}15\text{-}14}][NEt_4]\}^-$
1782-1768	$\{[Rh_{20}Sb_3(CO)_{36\text{-}35}][NEt_4]\}^{2-}$
1135-1106	$[Rh_{20}Sb_3(CO)_{35\text{-}32}]^{3-}$
1028-1014-1000-986-972-958	$\{[Rh_{10}Sb_3(CO)_{19\text{-}18\text{-}17\text{-}16\text{-}15\text{-}14}][NEt_4]\}^{2-}$
704-685-676	$\{[Rh_{10}Sb_3(CO)_{21\text{-}19\text{-}18}][NEt_4]\}^{3-}$

Table 5.6. ESI-MS signal assignments for $[Rh_{20}Sb_3(CO)_{36}][NEt_4]_3$.

As for the electron counting, since the structure can be seen as three pentagonal antiprisms (3 × 146 CVEs) fused through pentagonal faces (− 2 × 80 CVEs) and since one of the atoms of the metal skeleton (Sb) does not possess d orbitals and is present on two of the pentagonal antiprisms (−2 × 5 CVEs), $[Rh_{20}Sb_3(CO)_{36}]^{3-}$ should have 268 CVEs.

As a matter of fact, the CVEs for $[Rh_{20}Sb_3(CO)_{36}]^{3-}$ are 268, given by the 9 × 20 rhodium atoms (180), the 2 × 36 carbonyl ligands (72), the 5 × 2 interstitial Sb atoms (10), the surface Sb atom (3) and the negative charge (3).

V.VIII. Reactivity of $[Rh_{12}Sb(CO)_{27}]^{3-}$ under N_2 atmosphere

Once obtained and completely characterized $[Rh_{12}Sb(CO)_{27}]^{3-}$, we tested its stability under nitrogen atmosphere.

By IR monitoring, a progressive lowering of its ν_{CO} stretching frequencies was recorded in acetonitrile, both for terminal and bridging carbonyls. More specifically, the initial peaks at 2013(vs) and 1826(m) cm^{-1} gradually decreased down to 1995(s) and 1806(m, br) cm^{-1}, respectively, over 24 hours. When the latter solution was put back into CO atmosphere, the opposite phenomenon occurred and the ν_{CO} stretching frequencies returned to their original values. Assuming that the parent cluster maintained its metal structure throughout both processes, in the first case such lowering of CO frequencies is compatible with some ligand loss. In fact, the same negative charge has to be transferred, via π back-bonding, onto a

minor number of ligands, resulting in an overall decrease of the C−O bond strength and, consequently, in a lowering of the IR frequencies.

Unfortunately, we could not crystallize what we supposed to be an unsaturated species under nitrogen. However, this result encouraged us to repeat the synthesis of $[Rh_{12}Sb(CO)_{27}]^{3-}$ by using the same reaction conditions as before but carrying it out under N_2 atmosphere. This result will be presented in the following paragraph.

Crystallographic data for Rh-Sb carbonyl clusters

Compound	**1**$[NEt_4]_2 \cdot THF$	**2**$[NEt_4]_3$	**3**$[NEt_4]_3 \cdot 2(CH_3)_2CO$
Formula	$C_{46}H_{48}N_2O_{27}Rh_{11}Sb$	$C_{51}H_{60}N_3O_{27}Rh_{12}Sb$	$C_{66}H_{72}N_3O_{38}Rh_{20}Sb_3$
Fw	2314.62	2503.69	3938.71
Crystal system	Monoclinic	Monoclinic	Triclinic
Space group	P2c	*C*2/c	P-1
***a* (Å)**	11.4321(9)	20.020(5)	14.7194(4)
***b* (Å)**	39.045(3)	22.608(6)	15.1094(4)
***c* (Å)**	14.0588(12)	15.786(4)	24.6975(6)
α (deg)	90	90	100.929(2)
β (deg)	97.091(2)	102.489(3)	96.759(2)
γ (deg)	90	90	117.239(2)
Cell volume (Å^3)	6227.4(9)	6976(3)	4661.7(2)
Z	4	4	2
D (g/cm^3)	2.469	2.384	2.806
μ (mm^{-1})	3.339	3.214	4.366
F (000)	4400	4776	3692
θ limits (deg)	2.076-25.000	1.377-25.995	1.575-25.000
Index ranges	$-13 \leq h \leq 13$, $-46 \leq k \leq 46$, $-16 \leq l \leq 16$	$-24 \leq h \leq 24$, $-27 \leq k \leq 27$, $-19 \leq l \leq 19$	-17<=h<=17, -17<=k<=17, -29<=l<=29
Reflections collected	73965	20859	68897
Independent reflections	10968 [R(int) = 0.0276]	6770 [R(int) = 0.0647]	16390 [R(int) = 0.2549]
Completeness to θ max	99.9%	98.8%	99.9%
Data/restraints/ parameters	10968/818/1010	6770/12/432	16390 / 1142 / 1303
Goodness-of-fit	1.272	1.039	0.968
R_1 ($I > 2\sigma(I)$)	0.0212	0.0604	0.1004
wR_2 (all data)	0.0461	0.1822	0.3313
Largest diff. peak and hole, e Å^{-3}	0.522 and -0.861	2.987 and -1.559	5.189 and -2.014

Table 5.7. Crystallographic data for clusters 1, 2 and 3.

V.IX. Reactivity of $[Rh_7(CO)_{16}]^{3-}$ with $SbCl_3$ under N_2 atmosphere

Since in Rh-Ge system we had obtained different clusters by working under different atmospheres and since, above all, we had verified that it was possible to obtain an unsaturated icosahedral species by putting a solution of $[Rh_{12}Sb(CO)_{27}]^{3-}$ under N_2 atmosphere, we tested the reactivity of $[Rh_7(CO)_{16}]^{3-}$ with $SbCl_3$ under nitrogen.

As for all the previous reactions shown in these chapters, we used the IR spectroscopy to check the reaction paths. In these reaction conditions, in acetonitrile, we stopped the addition of the Sb^{3+} salt after 0.7 equivalents, because of the total disappearance of the ν_{CO} absorptions of $[Rh_7(CO)_{16}]^{3-}$. However, this reaction did not lead to the expected unsaturated icosahedral cluster, but to two higher nuclearity Rh-Sb compounds of similar solubility.

More specifically, at the end of the reaction, after the complete elimination of the $[Rh(CO)_2Cl_2]^-$ complex in ethanol and THF, the extraction in acetone solubilized the new $[Rh_{24}Sb_4(CO)_{44}]^{n-}$ cluster together with another (partially soluble) new $[Rh_{21}Sb_2(CO)_{38}]^{5-}$ species. The latter was completely separated with the subsequent extraction in acetonitrile. Both clusters were crystallized as salts of $[NEt_4]^+$ by layering the acetone and acetonitrile solutions with hexane and di-isopropyl ether, respectively. In the case of the acetone solution, this gave rise to two different shaped crystals which were manually separated and both analysed by X-ray diffraction. We tried to perform the $[NEt_4]^+$ metathesis with $[NMe_4]^+$, $[NMe_3Bz]^+$ and $[NPr_4]^+$, but these counter-ions never imparted such a different solubility to the clusters so to allow their complete separation in solution.

The $[Rh_{21}Sb_2(CO)_{38}]^{5-}$ species deserves a special mention. We crystallized it several times and the diffraction analysis identified four different unit cells, which did not represent polymorphs of the same compound but they contained co-crystallized isomers of the cluster with a different number of carbonyl ligands, and in an arbitrary ratio. More specifically, the structural data showed the existence of three compounds, namely $[Rh_{21}Sb_2(CO)_{38}]^{5-}$, $[Rh_{21}Sb_2(CO)_{39}]^{5-}$ and $[Rh_{21}Sb_2(CO)_{40}]^{5-}$.

The difference in the carbonyl ligands was not significantly detected in their IR spectra in solution, but a closer look at some of the ESI-MS spectra showed minor peaks related to species with up to 40 ligands (see later). Unfortunately, we did not succeed in separating the three $[Rh_{21}Sb_2(CO)_{38+x}]^{5-}$ (x = 0, 1, 2) clusters neither in the solid state nor in solution.

Since we were not successful in obtaining any unsaturated icosahedral species in the reaction conditions aforementioned, we chose to investigate the reactivity of $[Rh_7(CO)_{16}]^{3-}$ with $SbCl_3$ by changing, first of all, the reaction solvent into acetone, to promote its possible precipitation from the mother solution so to subtract it from potential subsequent reactions.

We conducted the reaction between $[Rh_7(CO)_{16}][NEt_4]_3$ and $SbCl_3$ in acetone under nitrogen atmosphere till a final stoichiometric Rh_7:Sb^{3+} ratio of 1:0.8, necessary to consume the cluster precursor. The reaction path appeared more complicated than the one in CO, as inferred by IR monitoring. As expected, some insoluble residue was found in the mother solution at the end of the reaction, making the filtration a necessary operation before the work-up of the solution. After drying the latter under vacuum, the extraction in THF not only allowed the elimination of the $[Rh(CO)_2Cl_2]^-$ complex, but the IR spectrum revealed the presence of an unidentified compound, whose poor yield prevented us from performing any further analysis. However, the extraction in acetone allowed us to isolate a species whose ν_{CO} stretching frequencies were compatible with those observed during the reactivity of $[Rh_{12}Sb(CO)_{27}]^{3-}$ under N_2 (see above). The new $[Rh_{12}Sb(CO)_{24}]^{4-}$ unsaturated compounds was crystallized as salt of $[NEt_4]^+$ by layering di-isopropyl ether on the acetonitrile solution (where the cluster had been transferred to). [11] The last extraction in acetonitrile solubilized some residual $[Rh_{21}Sb_2(CO)_{38+x}]^{5-}$, which was present in a very small quantity. In fact, this cluster precipitated from the mother solution as it is only partially soluble in acetone, and it was separated from the reaction mixture by a simple filtration. After drying the residue under vacuum, the cluster was extracted in acetonitrile, making this synthesis the best way to prepare $[Rh_{21}Sb_2(CO)_{38+x}]^{5-}$.

Notably, when $[Rh_{12}Sb(CO)_{24}]^{4-}$ is exposed to CO atmosphere in solution, its IR spectrum perfectly overlaps the one of $[Rh_{12}Sb(CO)_{27}]^{3-}$, indicating an equilibrium between the two clusters driven by the presence/absence of CO atmosphere. However, the difference in their negative charge makes it more complicated than it appears and so far we have not been able to completely disclose it.

Nevertheless, this experimental result makes $[Rh_{12}Sb(CO)_{27}]^{3-}$ a rare example of a CO-releasing transition-metal carbonyl cluster, which could be relevant in that field of research. [12]

V.X. Molecular structure of the $[Rh_{21}Sb_2(CO)_{38+x}]^{5-}$ cluster

The molecular structure of $[Rh_{21}Sb_2(CO)_{38+x}]^{5-}$ (4) is represented in Figure 5.9.

As $[Rh_{21}Sb_2(CO)_{38+x}][NEt_4]_5 \cdot 4CH_3CN$ the compound crystallized in the triclinic *P*-1 and Z = 2, so the unit cell contains two cluster units, ten cations and eight molecules of acetonitrile, all arranged in an ionic solid fashion. We analysed other crystals which showed different cells and Z, but we report here the one with the best data.

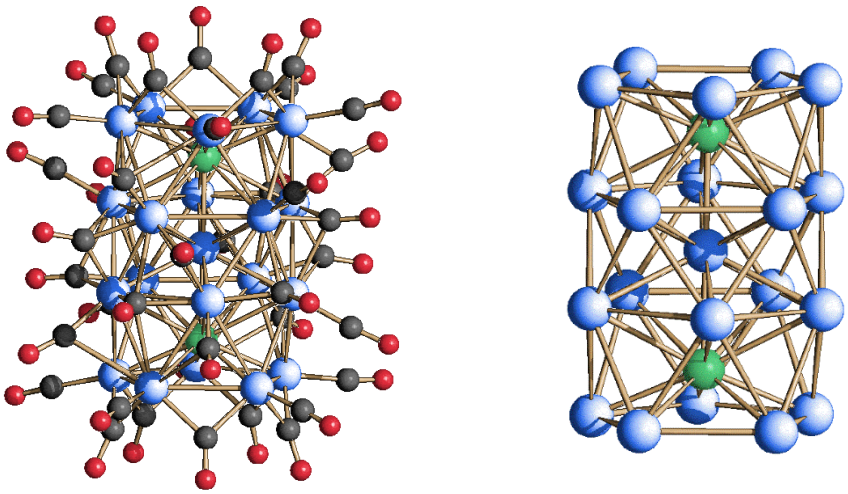

Figure 5.9. Molecular structure of $[Rh_{21}Sb_2(CO)_{38}]^{5-}$ (left) and its metal skeleton (right). Rh atoms are depicted in blue, Sb atoms are depicted in green, C atoms are in grey and O atoms are in red.

The independent unit contains two half cluster molecules and they differ from the number of CO ligands. More specifically, while the CO content of each cluster is on average of 38.2, one whole isomer is actually stabilized by 38 CO ligands, of which 20 terminally bonded, 14 edge-bridging and 4 face-bridging. Conversely, the second independent half cluster shows an extra CO ligand with a 20% occupation factor, which could mean the presence of either a $[Rh_{21}Sb_2(CO)_{39}]^{5-}$ (40%) or a $[Rh_{21}Sb_2(CO)_{40}]^{5-}$ (20%). We believe that both exist, as inferred from the ESI-MS analyses. The extra ligands show a bridging coordination.

The metal skeleton of $[Rh_{21}Sb_2(CO)_{38+x}]^{5-}$ is really similar to the one of $[Rh_{20}Sb_3(CO)_{36}]^{3-}$ (previously described) and consists of a Rh-centred $Rh_{11}Sb_2$ icosahedron capped by two pentagonal Rh_5 faces.

Sb(1)-Rh(2)	2.5128(9)
Sb(1)-Rh(9)	2.6470(12)
Sb(1)-Rh(10)	2.6529(13)
Sb(1)-Rh(12)	2.6581(10)
Sb(1)-Rh(11)	2.6730(10)
Sb(1)-Rh(8)	2.6972(10)
Sb(1)-Rh(4)#1	2.9004(13)
Sb(1)-Rh(7)#1	2.9011(14)
Sb(1)-Rh(6)#1	2.9097(11)
Sb(1)-Rh(3)#1	2.9242(11)
Sb(1)-Rh(5)	2.9389(10)
Rh(2)-Sb(1)#1	2.5128(9)
Rh(3)-Sb(1)#1	2.9242(11)
Rh(4)-Sb(1)#1	2.9004(13)
Rh(6)-Sb(1)#1	2.9096(11)
Rh(7)-Sb(1)#1	2.9011(14)
Rh(2)-Rh(7)	2.7867(9)
Rh(2)-Rh(7)#1	2.7867(9)
Rh(2)-Rh(3)#1	2.8024(11)
Rh(2)-Rh(3)	2.8024(11)
Rh(2)-Rh(6)#1	2.8114(10)

Rh(2)-Rh(4)#1	2.8114(11)
Rh(2)-Rh(6)	2.8114(10)
Rh(2)-Rh(4)	2.8114(11)
Rh(2)-Rh(5)#1	2.8305(12)
Rh(2)-Rh(5)	2.8306(12)
Rh(3)-Rh(5)	2.7733(12)
Rh(3)-Rh(4)#1	2.7970(11)
Rh(3)-Rh(9)#1	2.8898(11)
Rh(3)-Rh(8)#1	2.9296(13)
Rh(3)-Rh(7)	2.9394(12)
Rh(3)-Rh(6)	3.0534(12)
Rh(4)-Rh(7)#1	2.7062(10)
Rh(4)-Rh(3)#1	2.7970(11)
Rh(4)-Rh(10)#1	2.8698(12)
Rh(4)-Rh(12)#1	2.9014(11)
Rh(4)-Rh(6)	2.9446(12)
Rh(4)-Rh(5)#1	3.0909(11)
Rh(5)-Rh(6)	2.7879(11)
Rh(5)-Rh(11)	2.8712(15)
Rh(5)-Rh(12)	2.8829(13)
Rh(5)-Rh(7)#1	3.0705(10)

Rh(5)-Rh(4)#1	3.0909(12)	Rh(8)-Rh(6)#1	2.9172(15)
Rh(6)-Rh(7)#1	2.7917(14)	Rh(8)-Rh(3)#1	2.9296(13)
Rh(6)-Rh(10)#1	2.8978(10)	Rh(9)-Rh(7)#1	2.8550(12)
Rh(6)-Rh(8)#1	2.9170(15)	Rh(9)-Rh(11)	2.8781(12)
Rh(7)-Rh(4)#1	2.7062(10)	Rh(9)-Rh(3)#1	2.8897(11)
Rh(7)-Rh(6)#1	2.7916(14)	Rh(10)-Rh(4)#1	2.8698(12)
Rh(7)-Rh(9)#1	2.8550(12)	Rh(10)-Rh(12)	2.8705(12)
Rh(7)-Rh(11)#1	2.9046(10)	Rh(10)-Rh(6)#1	2.8979(10)
Rh(7)-Rh(5)#1	3.0704(10)	Rh(11)-Rh(12)	2.8744(12)
Rh(8)-Rh(9)	2.8734(11)	Rh(11)-Rh(7)#1	2.9047(11)
Rh(8)-Rh(10)	2.8781(10)	Rh(12)-Rh(4)#1	2.9014(11)

Table 5.8. Most relevant bond lengths for the first isomer of $[Rh_{21}Sb_2(CO)_{38+x}]^{5-}$.

Sb(21)-Rh(22)	2.5137(9)	Rh(22)-Rh(24)#2	2.8182(10)
Sb(21)-Rh(29)	2.6488(9)	Rh(22)-Rh(24)	2.8183(10)
Sb(21)-Rh(30)	2.6529(13)	Rh(22)-Rh(26)#2	2.8193(11)
Sb(21)-Rh(27)	2.6570(11)	Rh(22)-Rh(26)	2.8193(11)
Sb(21)-Rh(31)	2.6586(9)	Rh(22)-Rh(25)	2.8263(10)
Sb(21)-Rh(32)	2.6843(11)	Rh(22)-Rh(25)#2	2.8263(10)
Sb(21)-Rh(23)#2	2.8920(10)	Rh(23)-Rh(28)#2	2.7199(10)
Sb(21)-Rh(28)#2	2.9001(10)	Rh(23)-Rh(24)#2	2.7901(14)
Sb(21)-Rh(26)#2	2.9064(14)	Rh(23)-Rh(27)#2	2.8777(13)
Sb(21)-Rh(24)#2	2.9206(12)	Rh(23)-Rh(31)#2	2.8903(15)
Sb(21)-Rh(25)	2.9571(13)	Rh(23)-Rh(26)	2.9434(11)
Rh(22)-Sb(21)#2	2.5136(9)	Rh(23)-Rh(25)#2	3.0616(12)
Rh(23)-Sb(21)#2	2.8919(10)	Rh(24)-Rh(25)	2.7715(12)
Rh(24)-Sb(21)#2	2.9206(12)	Rh(24)-Rh(23)#2	2.7901(14)
Rh(26)-Sb(21)#2	2.9064(14)	Rh(24)-Rh(29)#2	2.8912(12)
Rh(28)-Sb(21)#2	2.9000(10)	Rh(24)-Rh(32)#2	2.9139(12)
Rh(22)-Rh(28)	2.7881(12)	Rh(24)-Rh(28)	2.9579(12)
Rh(22)-Rh(28)#2	2.7881(11)	Rh(24)-Rh(26)	3.0749(11)
Rh(22)-Rh(23)	2.7923(11)	Rh(25)-Rh(26)	2.7915(11)
Rh(22)-Rh(23)#2	2.7923(11)	Rh(25)-Rh(30)	2.8816(12)

Rh(25)-Rh(27)	2.8855(13)	Rh(28)-Rh(30)#2	2.9009(11)
Rh(25)-Rh(23)#2	3.0616(13)	Rh(28)-Rh(25)#2	3.0629(13)
Rh(25)-Rh(28)#2	3.0628(13)	Rh(29)-Rh(28)#2	2.8696(15)
Rh(26)-Rh(28)#2	2.7857(13)	Rh(29)-Rh(30)	2.8717(11)
Rh(26)-Rh(31)#2	2.8954(10)	Rh(29)-Rh(32)	2.8779(12)
Rh(26)-Rh(32)#2	2.9085(11)	Rh(29)-Rh(24)#2	2.8911(12)
Rh(27)-Rh(30)	2.8476(11)	Rh(30)-Rh(28)#2	2.9009(11)
Rh(27)-Rh(31)	2.8669(11)	Rh(31)-Rh(32)	2.8769(13)
Rh(27)-Rh(23)#2	2.8776(13)	Rh(31)-Rh(23)#2	2.8904(15)
Rh(28)-Rh(23)#2	2.7200(10)	Rh(31)-Rh(26)#2	2.8953(10)
Rh(28)-Rh(26)#2	2.7857(13)	Rh(32)-Rh(26)#2	2.9085(12)
Rh(28)-Rh(29)#2	2.8695(15)	Rh(32)-Rh(24)#2	2.9139(12)

Table 5.9. Most relevant bond lengths for the second isomer of $[Rh_{21}Sb_2(CO)_{38+x}]^{5-}$.

The two half cluster molecules in the independent unit are only marginally different in their interatomic metallic distances. The Rh-Rh distances vary from 2.7062(10) to 3.0909(12) Å and from 2.7199(10) to 3.0749(11) Å in the two isomers, with average values of 2.8741 and 2.8723 Å, respectively. These average values are slightly shorter than the average one of Rh-Rh bonds present in $[Rh_{20}Sb_3(CO)_{36}]^{3-}$ cluster (2.893 Å). The Rh-Sb bond lengths in the two isomers of $[Rh_{21}Sb_2(CO)_{38+x}]^{5-}$ involving the inner Rh atoms (Sb(1)-Rh(2) and Sb(21)-Rh(22)) are the shortest, being 2.5128(9) Å and 2.5137(9) Å, respectively, and shorter than those in the $[Rh_{20}Sb_3(CO)_{36}]^{3-}$ cluster. The bond distances with the peripheral Rh atoms are significantly longer as they span from 2.6470(12) to 2.9389(10) Å and from 2.6488(9) to 2.9571(13) Å in the two isomers, with average values of 2.8241 and 2.8212 Å, respectively.

The maximum size of the $[Rh_{21}Sb_2(CO)_{38+x}]^{5-}$ cluster, measured from the outermost oxygen atoms of the carbonyl ligands and including twice the oxygen van der Waals radius, is 1.6 nm.

V.XI. IR and ESI-MS characterization and electron counting of the $[Rh_{21}Sb_2(CO)_{38+x}]^{5-}$ cluster

$[Rh_{21}Sb_2(CO)_{38+x}]^{5-}$ as salt of $[NEt_4]^+$ is partially soluble in acetone, completely soluble in acetonitrile and DMF and stable, but not soluble, in water. The same species as salt of $[NMe_3Bz]^+$ (Bz = benzyl) is not soluble in acetone.

We recorded its IR spectrum in CH_3CN, which shows ν_{CO} absorptions are at 1995(vs), 1954(w) and 1805(ms) cm^{-1}.

The ESI-MS analysis, recorded on a solution of $[Rh_{21}Sb_2(CO)_{38+x}][NMe_3Bz]_5$ in acetonitrile, shows three groups of peaks of different intensity. The lower intensity group, which starts at 1795 m/z, can be attributed to the $\{[Rh_{21}Sb_2(CO)_{37}][NMe_3Bz]\}^{2-}$ ion, the one starting at 1197 m/z is related to $\{[Rh_{21}Sb_2(CO)_{37}][NMe_3Bz]\}^{3-}$, and finally the peak at 1138 m/z corresponds to the $[Rh_{21}Sb_2(CO)_{36}]^{3-}$ ion. They are all accompanied by further signals due to consecutive CO loss.

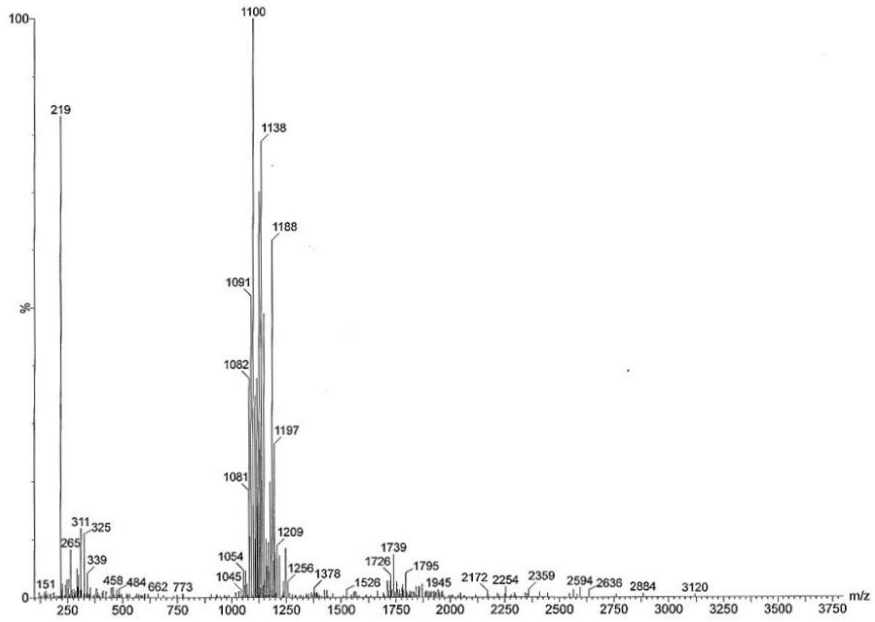

Figure 5.10. ESI-MS spectrum of $[Rh_{21}Sb_2(CO)_{38+x}][NMe_3Bz]_5$ recorded in CH_3CN solution.

Signals or groups of signals (m/z)	Corresponding Ions
1810-1795-1739-1726	$\{[Rh_{21}Sb_2(CO)_{37\text{-}33\text{-}32}][NMe_3Bz]\}^{2-}$
1197-1188-1178-1149	$\{[Rh_{21}Sb_2(CO)_{37\text{-}36\text{-}35\text{-}32}][NMe_3Bz]\}^{3-}$
1138-1128-1100-1091-1082-1054-1045	$[Rh_{21}Sb_2(CO)_{36\text{-}35\text{-}32\text{-}31\text{-}30\text{-}27\text{-}26}]^{3-}$

Table 5.10. ESI-MS signal assignments for $[Rh_{21}Sb_2(CO)_{38+x}][NMe_3Bz]_5$.

From this particular spectrum we did not have significant evidences of the presence of more than 38 CO ligands on the cluster. However, as we recorded several spectra, we were able to actually detect a $\{[Rh_{21}Sb_2(CO)_{40}]\}^{3-}$ species in a few of them. This detail is shown in Figure 5.11.

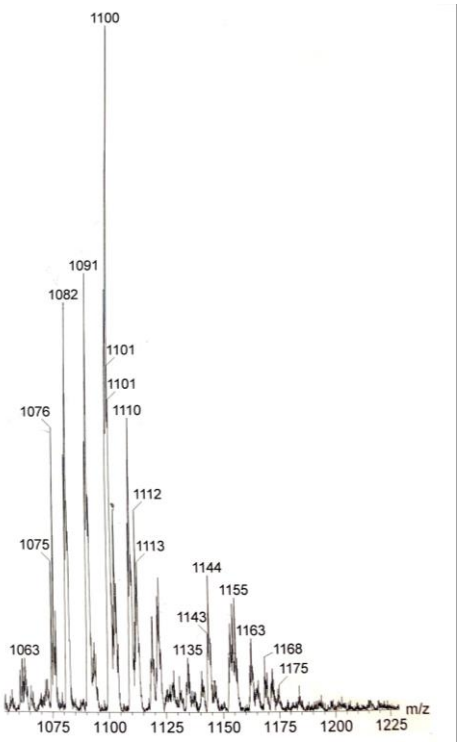

Figure 5.11. Close-up of the ESI-MS of $[Rh_{21}Sb_2(CO)_{38+x}]^{5-}$ (x = 0-2) recorded in CH_3CN solution, showing signals attributable to the $\{[Rh_{21}Sb_2(CO)_{40}]\}^{3-}$ (1175 m/z) and $\{[Rh_{21}Sb_2(CO)_{39}]\}^{3-}$ (1166 m/z) ions.

As for the electron counting, since the structure can be seen as three pentagonal antiprisms (3 × 146 CVEs) fused through pentagonal faces (−2 × 80 CVEs) where, differently from the previous case of $[Rh_{20}Sb_3(CO)_{36}]^{3-}$, all the atoms constituting the skeleton possess d orbitals, $[Rh_{21}Sb_2(CO)_{38+x}]^{5-}$ should have 278 CVEs.

Actually, $[Rh_{21}Sb_2(CO)_{38}]^{5-}$ presents 280 CVEs, given by the 9 × 21 rhodium atoms (189), the 2 × 38 carbonyl ligands (76), the 5 × 2 Sb atoms (10), and the negative charge (5). The $[Rh_{21}Sb_2(CO)_{39}]^{5-}$ and $[Rh_{21}Sb_2(CO)_{40}]^{5-}$ clusters possess 282 and 284 CVEs, respectively. Therefore, they do not conform to the Polyhedral Skeleton Electron Pair Theory. Actually, this has proved to be not always suitable to predict the number of cluster valence electrons as the cluster nuclearity increases. [13]

Moreover, despite their structural similarity, the electron counting of $[Rh_{21}Sb_2(CO)_{38}]^{5-}$ and $[Rh_{20}Sb_3(CO)_{36}]^{3-}$ are remarkably different, because of the absence/presence of Sb on the metal skeleton.

V.XII. Molecular structure of the $[Rh_{24}Sb_4(CO)_{44}]^{n-}$ cluster

$[Rh_{24}Sb_4(CO)_{44}]^{n-}$ (5) is the highest nuclearity Rh-Sb carbonyl cluster to date. Unfortunately, its molecular structure has not been totally determined yet because of the low quality of the obtained crystals, so we are not yet able to unambiguously express the cluster charge.

Its molecular structure is illustrated in Figure 5.12.

The $[Rh_{24}Sb_4(CO)_{44}][NEt_4]_n$ crystallized in the $P2_1/n$ space group with Z = 4.

The metal skeleton consists of three uncompleted Sb-centred $Rh_{10}Sb_2$ icosahedra fused together and sharing their capping atom, which is the inner Sb one. It may be also described as a Sb-centred Rh_9Sb_4 icosahedron capped by three pentagonal Rh faces.

This structure is stabilized by 44 carbonyl ligands, of which 20 terminally bonded, 19 edge-bridging and 5 face-bridging.

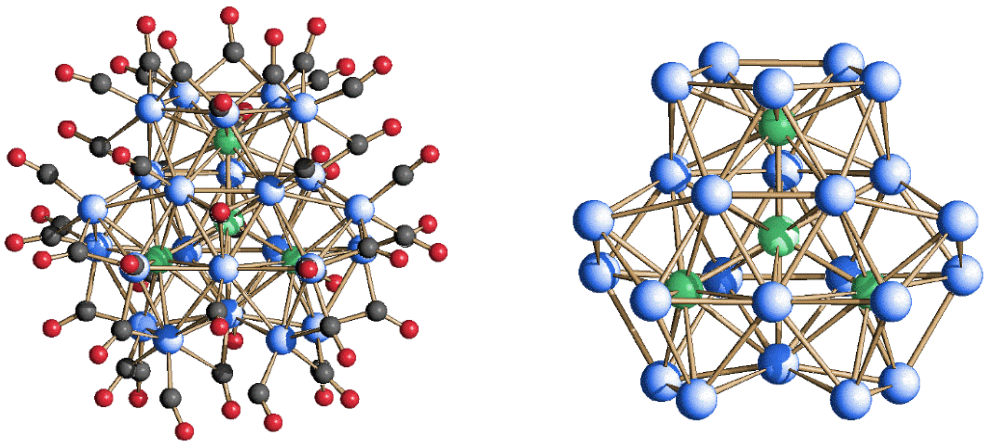

Figure 5.12. Molecular structure of $[Rh_{24}Sb_4(CO)_{44}]^{n-}$ (left) and its metal skeleton (right). Rh atoms are depicted in blue, Sb atoms are depicted in green, C atoms are in grey and O atoms are in red.

The maximum size of the $[Rh_{24}Sb_4(CO)_{44}]^{n-}$ cluster, measured from the outermost oxygen atoms of the carbonyl ligands and including twice the oxygen van der Waals radius, is 1.7 nm.

V.XIII. IR and ESI-MS characterization of the $[Rh_{24}Sb_4(CO)_{44}]^{n-}$ cluster

The $[Rh_{24}Sb_4(CO)_{44}]^{n-}$ cluster as salt of $[NEt_4]^+$ is soluble in acetone, acetonitrile and DMF and stable, but not soluble, in water.

Its IR spectrum recorded in CH_3CN on a few crystals shows ν_{CO} absorptions at 1993(vs) and 1806(mw) cm^{-1}.

The $[Rh_{24}Sb_4(CO)_{44}]^{n-}$ cluster was also analysed by ESI-MS spectrometry. However, the spectrum shows that in experimental conditions this compound heavily breaks giving rise to many smaller fragments.

V.XIV. Molecular structure of the $[Rh_{12}Sb(CO)_{24}]^{4-}$ cluster

The molecular structure of $[Rh_{12}Sb(CO)_{24}]^{4-}$ (6) is illustrated in Figure 5.13. The $[Rh_{12}Sb(CO)_{24}][NEt_4]_4 \cdot 2CH_3CN$ crystallized in the *P*-1 space group and the Sb atom lays on the inversion centre, so the asymmetric unit only contains half a cluster, two cations and one solvent molecule (Z = 1).

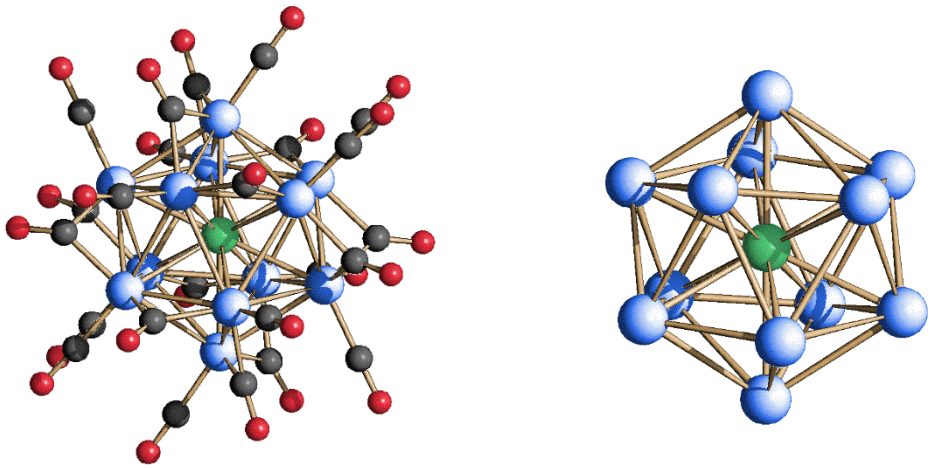

Figure 5.13. Molecular structure of $[Rh_{12}Sb(CO)_{24}]^{4-}$ (left) and its metal skeleton (right). Rh atoms are depicted in blue, Sb atoms are depicted in green, C atoms are in grey and O atoms are in red.

The metal core is really similar to that of the parent icosahedral compound, but it is rather more regular and compact, as inferred by the Rh-Rh and Rh-Sb bond distances, reported in Table 5.11. In fact, although the former distances present an average of 2.974 Å, very similar to the one of $[Rh_{12}Sb(CO)_{27}]^{3-}$, they span from 2.7835(9) to 3.0448(9) Å and no longer bonds are present. The shrinking of the icosahedron is also reflected in the Rh-Sb bond lengths, whose average is 2.7788 Å, going from 2.7454(6) to 2.8016(7) Å. Moreover, the metal skeleton is stabilized by 24 CO ligands, of which 12 are terminally bonded and the remaining 12, edge-bridged.

Sb(1)-Rh(3)#1	2.7454(6)
Sb(1)-Rh(3)	2.7454(6)
Sb(1)-Rh(4)#1	2.7655(7)
Sb(1)-Rh(4)	2.7655(6)
Sb(1)-Rh(5)	2.7865(6)
Sb(1)-Rh(5)#1	2.7865(6)
Sb(1)-Rh(2)#1	2.7868(6)
Sb(1)-Rh(2)	2.7868(6)
Sb(1)-Rh(6)	2.7870(7)
Sb(1)-Rh(6)#1	2.7870(7)
Sb(1)-Rh(7)#1	2.8016(7)
Sb(1)-Rh(7)	2.8016(7)
Rh(2)-Rh(5)	2.7892(9)
Rh(2)-Rh(6)	2.7898(10)
Rh(2)-Rh(7)#1	3.0014(10)
Rh(2)-Rh(3)#1	3.0120(9)
Rh(2)-Rh(4)#1	3.0187(9)

Rh(3)-Rh(5)	2.7835(9)
Rh(3)-Rh(7)	2.7878(10)
Rh(3)-Rh(4)#1	2.9891(10)
Rh(3)-Rh(6)#1	3.0031(10)
Rh(3)-Rh(2)#1	3.0121(9)
Rh(4)-Rh(7)	2.7898(9)
Rh(4)-Rh(6)	2.8048(9)
Rh(4)-Rh(3)#1	2.9891(10)
Rh(4)-Rh(5)#1	2.9974(11)
Rh(4)-Rh(2)#1	3.0187(9)
Rh(5)-Rh(4)#1	2.9973(11)
Rh(5)-Rh(6)	3.0040(9)
Rh(5)-Rh(7)	3.0580(9)
Rh(6)-Rh(3)#1	3.0030(10)
Rh(6)-Rh(7)	3.0448(9)
Rh(7)-Rh(2)#1	3.0014(10)

Table 5.11. Most relevant bond lengths for $[Rh_{12}Sb(CO)_{24}]^{4-}$.

The maximum size of $[Rh_{12}Sb(CO)_{24}]^{4-}$, measured from the outermost oxygen atoms of the COs and including twice the oxygen van der Waals radius, is 1.4 nm.

V.XV. IR and ESR characterization and electron counting of the $[Rh_{12}Sb(CO)_{24}]^{4-}$ cluster

$[Rh_{12}Sb(CO)_{24}]^{4-}$ as salt of $[NEt_4]^+$ is well soluble in acetone, acetonitrile and DMF and stable, but not soluble, in water.

Its IR spectrum recorded in CH_3CN shows ν_{CO} absorptions at 1992(vs) and 1805(ms) cm^{-1}. As for the electron counting, the $[Rh_{12}Sb(CO)_{24}]^{4-}$ cluster presents 165 CVEs, given by the 9 × 12 rhodium atoms (108), the 2 × 24 carbonyl ligands (48), the interstitial Sb atom (5), and the negative charge (4).

As we saw before, usually an icosahedral species presents 170 CVEs to conform to the electron counting rules; thus, this species is electronically unsaturated. Actually, it is not so common for clusters to be stable as paramagnetic species, that is why we performed the ESR (Electron Spin Resonance) analysis in solution of $[Rh_{12}Sb(CO)_{24}]^{4-}$, but no evident signals were observed. However, for paramagnetic carbonyl clusters of such nuclearity, it has been previously reported that ESR experiments may show such broad signals that can be quite difficult, if not impossible, to detect, even in the solid state. [14]

The difference in the CVE between the $[Rh_{12}Sb(CO)_{27}]^{3-}$ and $[Rh_{12}Sb(CO)_{24}]^{4-}$ clusters is accompanied by a difference in the Rh-Rh and Rh-Sb distances, similarly to what happens for the $[Rh_{12}Sn(CO)_{27}]^{4-}$ and $[Rh_{12}Sn(CO)_{25}]^{4-}$ species. More specifically, the interactions are shorter, therefore stronger, in the more unsaturated compound.

In Table 5.12 the average bond lengths of $[Rh_{12}Sb(CO)_{27}]^{3-}$ and $[Rh_{12}Sb(CO)_{24}]^{4-}$ are reported.

Bond lengths	$[Rh_{12}Sb(CO)_{27}]^{3-}$ (170 CVEs)	$[Rh_{12}Sb(CO)_{24}]^{4-}$ (165 CVEs)
Rh-Rh average (Å)	2.982	2.974
Rh-Sb average (Å)	2.823	2.779

Table 5.12. Rh-Rh and Rh-Sb average bond lengths in the $[Rh_{12}Sb(CO)_{27}]^{3-}$ and $[Rh_{12}Sb(CO)_{24}]^{4-}$ clusters.

Crystallographic data for Rh-Sb carbonyl clusters

Compound	**4**$[NEt_4]_5 \cdot 4CH_3CN$	**6**$[NEt_4]_4 \cdot 2CH_3CN$
Formula	$C_{86.20}H_{112}N_9O_{38.20}Rh_{21}Sb_2$	$C_{60}H_{86}N_6O_{24}Rh_{12}Sb$
Fw	4290.05	2632.01
Crystal system	Triclinic	Triclinic
Space group	*P*-1	*P*-1
***a* (Å)**	14.705(7)	12.9368(3)
***b* (Å)**	17.825(8)	13.6048(3)
***c* (Å)**	22.389(9)	14.0893(3)
α (deg)	94.705(10)	61.9360(10)
β (deg)	94.827(8)	67.1360(10)
γ (deg)	92.555(8)	70.8180(10)
Cell volume (Å^3)	5820(4)	1983.59(8)
Z	2	1
D (g/cm^3)	2.448	2.203
μ (mm^{-1})	3.419	2.830
F (000)	4090	1271
θ limits (deg)	1.392-25.000	1.707-25.000
Index ranges	$-17 \leq h \leq 17$, $-21 \leq k \leq 21$, $-26 \leq l \leq 26$	$-15 \leq h \leq 15$, $-16 \leq k \leq 16$, $-16 \leq l \leq 16$
Reflections collected	70284	27980
Independent reflections	20488 [R(int) = 0.0353]	6969 [R(int) = 0.0676]
Completeness to θ max	99.9%	99.8%
Data/restraints/ parameters	20488/318/1534	6969/609/632
Goodness-of-fit	1.026	1.007
R_1 ($I > 2\sigma(I)$)	0.0320	0.0424
wR_2 (all data)	0.0832	0.1109
Largest diff. peak and hole, e Å^{-3}	1.585 and -1.266	1.678 and -1.141

Table 5.13. Crystallographic data for clusters 4 and 6.

V.XVI. Reactions of metal carbonyl clusters with phosphines

Phosphine ligands are good σ-donors and poor π-acceptors and are found not only in terminal coordination sites, but also as bridging ligands. [15] Their ability to back-donate to the metal can be increased by using more electronegative substituents, *e.g.*, $P(OR)_3$ or PF_3. In general, the addition of phosphines to metal carbonyl clusters may follow three common reaction pathways:

- Simple addition;
- Substitution of one or more carbonyl ligands;
- Degradation to lower nuclearity species or mononuclear compounds.

Unsaturated clusters may add ligands without any major structural rearrangement. There are several examples of reactions where the carbonyls are replaced by phosphine ligands, [16, 17] among which $Rh_4(CO)_{10}(PPh_3)_2$, $Rh_4(CO)_{11}P(OPh)_3$ [18] and $Ru_3(CO)_{12-x}(PTA)_x$ (x = 1 (4), 2 (5), 3 (6)). [19]

It must be remarked that these studies have been mainly carried out on neutral clusters. Conversely, the replacement of CO with PR_3 in anionic carbonyl clusters is not an obvious reaction, since the anionic charge should favour the presence of the more acidic CO compared to stronger σ-donors such as phosphines.

Large anionic carbonyl clusters do not usually react with phosphines or, if so, the reaction results in degradation to lower nuclearity species. In some cases, this process can be used for the selective synthesis of homoleptic carbonyl clusters, such as the conversion of $[Ni_{13}Sb_2(CO)_{24}]^{3-}$ into $[Ni_{11}Sb_2(CO)_{18}]^{3-}$ by addition of PPh_3 and elimination of $Ni(CO)_3(PPh_3)$. [2] In very few cases, an opposite process has been observed, *i.e.*, cluster condensation to higher nuclearity species upon treatment with PPh_3, such for instance the formation of $[Ni_{16}(C_2)_2(CO)_{23}]^{4-}$ [20] by reacting $[Ni_{10}(C_2)(CO)_{16}]^{2-}$ with PPh_3.

Therefore, we decided to test the reactivity of the medium nuclearity $[Rh_{12}Sb(CO)_{27}]^{3-}$ with the addition of PPh_3 under CO atmosphere and N_2 one, in order to try to obtain new Rh-Sb carbonyl clusters with phosphines. Moreover, the presence of different ligands rather than carbonyls could, in principle, impart different physical properties to the cluster. For instance, the partial substitution of

some CO ligands with PTA (1, 3, 5-Triaza-7-phosphaadamantane) on a certain species can make this one more soluble in water. It is exactly what happens to $[Pt_{12}(CO)_{24}]^{2-}$ and $[Pt_{15}(CO)_{30}]^{2-}$ Chini clusters, which after the reaction with PTA lose come carbonyl ligands in favour of the phosphine ones, transforming into $[Pt_{12}(CO)_{20}(PTA)_4]^{2-}$ and $[Pt_{15}(CO)_{25}(PTA)_5]^{2-}$ respectively and becoming partially soluble in water. [21]

General results

The reaction of the icosahedral $[Rh_{12}Sb(CO)_{27}]^{3-}$ cluster with PPh_3 leads to the formation of complete different species, as shown in Figure 5.16, depending on the stoichiometric ratio and the reaction atmosphere (CO and N_2).

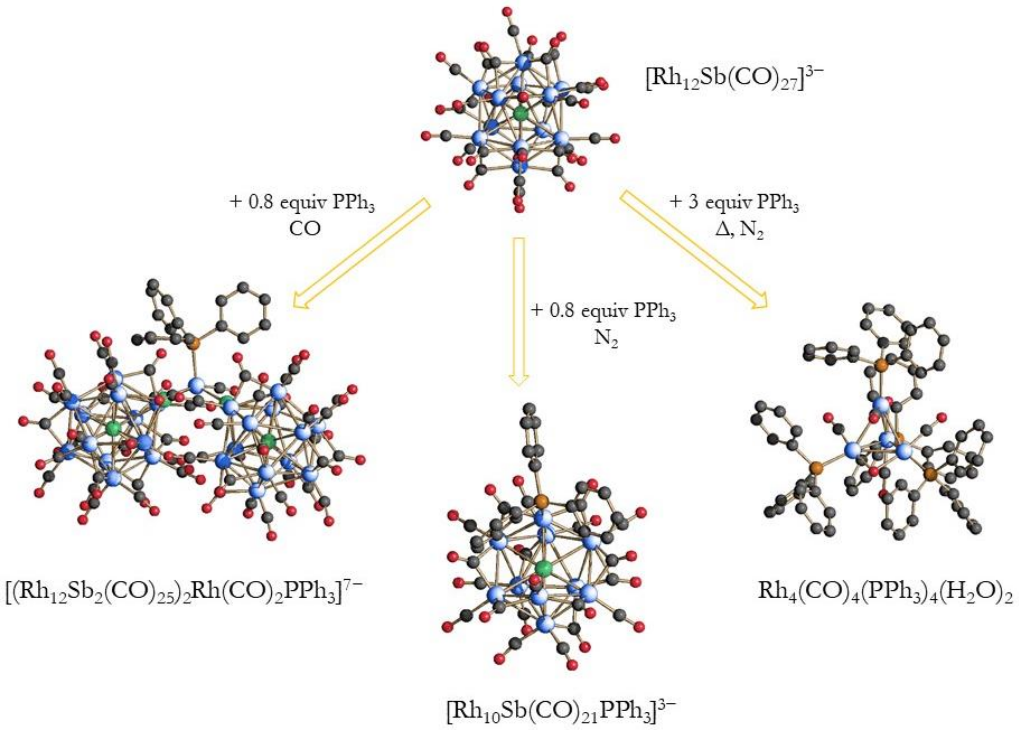

Figure 5.14. Reaction scheme of Rh-Sb system with PPh_3. Rh atoms are depicted in blue, Sb atoms are depicted in green, P atoms are depicted in orange, C atoms are in grey and O atoms are in red. H atoms have been omitted for sake of clarity.

V.XVII. Reactivity of $[Rh_{12}Sb(CO)_{27}]^{3-}$ with PPh_3 under CO atmosphere

The good yield of the coordinatively and electronically saturated icosahedral $[Rh_{12}Sb(CO)_{27}]^{3-}$ cluster allowed us to use this species as a starting material in further reactions. In particular, we investigated the possibility to partially substitute some CO ligands with others, in order to prepare compounds with potentially different physical and chemical properties. We started by using PPh_3, which is easy and safe to handle.

We reacted $[Rh_{12}Sb(CO)_{27}]^{3-}$ with less than one equivalent of PPh_3 in acetonitrile under CO atmosphere. At the end of the reaction, the IR spectrum of the mother solution showed signals at lower frequencies than those of the starting material, indicating the possible ligand substitution. Without any further work-up, di-isopropyl ether was layered on top of the solution and the new dimeric $[(Rh_{12}Sb_2(CO)_{25})_2Rh(CO)_2PPh_3]^{7-}$ cluster crystallized as salt of $[NEt_4]^+$.

To our surprise, the phosphine ligand did not directly coordinate onto the original cluster but, after partly decomposing the starting material into smaller Rh complexes, it was the newly formed $Rh(CO)_2PPh_3$ fragment which coordinated onto two $\{Rh_{12}Sb(CO)_{25}Sb\}$ units. This behaviour could be attributed to the competition between the phosphine and the excess of CO, due to the reaction conditions.

V.XVIII. Molecular structure of the $[(Rh_{12}Sb_2(CO)_{25})_2Rh(CO)_2PPh_3]^{7-}$ cluster

The molecular structure of $[(Rh_{12}Sb_2(CO)_{25})_2Rh(CO)_2PPh_3]^{7-}$ (7) anion is illustrated in Figure 5.15.

The $[(Rh_{12}Sb_2(CO)_{25})_2Rh(CO)_2PPh_3][NEt_4]_7 \cdot CH_3CN$ compound crystallized in the *C*2/c space group and the unit cell contains eight cluster compounds, fifty-six ammonium cations and eight acetonitrile solvent molecules (Z = 8). The independent unit is also large as it comprises the whole dimeric species along with the seven cations and the acetonitrile molecule.

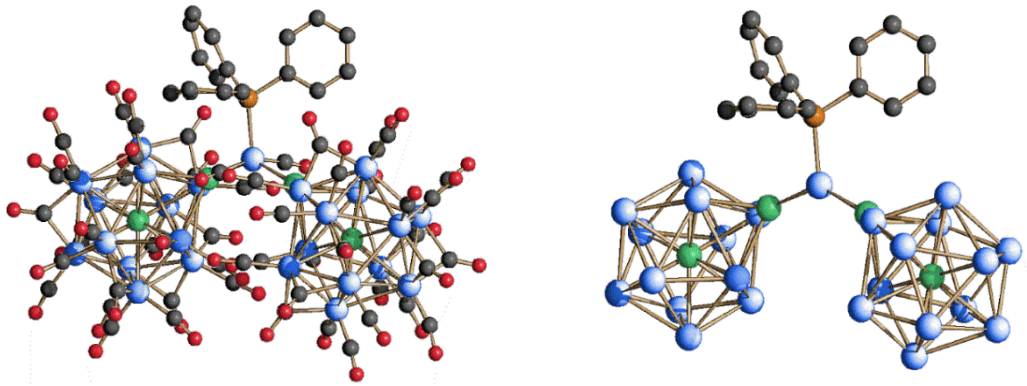

Figure 5.15. Molecular structure of $[(Rh_{12}Sb_2(CO)_{25})_2Rh(CO)_2PPh_3]^{7-}$ (left) and its metal skeleton (right). Rh atoms are depicted in blue, Sb atoms are depicted in green, P atoms are depicted in orange, C atoms are in grey and O atoms are in red. Hydrogen atoms have been omitted for sake of clarity.

The cluster is made by two slightly distorted heteroleptic icosahedral $\{Rh_{12}Sb(CO)_{25}\}$ units, with the second Sb atom on the surface capping a triangular face and acting as a ligand, joined by a $\{Rh(CO)_2PPh_3\}$ fragment. The Sb-Rh and Rh-Rh bond distances are reported in Tables 5.13 and 5.14. As illustrated, the Sb-Rh bond lengths vary from 2.769(3) to 2.925(3) Å for the first unit (average 2.812 Å) and from 2.753(3) to 2.916(3) Å (average 2.815 Å) for the second one. Their values are higher than the ones observed for $[Rh_{12}Sb(CO)_{24}]^{4-}$ but lower than those found in $[Rh_{12}Sb(CO)_{27}]^{3-}$. Note that the Sb-Rh bonds for the Sb atom coordinated on the cluster surface of each unit are shorter, that is 2.552 and 2.550 Å (average values), respectively. The Rh-Rh distances for the first unit span from 2.793(3) to 3.124(3) (average 2.957 Å), similar to the ones in the second unit which are in the 2.781(3)-3.150(3) Å range (average 2.960 Å). Again, these values are in between the ones of the $[Rh_{12}Sb(CO)_{27}]^{3-}$ and $[Rh_{12}Sb(CO)_{24}]^{4-}$ homoleptic clusters, indicating a similar intermediate deviation from the regular icosahedral geometry. The bond lengths between the two surface Sb atoms and the central Rh coordinated to the PPh_3 are 2.586(3) and 2.852(2) Å. As for the carbonyl ligands of the two

icosahedral units, in both cases 12 out of 25 are terminally bonded to the Rh atoms, while the remaining 13 are edge-bridged.

Sb(1)-Rh(7)	2.769(3)
Sb(1)-Rh(11)	2.773(3)
Sb(1)-Rh(4)	2.777(3)
Sb(1)-Rh(13)	2.790(3)
Sb(1)-Rh(8)	2.793(3)
Sb(1)-Rh(2)	2.801(3)
Sb(1)-Rh(10)	2.801(3)
Sb(1)-Rh(6)	2.801(3)
Sb(1)-Rh(12)	2.814(3)
Sb(1)-Rh(3)	2.821(3)
Sb(1)-Rh(9)	2.876(3)
Sb(1)-Rh(5)	2.925(3)
Rh(2)-Rh(7)	2.793(3)
Rh(2)-Rh(6)	2.799(3)
Rh(2)-Rh(4)	2.960(3)
Rh(2)-Rh(3)	3.017(3)
Rh(2)-Rh(5)	3.104(3)
Rh(3)-Rh(8)	2.828(4)
Rh(3)-Rh(7)	2.855(3)
Rh(3)-Rh(4)	2.960(3)
Rh(3)-Rh(12)	2.999(3)
Rh(4)-Rh(9)	2.884(4)
Rh(4)-Rh(5)	2.918(3)

Rh(4)-Rh(8)	2.973(3)
Rh(5)-Rh(9)	2.845(4)
Rh(5)-Rh(10)	2.918(3)
Rh(5)-Rh(6)	2.952(3)
Rh(6)-Rh(11)	3.014(3)
Rh(6)-Rh(10)	3.028(4)
Rh(6)-Rh(7)	3.069(3)
Rh(7)-Rh(11)	3.043(3)
Rh(7)-Rh(12)	3.082(3)
Rh(8)-Rh(12)	2.811(3)
Rh(8)-Rh(13)	3.005(4)
Rh(8)-Rh(9)	3.099(4)
Rh(9)-Rh(10)	2.894(4)
Rh(9)-Rh(13)	3.124(3)
Rh(10)-Rh(13)	2.932(4)
Rh(10)-Rh(11)	3.007(3)
Rh(11)-Rh(13)	2.937(3)
Rh(11)-Rh(12)	3.030(3)
Rh(12)-Rh(13)	2.820(4)
Rh(6)-Sb(14)	2.529(2)
Rh(7)-Sb(14)	2.506(3)
Rh(11)-Sb(14)	2.620(3)
Sb(14)-Rh(35)	2.586(3)

Table 5.14. Most relevant bond lengths for the first unit $\{Rh_{12}Sb(CO)_{25}Sb\}$ of $[(Rh_{12}Sb_2(CO)_{25})_2Rh(CO)_2PPh_3]^{7-}$.

Sb(21)-Rh(30)	2.753(3)	Rh(24)-Rh(29)	3.120(3)
Sb(21)-Rh(29)	2.766(3)	Rh(25)-Rh(31)	2.847(3)
Sb(21)-Rh(26)	2.780(3)	Rh(25)-Rh(30)	2.884(3)
Sb(21)-Rh(27)	2.787(3)	Rh(25)-Rh(26)	2.911(3)
Sb(21)-Rh(23)	2.787(3)	Rh(26)-Rh(31)	2.914(4)
Sb(21)-Rh(24)	2.789(2)	Rh(26)-Rh(27)	2.919(3)
Sb(21)-Rh(32)	2.790(3)	Rh(26)-Rh(32)	2.979(3)
Sb(21)-Rh(22)	2.802(3)	Rh(27)-Rh(32)	2.839(3)
Sb(21)-Rh(33)	2.820(3)	Rh(27)-Rh(28)	3.053(3)
Sb(21)-Rh(28)	2.888(3)	Rh(28)-Rh(32)	2.813(3)
Sb(21)-Rh(25)	2.904(3)	Rh(28)-Rh(33)	2.831(3)
Sb(21)-Rh(31)	2.916(3)	Rh(28)-Rh(29)	2.977(3)
Rh(22)-Rh(24)	2.781(3)	Rh(29)-Rh(33)	2.900(3)
Rh(22)-Rh(23)	2.806(3)	Rh(29)-Rh(30)	3.029(3)
Rh(22)-Rh(27)	2.977(3)	Rh(30)-Rh(31)	2.903(3)
Rh(22)-Rh(26)	3.005(3)	Rh(30)-Rh(33)	2.944(3)
Rh(22)-Rh(25)	3.138(3)	Rh(31)-Rh(32)	3.103(3)
Rh(23)-Rh(27)	2.912(3)	Rh(31)-Rh(33)	3.150(3)
Rh(23)-Rh(29)	2.981(3)	Rh(32)-Rh(33)	2.975(3)
Rh(23)-Rh(24)	3.073(3)	Rh(23)-Sb(34)	2.532(2)
Rh(23)-Rh(28)	3.159(3)	Rh(24)-Sb(34)	2.504(2)
Rh(24)-Rh(25)	2.920(3)	Rh(29)-Sb(34)	2.614(3)
Rh(24)-Rh(30)	2.969(3)	Sb(34)-Rh(35)	2.582(2)

Table 5.15. Most relevant bond lengths for the second unit $\{Rh_{12}Sb(CO)_{25}Sb\}$ of $[(Rh_{12}Sb_2(CO)_{25})_2Rh(CO)_2PPh_3]^{7-}$.

V.XIX. IR and ^{31}P-NMR characterization of the $[(Rh_{12}Sb_2(CO)_{25})_2Rh(CO)_2PPh_3]^{7-}$ cluster

$[(Rh_{12}Sb_2(CO)_{25})_2Rh(CO)_2PPh_3]^{7-}$ as salt of $[NEt_4]^+$ is soluble in acetone, acetonitrile and DMF.

Its IR spectrum recorded in CH_3CN shows ν_{CO} absorptions at 2022 (sh), 1998(vs), 1806(ms) and 1767(m) cm^{-1}. This compound was also characterized by NMR spectroscopy. The $^{31}P\{^1H\}$ NMR spectrum of crystals recorded in CD_3CN at 298 K shows a doublet centred at δ_P = 29.9 ppm with $^1J_{Rh-P}$ = 128 Hz, as previously found in analogous Rh(I) compounds. [22, 23, 24] The ^{31}P-NMR spectrum of $[(Rh_{12}Sb_2(CO)_{25})_2Rh(CO)_2PPh_3][NEt_4]_7$ (Figure 5.16) is fully consistent with its solid state structure, which contains just one PPh_3 bound to a single rhodium atom. Furthermore, the diagnostic signal has been detected as the major one in the crude, along with other signals of unidentified by-products.

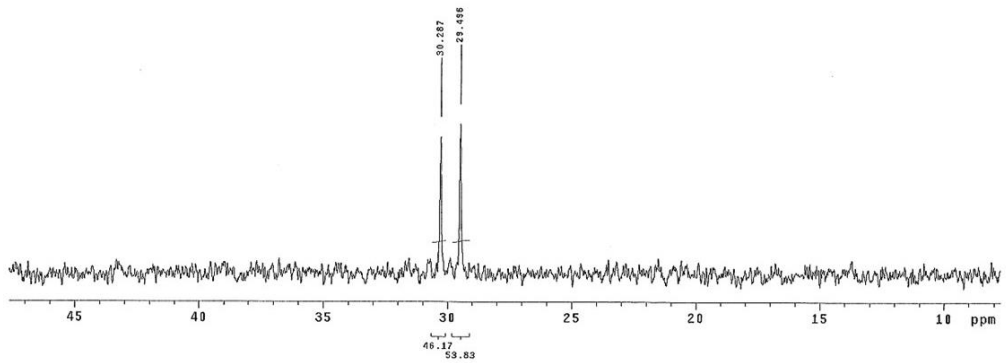

Figure 5.16. $^{31}P\{^1H\}$ NMR spectrum of $[(Rh_{12}Sb_2(CO)_{25})_2Rh(CO)_2PPh_3]^{7-}$ in CD_3CN at 298 K.

V.XX. Reactivity of $[Rh_{12}Sb(CO)_{27}]^{3-}$ with PPh_3 under N_2 atmosphere

At this point, we decided to evaluate the reactivity of $[Rh_{12}Sb(CO)_{27}]^{3-}$ with PPh_3 in the same reaction conditions above discussed but under nitrogen atmosphere. Indeed, since the icosahedral cluster precursor spontaneously loses CO when put under N_2, it could have been interesting to carry out the previous reaction in more favourable conditions, with the aim of directly substitute some CO ligands with PPh_3 without forming any $Rh(CO)_xPPh_3$ complex.

As expected, this reaction led to a very different cluster compound from the above reported, namely $[Rh_{10}Sb(CO)_{21}PPh_3]^{3-}$. Also in this case, the acetonitrile mother solution was directly layered on with di-isopropyl ether, with no further work-up. Unlike the previous case, the phosphine here directly coordinated to the metal skeleton, which partially fragmented with respect to the cluster precursor. This species crystallized as $[NEt_4]^+$ salt.

We also tested the reactivity of $[Rh_{12}Sb(CO)_{27}]^{3-}$ with a strong excess of PPh_3. Actually, this great amount of phosphine did not seem to have any effect on the mixture, so we decided to heat the acetonitrile solution at reflux for 90 minutes to promote the Rh-CO cleavage. [25] The combination of these two factors led to obtain a mixture showing an IR spectrum of unknown species.

Also in this case, the acetonitrile mother solution was directly layered on with di-isopropyl ether, with no further work-up but unfortunately, we did not obtain crystals for characterizing the unknown species, but a solution and an amorphous solid which were separately treated. The solution, dried under vacuum, washed with water and dissolved into CH_2Cl_2 was then layered on with hexane, giving crystals of what we hypothetically formulated as $Rh_4(CO)_4(PPh_3)_4(H_2O)_2$, while the solid dissolved into acetonitrile was characterized as a complex of Rh(I). They both represent the outcome of the partial degradation of the icosahedral cluster precursor.

The role of water molecules acting as ligands in a metal carbonyl cluster is quite unusual. In the case of $Rh_4(CO)_4(PPh_3)_4(H_2O)_2$, due to a very low yield, it was not

possible to perform further spectroscopic analyses (such as ^{1}H NMR and solid IR) to confirm the actual presence of water molecules in the cluster. The formulation was therefore done only based on both the X-ray data, which showed two oxygen atoms bridging two Rh metals, and the electron counting. Further investigation is mandatory in order to ascertain the true nature of the oxygen-bearing ligands in the above species.

V.XXI. Molecular structure of the $[Rh_{10}Sb(CO)_{21}PPh_3]^{3-}$ cluster

The molecular structure of $[Rh_{10}Sb(CO)_{21}PPh_3]^{3-}$ (8) cluster is illustrated in Figure 5.17.

The $[Rh_{10}Sb(CO)_{21}PPh_3][NEt_4]_3 \cdot CH_3CN$ crystallized in the monoclinic $P2_1/c$ ($Z = 4$), and the unit cell contains four cluster units, twelve cations and four molecules of acetonitrile, all arranged in an ionic solid fashion. The metal skeleton is based on a broken icosahedron made of ten Rh atoms, centred by the unique Sb atom and coordinated to one PPh_3, as well as to 21 carbonyl ligands of which 12 are terminally bonded to the Rh atoms, while the remaining 9 are edge-bridged.

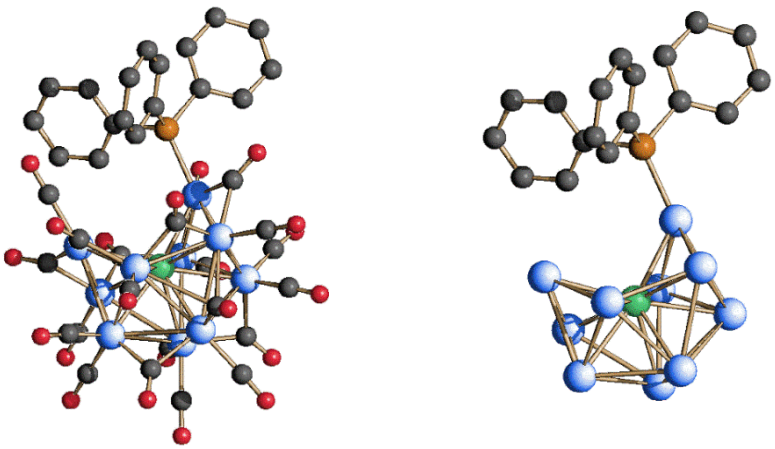

Figure 5.17. Molecular structure of $[Rh_{10}Sb(CO)_{21}PPh_3]^{3-}$ (left) and its metal skeleton (right). Rh atoms are depicted in blue, Sb atoms are depicted in green, P atoms are depicted in orange, C atoms are in grey and O atoms are in red. Hydrogen atoms have been omitted for sake of clarity.

Sb(1)-Rh(2)	2.6189(3)	Rh(3)-Rh(9)	3.0286(4)
Sb(1)-Rh(6)	2.6862(3)	Rh(4)-Rh(9)	2.9051(4)
Sb(1)-Rh(3)	2.6878(3)	Rh(4)-Rh(11)	2.9269(4)
Sb(1)-Rh(7)	2.6967(3)	Rh(4)-Rh(6)	2.9983(4)
Sb(1)-Rh(11)	2.7370(3)	Rh(4)-Rh(10)	3.0526(4)
Sb(1)-Rh(4)	2.7503(3)	Rh(5)-Rh(8)	2.9407(4)
Sb(1)-Rh(9)	2.7653(3)	Rh(5)-Rh(9)	2.9999(4)
Sb(1)-Rh(8)	2.7672(3)	Rh(6)-Rh(11)	2.8337(4)
Sb(1)-Rh(5)	2.7683(3)	Rh(7)-Rh(8)	2.8697(4)
Sb(1)-Rh(10)	2.7870(3)	Rh(7)-Rh(11)	2.8935(4)
Rh(2)-Rh(7)	2.8345(3)	Rh(7)-Rh(10)	2.9842(4)
Rh(2)-Rh(5)	2.8714(4)	Rh(8)-Rh(10)	2.8999(4)
Rh(2)-Rh(8)	3.0568(4)	Rh(8)-Rh(9)	3.0011(4)
Rh(3)-Rh(6)	2.8246(4)	Rh(9)-Rh(10)	2.8579(4)
Rh(3)-Rh(4)	2.8715(4)	Rh(10)-Rh(11)	3.0291(4)
Rh(3)-Rh(5)	2.8805(3)		

Table 5.16. Most relevant bond lengths for $[Rh_{10}Sb(CO)_{21}PPh_3]^{3-}$.

The Sb-Rh and Rh-Rh bond distances are reported in Table 5.15. As illustrated, the Sb-Rh bond lengths vary from 2.6189(3) to 2.7870(3) Å with an average of 2.7265 Å. The Rh-Rh distances span from 2.8246(4) to 3.0568(4) (average 2.9315 Å). As expected, their values are lower than the ones observed for both $[Rh_{12}Sb(CO)_{24}]^{4-}$ and $[Rh_{12}Sb(CO)_{27}]^{3-}$.

V.XXII. IR and ^{31}P-NMR characterization of the $[Rh_{10}Sb(CO)_{21}PPh_3]^{3-}$ cluster

$[Rh_{10}Sb(CO)_{21}PPh_3]^{3-}$ as salt of $[NEt_4]^+$ is soluble in acetone, acetonitrile and DMF. Its IR spectrum recorded in CH_3CN shows ν_{CO} absorptions at 1991 (vs), 1981(sh), 1844(m), 1805(m) and 1762(ms) cm^{-1}.

Thanks to the presence of the phosphine ligand, we characterized the cluster compound by NMR spectroscopy. The $^{31}P\{^1H\}$ NMR spectrum of some crystals

dissolved in CD_3CN at 298 K shows a doublet of multiplets centred at δ_P 33.38 ppm with $^1J_{Rh-P}$ = 249 Hz and $^2J_{Rh-P}$ = 5 Hz (Figure 5.18). These values are consistent with those reported for other Rh clusters coordinated to phosphines. [26]

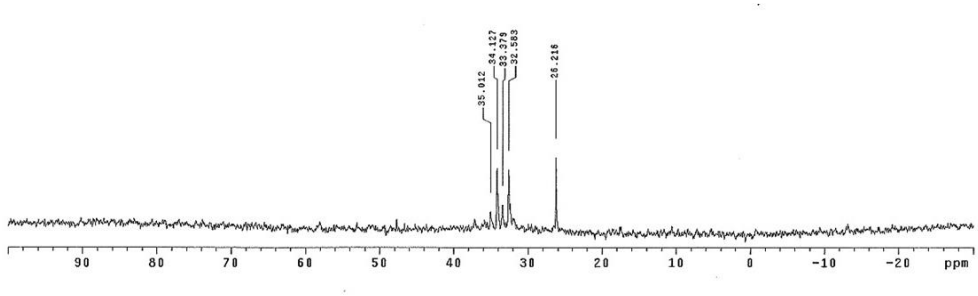

Figure 5.18. $^{31}P\{^1H\}$ NMR spectrum of $[Rh_{10}Sb(CO)_{21}PPh_3]^{3-}$ in CD_3CN at 298 K.

As a matter of fact, the presence of multiplets shows that in this case PPh_3 is coordinated to a proper cluster, since the $^2J_{Rh-P}$ is present. Indeed, P not only couples with the Rh atom to which is bound but also with some of the others that constitute the skeleton. The low $^2J_{Rh-P}$ is given by the delocalized electronic density caused by the Rh-Rh interactions, which are not two-centre two-electrons bonds.

V.XXIII. Molecular structure of the $Rh_4(CO)_4(PPh_3)_4(H_2O)_2$ cluster

The molecular structure of $Rh_4(CO)_4(PPh_3)_4(H_2O)_2$ (9) cluster is illustrated in Figure 5.19. The hydrogen atoms in the water molecules were added geometrically. The cluster crystallized in the monoclinic *C*2/c and Z = 24.

The Rh-Rh distances in $Rh_4(CO)_4(PPh_3)_4(H_2O)_2$ span from 2.7632(11) to 2.8861(11) with an average of 2.8338 Å.

Rh(1)-Rh(2)	2.7999(10)	Rh(2)-Rh(3)	2.7632(11)
Rh(1)-Rh(3)	2.8425(11)	Rh(2)-Rh(4)	2.8398(11)
Rh(1)-Rh(4)	2.8861(11)	Rh(3)-Rh(4)	2.8713(11)

Table 5.17. Most relevant bond lengths for $Rh_4(CO)_4(PPh_3)_4(H_2O)_2$.

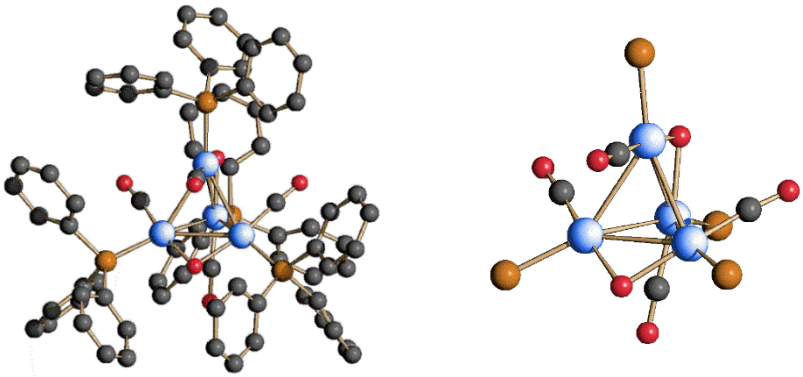

Figure 5.19. Left: molecular structure of $Rh_4(CO)_4(PPh_3)_4(H_2O)_2$. Right: close-up without the aryl substituents. Rh atoms are depicted in blue, P atoms are depicted in orange, C atoms are in grey and O atoms are in red. Hydrogen atoms have been omitted everywhere for sake of clarity.

It is interesting to make a comparison among this cluster and two known and very similar compounds, $Rh_4(CO)_{10}(PPh_3)_2$ and $Rh_4(CO)_{12}$, in terms of Rh-Rh bond lengths. The Rh-Rh distances in $Rh_4(CO)_{10}(PPh_3)_2$ span from 2.679(2) to 2.788(2) with an average of 2.729 Å, while in $Rh_4(CO)_{12}$ the Rh-Rh distances vary from 2.6581(16) to 2.7649(18) with an average value of 2.6982 Å

Rh(1)-Rh(2)	2.692(1)	Rh(2)-Rh(3)	2.788(2)
Rh(1)-Rh(3)	2.679(2)	Rh(2)-Rh(4)	2.771(2)
Rh(1)-Rh(4)	2.751(2)	Rh(3)-Rh(4)	2.692(2)

Table 5.18. Most relevant bond lengths for $Rh_4(CO)_{10}(PPh_3)_2$.

r

Rh(1)-Rh(2)	2.6716(19)	Rh(2)-Rh(3)	2.695(12)
Rh(1)-Rh(3)	2.6890(12)	Rh(2)-Rh(4)	2.7649(18)
Rh(1)-Rh(4)	2.6581(16)	Rh(3)-Rh(4)	2.7107(12)

Table 5.19. Most relevant bond lengths for $Rh_4(CO)_{12}$.

The longer Rh-Rh contacts are found in the more phosphine substituted Rh_4 cluster (average 2.8338 Å), while the homoleptic species holds the shorter ones (average 2.6982 Å). The $Rh_4(CO)_{10}(PPh_3)_2$ displays intermediate average Rh-Rh bond lengths (2.729 Å). This could be due to multiple reasons, such as the major steric hindrance of the PPh_3 ligands comparing with that of CO, and the higher electronic density sustained by the Rh atoms in the more substituted cluster.

V.XXIV. IR characterization of the $Rh_4(CO)_4(PPh_3)_4(H_2O)_2$ cluster

Its IR spectrum recorded in CH_2Cl_2 displays ν_{CO} absorptions at 1979(m) and 1918(vs) cm^{-1}. It is interesting to make the comparison among this species and the other Rh_4 differently substituted and above taken into consideration. The spectrum of $Rh_4(CO)_{12}$ recorded in hexane shows ν_{CO} absorptions at 2074(vs), 2069(vs), 2043(s) and 1885(s) cm^{-1}, while the spectrum of $Rh_4(CO)_{10}(PPh_3)_2$ recorded in CH_2Cl_2 displays ν_{CO} absorptions at 2067(s), 2042(s), 2017(s), 1850(ms) and 1825(sh) cm^{-1}. The spectrum of $Rh_4(CO)_4(PPh_3)_4(H_2O)_2$ presents the lowest frequencies because of the combination of the major number of PPh_3 and the minor one of CO ligands coordinated to the same metal skeleton. Indeed, this way the metal skeleton needs to sustain a higher electronic density which cannot be back-bonded on just four carbonyl ligands.

Crystallographic data for Rh-Sb carbonyl clusters with PPh_3

Compound	**7**$[NEt_4]_7 \cdot CH_3CN$	**8**$[NEt_4]_3 \cdot CH_3CN$	**9**
Formula	$C_{128}H_{158}N_8O_{52}PRh_{25}Sb_4$	$C_{67}H_{82}N_4O_{21}PRh_{10}Sb$	$C_{76}H_{64}O_6P_4Rh_4$
Fw	5731.33	2461.18	1608.79
Crystal system	Monoclinic	Monoclinic	Monoclinic
Space group	*C*/2c	P21/c	*C*/2c
***a* (Å)**	42.0905(12)	21.9963(11)	61.965(8)
***b* (Å)**	24.2781(7)	16.6173(8)	15.6864(19)
***c* (Å)**	34.1882(9)	21.1485(10)	20.853(3)
α (deg)	90	90	90
β (deg)	104.912(2)	91.3080(10)	100.596(3)
γ (deg)	90	90	90
Cell volume (Å^3)	33759.6(17)	7728.2(6)	19923(4)
Z	8	4	12
D (g/cm^3)	2.255	2.115	1.609
μ (mm^{-1})	3.082	2.511	1.127
F (000)	21936	4784	9696
θ limits (deg)	1.468-25.000	1.536-25.000	0.0669-24.999
Index ranges	-50≤ *h* ≤50, -27≤ *k* ≤28, -40≤ *l* ≤40	-26≤ *h* ≤26, -19≤ *k* ≤19, -25≤ *l* ≤25	-73≤ *h* ≤73, -18≤ *k* ≤18, -24≤ *l* ≤24
Reflections collected	139944	87637	119973
Independent reflections	29699 [R(int) = 0.0987]	13515 [R(int) = 0.0248]	17536 [R(int) = 0.0659]
Completeness to θ max	99.9%	99.4%	100%
Data/restraints/ parameters	29699/1777/2257	13515/310/1010	17536/685/1253
Goodness-of-fit	1.067	1.148	1.347
R_1 (I > 2σ(I))	0.1026	0.0233	0.0881
wR_2 (all data)	0.2557	0.0538	0.1826
Largest diff. peak and hole, e Å^{-3}	2.231 and -2.248	1.059 and -1.256	1.811 and -1.603

Table 5.20. Crystallographic data for clusters 7, 8 and 9.

1 J. L. Vidal, *J. Organomet. Chem.* **1981**, *213*, 351.

2 V. G. Albano, F. Demartin, C. Femoni, M. C. Iapalucci, G. Longoni, M. Monari, P. Zanello, *J. Organomet. Chem.* **2000**, *593*, 325.

3 P. D. Mlynek, L. F. Dahl, *Organometallics* **1997**, *16*, 1641.

4 V. G. Albano, F. Demartin, M. C. Iapalucci, G. Longoni, A. Sironi, V. Zanotti, *Chem. Commun.* **1990**, 547.

5 C. Femoni, M. C. Iapalucci, G. Longoni, S. Zacchini, I. Ciabatti, R. G. D. Valle, M. Mazzani, M. Ricco, *Eur. J. Inorg. Chem.* **2014**, 4141.

6 C. Femoni, M. C. Iapalucci, G. Longoni, P. H. Svensson, *Chem. Commun.* **2000**, *8*, 655.

7 Y.-Z. Li, R. Ganguly, W. K. Leong, Y. Liu, *Eur. J. Inorg. Chem.* **2015**, 3861.

8 G. Chen, W. K. Leong, *J. Clust. Sci.* **2006**, *17*, 111.

9 Y.-Z. Li, R. Ganguly, W. K. Leong, *J. Organomet. Chem.* **2016**, *820*, 46.

10 M. W. Lum, W. K. Leong, *Inorg. Chim. Acta* **2004**, *357*, 769.

11 C. Femoni, I. Ciabatti, M. C. Iapalucci, S. Ruggieri, S. Zacchini, *Pro. Nat. Sci-Mater.* **2016**, *26*, 461.

12 S. García-Gallego, G. J. L. Bernardes, *Angew. Chem. Int. Ed.* **2014**, *53*, 9712.

13 D. Collini, C. Femoni, M. C. Iapalucci, G. Longoni, P. Zanello, *Perspectives in Organometallic Chemistry* C. G. Screttas and B. R. Steele Eds., The Royal Society of Chemistry **2003**, *287*, 183.

14 V. G. Albano, F. Demartin, C. Femoni, M. C. Iapalucci, G. Longoni, M. Monari, P. Zanello, *J. Organomet. Chem.* **2000**, *593*, 325.

15 T. Pechmann, C. D. Brandt, H. Werner, *Chem. Eur. J.* **2004**, *10*, 728.

16 M. D. Vargas, J. N. Nicholls, *Adv. Inorg. Chem. Radiochem.* **1986**, *30*, 123.

17 P. Chini, *J. Organomet. Chem.* **1980**, *200*, 37.

18 B. T. Heaton, L. Longhetti, D. M. P. Mingos, C. E. Briant, P. C. Minshall, B. R. C. Theobald, L. Garlaschelli, U. Sartorelli, *J. Organomet. Chem.* **1981**, *213*, 333.

19 N. Mager, K. Robeyns, S. Hermans, *J. Organomet. Chem.* **2015**, *794*, 48.

20 A. Ceriotti, G. Longoni, M. Manassero, N. Masciocchi, G. Piro, L. Resconi, M. Sansoni, *J. Chem. Soc., Chem. Commun.* **1985**, 1402.

21 L. K. Batchelor, B. Berti, C. Cesari, I. Ciabatti, P. J. Dyson, C. Femoni, M. C. Iapalucci, M. Mor, S. Ruggieri, S. Zacchini, *Dalton Trans.* **2018**, *47,* 4467.

22 H. S. Lee, J. Y. Bae, J. Ko, Y. S. Kang, H. S. Kim, S. J. Kim, J. H. Chung, S. O. Kang, *J. Organomet. Chem.* **2000**, *614*, 83.

23 H. J. Haupt, U. Flörke, H. G. Beckers, *Inorg. Chem.* **1994**, *33*, 3481.

24 O. Koshevoy, O. V. Sizova, S. P. Tunik, A Lough, A. J. Poë, *Eur. J. Inorg. Chem.* **2005**, 4516.

25 R. Della Pergola, E. Comensoli, L. Garlaschelli, M. Manassero, M. Sansoni, D. Strumolo, *Eur. J. Inorg. Chem*. **2003**, 213.

26 S. P. Tunik, A. V. Vlasov, K. V. Kogdov, G. L. Starova, A. B. Nikol'skii, *J. Organomet. Chem*. **1994**, *479*, 59.

CHAPTER VI

New Rhodium-Gold Carbonyl Clusters

During the last period of my Ph.D. we started to investigate the Rh-Au system.

Gold has always been considered a substance of great value, but in-depth study of the chemistry of gold only took off relatively recently. This started with the first organometallic compounds, followed by molecular clusters, [1] colloids and nanoparticles (AuNPs) [2] and, most recently, atomically-precise gold nanoclusters. [3]

The interest in such a topic mainly derives from the potential application of heterometallic clusters in catalysis, where the combined action of different metals may enhance catalytic properties, [4] but these clusters can also serve as models of the modifications to the substrate that arise at a molecular level.

Most heterometallic gold cluster compounds are synthesized from the reaction of a pre-formed carbonyl cluster with Au(I) complexes of various nature, the most common by far being of $[AuL]^+$ or $[Au_2L']^{2+}$ type (L = phosphine; L' = bidentate phosphine).

The resulting species can be surface-decorated heterometallic clusters with AuL fragments acting as stabilizing ligands, [5, 6, 7, 8] sandwiched cluster units connected by naked Au atoms [9, 10, 11] and clusters with gold atoms embedded in the metal framework. [12, 13, 14]

The reaction of a transition metal carbonyl cluster with Au(I) complexes generally results in an adduct where the cluster core remains intact and the gold complex acts as a ligand, decorating its surface.

The gold compounds employed in the synthesis have the general formula AuLX or $Au_2L'X_2$, where L is an alkyl or aryl phosphine ligand, L' is a bidentate phosphine ligand and X is a halide, mostly chloride or other non-coordinating anions like $[BF_4]^-$ or $[PF_6]^-$.

The plethora of species documented in the scientific literature gives a very clear indication of the breadth and depth of the investigation in this chemistry. [15] These papers cover over four decades of research, starting from 1970 and ending in 2016, although most of the work was concentrated in the eighties and nineties. Figure 6.1 shows a graphical overview of the highest nuclearity species bearing monodentate phosphine ligands.

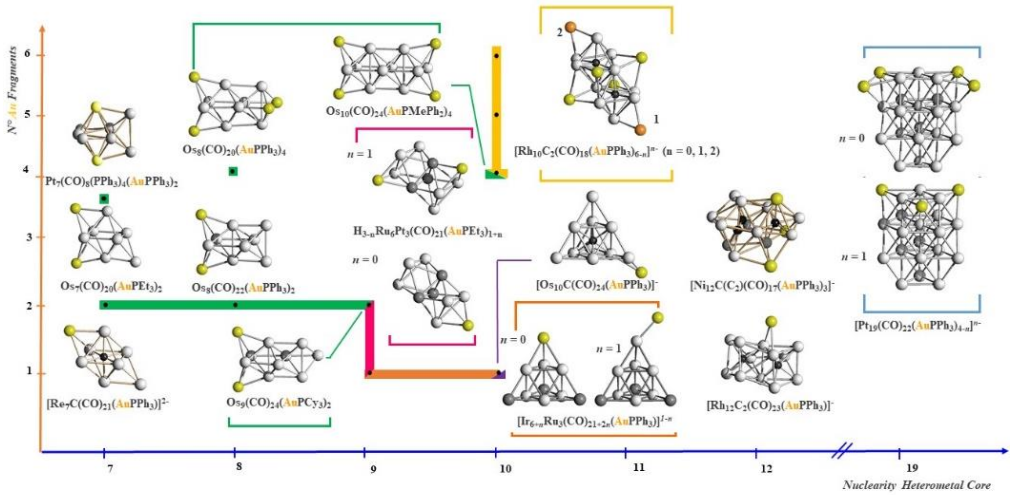

Figure 6.1. Overview of some selected examples of transition metal carbonyl clusters surface-decorated by $[AuL]^+$ fragments. Yellow spheres indicate gold. Cluster and gold ligands have been omitted for sake of clarity.

The chemistry of carbonyl clusters with Au atoms embedded in their metal frame is dominated by the heterometallic gold clusters of Pd and Fe, with only scattered examples of Mo, [12] Os [16] and Ni [14] species (Figure 6.2). Both Au(I) and Au(III) complexes can be used to prepare clusters with gold embedded in their metal frameworks. The synthesis of the higher nuclearity species is generally based on the redox condensation method. For instance, the synthesis of higher nuclearity bimetallic Fe–Au clusters, a redox condensation between $[Fe_3(CO)_{11}]^{2-}$ and $[AuCl_4]^-$ takes place. [13] The absence of heterometallic gold carbonyl compounds of Pt and Rh is remarkable, given that high nuclearity clusters of these metals are

well known. This lack of heterometallic Rh-Au clusters encouraged us to investigate this system in order to try to obtain new Rh species with gold encapsulated in the metal cage. Also in this case, we exploited the redox condensation method, using as starting material $[Rh_7(CO)_{16}]^{3-}$.

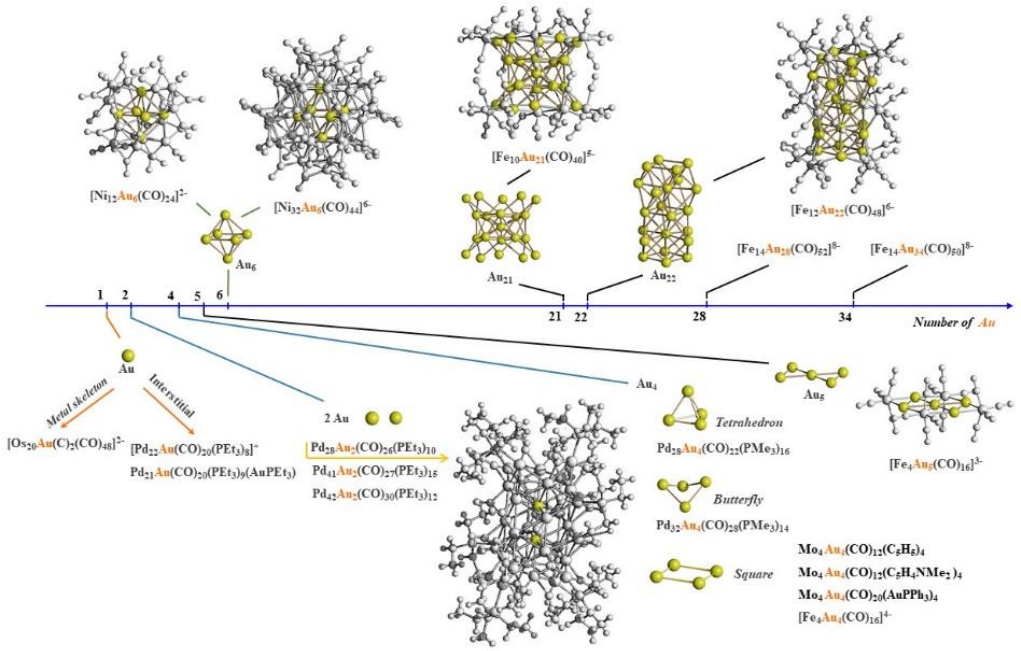

Figure 6.2. Graphical overview of carbonyl clusters containing Au atoms totally embedded in their metal framework. Yellow spheres indicate gold.

General results

The following sections show the study of the reactivity of the $[Rh_7(CO)_{16}][NEt_4]_3$ cluster precursor with $[AuCl_4]^-$ and $[AuBr_4]^-$ in different reaction conditions. The solvent plays a key role in the study of this system, leading to the formation of different species. Another very important parameter is the atmosphere; indeed the nitrogen one, always exploited in the other previously analysed systems, in this case did not allow us to obtain any new product. This is probably due to an equilibrium reaction which is shifted towards the cluster precursor under nitrogen. Conversely, under CO atmosphere we obtained several new nanoclusters, therefore this chapter will only focus on the study of the Rh-Au system under carbon monoxide.

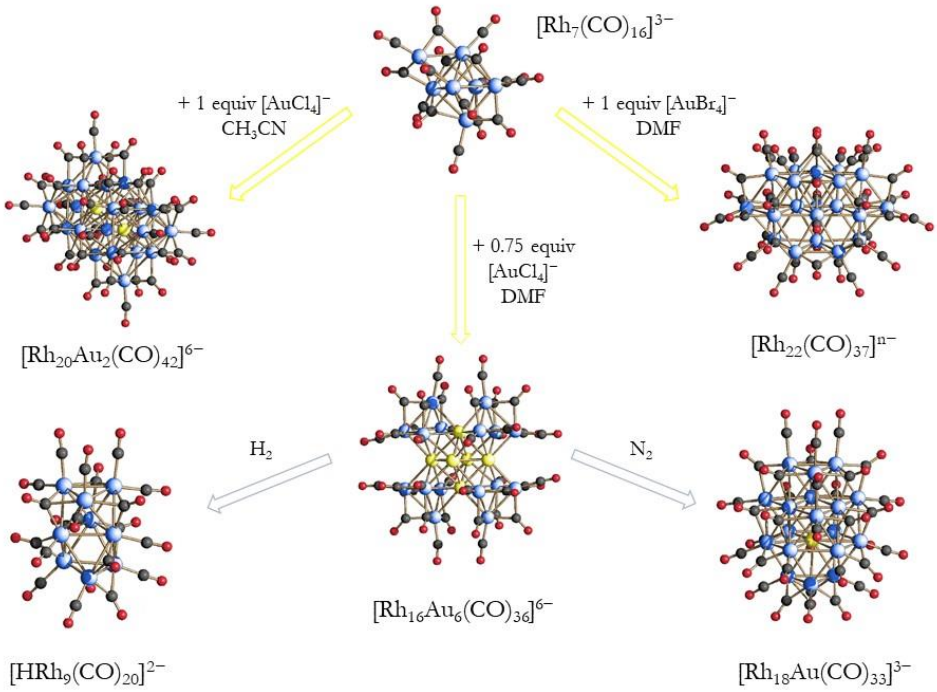

Figure 6.3. Reaction scheme of Rh-Au system. Rh atoms are depicted in blue, Au atoms are depicted in yellow, C atoms are in grey and O atoms are in red.

VI.I. Reactivity of $[Rh_7(CO)_{16}]^{3-}$ with $[AuCl_4]^-$ under CO atmosphere

The Rh-Au system behaves totally differently from all the other systems previously analysed and it will need further investigation to completely unravel it.

We carried out the first reactions in almost the same conditions followed in the other systems, so we reacted $[Rh_7(CO)_{16}][NEt_4]_3$ with 1 equivalent of $[AuCl_4][NMe_3Bz]$ in acetonitrile under CO atmosphere, at room temperature. At the end of the reaction, the IR spectrum presented the complete disappearance of ν_{CO} absorptions of the cluster precursor. The work-up of the mother solution was carried out following the usual procedure. Notably, no $[Rh(CO)_2Cl_2]^-$ was detected. The extraction in THF separated the already known $[Rh_{12}(CO)_{30}]^{2-}$ homometallic cluster [17], while the subsequent acetone extraction showed IR peaks of an unknown species which, unfortunately, we were not able to characterize. Conversely, a new Rh-Au cluster was extracted in acetonitrile and crystallized by layering di-isopropyl ether on the top of the solution. The obtained well-shaped crystals allowed us to identify it as $[Rh_{20}Au_2(CO)_{42}]^{6-}$, which represented the first Rh cluster with Au atoms embedded in the metal skeleton.

This result encouraged us to keep widen the investigation of this system, so we repeated this reaction under the same conditions but in a different, less coordinating solvent, such as DMF.

The reaction between $[Rh_7(CO)_{16}][NEt_4]_3$ and 1 equivalent of $[AuCl_4]^-$ in DMF under CO atmosphere and at room temperature took a totally different path and led to the synthesis of a yet another different heterometallic species, namely $[Rh_{16}Au_6(CO)_{36}]^{6-}$. [18] More specifically, at the end of the reaction the mixture was precipitated with an excess of $[NEt_4]Br$ and water because of the high boiling point of the solvent (153° C), which prevented us from drying the solution under vacuum. After filtration we proceeded with the usual work-up. The known homometallic $[Rh_{12}(CO)_{30}]^{2-}$ cluster was isolated in acetone, while the new $[Rh_{16}Au_6(CO)_{36}]^{6-}$ cluster was extracted in acetonitrile. The compound was crystallized as salt of $[NEt_4]^+$ by layering di-isopropyl ether onto the acetonitrile

solution. Notably, it is sufficient a Rh_7:Au^{3+} molar ratio of 1:0.75 to obtain this cluster. However, further additions of $[AuCl_4]^-$ to $[Rh_7(CO)_{16}]^{3-}$ beyond 1 equivalent led always to the same species but with a major amount of by-products.

VI.II. Molecular structure of the $[Rh_{20}Au_2(CO)_{42}]^{6-}$ cluster

The molecular structure of $[Rh_{20}Au_2(CO)_{42}]^{6-}$ (1) is illustrated in Figure 6.4.

The $[Rh_{20}Au_2(CO)_{42}][NEt_4]_6 \cdot 6CH_3CN$ compound crystallized in the trigonal *R*-3 space group, with Z = 3.

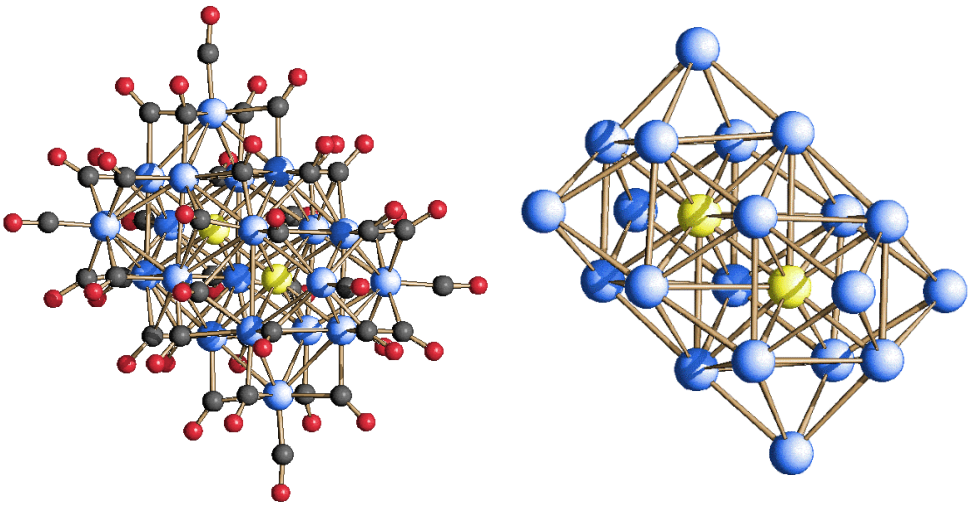

Figure 6.4. Molecular structure of $[Rh_{20}Au_2(CO)_{42}]^{6-}$ (left) and its metal skeleton (right). Rh atoms are depicted in blue, Au atoms are depicted in yellow, C atoms are in grey and O atoms are in red.

The metal skeleton of $[Rh_{20}Au_2(CO)_{42}]^{6-}$ consists of two interpenetrated Rh_7Au cubic cages centred by the other Au atom and capped on the six faces by just as many Rh atoms (highlighted in Figure 6.5). It is stabilized by 42 ligands of which 6 terminally bonded, 24 edge-bridging and 12 face-bridging.

The Rh-Au bond distances vary from 2.550(3) to 3.251(2) Å (average 2.862 Å), while the Rh-Rh bonds are on average 2.915 Å long and they span from 2.808(3) to 3.066(3) Å.

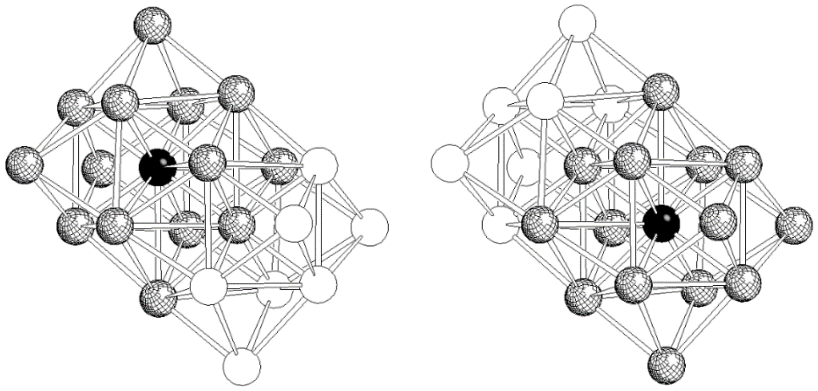

Figure 6.5. The two capped cubic cages which together constitute the metal skeleton of $[Rh_{20}Au_2(CO)_{42}]^{6-}$. For each highlighted unit, the blackened sphere represents the interstitial gold atom.

Au(1)-Au(1)#1	2.550(3)
Au(1)-Rh(4)#2	2.625(2)
Au(1)-Rh(4)#3	2.625(2)
Au(1)-Rh(4)	2.625(2)
Au(1)-Rh(3)	2.636(4)
Au(1)-Rh(2)#3	2.760(2)
Au(1)-Rh(2)	2.760(2)
Au(1)-Rh(2)#2	2.760(2)
Au(1)-Rh(2)#4	3.251(2)
Au(1)-Rh(2)#5	3.251(2)
Au(1)-Rh(2)#1	3.251(2)
Rh(2)-Au(1)#1	3.251(2)
Rh(2)-Rh(5)	2.808(3)
Rh(2)-Rh(4)#4	2.856(3)
Rh(2)-Rh(2)#4	2.911(2)

Rh(2)-Rh(2)#5	2.911(2)
Rh(2)-Rh(4)#2	3.065(3)
Rh(2)-Rh(4)	3.066(3)
Rh(3)-Rh(5)#3	2.868(2)
Rh(3)-Rh(5)	2.868(2)
Rh(3)-Rh(5)#2	2.868(2)
Rh(3)-Rh(4)#2	2.935(3)
Rh(3)-Rh(4)#3	2.935(3)
Rh(3)-Rh(4)	2.935(3)
Rh(4)-Rh(2)#5	2.856(3)
Rh(4)-Rh(5)#3	2.870(3)
Rh(4)-Rh(5)	2.875(4)
Rh(4)-Rh(2)#3	3.065(3)
Rh(5)-Rh(4)#2	2.870(3)

Table 6.1. Most relevant bond lengths for $[Rh_{20}Au_2(CO)_{42}]^{6-}$.

The maximum size of the $[Rh_{20}Au_2(CO)_{42}]^{6-}$ cluster, measured from the outermost oxygen atoms of the carbonyl ligands and including twice the oxygen van der Waals radius, is 1.8 nm.

VI.III. IR characterization of $[Rh_{20}Au_2(CO)_{42}]^{6-}$

This species is soluble in acetonitrile and DMF and stable, but not soluble, in water. Its IR spectrum recorded in CH_3CN presents ν_{CO} absorptions at 1989(vs) and 1843(ms) cm^{-1}.

VI.IV. Molecular structure of the $[Rh_{16}Au_6(CO)_{36}]^{6-}$ cluster

The molecular structure of $[Rh_{16}Au_6(CO)_{36}]^{6-}$ (2) is illustrated in Figure 6.6.

The cluster crystallized in the monoclinic $P2_1/n$ space group, with Z = 2, and the unit cell also contains four acetonitrile molecules, two per each cluster unit. Being the third angle of the cell very close to 90°, and being two of the edges nearly equivalent, thus describing quasi-rectangular and quasi-square faces, the solid packing is reminiscent of a *bcc* lattice of $[Rh_{16}Au_6(CO)_{36}]^{6-}$ molecules with embedded cations and the solvent molecules filling the voids.

The metal structure of $[Rh_{16}Au_6(CO)_{36}]^{6-}$ consists of an inner octahedron of Au atoms surrounded by four Rh_4Au_2 octahedra, built on each edge of the squared base of the inner polyhedron. The metal skeleton is stabilized by 36 ligands coordinated on each external Rh_4 fragment and equally divided into 4 terminal and 5 edge-bridging groups.

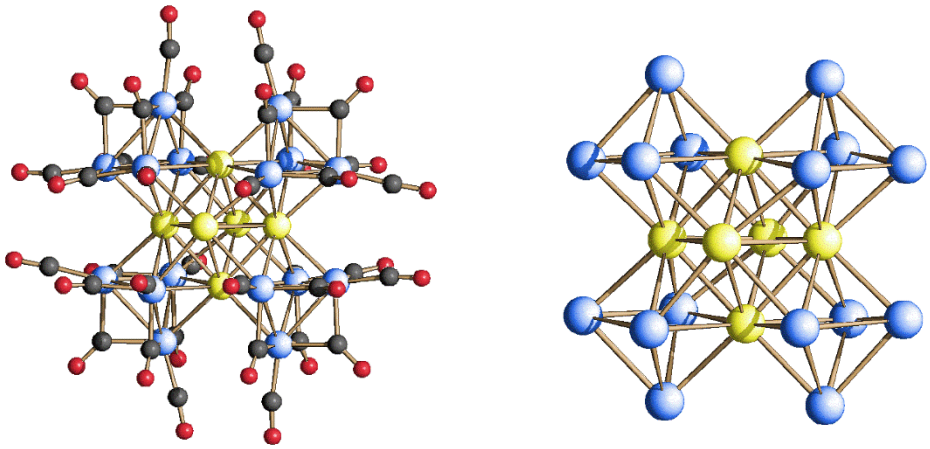

Figure 6.6. Molecular structure of $[Rh_{16}Au_6(CO)_{36}]^{6-}$ (left) and its metal skeleton (right). Rh atoms are depicted in blue, Au atoms are depicted in yellow, C atoms are in grey and O atoms are in red.

This structure is reminiscent of the $[Ni_{12}Au_6(CO)_{24}]^{2-}$ cluster obtained by Dahl in 1991, [19] which formally arises from the condensation of four $Ni_3(CO)_6$ fragments in an anti-prismatic orientation on four alternate faces of a central Au_6 octahedron. They both represent remarkable examples of aurophilicity. [20]

The Au-Au bond lengths range from 2.7401(5) to 3.1094(5) Å, with an average value of 2.8922 Å; these values are noticeably more spread than those observed in the $[Ni_{12}Au_6(CO)_{24}]^{2-}$ cluster, which vary from 2.786(2) Å to 2.882(2) Å. The Rh-Au bond distances are within a close range, varying from 2.7122(8) to 2.8899(8) Å (average 2.7988 Å). Finally, the Rh-Rh bonds are on average 2.8408 Å long and have very close values, as they span from 2.8089(10) to 2.8706(10) Å.

The minimum and maximum sizes of the $[Rh_{16}Au_6(CO)_{36}]^{6-}$ cluster, measured from the outermost oxygen atoms of the carbonyl ligands and including twice the oxygen van der Waals radius, are 1.3 and 1.7 nm, respectively.

Au(1)-Au(2)	2.7401(5)	Au(3)-Rh(9)	2.7511(8)
Au(1)-Au(2)#1	2.7435(5)	Au(3)-Rh(8)#1	2.7657(8)
Au(1)-Au(3)#1	2.8664(5)	Au(3)-Rh(4)	2.7693(8)
Au(1)-Au(3)	2.9702(5)	Au(3)-Rh(5)#1	2.7719(8)
Au(2)-Au(1)#1	2.7436(5)	Rh(5)-Au(3)#1	2.7720(8)
Au(2)-Au(3)	2.8814(5)	Rh(8)-Au(3)#1	2.7657(8)
Au(2)-Au(3)#1	3.1094(5)	Rh(8)-Au(2)#1	2.8459(8)
Au(3)-Au(1)#1	2.8663(5)	Rh(9)-Au(2)#1	2.8357(8)
Au(3)-Au(2)#1	3.1092(5)	Rh(4)-Rh(10)	2.8274(11)
Au(1)-Rh(6)	2.7238(8)	Rh(4)-Rh(7)	2.8524(10)
Au(1)-Rh(10)	2.7468(8)	Rh(5)-Rh(7)	2.8294(10)
Au(1)-Rh(4)	2.7852(8)	Rh(5)-Rh(10)	2.8706(10)
Au(1)-Rh(8)	2.8292(8)	Rh(6)-Rh(8)	2.8302(10)
Au(1)-Rh(5)	2.8734(8)	Rh(6)-Rh(11)#1	2.8305(10)
Au(1)-Rh(9)	2.8745(8)	Rh(6)-Rh(9)	2.8605(10)
Au(2)-Rh(7)	2.7122(8)	Rh(7)-Rh(10)	2.8089(10)
Au(2)-Rh(11)	2.7323(8)	Rh(8)-Rh(11)#1	2.8383(11)
Au(2)-Rh(9)#1	2.8357(8)	Rh(9)-Rh(11)#1	2.8569(11)
Au(2)-Rh(8)#1	2.8459(8)	Rh(11)-Rh(6)#1	2.8305(10)
Au(2)-Rh(5)	2.8489(8)	Rh(11)-Rh(8)#1	2.8383(11)
Au(2)-Rh(4)	2.8899(8)	Rh(11)-Rh(9)#1	2.8569(11)

Table 6.2. Most relevant bond lengths for $[Rh_{16}Au_6(CO)_{36}]^{6-}$.

VI.V. IR and ESI-MS characterization and electron counting of the $[Rh_{16}Au_6(CO)_{36}]^{6-}$ cluster

$[Rh_{16}Au_6(CO)_{36}]^{6-}$ as salt of $[NEt_4]^+$ is soluble in acetone, acetonitrile and DMF and stable, but not soluble, in water.

Its IR spectrum recorded in CH_3CN shows ν_{CO} absorptions at 2001(s) and 1805(ms) cm^{-1}.

We also performed the ESI-MS analysis to further characterize the Rh-Au species and this showed that the cluster is not stable in the experimental conditions and

heavily breaks. Only two signals at 1285 and 1241 m/z could be attributed to the $\{[Rh_{16}Au_6(CO)_{32}][NEt_4]\}^{3-}$ and $\{[Rh_{16}Au_6(CO)_{32}]\}^{3-}$ ions, respectively.

As for the electron counting, as the $[Rh_{16}Au_6(CO)_{36}]^{6-}$ cluster can be seen as composed of five octahedra (5 × 86 CVEs) fused through four edges (−4 × 34 CVEs) with eight additional Rh-Au bonds (−8 × 2 CVEs), we expect it to have 278 CVEs in total. Actually, the latter bonds are this way formally considered as two-centre two-electron interactions, which is not totally correct in metals.

Conversely, the $[Rh_{16}Au_6(CO)_{36}]^{6-}$ cluster presents 288 CVEs, given by the 9 × 16 rhodium atoms (144), the 11 × 6 gold atoms (66), the 2 × 36 carbonyl ligands (72) and the negative charge (6).

VI.VI. Reactivity of $[Rh_{16}Au_6(CO)_{36}]^{6-}$ under N_2

Once the $[Rh_{16}Au_6(CO)_{36}]^{6-}$ was obtained and completely characterized, we tested its stability under different atmospheres, such as nitrogen and hydrogen.

An acetone solution of $[Rh_{16}Au_6(CO)_{36}]^{6-}$ was placed under vacuum for a few minutes, purged with N_2 and then left to stand overnight under stirring. The resulting solution, separated from the solid that had precipitated during the reaction, presented different ν_{CO} absorptions from the ones of the starting cluster: 2012(sh), 1991(s), 1856(sh) and 1836(m) cm^{-1}. The compound was characterized as $[Rh_{18}Au(CO)_{33}][NEt_4]_3$ through the X-ray analysis of the crystals obtained by layering di-isopropyl ether onto the acetonitrile solution, where the compound had been transferred to.

VI.VII. Molecular structure of the $[Rh_{18}Au(CO)_{33}]^{3-}$ cluster

The molecular structure of $[Rh_{18}Au(CO)_{33}]^{3-}$ (3) is illustrated in Figure 6.7.

$[Rh_{18}Au(CO)_{33}][NEt_4]_3 \cdot 2CH_3CN$ crystallized in the monoclinic *C*2 space group, with Z = 4.

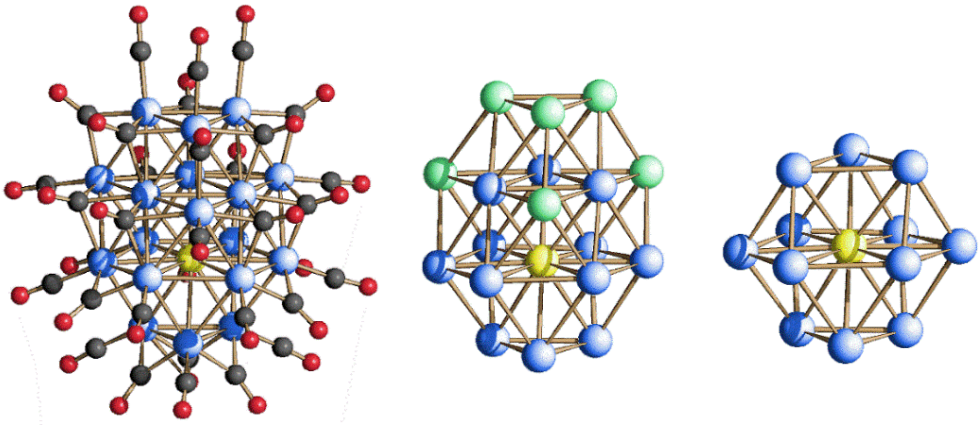

Figure 6.7. Molecular structure of $[Rh_{18}Au(CO)_{33}]^{3-}$ (left), its metal skeleton (centre) and Rh cuboctahedron centred by the Au atom (right). Rh atoms are depicted in blue and green, Au atoms are depicted in yellow, C atoms are in grey and O atoms are in red.

The metal skeleton of $[Rh_{18}Au(CO)_{33}]^{3-}$ is based on a cuboctahedron of Rh atoms centred by the unique Au. This structure is capped on three square faces by three rhodium atoms, giving rise to three Rh_5Au octahedra. The last three Rh atoms form a triangular cap on the top face of the cuboctahedron, in an anti-prismatic fashion. The metal skeleton is stabilized by 33 carbonyl ligands, of which 15 terminally bonded, 9 edge-bridging and 9 face-bridging.

The Rh-Au bond distances vary from 2.7434(8) to 2.9367(9) Å (average 2.8288 Å). The Rh-Rh bonds are on average 2.8071 Å long and span from 2.7075(10) to 3.0100(11) Å.

The maximum size of the $[Rh_{18}Au(CO)_{33}]^{3-}$ cluster, measured from the outermost oxygen atoms of the carbonyl ligands and including twice the oxygen van der Waals radius, is 1.6 nm.

Au(1)-Rh(2)	2.7434(8)	Rh(4)-Rh(15)	2.8781(11)
Au(1)-Rh(7)	2.7506(8)	Rh(5)-Rh(11)	2.7490(11)
Au(1)-Rh(5)	2.7596(10)	Rh(5)-Rh(6)	2.8766(12)
Au(1)-Rh(16)	2.7632(9)	Rh(5)-Rh(8)	2.9406(11)
Au(1)-Rh(15)	2.8031(9)	Rh(6)-Rh(8)	2.7190(10)
Au(1)-Rh(17)	2.8097(9)	Rh(6)-Rh(9)	2.7460(10)
Au(1)-Rh(8)	2.8322(9)	Rh(7)-Rh(18)	2.7079(11)
Au(1)-Rh(18)	2.8578(10)	Rh(7)-Rh(12)	2.7427(10)
Au(1)-Rh(11)	2.8884(9)	Rh(7)-Rh(14)	2.7810(11)
Au(1)-Rh(10)	2.8957(9)	Rh(7)-Rh(19)	2.7978(11)
Au(1)-Rh(3)	2.9057(9)	Rh(7)-Rh(15)	2.8537(12)
Au(1)-Rh(4)	2.9367(9)	Rh(7)-Rh(13)	2.8901(11)
Rh(2)-Rh(5)	2.7326(11)	Rh(8)-Rh(17)	2.7528(11)
Rh(2)-Rh(12)	2.7488(10)	Rh(8)-Rh(11)	2.9162(12)
Rh(2)-Rh(6)	2.7772(11)	Rh(9)-Rh(13)	2.7867(11)
Rh(2)-Rh(14)	2.8201(11)	Rh(9)-Rh(12)	2.7868(10)
Rh(2)-Rh(4)	2.8544(12)	Rh(10)-Rh(16)	2.7756(11)
Rh(2)-Rh(9)	2.8883(12)	Rh(10)-Rh(11)	2.7784(11)
Rh(2)-Rh(7)	2.9627(11)	Rh(10)-Rh(15)	2.8237(10)
Rh(2)-Rh(3)	3.0100(11)	Rh(11)-Rh(16)	2.7911(12)
Rh(3)-Rh(8)	2.7075(10)	Rh(12)-Rh(13)	2.7729(11)
Rh(3)-Rh(17)	2.7089(10)	Rh(12)-Rh(14)	2.8839(11)
Rh(3)-Rh(9)	2.7169(10)	Rh(13)-Rh(19)	2.7254(10)
Rh(3)-Rh(13)	2.7173(10)	Rh(14)-Rh(15)	2.7260(10)
Rh(3)-Rh(19)	2.7848(12)	Rh(15)-Rh(18)	2.7671(11)
Rh(3)-Rh(6)	2.8054(12)	Rh(16)-Rh(18)	2.8183(11)
Rh(3)-Rh(7)	2.9925(10)	Rh(16)-Rh(17)	2.9271(12)
Rh(4)-Rh(5)	2.7592(11)	Rh(17)-Rh(19)	2.7008(10)
Rh(4)-Rh(14)	2.7658(10)	Rh(17)-Rh(18)	2.9035(11)
Rh(4)-Rh(10)	2.7779(10)	Rh(18)-Rh(19)	2.8923(12)

Table 6.3. Most relevant bond lengths for $[Rh_{18}Au(CO)_{33}]^{3-}$.

VI.VIII. IR characterization of the $[Rh_{18}Au(CO)_{33}]^{3-}$ cluster

$[Rh_{18}Au(CO)_{33}]^{3-}$ as salt of $[NEt_4]^+$ is soluble in acetone, acetonitrile and DMF and stable, but not soluble, in water.

Its IR spectrum recorded in CH_3CN shows ν_{CO} absorptions at 2019(vs), 1994(ms), 1960(sh) and 1819(ms) cm^{-1}.

VI.IX. Reactivity of $[Rh_{16}Au_6(CO)_{36}]^{6-}$ under H_2

An acetone solution of $[Rh_{16}Au_6(CO)_{36}][NEt_4]_6$ was placed under vacuum for a few minutes, purged with H_2 and then left to stand overnight under stirring. The resulting solution, separated from the solid which had precipitated during the reaction presented different ν_{CO} absorptions from the ones of the starting cluster: 2010(sh), 1992(s) and 1829(m) cm^{-1}, and underwent a further change after a first purification realized by layering hexane on the acetone solution. More specifically, a solid residue separated from the solution and, after filtration, it was dissolved in acetonitrile. After layering di-isopropyl ether onto the solution, crystals of $[Rh_9(CO)_{20}][NEt_4]_2$ were obtained. This was a totally unexpected product. Indeed, we had hypothesised that $[Rh_{16}Au_6(CO)_{36}]^{6-}$ would not have been stable also under H_2 and that a structural rearrangement could occur, but still leading to the formation of an heterometallic Rh-Au cluster. Notably, the same metal skeleton is found in the $[Rh_9(CO)_{19}]^{3-}$, which has been known for a long time. [21] However, the latter was obtained by condensation of the $[Rh_5(CO)_{15}]^-$ anion [22] with the $[Rh_4(CO)_{11}]^{2-}$ dianion [23] at room temperature.

VI.X. Molecular structure of the $[Rh_9(CO)_{20}]^{2-}$ cluster

The molecular structure of $[Rh_9(CO)_{20}]^{2-}$ (4) is illustrated in Figure 6.8.

The $[Rh_9(CO)_{20}][NEt_4]_2$ crystallized in the triclinic *P*-1 space group, with Z = 4.

The metal skeleton is based on two Rh octahedra sharing a triangular face and stabilized by 20 carbonyl ligands, of which 11 terminally bonded, 6 edge-bridging and 3 face-bridging.

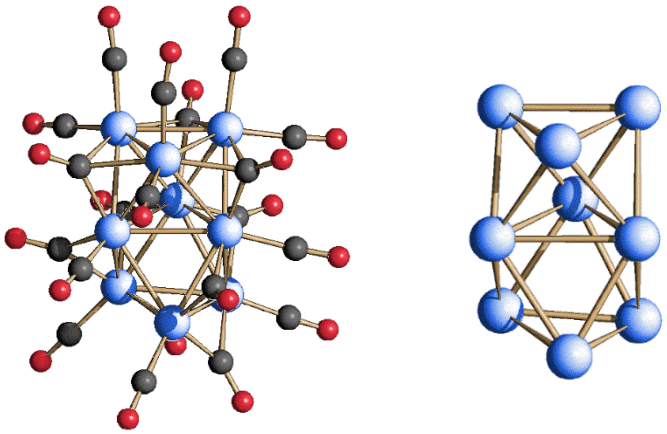

Figure 6.8. Molecular structure of $[Rh_9(CO)_{20}]^{2-}$ (left) and its metal skeleton (right). Rh atoms are depicted in blue, C atoms are in grey and O atoms are in red.

The independent unit contains two isomers, which are only marginally different in their interatomic distances. The Rh-Rh distances vary from 2.6872(16) to 3.0039(17) Å and from 2.6909(15) to 3.0347(16) Å in the two isomers, with average values of 2.7931 and 2.7969 Å, respectively.

Rh(1)-Rh(7)	2.7291(16)
Rh(1)-Rh(4)	2.7699(15)
Rh(1)-Rh(2)	2.7799(16)
Rh(1)-Rh(3)	2.8256(15)
Rh(1)-Rh(6)	2.9118(15)
Rh(1)-Rh(5)	2.9272(16)
Rh(2)-Rh(3)	2.6872(16)
Rh(2)-Rh(9)	2.7597(16)
Rh(2)-Rh(4)	2.8015(16)
Rh(3)-Rh(9)	2.7110(17)
Rh(3)-Rh(8)	2.7123(17)

Rh(3)-Rh(5)	2.7423(17)
Rh(3)-Rh(6)	2.8539(16)
Rh(4)-Rh(6)	2.7415(17)
Rh(4)-Rh(9)	2.7591(17)
Rh(5)-Rh(8)	2.7543(17)
Rh(5)-Rh(7)	2.7899(17)
Rh(6)-Rh(9)	2.7797(18)
Rh(6)-Rh(8)	2.8008(18)
Rh(6)-Rh(7)	2.8146(18)
Rh(7)-Rh(8)	3.0039(17)

Table 6.4. Most relevant bond lengths for the first isomer of $[Rh_9(CO)_{20}]^{2-}$.

Rh(11)-Rh(18)	2.7265(15)
Rh(11)-Rh(12)	2.7759(15)
Rh(11)-Rh(17)	2.7885(15)
Rh(11)-Rh(13)	2.8072(15)
Rh(11)-Rh(14)	2.9180(15)
Rh(11)-Rh(19)	2.9278(15)
Rh(12)-Rh(13)	2.6909(15)
Rh(12)-Rh(16)	2.7652(15)
Rh(12)-Rh(17)	2.7999(16)
Rh(13)-Rh(15)	2.7030(15)
Rh(13)-Rh(16)	2.7346(15)

Rh(13)-Rh(19)	2.7529(15)
Rh(13)-Rh(14)	2.8528(15)
Rh(14)-Rh(17)	2.7265(16)
Rh(14)-Rh(16)	2.7791(16)
Rh(14)-Rh(15)	2.8068(16)
Rh(14)-Rh(18)	2.8272(16)
Rh(15)-Rh(19)	2.7772(16)
Rh(15)-Rh(18)	3.0347(16)
Rh(16)-Rh(17)	2.7477(16)
Rh(18)-Rh(19)	2.7916(16)

Table 6.5. Most relevant bond lengths for the second isomer of $[Rh_9(CO)_{20}]^{2-}$.

It is interesting to make a comparison between this species and the known $[Rh_9(CO)_{19}]^{3-}$ cluster, where the Rh-Rh distances vary from 2.712(1) to 2.852(1) Å, with a shorter average value of 2.759 Å.

Rh(1)-Rh(2)	2.822(1)
Rh(1)-Rh(3)	2.823(1)
Rh(1)-Rh(5)	2.770(1)
Rh(1)-Rh(6)	2.762(1)
Rh(2)-Rh(3)	2.836(1)
Rh(2)-Rh(4)	2.727(1)
Rh(2)-Rh(5)	2.725(1)
Rh(3)-Rh(4)	2.712(1)
Rh(3)-Rh(6)	2.742(1)
Rh(4)-Rh(5)	2.725(1)
Rh(4)-Rh(6)	2.716(1)

Rh(4)-Rh(8)	2.745(1)
Rh(4)-Rh(9)	2.733(1)
Rh(5)-Rh(6)	2.742(1)
Rh(5)-Rh(7)	2.769(1)
Rh(5)-Rh(8)	2.733(1)
Rh(6)-Rh(7)	2.733(1)
Rh(6)-Rh(9)	2.752(1)
Rh(7)-Rh(8)	2.852(1)
Rh(7)-Rh(9)	2.765(1)
Rh(8)-Rh(9)	2.758(1)

Table 6.6. Most relevant bond lengths for $[Rh_9(CO)_{19}]^{3-}$.

VI.XI. IR analysis, electron counting and ^{1}H-NMR characterization of the $[Rh_9(CO)_{20}]^{2-}$ cluster

$[Rh_9(CO)_{20}]^{2-}$ as salt of $[NEt_4]^+$ is soluble in acetonitrile and DMF and stable, but not soluble, in water.

Its IR spectrum recorded in CH_3CN shows ν_{CO} absorptions at 1988(s), 1967(ms), 1964(m) and 1825(mw) cm^{-1}.

The $[Rh_9(CO)_{20}]^{2-}$ cluster, being constituted of two fused octahedra which share a triangular face, should have 2 × 86 CVEs, to which it is necessary to subtract 48 CVEs of the shared triangular face, for a final counting of 124 CVEs.

However, it presents 123 CVEs, one electron less than expected, given by the 9 × 9 rhodium atoms (81), the 2 × 20 carbonyl ligands (40) and the negative charge (2).

When looking at the already known $[Rh_9(CO)_{19}]^{3-}$ cluster we obtain an electron counting of 122 CVEs (two electrons less than expected), given by the 9 × 9 rhodium atoms (81), the 2 × 19 carbonyl ligands (38) and the negative charge (3).

The odd electron count of the new $[Rh_9(CO)_{20}]^{2-}$ would make it paramagnetic, which is not so common for clusters of such nuclearity. This, combined with the fact that the species was obtained under H_2 atmosphere, led us to conclude that the cluster could be an hydride species.

In order to verify our theory, we characterized this cluster by ^{1}H-NMR spectroscopy. The spectrum (Figure 6.9) recorded in CD_3CN at 298 K actually shows a multiplet centred at $\delta = -26.82$ ppm compatible with the hydride signal. [24] In the spectrum there are other minor signals attributable to impurities, which could not be separated from the solid sample used for the analysis because of the very low amount of obtained crystals.

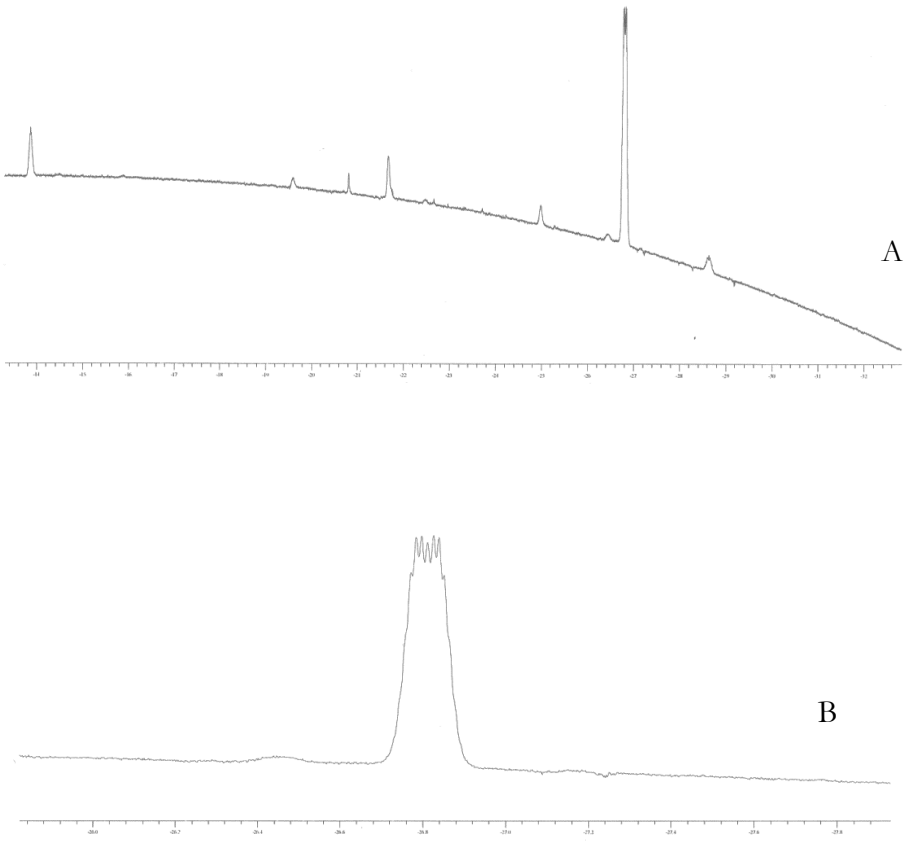

Figure 6.9. ^{1}H-NMR spectrum of $[HRh_9(CO)_{20}]^{2-}$ in CD_3CN at 298 K (A), close-up of the hydride signal of ^{1}H-NMR spectrum of $[HRh_9(CO)_{20}]^{2-}$.

Through the ^{1}H NMR spectroscopy we confirmed our hypothesis on the hydride nature of the homometallic cluster, which was therefore reformulated as $[HRh_9(CO)_{20}]^{2-}$. Thus, the cluster results to be diamagnetic and the electron counting becomes 124 CVEs, conform to the Polyhedral Skeleton Electron Pair Theory (PSEPT). Moreover, the presence of the hydride atom could explain the slightly longer Rh-Rh contacts when compared with those of the $[Rh_9(CO)_{19}]^{3-}$, as the presence of an interstitial hydrogen atom would swell the cluster.

VI.XII. Reactivity of $[Rh_7(CO)_{16}]^{3-}$ with $[AuBr_4]^-$ under CO atmosphere

After the investigation of the reactivity of $[Rh_7(CO)_{16}]^{3-}$ with $[AuCl_4]^-$, we decided to test the reactivity of our homometallic cluster precursor with $[AuBr_4]^-$, to check the role of the halide. The reaction was carried out in DMF under CO atmosphere with the aim of obtaining the same reaction solution which had led to the $[Rh_{16}Au_6(CO)_{36}]^{6-}$ cluster, reaching a final stoichiometric Rh_7:Au^{3+} ratio of 1:1. During the work-up, in acetone we extracted a mixture of two homometallic Rh clusters: the known $[Rh_{12}(CO)_{30}]^{2-}$ and the higher nuclearity $[Rh_{22}(CO)_{37}]^{n-}$. These two species were separated by layering di-isopropyl ether onto the acetonitrile solution (where the mixture had been transferred to). Indeed, the former cluster remained in solution, while the latter precipitated in a crystalline form. Unfortunately, we were not able to unambiguously ascertain the number of the counter-ions, therefore we could not assign the negative charge on the $[Rh_{22}(CO)_{37}]^{n-}$ cluster.

VI.XIII. Molecular structure of the $[Rh_{22}(CO)_{37}]^{n-}$ cluster

The molecular structure of $[Rh_{22}(CO)_{37}]^{n-}$ (5) is illustrated in Figure 6.10.

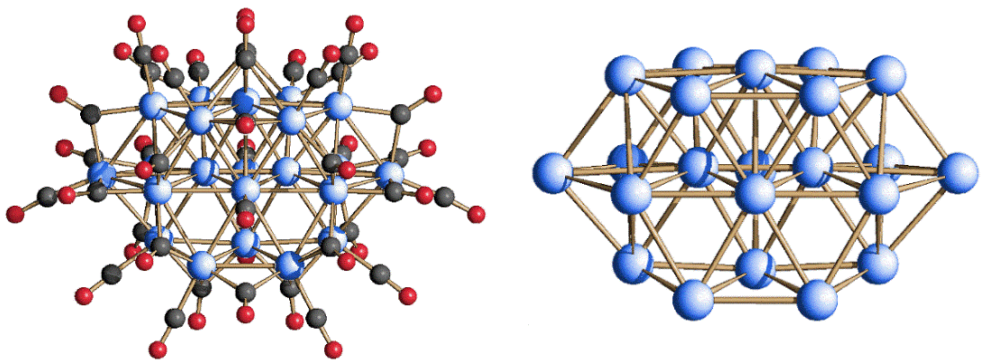

Figure 6.10. Molecular structure of $[Rh_{22}(CO)_{37}]^{n-}$ (left) and its metal skeleton (right). Rh atoms are depicted in blue, C atoms are in grey and O atoms are in red.

Rh(1)-Rh(2)	2.6216(15)
Rh(1)-Rh(2)#1	2.6216(15)
Rh(1)-Rh(5)#1	2.7762(11)
Rh(1)-Rh(5)	2.7762(11)
Rh(1)-Rh(7)	2.7968(16)
Rh(1)-Rh(7)#1	2.7969(17)
Rh(1)-Rh(6)#1	2.8174(16)
Rh(1)-Rh(6)	2.8174(16)
Rh(1)-Rh(3)	3.101(2)
Rh(2)-Rh(2)#1	2.572(2)
Rh(2)-Rh(5)#1	2.6686(14)
Rh(2)-Rh(9)#1	2.6683(16)
Rh(2)-Rh(3)	2.6790(17)
Rh(2)-Rh(11)#1	2.7190(16)
Rh(2)-Rh(4)	2.7227(17)
Rh(2)-Rh(10)	2.7267(16)
Rh(2)-Rh(13)#1	2.7327(16)
Rh(2)-Rh(8)#1	2.7512(16)
Rh(3)-Rh(2)#1	2.6791(17)
Rh(3)-Rh(8)#1	2.8161(17)
Rh(3)-Rh(8)	2.8162(17)
Rh(3)-Rh(6)	2.8386(16)
Rh(3)-Rh(6)#1	2.8386(16)
Rh(3)-Rh(11)	2.9249(13)
Rh(3)-Rh(11)#1	2.9250(13)
Rh(4)-Rh(2)#1	2.7226(16)
Rh(4)-Rh(9)	2.7502(12)
Rh(4)-Rh(9)#1	2.7503(12)
Rh(4)-Rh(10)	2.753(2)

Rh(4)-Rh(7)	2.9398(16)
Rh(4)-Rh(7)#1	2.9399(17)
Rh(5)-Rh(2)#1	2.6687(14)
Rh(5)-Rh(12)	2.7544(16)
Rh(5)-Rh(7)	2.7759(16)
Rh(5)-Rh(6)	2.7949(15)
Rh(5)-Rh(11)	3.0176(17)
Rh(5)-Rh(9)	3.1236(17)
Rh(6)-Rh(6)#1	2.8939(19)
Rh(6)-Rh(11)	2.9398(16)
Rh(7)-Rh(7)#1	2.775(2)
Rh(7)-Rh(9)	2.7857(15)
Rh(8)-Rh(13)	2.6860(17)
Rh(8)-Rh(2)#1	2.7513(17)
Rh(8)-Rh(11)	2.7686(16)
Rh(8)-Rh(8)#1	2.801(2)
Rh(8)-Rh(10)	2.8013(18)
Rh(9)-Rh(2)#1	2.6682(16)
Rh(9)-Rh(13)	2.7836(17)
Rh(9)-Rh(12)	2.7866(18)
Rh(10)-Rh(2)#1	2.7267(16)
Rh(10)-Rh(8)#1	2.8013(18)
Rh(10)-Rh(13)	2.8756(14)
Rh(10)-Rh(13)#1	2.8756(14)
Rh(11)-Rh(2)#1	2.7191(16)
Rh(11)-Rh(12)	2.7958(18)
Rh(12)-Rh(13)	2.846(2)
Rh(13)-Rh(2)#1	2.7327(16)

Table 6.7. Most relevant bond lengths for $[Rh_{22}(CO)_{37}]^{n-}$.

The $[Rh_{22}(CO)_{37}][NEt_4]_n \cdot xCH_3CN$ compound crystallized in the monoclinic *C*2/m space group, with Z = 4.

The metal skeleton is based on two interpenetrated distorted centred and penta-capped cubes of Rh atoms. It is stabilized by 37 carbonyl ligands, of which 16 terminally bonded, 17 edge-bridging and 4 face-bridging. Unfortunately, the tetrametylammonium ions and the acetonitrile molecules were disordered in the unit cell and their number could not be clearly determined. However, the metal connectivity and the number of carbonyl ligands have been correctly identified. The Rh-Rh distances vary from 2.572(2) to 3.1236(17) Å, with average value of 2.7896 Å.

This cluster recalls the Martinengo's $[Rh_{22}(CO)_{37}]^{4-}$, obtained by refluxing mixtures of $Rh_4(CO)_{12}$ and NaOH in 2-propanol in the ratio of one OH^- for every 5-5.5 Rh atoms, for 4-6 h under nitrogen. [25] However, it presents a different metal structure and CO ligands disposition (Figure 6.11).

Indeed, its metal skeleton is based on a mixed hcp/ccp arrangement but the Rh-Rh distances are very similar (on average) to those of the new cluster, as they vary from 2.729(2) to 2.883(2) Å, with an average value of 2.798 Å.

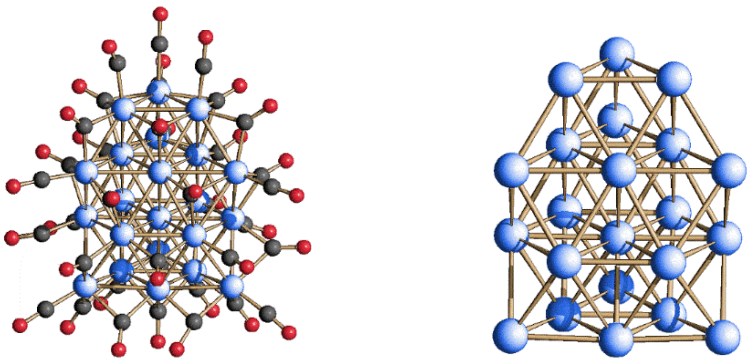

Figure 6.11. Molecular structure of $[Rh_{22}(CO)_{37}]^{4-}$ (left) and its metal skeleton (right) obtained by Martinengo et al. Rh atoms are depicted in blue, C atoms are in grey and O atoms are in red.

Furthermore, it is possible to compare these two clusters also with the $[H_{8-n}Rh_{22}(CO)_{35}]^{n-}$ (n = 4, 5) hydride species, firstly obtained by Vidal in 1981 [26] and then further characterized in 2011. [27] They both present a very similar metal skeleton to the one of the new $[Rh_{22}(CO)_{37}]^{n-}$, but are stabilized by a different number of CO ligands. Indeed, the 35 carbonyls are divided into 12 terminally bonded (versus 16 of the new species), 21 edge-bridging (versus 17) and 2 face-bridging (versus 4). However, the Rh-Rh distances of the older isomers vary from 2.480(2) to 3.148(2) Å, with an average value of 2.785 Å, only slightly shorter than the one found in the new $[Rh_{22}(CO)_{37}]^{n-}$ (2.7896 Å).

The maximum size of the $[Rh_{22}(CO)_{37}]^{n-}$ cluster, measured from the outermost oxygen atoms of the carbonyl ligands and including twice the oxygen van der Waals radius, is 1.8 nm.

VI.XIV. IR characterization of the $[Rh_{22}(CO)_{37}]^{n-}$ cluster

$[Rh_{22}(CO)_{37}]^{n-}$ as salt of $[NEt_4]^+$ is soluble in acetone, acetonitrile and DMF and stable, but not soluble, in water.

Its IR spectrum recorded in CH_3CN shows ν_{CO} absorptions at 2012(vs), 1959(w), 1857(sh), 1842(w) and 1810(m) cm^{-1}.

Crystallographic data for Rh-Au carbonyl clusters

Compound	**2**$[NEt_4]_6 \cdot 2CH_3CN$	**3**$[NEt_4]_3 \cdot 2CH_3CN$
Formula	$C_{88}H_{126}N_8O_{36}Rh_{16}Au_6$	$C_{61}H_{66}N_5O_{33}Rh_{18}Au$
Fw	4700.32	3446.53
Crystal system	Monoclinic	Monoclinic
Space group	$P2_1/n$	C2
***a* (Å)**	16.6663(10)	22.777(6)
***b* (Å)**	16.5974(10)	15.526(4)
***c* (Å)**	21.5097(13)	26.221(7)
α (deg)	90	90
β (deg)	91.4980(10)	117.884(6)
γ (deg)	90	90
Cell volume (Å^3)	5947.9(6)	8196(4)
Z	2	4
D (g/cm^3)	2.624	2.793
μ (mm^{-1})	9.592	5.380
F (000)	4384	6480
θ limits (deg)	1.959 to 24.999	1.964-25.000
Index ranges	-19≤ h ≤19, -19≤ k ≤19, -25≤ l ≤25	-27≤ *h* ≤27, -18≤ *k* ≤18, -31≤ *l* ≤31
Reflections collected	68968	47599
Independent reflections	10453 [R(int) = 0.0464]	14434 [R(int) = 0.0371]
Completeness to θ max	99.7%	99.9%
Data/restraints/ parameters	10453/220/734	14434/243/1111
Goodness-of-fit	1.206	1.030
R_1 (I > 2σ(I))	0.0441	0.0253
wR_2 (all data)	0.0776	0.0616
Largest diff. peak and hole, e Å^{-3}	1.815 and -1.923	1.572 and -1.513

Table 6.8. Crystallographic data for clusters 2 and 3.

1 B. K. Teo, X. Shi, Z. Hong, *J. Am. Chem. Soc.* **1991**, *113*, 4329.

2 G. Schmid, B. Corain, *Eur. J. Inorg. Chem.* **2003**, 3081.

3 G. Li, R. Jin, *Acc. Chem. Res.* **2013**, *46*, 1749.

4 P. Buchwalter, J. Rosé, P. Braunstein, *Chem. Rev.* **2015**, *115*, 28.

5 L. Cerchi, A. Fumagalli, S. Fedi, P. Zanello, F. Fabrizi De Biani, F. Laschi, L. Garlaschelli, P. Macchi, A. Sironi, *Inorg. Chem.* **2012**, *51*, 9171.

6 M. Bortoluzzi, I. Ciabatti, C. Femoni, M. Hayatifar, M.C. Iapalucci, G. Longoni, S. Zacchini, *Dalton Trans.* **2014**, *43*, 13471.

7 A. Ceriotti, P. Macchi, A. Sironi, S. El Afefey, M. Daghetta, S. Fedi, F. Fabrizi De Biani, R. Della Pergola, *Inorg. Chem.* **2013**, *52*, 1960.

8 R. D. Adams, Y. Kan, Q. Zhang, *Organometallics* **2012**, *31*, 8639.

9 C. Femoni, M. C. Iapalucci, G. Longoni, C. Tiozzo, J. Wolowska, S. Zacchini, E. Zazzaroni, *Chem. Eur. J.* **2007**, *13*, 6544.

10 C. Cathey, J. Lewis, P. R. Raithby, M. C. Ramírez de Arellano, *J. Chem. Soc., Dalton Trans.* **1994**, 3331.

11 I. Ciabatti, C. Femoni, M. C. Iapalucci, G. Longoni, S. Zacchini, S. Fedi, F. Fabrizi De Biani, *Inorg. Chem.* **2012**, *51*, 11753.

12 P. Croizat, S. Sculfort, R. Welter, P. Braunstein, *Organometallics* **2016**, *35*, 3949.

13 C. Femoni, M. C. Iapalucci, G. Longoni, C. Tiozzo, S. Zacchini, *Angew. Chem. Int. Ed.* **2008**, *47*, 6666.

14 N. T. Tran, M. Kawano, D. R. Powell, R. K. Hayashi, C. F. Campana, L. F. Dahl, *J. Am. Chem. Soc.* **1999**, *121*, 5945.

15 I. Ciabatti, C. Femoni, M. C. Iapalucci, S. Ruggieri, S. Zacchini, *Coord. Chem. Rev.* **2018**, *355*, 27.

16 S. R. Drake, K. Henrick, B. F. G. Johnson, J. Lewis, M. McPartlin, J. Morris, *J. Chem. Soc., Chem. Commun.* **1986**, 928.

17 V. G. Albano, P. L. Bellon, *J. Organomet. Chem.* **1969**, *19*, 405.

18 C. Femoni, M. C. Iapalucci, S. Ruggieri, S. Zacchini, *Acc. Chem. Res.* **2018**, *51*, 2748.

19 A. J. Whoolery, L. F. Dahl, *J. Am. Chem. Soc.* **1991**, *113*, 6683.

20 H. Schmidbaur, A. Schier, *Chem. Soc. Rev.* **2008**, *37*, 1931.

21 S. Martinengo, A. Fumagalli, R. Bonfichi, G. Ciani, A. Sironi, *Chem. Commun.* **1982**, 825.

22 A. Fumagalli, T. F. Koetzle, F. Takusagawa, P. Chini, S. Martinengo, B. T. Heaton, *J. Am. Chem. Soc.* **1980**, *102*, 1740.

23 S. Martinengo, A. Fumagalli, P. Chini, V. G. Albano, G. Ciani, *J. Organomet. Chem*. **1976**, *116*, 333.

24 C. Allevi, B. T. Heaton, C. Seregni, L. Strona, R. J. Goodfellow, P. Chini, S. Martinengo, *J. Chem. Soc., Dalton Trans.* **1986**, 1375.

25 S. Martinengo, G. Ciani, A. Sironi, *J. Am. Chem. Soc.* **1980**, *192*, 7564.

26 J. L. Vidal, R. C. Schoening, J. M. Troup, *Inorg. Chem*. **1981**, *20*, 227.

27 D. Collini, F. Fabrizi De Biani, D. S. Dolzhnikov, C. Femoni, M. C. Iapalucci, G. Longoni, C. Tiozzo, S. Zacchini, P. Zanello, *Inorg. Chem.* **2011**, *50*, 2790.

CHAPTER VII

Preliminary Biological Activity of some Rh Carbonyl Clusters

High nuclearity clusters are potentially interesting as anticancer agents as their large size could enable them to selectively accumulate in tumours. [1] There is also interest in CO-releasing compounds and therefore both the metal atoms and the CO ligands could potentially exert relevant biological effects. [2] Several studies on low nuclearity carbonyl clusters, mainly focused on Os [3, 4, 5, 6] and Ru [7] compounds, illustrate their potential as anticancer compounds. To the best of our knowledge, no such studies had been performed on Rh clusters before.

During my period at Ecole Polytechnique Fédérale de Lausanne (EPFL), under the supervision of Professor Paul J. Dyson, I had the possibility of testing some of our Rh cluster compounds against the human ovarian cancer cell line (A2780), its cisplatin-resistant strain (A2780cisR) and non-tumorigenic human embryonic kidney cells (HEK-293).

Cancer cells were grown in RPMI-1640 GlutaMax medium supplemented with 10% fetal bovine serum (FBS) and 1% penicillin/ streptomycin (p/s) at 37°C and 5% CO_2. HEK-293 cells were grown in DMEM medium, with 10% FBS and 1% p/s at 37°C and 5% CO_2. Cytotoxicity was determined using the MTT assay (MTT = 3-(4,5-dimethyl-2-thiazolyl)-2,5-diphenyl-2H-tetrazolium bromide).

Cells were seeded in 96–well plates with 100 μL of cell solution per well and pre-incubated for 24 hours in medium supplemented with 10% FBS and 1% p/s. Cluster compounds were prepared as DMSO (dimethyl sulfoxide) solution, then dissolved in the culture medium and serially diluted to the appropriate concentration to give a final DMSO concentration of 0.5%. Subsequently, 100 μL of the solution were added to each well and the plates incubated for further 72 hours. MTT (20 μL of 5 mg/mL in phosphate-buffered saline (PBS)) was then

added to each well and the plates incubated for a further 3 hours. The culture medium was aspirated, and the purple formazan crystals formed by the mitochondrial dehydrogenase activity of vital cells were dissolved in DMSO. The optical density, directly proportional to the number of surviving cells, was quantified at 590 nm using a multi-well plate reader (Spectramax M5e, Molecular Devices) and the fraction of surviving cells was calculated from the absorbance of untreated control cells. Evaluation was based on three independent experiments, each comprising four microcultures per concentration level.
All the data about these tests have been reported in Table 7.1.

Compounds	**IC_{50} (A2780) [μM]**	**IC_{50} (A2780cisR) [μM]**	**IC_{50} (HEK-293) [μM]**
$[Rh_4(CO)_{12}]$	30.8 ± 2.9	10.8 ± 1	38.2 ± 0.9
$[Rh_{12}Bi(CO)_{27}]^{3-}$	>200	>200	>200
$[Rh_{12}Sb(CO)_{27}]^{3-}$	43.8 ± 1	44.3 ± 2	NR
$[Rh_{12}Sb(CO)_{24}]^{4-}$	NR	NR	NR
$[Rh_{21}Sb_2(CO)_{38+x}]^{5-}$	87.8 ± 5.9	NR	NR
$[Rh_{13}Ge(CO)_{25}]^{3-}$	14.1 ± 0.7	8.8 ± 0.6	13.5 ± 0.8
$[Rh_{14}Ge_2(CO)_{30}]^{2-}$	16.5 ± 1	13.7 ± 0.4	9.1 ± 0.9
Cisplatin Ref.	1.9 ± 0.7	23 ± 3	6.4 ± 0.7

Table 7.1. IC_{50} values of Rh clusters on A2780, A2780cisR and HEK-293 cells after 72 hours. NR = Not reproducible.

The only homometallic Rh cluster I tested is the neutral $Rh_4(CO)_{12}$, which showed interesting results and also a certain selectivity on cancer cells. Indeed, it presents a lower IC_{50} value against the A2780cisR cells than against the healthy ones (10.8 ± 1 vs. 38.2 ± 0.9 μM).
Subsequently, I tested some of the clusters belonging to three of the heterometallic systems that we investigated over these years: Rh-Bi, Rh-Sb and Rh-Ge. It was interesting to see how each system behaved differently from the others.
In the case of Rh-Bi system, the only cluster I tested was the icosahedral $[Rh_{12}Bi(CO)_{27}][NEt_4]_3$ because of its high yield. However, the cluster is not active

at all, since it has showed too high IC_{50} values against all the three cell lines (>200 μM). In the case of the Rh-Sb system, the selected species were $[Rh_{12}Sb(CO)_{27}][NEt_4]_3$, $[Rh_{12}Sb(CO)_{24}][NEt_4]_4$, and $[Rh_{21}Sb_2(CO)_{38+x}][NEt_4]_5$, because they were readily available.

However, they did not give reproducible results, probably owing to their incomplete solubility and partial decomposition in the media.

Conversely, the most interesting results were obtained by studying the cytotoxicity of two Rh-Ge clusters, namely $[Rh_{13}Ge(CO)_{25}][NEt_4]_3$ and $[Rh_{14}Ge_2(CO)_{30}][NEt_4]_2$, which could be obtained in high yields. These compounds displayed reasonably low and reproducible IC_{50} values. In the A2780 cell line the two species essentially displayed the same IC_{50} values (14.1 ± 0.7 and 16.5 ± 1.0 μM, respectively). However, the former resulted to be slightly more cytotoxic than the latter in the A2780cisR cancer cell line (8.8 ± 0.6 vs. 13.7 ± 0.4 μM). Indeed, the stereochemical analysis of the carbonyl ligands shows that in $[Rh_{13}Ge(CO)_{25}]^{3-}$ the metal core is more exposed to the external environment than in $[Rh_{14}Ge_2(CO)_{30}]^{2-}$, as shown in Figure 7.1.

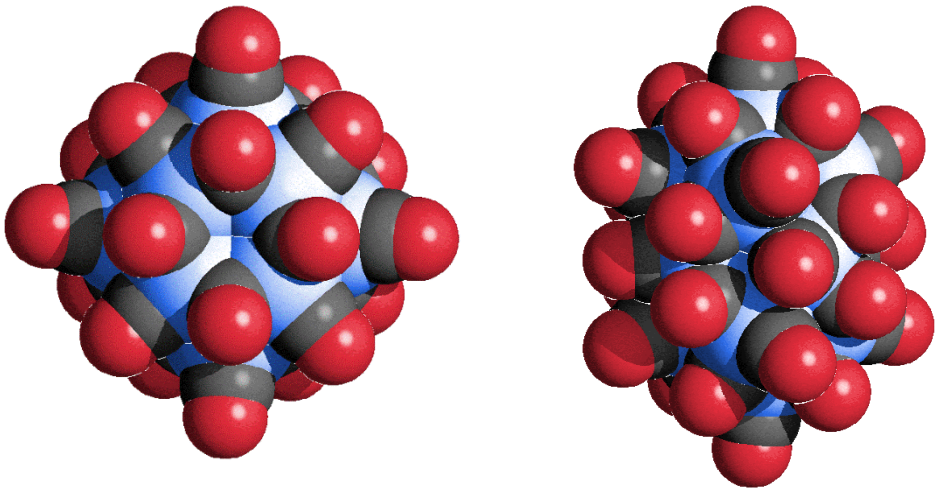

Figure 7.1. Molecular structures of clusters $[Rh_{13}Ge(CO)_{25}]^{3-}$ (left) and $[Rh_{14}Ge_2(CO)_{30}]^{2-}$ (right) in their space-filling views. Rh atoms are depicted in blue, C atoms are in grey, O atoms are in red.

This could make the former more accessible to other ligands and, consequently, more reactive, which is the case regarding the reactivity of these two clusters towards CO (Chapter IV). This difference in reactivity might explain the different cytotoxicity here, although the different charged states of the clusters may also play a role.

The cytotoxicity of the high nuclearity platinum clusters $[Pt_{12}(CO)_{20}(PTA)_4]^{2-}$ and $[Pt_{15}(CO)_{25}(PTA)_5]^{2-}$ had been reported in the same cell lines and the values (6.13 ± 0.7 and 22.3 ± 1.4 μM, respectively) [8] are similar to those reported here for Rh-Ge clusters.

However, the two analysed Rh-Ge clusters did not display any apparent cancer cell selectivity, showing similar IC_{50} values in non-tumorigenic human embryonic kidney cells even if $[Rh_{13}Ge(CO)_{25}]^{3-}$ showed a slightly higher cytotoxicity against cancer cells pretreated with cisplatin than against the healthy cells.

1 K. V. Kong, W. K. Leong, L. H. K. Lim, *J. Organomet. Chem.* **2009**, *694*, 834.

2 A. Arrais, E. Gabano, M. Ravera, D. Osella, *Inorg. Chim. Acta* **2018**, *470*, 3.

3 H. Z. S. Lee, W. K. Leong, S. Top, A. Vessières, *ChemMedChem* **2014**, *9*, 1453.

4 A. A. Nazarov, Y. N. Nosova, O. V. Mikhalev, O. N. Kovaleva, P. J. Dyson, E. R. Milaeva, *Russ. Chem. Bull., Int. Ed.* **2016**, *65*, 546.

5 E. Rosenberg, F. Spada, K. Sugden, B. Martin, R. Gobetto, L. Milone, A. Viale, *J. Organomet. Chem.* **2004**, *689*, 4729.

6 D. Colangelo, A. Ghiglia, A. Ghezzi, M. Ravera, E. Rosenberg, F. Spada, D. Osella, *J. Inorg. Biochem.* **2005**, *99*, 505.

7 A. A. Nazarov, M. Baquié, P. Nowak-Sliwinska, O. Zava, J. R. van Beijum, M. Groessl, D. M. Chisolm, Z. Ahmadi, J. S. McIndoe, A. W. Griffioen, H. van den Bergh, P. J. Dyson, *Sci. Rep.* **2013**, *3*, 1485.

8 L. K. Batchelor, B. Berti, C. Cesari, I. Ciabatti, P. J. Dyson, C. Femoni, M. C. Iapalucci, M. Mor, S. Ruggieri, S. Zacchini, *Dalton Trans.* **2018**, *47,* 4467.

CHAPTER VIII

$Rh_4(CO)_{12}$ in Steam Reforming Process

In the last period of my Ph.D. we started a collaboration with another research group of our Department specialized in catalysis, managed by Prof. Basile. We tested some of our Rh cluster compounds as catalysts in the steam reforming process (SR) carried out at low temperature. The synthesis and tests were carried out together with Andrea Fasolini, a Ph.D. student in the catalysis group.

Notably, the $Rh_4(CO)_{12}$ cluster had been studied almost thirty years ago for catalysing the hydrosilylation of isoprene, cyclohexanone and ciclohexenone [1] or, more recently, the hydroformylation of cyclopentene co-promoted with $HMn(CO)_5$. [2] The neutral Rh cluster, supported on alumina, had also been tested in 2001 in the catalytic partial oxidation (CPO) process. [3]

Steam reforming is a process used for producing hydrogen, carbon monoxide, or other useful products from hydrocarbon fuels. It can be carried out by reacting methane, ethane, methanol, ethanol, acetone or heavier hydrocarbons. [4] The most used reactant is methane because of the high H/C ratio; indeed, carbon is responsible for the coke deposition and consequently, for the deactivation of the catalyst.

The endothermic reaction involved in SR process is shown below in equation (1).

$$CH_4 + H_2O \rightleftharpoons CO + 3H_2 \qquad \Delta H° = +206 \text{ kJ/mol} \qquad (1)$$

The most used catalysts in steam reforming are nickel or rhodium supported on aluminium oxides, magnesium oxides or mixed ones. Nevertheless, these catalysts are easily deactivated because of coke deposition. [5] Coke's formation is related to the decomposition of methane which, after its dissociation on the catalyst's surface,

gives rise to the very reactive C_{alfa} particles, that are able to interact with other carbon atoms thus forming coke. [6]

Usually, the SR is followed by another process able to remove CO and increase the amount of H_2, for instance the slightly exothermic water gas shift (WGS) process, shown in equation (2).

$$CO + H_2O \rightleftharpoons CO_2 + H_2 \qquad \Delta H° = -41.2 \text{ kJ/mol} \qquad (2)$$

Steam reforming in industry is normally carried out at 900 °C and 5-25 atm, because of the endothermic nature of the reaction. However, in the process investigated in this work, the reaction temperature was decreased down to 400-500°C. In fact, the final aim is to run the SR reaction inside a Pd-based membrane, which is able to selectively separate H_2 from the gas mixture and, therefore, increase the methane conversion by shifting the equilibrium towards the product formation. A partial pressure of H_2 greater than 1 atm is highly desirable, as this favours the hydrogen release through the membrane outside the reactor.

There are many membranes based on nickel or platinum, but they do not show the same performances as the Pd ones. [7] However, the Pd membrane needs to work at temperatures lower than 600°C due to hydrogen desorption.

In the reaction conditions palladium can lose flexibility over time. This phenomenon is known as hydrogen embrittlement, and it may cause the rupture of the membrane. This problem may be overcome by doping the membrane with other metals, such as Ag, Cu, Fe, Ni, Pt.

In steam reforming at low temperatures the catalysts play a key role, since in such conditions SR is not favoured and needs a very active catalyst to maximize the methane conversion. Moreover, SR is a process with an increase of entropy, therefore it is not favoured by an increase of pressure.

Ni catalysts are very active and not so expensive, but noble-metal catalysts are also widespread, even if more expensive, because they are very active, less prone to sintering and they produce less coke than the nickel ones. [8]

The best catalyst supports employed in this process are CeO_2, ZrO_2 and their mixed oxides because they are able to store oxygen, possess redox properties that help carbon removal from the surface and good mechanical and thermal resistance. Our collaboration with the catalysis research group was born with the aim of finding an active Rh catalyst in the SR process at lower temperatures than 500 °C. Since the neutral $Rh_4(CO)_{12}$ cluster had been previously tested by Basini et al., we decided to start our investigation from this carbonyl species.

The first support we evaluated was the mixed $Ce_{0.5}Zr_{0.5}O_2$ oxide (CZOm750, prepared through phase-inverted water-in-oil microemulsion), which has the advantage of accumulate oxygen when it is in excess in relation to the fuel, and release it when there is an excess of fuel; [9] in addition it had proved to perform better than a more classical Ce-Zr oxide support. [10] Thanks to this property, the catalyst is more resistant to the deactivation caused by coke, because the oxygen released by the support reacts with it to give CO and CO_2.

As for the active phase, we compared two Rh-precursor compounds, $Rh(NO_3)_3$ and the neutral $Rh_4(CO)_{12}$ cluster, in order to find the best conditions to carry out the process and the best catalyst in such conditions. The former species was impregnated on the support according to the incipient wetness impregnation (IWI) technique, where the volume of the solution containing the Rh precursor is equal to the total volume of the pores on the support. Conversely, the cluster compound was deposited on the support by reacting an hexane solution of $Rh_4(CO)_{12}$ with a slurry of $Ce_{0.5}Zr_{0.5}O_2$ in the same solvent, under CO atmosphere.

Both catalysts were pelleted and treated under N_2 at 500 °C, cooled down at 200 °C and then heated again at 500 °C under H_2 at 10% for one night. At this point we tested the two different Rh catalysts in the SR process by varying temperature, pressure, steam-to-carbon ratio (S/C) and gas hourly space velocity (GHSV), but keeping the same Rh concentration in both, namely 0.6% (w/w) in rhodium (Table 8.1).

Every three experiments a reference test at GHSV = 30000 h^{-1}, P = 1 atm and S/C = 1.5 was carried out in order to evaluate the deactivation of the catalyst. The

conversion of the methane was the parameter considered to evaluate the catalytic activity and was compared, for each set of experimental conditions, with the conversion calculated at the thermodynamic equilibrium through the CEA-NASA software.

Control parameters	Reaction conditions			
T (°C)	350	400	450	500
P (atm)	1	3	5	10
GHSV (h^{-1})	30000	50000		100000
S/C ratio	1	1.5	2	3

Table 8.1. Experimental conditions employed to test the two Rh catalysts in steam reforming process.

VIII.I. Catalytic tests using $Rh_4(CO)_{12}$ on CZOm750 R500 (0.6%)

1) GHSV = 30000 h^{-1}, P = 1 atm, S/C = 3

We carried out tests at fixed GHSV, P and S/C values but by varying the reaction temperature. As reported below, in all the experiments the methane conversion (X CH_4) was much lower than the equilibrium one (X CH_4 eq). This was probably due to the dilution provided by the high amount of steam. Moreover, a decrease of temperature caused a further decrease of the conversion, according to the reaction thermodynamics.

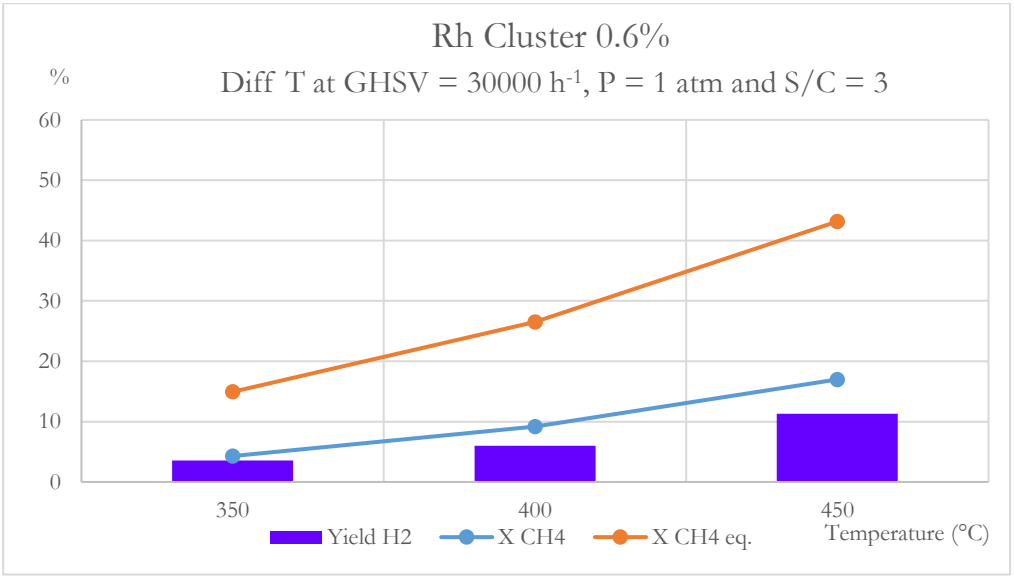

Figure 8.1. Comparison among tests carried out at different T and fixed GHSV, P and S/C values.

Temperature	X CH_4	X CH_4 eq.	Yield H_2	P H_2 out	% H_2 out
350	4.3	10.6	3.5	0.04	4.3
400	9.2	17.3	6.0	0.08	7.8
450	17.0	26.2	11.3	0.14	14.0

Table 8.2. Comparison among tests carried out at different T and fixed GHSV, P and S/C values.

2) GHSV = 30000 h^{-1}, P = 1 atm, T = 500 °C

This set of experiments was carried out at different S/C ratios. In these conditions the methane conversion was close to the one at the equilibrium and, as expected, it increased with S/C. However, for higher S/C the conversion was much lower than the equilibrium one, highlighting the kinetic limit in these conditions. It is interesting to note that for S/C = 1.5, the conversion was almost at the thermodynamic equilibrium.

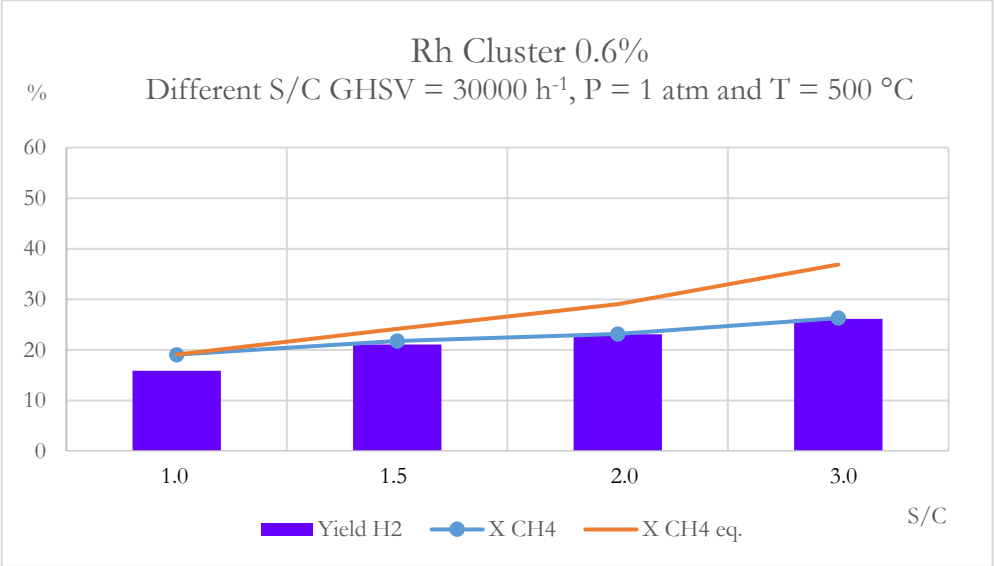

Figure 8.2. Comparison among tests carried out at different S/C and fixed GHSV, P and T.

S/C	X CH_4	X CH_4 eq.	Yield H_2	P H_2 out	% H_2 out
1.0	19.1	19.1	15.9	0.27	27.3
1.5	21.8	24.2	21.1	0.26	26.3
2.0	23.2	29.0	23.1	0.26	26.4
3.0	26.3	36.9	26.2	0.26	25.8

Table 8.3. Comparison among tests carried out at different S/C and fixed GHSV, P and T values.

3) S/C = 2, P = 1 atm, T = 500 °C

In these conditions, when GHSV increased the contact time decreased, so the methane conversion and the hydrogen yield decreased in turn. This is because at a minor contact time the reaction is under a kinetic control and has no time to reach the equilibrium. Therefore, a higher GHSV than 30000 h^{-1} is not recommended.

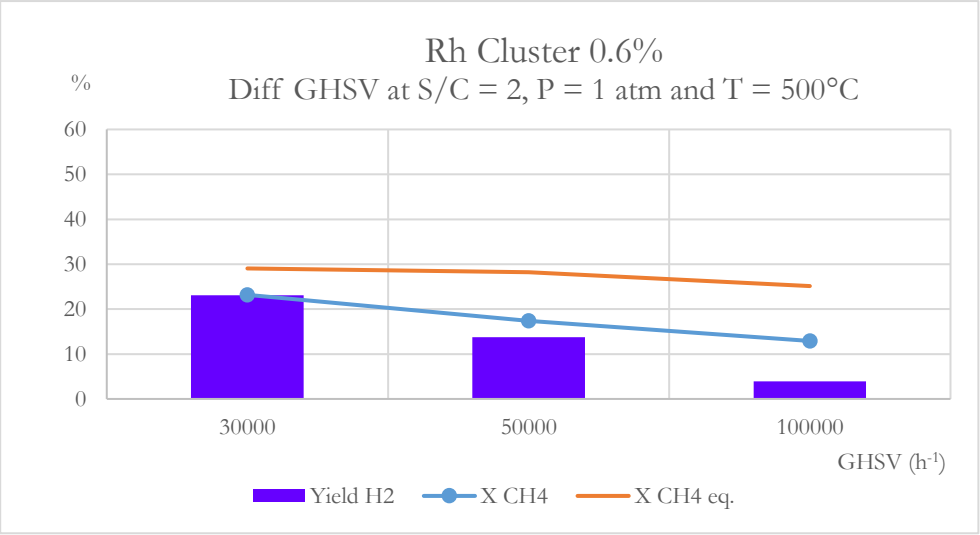

Figure 8.3. Comparison among tests carried out at different GHSV and fixed S/C, P and T values.

GHSV	X CH_4	X CH_4 eq.	Yield H_2	P H_2 out	% H_2 out
30000.0	23.2	29.0	23.1	0.26	26.4
50000.0	17.4	28.2	13.7	0.18	18.0
100000.0	12.9	25.1	3.9	0.07	7.0

Table 8.4. Comparison among tests carried out at different GHSV and fixed S/C, P and T.

4) GHSV = 30000 h^{-1}, S/C = 2, T = 500 °C

These tests indicated that, as expected, an increase of pressure led to minor methane conversions, because the SR is a process leading to an increase of moles. However, the best result in terms of reaching the equilibrium value and the higher H_2 partial pressure was recorded at a total pressure of 10 atm.

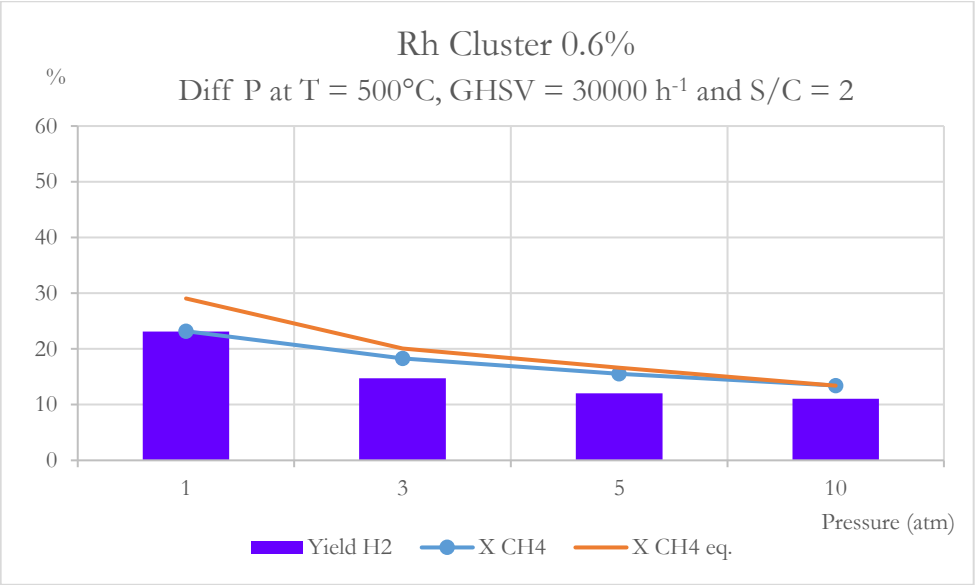

Figure 8.4. Comparison among tests carried out at different P and fixed S/C, GHSV and T values.

P	X CH_4	X CH_4 eq.	Yield H_2	P H_2 out	% H_2 out
1.0	23.1	29.0	23.0	0.26	26.4
3.0	18.2	20.0	14.7	0.57	18.9
5.0	15.5	16.6	12.0	0.82	16.3
10.0	13.4	13.4	11.0	1.62	16.2

Table 8.5. Comparison among tests carried out at different P and fixed S/C, GHSV and T values.

5) GHSV = 30000 h^{-1}, P = 10 atm, T = 500°C

Once determined the best pressure value, the aim was to find the highest value of hydrogen partial pressure by varying the S/C ratio at 500 °C. In the previous tests at 500 °C and S/C = 2, the partial pressure was 1.62 atm. Actually, the methane conversion increases with S/C and the partial pressure depends on the total pressure in the reactor. The best value recorded in these experiments was with S/C = 1, with a partial pressure of 2.2 atm. This result can be explained by the minor dilution of gas with lower S/C.

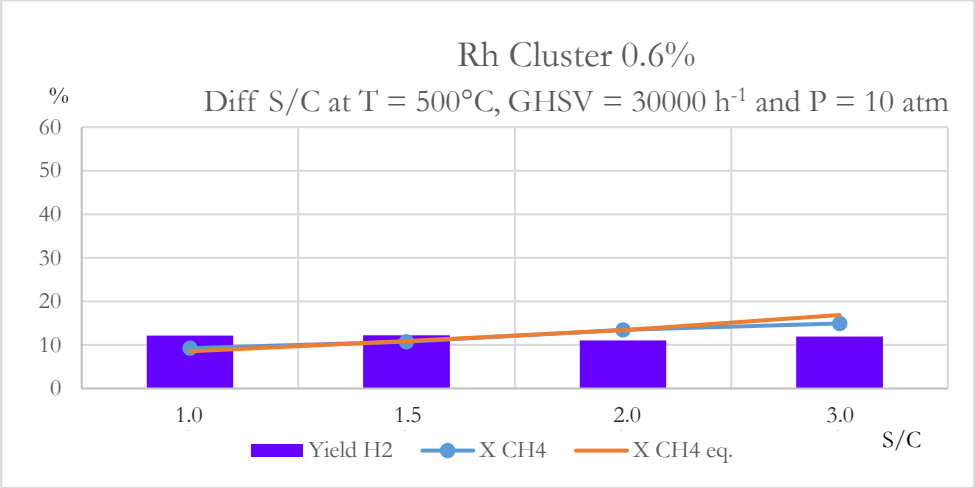

Figure 8.5. Comparison among tests carried out at different S/C and fixed GHSV, P and T values.

S/C	X CH_4	X CH_4 eq.	Yield H_2	P H_2 out	% H_2 out
1.0	8.2	8.5	12.1	2.20	22.0
1.5	10.7	10.9	12.2	1.77	17.7
2.0	13.4	13.4	11.0	1.62	16.2
3.0	14.9	16.8	11.9	1.53	15.4

Table 8.6. Comparison among tests carried out at different S/C and fixed GHSV, P and T values.

6) GHSV = 30000 h^{-1}, P = 10 atm, T = 450 °C

We repeated the same set of experiments but with a lower temperature. With an increase of S/C there was a slight increase of the conversion. The most interesting data was the partial pressure of hydrogen (1.72 atm) when S/C = 1, which could ensure a good separation of H_2 through the membrane.

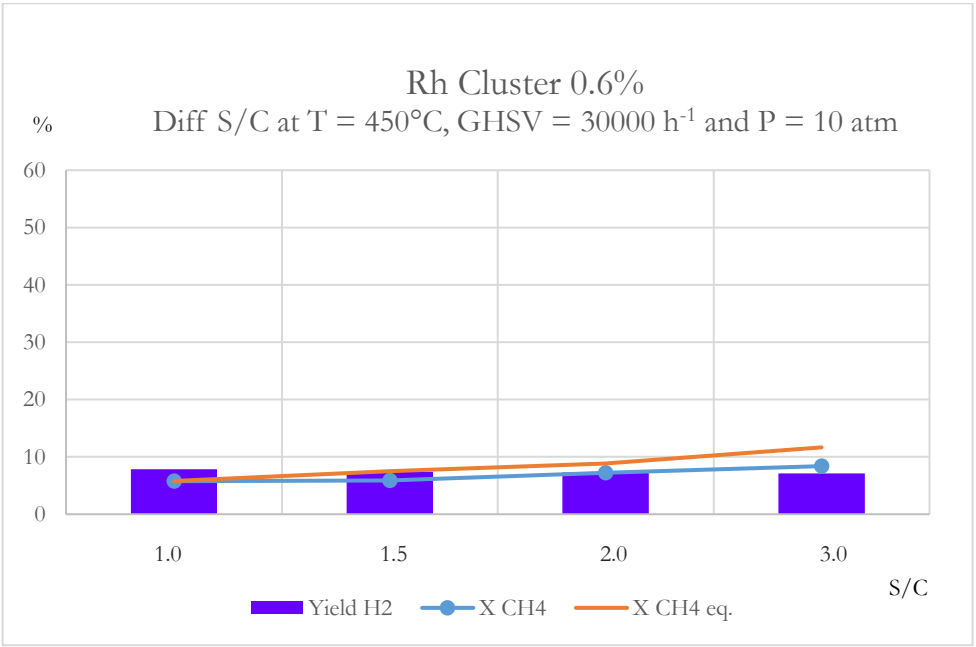

Figure 8.6. Comparison among tests carried out at different S/C and fixed GHSV, P and T values.

S/C	X CH_4	X CH_4 eq.	Yield H_2	P H_2 out	% H_2 out
1.0	5.7	5.8	7.9	1.72	17.2
1.5	5.9	7.5	7.4	1.04	10.4
2.0	7.2	8.8	7.3	0.91	9.1
3.0	8.4	11.6	7.1	0.84	8.4

Table 8.7. Comparison among tests carried out at different S/C and fixed GHSV, P and T values.

7) GHSV = 30000 h^{-1}, P = 10 atm, S/C = 1

Once the best GHSV, P and S/C were set, we carried out more experiments by varying the temperature. Considering the maximization of both the methane conversion (according with the equilibrium value in the experimental conditions) and the partial pressure of H_2 (which would allow the best membrane performance), these final tests allowed us to find the best experimental conditions to carry out SR of methane in a membrane reactor with Rh cluster catalyst: T = 450 °C, GHSV = 30000 h^{-1}, P = 10 atm, S/C = 1. In fact, although at 500°C a higher H_2 pressure is developed, working at 450°C would allow for a longer membrane life, which is an important factor to consider.

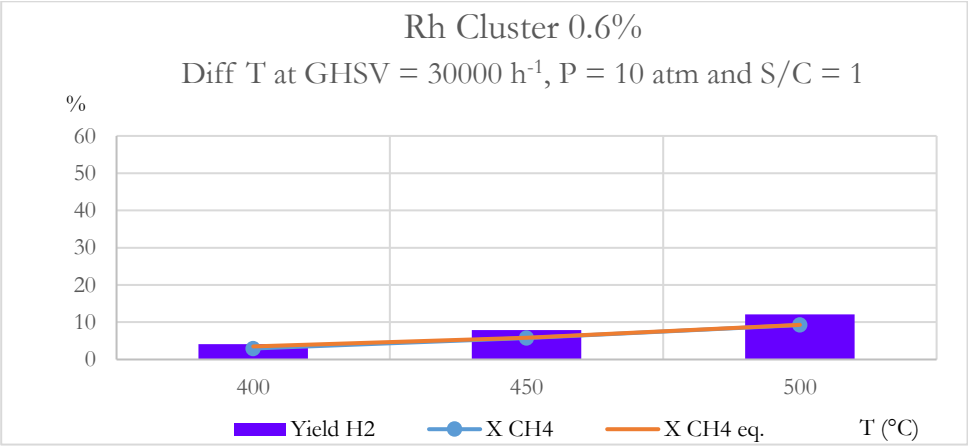

Figure 8.7. Comparison among tests carried out at different T and fixed GHSV, P and S/C values.

T	X CH_4	X CH_4 eq.	Yield H_2	P H_2 out	% H_2 out
400	2.9	3.5	4.2	1.0	10.0
450	5.5	5.8	7.9	1.72	17.2
500	8.0	9.3	12.1	2.20	22.0

Table 8.8. Comparison among tests carried out at different T and fixed GHSV, P and S/C values.

Further tests were carried out to evaluate the possible deactivation of the catalyst.

8) GHSV = 30000 h^{-1}, P = 1 atm, T = 500°C, S/C = 1.5

The monitoring tests to evaluate the catalyst deactivation were carried out at fixed GHSV, P, T and S/C values after every three experiments. An initial test was performed on the new catalyst as a reference. The catalyst did not show a stressed deactivation: all the tests presented a similar conversion, except the last one which had a lower conversion of 1.2 percentage points if compared to the previous test.

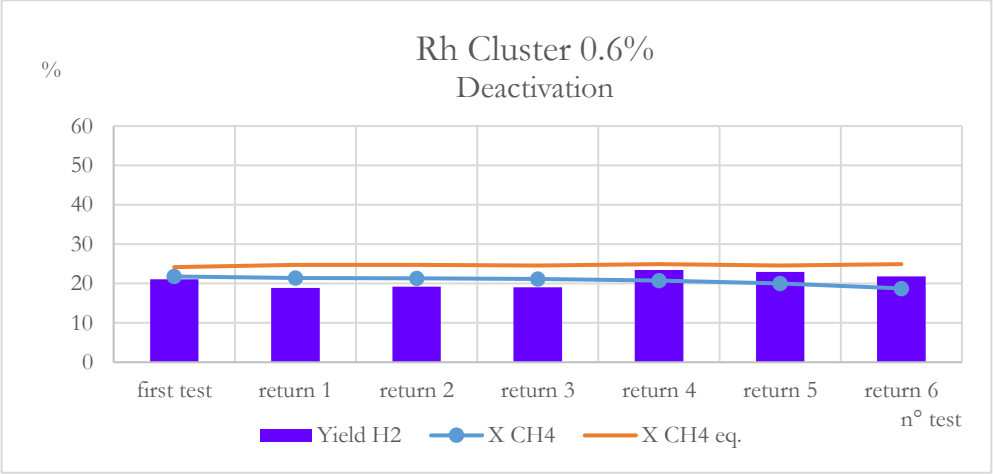

Figure 8.8. Comparison among consecutive tests carried out at fixed GHSV, P, T and S/C values.

Deactivation	X CH_4	X CH_4 eq.	Yield H_2	P H_2 out
First test	21.8	24.2	21.1	0.26
Return 1	21.4	24.7	18.9	0.24
Return 2	21.3	24.7	19.3	0.26
Return 3	21.1	24.6	19.0	0.26
Return 4	20.7	24.9	23.4	0.28
Return 5	20.0	24.6	23.0	0.27
Return 6	18.8	24.9	21.8	0.27

Table 8.9. Comparison among consecutive tests carried out at fixed GHSV, P, T and S/C.

The deactivation could arise from the Boudouard reaction, [11] which causes the coke formation and is particularly favoured at high pressures. This was confirmed by the Raman analysis, which showed the presence of carbon.

The same tests were carried out on Rh 0.6% (w/w) IWI catalyst and the results were almost equal to those shown by Rh cluster at the same concentration, so it was not possible to sustain which catalyst was better since they were both too much active in SR process. Therefore, we decreased the concentration of the two active phases in order to stress the differences between the two catalysts. To do that, we synthesized both catalysts at a concentration of 1% (w/w) and we physically carried out the dilution by mixing them with further support in order to reach a concentration of 0.05% (w/w).

For the reference test, used to evaluate the different activity of the two catalysts, fixed experimental conditions were chosen: GHSV = 30000 h^{-1}, P = 1 atm, T = 500°C, S/C = 1.5. Furthermore, the Rh cluster catalyst was tested in two different conditions: after treatment in H_2 flow (as the previous tests) and not treated.

VIII.II. Catalytic tests using $Rh_4(CO)_{12}$ on CZOm750 R500 (0.05%)

This test was carried out on the catalyst which had been previously treated under N_2 at 500 °C, cooled down at 200 °C and then heated again at 500 °C under H_2 at 10% for one night. The reactivity was 6-hour long and the discontinuities in the graph among the data series are due to the necessary time to cool down the reactor at the end of the day (tests were carried out over many days).

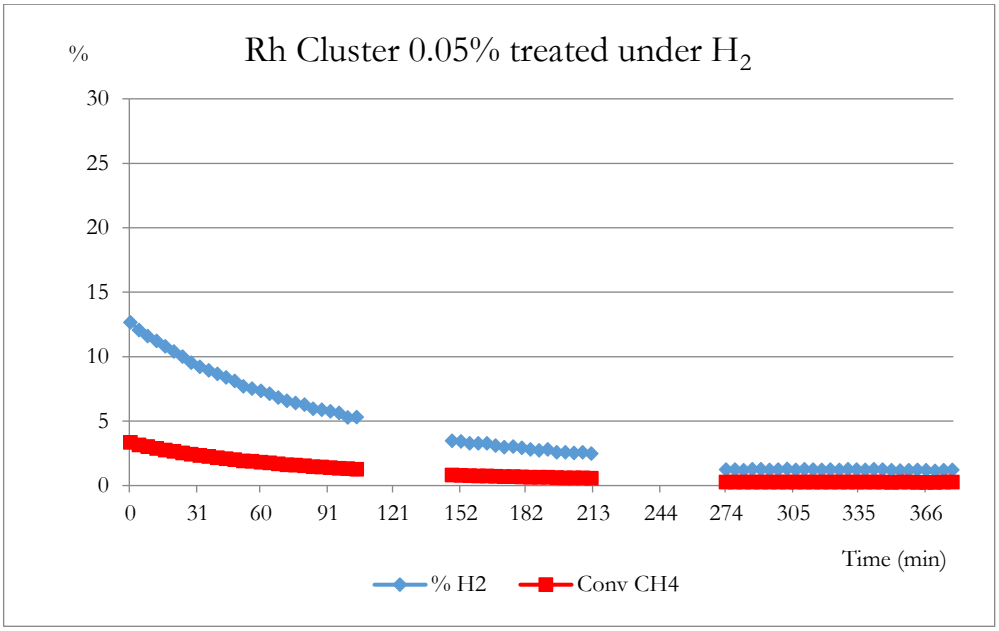

Figure 8.9. Comparison among consecutive tests carried out at fixed GHSV, P, T and S/C.

It is possible to note from the graph the decrease of the methane conversion which was the consequence of the partial deactivation of the catalyst. The conversion became constant after the first 4.5 h. This deactivation could be due to the formation of coke (confirmed by Raman spectroscopic analysis carried out on the spent catalyst) and to the partial sintering of the active phase, actually none of them particularly evident.

VIII.III. Catalytic tests using $Rh_4(CO)_{12}$ on CZOm750 (0.05%)

The same Rh catalyst without previous treatment under H_2 was tested in the SR process to verify whether this would make it active in this reaction.

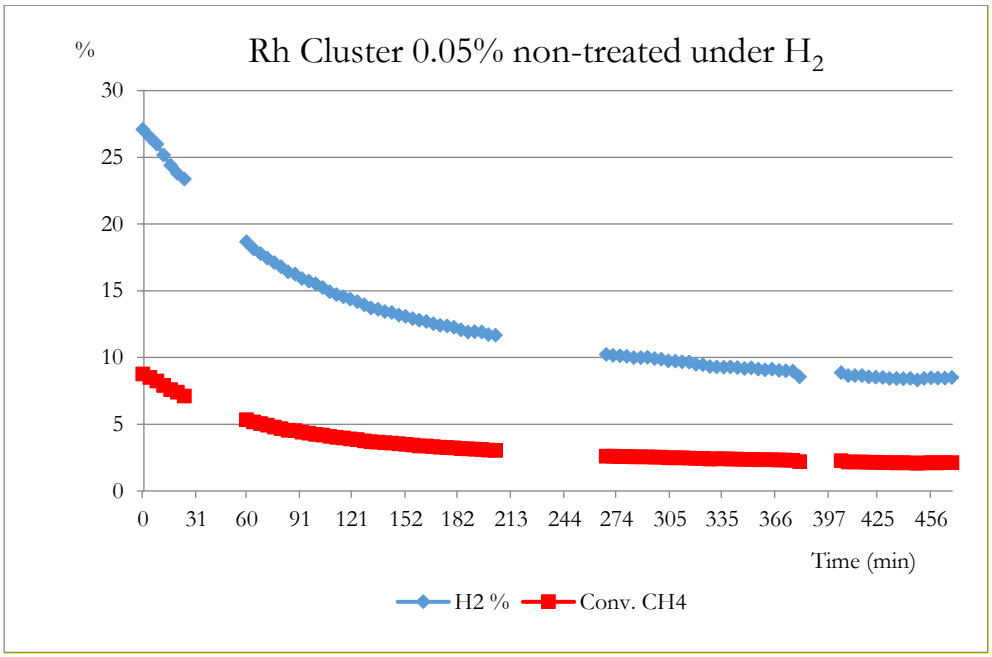

Figure 8.10. Comparison among consecutive tests carried out at fixed GHSV, P, T and S/C.

Like the previous case, there was an immediate decrease of the methane conversion. The deactivation could be partially due to the coke formation, but also to the sintering process related to the major mobility of the system on Ce/Zr oxide. Nevertheless, the starting conversion was nearly twice as high as the one observed for the cluster previously treated under H_2. The different active phase could have influenced the starting conversion: indeed, in the cluster previously treated under H_2 the active phase could contain metallic rhodium, while in the non-treated one the active phase was probably only represented by rhodium carbonyl.

These two tests have been then compared with that carried out on Rh IWI catalyst in the same experimental conditions about T, GHSV, P and S/C.

VIII.IV. Catalytic tests using Rh IWI on CZOm750 (0.05%)

Rh IWI catalyst was previously reduced under hydrogen to allow its activation.

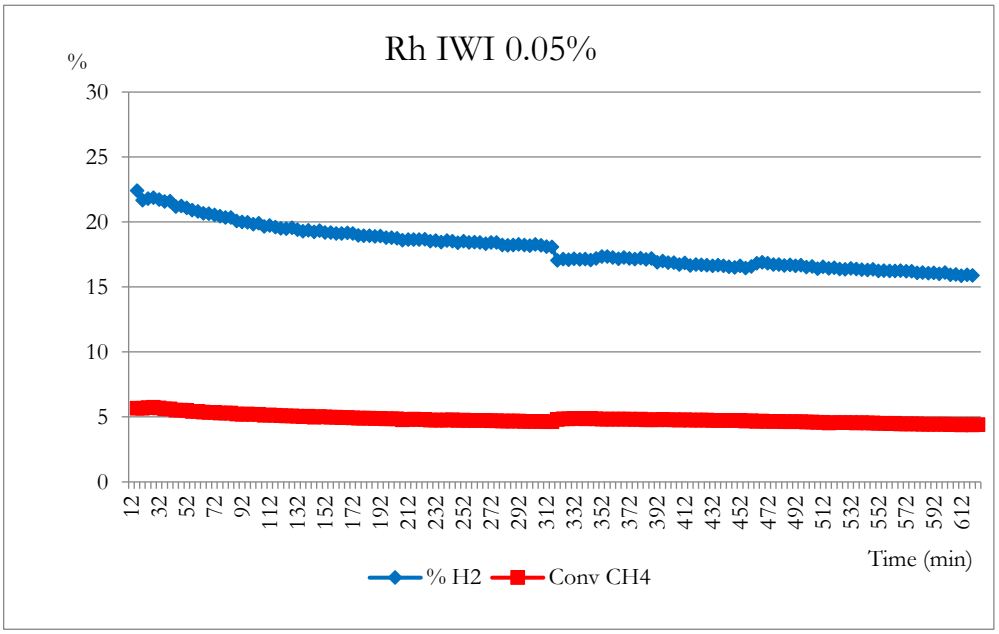

Figure 8.11. Comparison among consecutive tests carried out at fixed GHSV, P, T and S/C.

The Rh IWI catalyst showed a minor starting conversion than the non-treated Rh cluster catalyst, but it seemed to be stable and did not undergo any significant deactivation.

VIII.V. Comparison between Rh cluster 0.05% on ZOm750 and Rh IWI 0.05% on ZOm750

At this point, another support was investigated instead of $Ce_{0.5}Zr_{0.5}O_2$, namely ZrO_2 (ZOm750) to evaluate how the lack of CeO_2 in the structure could affect the results. Indeed, the mobile oxygen in ceria could create a certain instability in the cluster catalyst, where the metal is likely to be bonded through oxygen atoms.

In these last tests, the catalytic activities of both the non-treated Rh cluster and the reduced Rh IWI, supported on ZrO_2 were evaluated in the same experimental conditions used in the previous tests (GHSV = 30000 h^{-1}, P = 1 atm, T = 500 °C, S/C = 1.5) and at a concentration of 0.05% (w/w).

VIII.VI. Catalytic tests using $Rh_4(CO)_{12}$ cluster on ZOm750

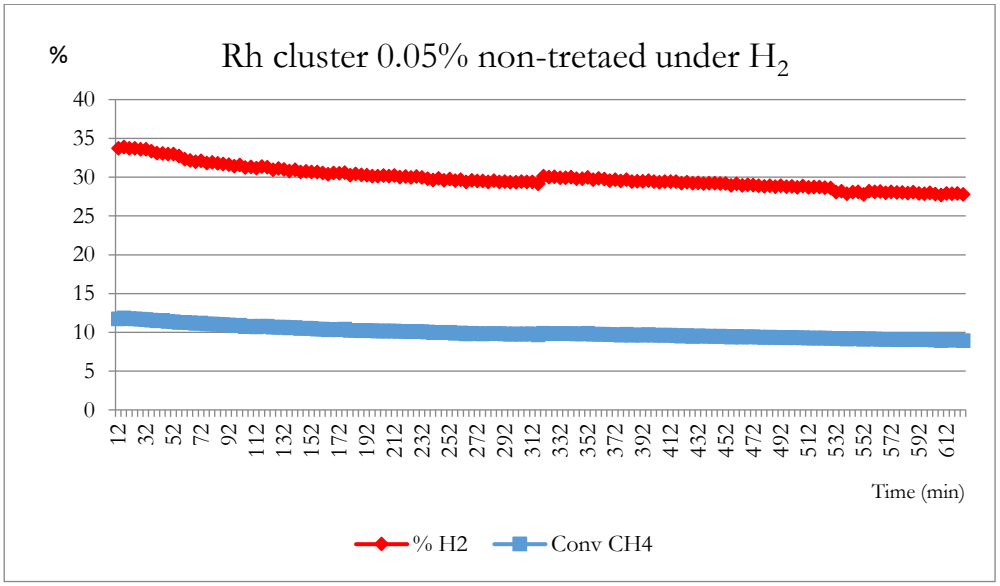

Figure 8.12. Comparison among consecutive tests carried out at fixed GHSV, P, T and S/C values.

From the graph it is evident that the hydrogen percentage product was much higher than the one obtained in the other tests at the same Rh concentration but on a different support. Furthermore, it is interesting to note how the Rh cluster catalyst did not rapidly deactivate in these conditions. The starting conversion was around 12% and after 10 h it reached a value of 9.5%. This result can be related to the major diameter of the pores on ZrO_2, which probably allowed a higher dispersion of the active phase.

VIII.VII. Catalytic tests using Rh IWI on ZOm750 R 500

Similarly to what happened with the cluster, with the Rh IWI catalyst the hydrogen percentage remained rather steady and high throughout the whole duration of the experiment (about 10 hours). The starting methane conversion was slightly lower than the one of the Rh cluster catalyst (10.9% vs 12%) but the deactivation equally seemed to be extremely slow.

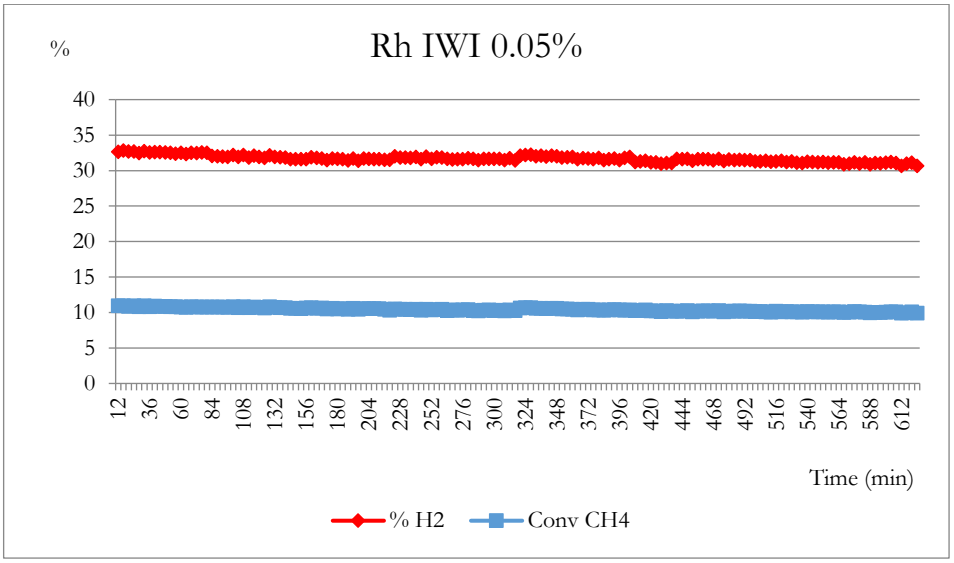

Figure 8.13. Comparison among consecutive tests carried out at fixed GHSV, P, T and S/C values.

In conclusion, we compared different Rh catalysts in order to evaluate which one could be the best in a SR process at low temperature and in which experimental conditions. The $Rh_4(CO)_{12}$ cluster supported on $Ce_{0.5}Zr_{0.5}O_2$ was less sensitive when not previously treated under H_2, but the best results were obtained with the Rh IWI active phase. Nevertheless, the results on the non-treated Rh cluster and the Rh IWI were comparable when the exploited support was ZrO_2. Indeed, in these conditions the deactivation of both catalysts was not relevant, but the starting methane conversion was higher when the Rh cluster catalyst was employed.

1 I. Ojima, R. J. Donovan, N. Clos, *Organometallics* **1991**, *10*, 2606.

2 C. Li, E. Widjaja, M. Garland, *Organometallics* **2004**, *23*, 4131.

3 J.-D. Grunwaldt, L. Basini, B. S. Clausen, *J. Catal.* **2001**, *200*, 321.

4 T. L. LeValley, A. R. Richard, M. Fan, *Int. J. Hydrog. Energy* **2014**, *39*, 16983.

5 S. D. Angeli and others, *Int. J. Hydrog. Energy* **2014**, *39.5*, 1979.

6 D. L. Trimm et al., *Catalysis Today* **1997**, *37*, 233.

7 S. Yun, S. T. Oyama, *J. Membr. Sci.* **2011**, *375*, 28.

8 E. Kikuchi, S. Tanaka, Y. Yamazaki, Y. Morita, *Bull. Japan Petrol. Inst.* **1974**, *16*, 95.

9 P. Pantu, G. R. Gavalas, *Applied Catalysis A: General* **2002**, *223*, 253.

10 F. Basile, R. Mafessanti, A. Fasolini, G. Fornasari, E. Lombardi, A. Vaccari, *J. Eur. Ceram. Soc.* **2019**, *39*, 41.

11 J. Hunt, A. Ferrari, A. Lita, M. Crosswhite, B. Ashley, A. E. Stiegman, *J. Phys. Chem. C* **2013**, *117*, 26871.

CHAPTER IX

Conclusions

During my Ph.D. we investigated the chemistry of heterometallic carbonyl rhodium clusters synthesizing several new atomically-precise species, whose sizes place them in the nanometric regime. They have been characterized through single crystal X-ray diffractometry, IR spectroscopy, ESI-MS spectrometry and, in the case of phosphine coordinated compounds, also by $^{31}P\{^{1}H\}$ NMR.

We focused our attention on four different systems: Rh-Bi, Rh-Ge, Rh-Sb and Rh-Au, which have been singularly examined in the previous chapters of this work.

For each analysed system the cluster precursor was the homometallic $[Rh_7(CO)_{16}]^{3-}$, in turn prepared from reduction of $Rh_4(CO)_{12}$ through CO in basic conditions. $[Rh_7(CO)_{16}]^{3-}$ has been so reacted with salts of the target heteroatoms, exploiting the redox condensation method, giving rise to new heterometallic Rh carbonyl nanoclusters. Moreover, in some cases, thanks to a collaboration with the EPFL in Lausanne, we evaluated the cytotoxicity of some of our compounds. Finally, we started a collaboration with another research group in order to test the catalytic role of Rh clusters.

As for the synthetic part, we can conclude that the redox condensation method has been very successful as it allowed us to obtain numerous new compounds. The first three systems analysed in this work (Rh-Bi, Rh-Ge and Rh-Sb) share the coordinatively and electronically saturated icosahedral $[Rh_{12}E(CO)_{27}]^{n-}$ (E = Bi, Ge, Sb), while the Rh-Au system did not show any similarity with the others.

The $[Rh_{12}E(CO)_{27}]^{n-}$ clusters (n = 3 when E = Sb, Bi; n = 4 when E = Ge) (Figure 9.1) present 170 CVEs and are stable under CO atmosphere.

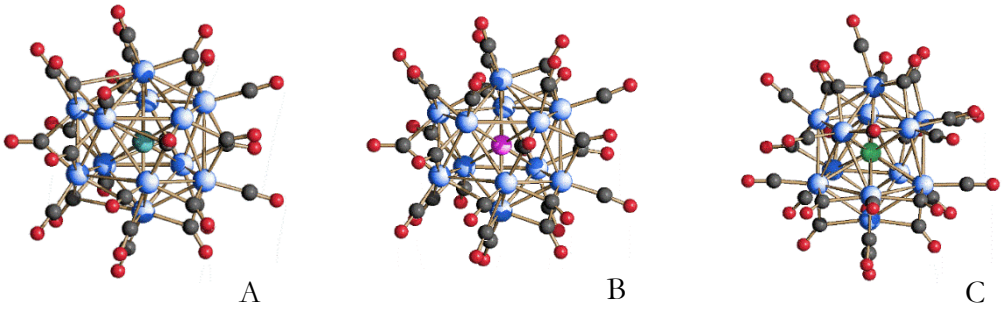

Figure 9.1. Molecular structures of $[Rh_{12}Bi(CO)_{27}]^{3-}$ (A), $[Rh_{12}Ge(CO)_{27}]^{4-}$ (B) and $[Rh_{12}Sb(CO)_{27}]^{3-}$ (C). Rh atoms are depicted in blue, Bi atom is depicted in light blue, Ge atom is depicted in magenta, Sb atom is depicted in green, C atoms are in grey and O atoms are in red.

However, it is sufficient to change the atmosphere from carbon monoxide to nitrogen to observe a very different behaviour of the three species. The most outstanding reaction is given by $[Rh_{12}Ge(CO)_{27}]^{4-}$, which under N_2 reversibly goes to the $[Rh_{13}Ge(CO)_{25}]^{3-}$parent compound (Figure 9.2).

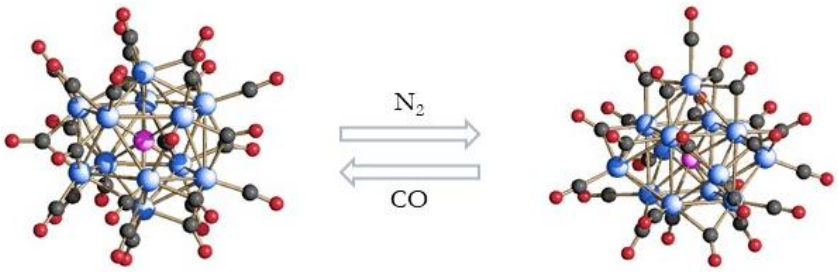

Figure 9.2. Equilibrium between $[Rh_{12}Ge(CO)_{27}]^{4-}$ (left) and $[Rh_{13}Ge(CO)_{25}]^{3-}$ (right) based on different atmospheres.

Instead, the $[Rh_{12}Sb(CO)_{27}]^{3-}$ cluster under N_2 atmosphere keeps its original geometry but spontaneously loses some CO ligands. The obtaining of the coordinatively and electronically unsaturated $[Rh_{12}Sb(CO)_{24}]^{4-}$ cluster, which turns into the $[Rh_{12}Sb(CO)_{27}]^{3-}$ parent compound under CO, indicates a sort of equilibrium between the two clusters driven by the presence/absence of CO

atmosphere (Figure 9.3). It is important to underline that the difference in the negative charge between the two clusters makes the equilibrium more complicated than it appears.

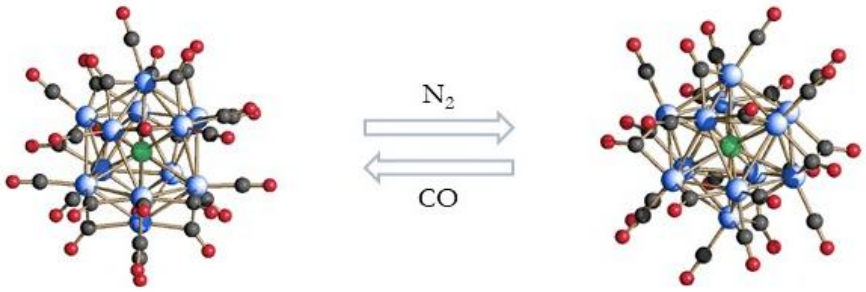

Figure 9.3. Equilibrium between $[Rh_{12}Sb(CO)_{27}]^{3-}$ (left) and $[Rh_{12}Sb(CO)_{24}]^{4-}$ (right) based on different atmospheres.

The only icosahedral cluster stable under nitrogen atmosphere is $[Rh_{12}Bi(CO)_{27}]^{3-}$. It is indeed necessary to heat the solution of this cluster under N_2 to force the loss of some CO ligands, in line with Rh-Sn system (Figure 9.4). Unfortunately, unlike this, it has not been possible to crystallize the supposedly unsaturated icosahedral species, so our conclusions were based on spectroscopic evidences.

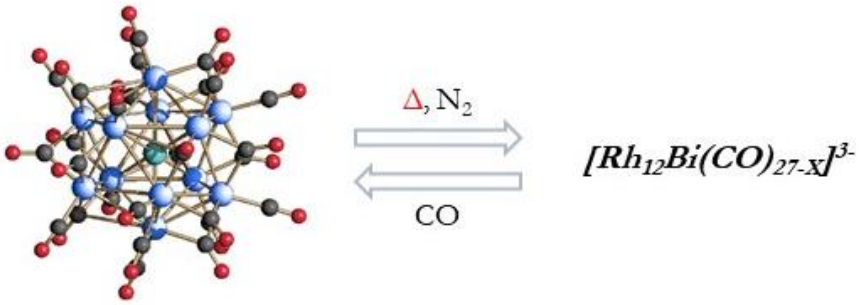

Figure 9.4. Equilibrium between $[Rh_{12}Bi(CO)_{27}]^{3-}$ (left) and $[Rh_{12}Bi(CO)_{27-x}]^{3-}$ (right) based on different atmospheres and through thermal treatment.

To underline the differences among these four Rh-Bi, Rh-Ge, Rh-Sb and Rh-Au systems, we can compare the highest nuclearity species obtained for each one and hosting an interstitial heteroatom. As we can see, despite the fact that we used the same cluster precursor as starting material and exploited the same redox condensation method, by changing the heteroatom and the reaction conditions we obtained clusters of different structure and nuclearity (Figure 9.5).

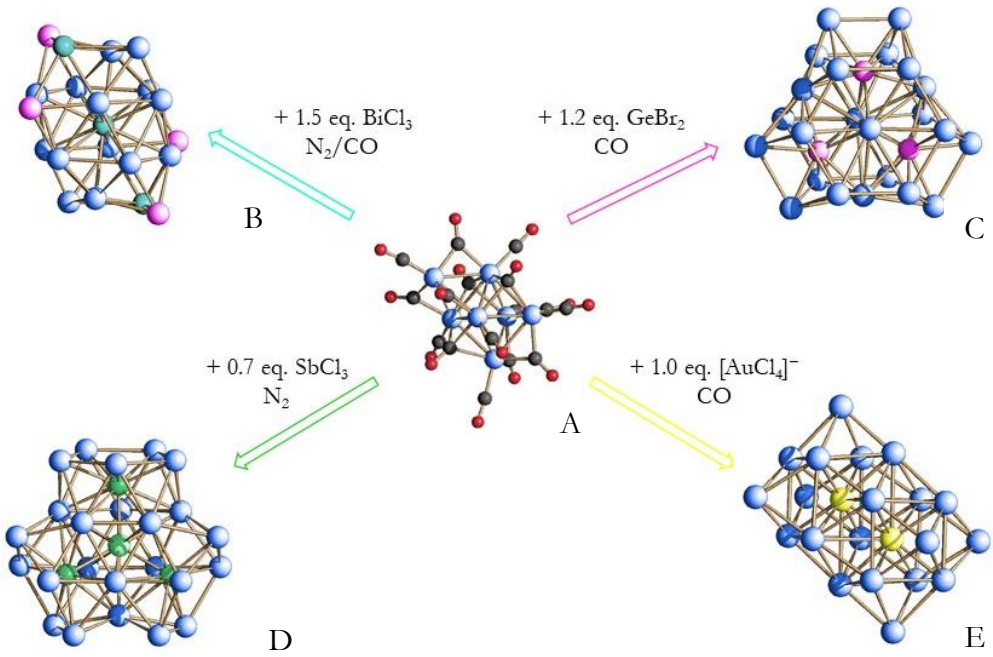

Figure 9.5. Scheme reporting the metal skeletons of the highest nuclearity clusters obtained for each system analysed, starting from $[Rh_7(CO)_{16}]^{3-}$ (A). Metal skeleton of $[Rh_{17}Bi_3(CO)_{33}]^{4-}$ (B), $[Rh_{23}Ge_3(CO)_{41}]^{5-}$ (C), $[Rh_{24}Sb_4(CO)_{44}]^{n-}$ (D) and $[Rh_{20}Au_2(CO)_{42}]^{6-}$ (E).

The $[Rh_{17}Bi_3(CO)_{33}]^{4-}$ and $[Rh_{24}Sb_4(CO)_{44}]^{n-}$ compounds, despite their difference in nuclearity, are both based on the icosahedral metal cage, which is capped in the former case and fused with other icosahedra in the latter. Actually, this is a common feature in all the other compounds belonging to both the Rh-Bi and Rh-Sb systems.

Conversely, $[Rh_{23}Ge_3(CO)_{41}]^{5-}$ is based on a fusion of sphenocorona-like units, which present smaller cavities than the icosahedral one. This different geometry is coherent with the smaller dimensions of germanium atom (compared to Sb or Bi ones), that consequently prefers to be lodged in a smaller rhodium cage, but it is not shared by the other lower-nuclearity Rh-Ge species.

The last species taken into consideration here is $[Rh_{20}Au_2(CO)_{42}]^{6-}$, whose skeleton consists of two interpenetrated capped cubic cages. In this case, the geometry on which the cluster is based on is not representative of the entire system Rh-Au, since the three heterometallic clusters reported in this work are based on very different metal structures.

It is possible to sum up the chemistry of these four systems in a scheme that reports the cluster nuclearity versus the number of salt's equivalents added to the cluster precursor (Figure 9.6). The scheme does illustrate only some key species and not all the compounds discussed in this work; in some cases only the name of the cluster is reported, for sake of clarity.

It is clear that the investigation of these four Rh-Bi, Rh-Ge, Rh-Sb and Rh-Au systems, in either similar and different reaction conditions (such as atmospheres, solvents and stoichiometric ratios) has led to very different cluster compounds.

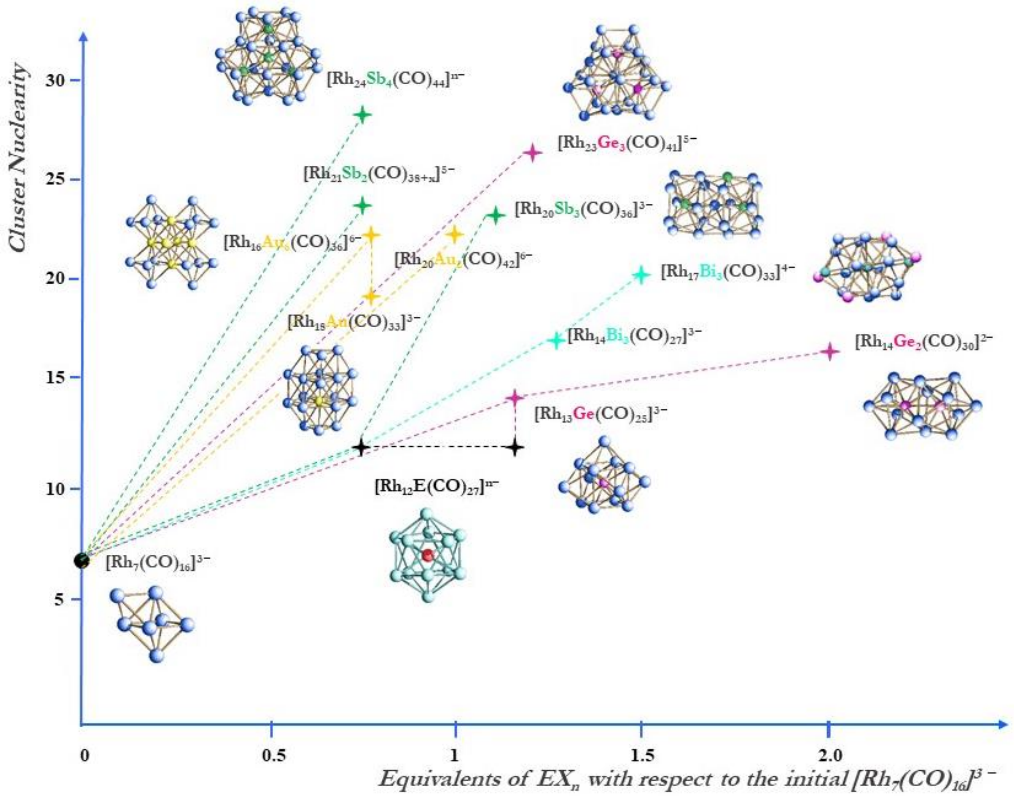

Figure 9.6. Scheme summing up the chemistry of the four systems analysed in this work. Growing of some heterometallic Rh carbonyl clusters *vs* added equivalents of EX_n with respect to the initial $[Rh_7(CO)_{16}]^{3-}$. Rh-Bi clusters and Bi atoms are indicated with a light blue mark, Rh-Sb clusters and Sb atoms in green, Rh-Ge clusters and Ge atoms in magenta, Rh-Au clusters and Au atoms in yellow.

In order to expand the heterometallic Rh clusters family it could be interesting to investigate the reactivity of the $[Rh_7(CO)_{16}][NEt_4]_3$ precursor with silicon derivatives, beyond other post-transition elements. As matter of fact, the unique metal cluster species containing Si known to date is $[Co_9Si(CO)_{21}]^{2-}$, which was obtained by reacting μ_4-$Si[Co_2(CO)_7]_2$ with an excess of $[Co(CO)_4]^-$ in CH_2Cl_2 at 40 °C. [1] This last Co-Si species was obtained in turn by reacting SiH_4 with $Co_2(CO)_8$ in hexane. [2]

Besides the synthesis, the reactivity and the characterization of these new heterometallic cluster compounds, during my Ph.D. we also evaluated their possible role as cytotoxic agents against three different cell lines: A2780, A2780cisR and HEK-293. Also in this case, as shown in Chapter VII, compounds belonging to different systems behaved differently. Indeed, the analyzed Rh-Bi clusters did not show any cytotoxicity, while the Rh-Sb species did not present reproducible IC_{50} values The best results were registered for Rh-Ge clusters, which not only showed low IC_{50} values, but in the case of the $[Rh_{13}Ge(CO)_{25}]^{3-}$ cluster, also a slightly higher cytotoxicity against cancer cells pretreated with cisplatin than against the healthy cells.

In the future it could be interesting to analyze the possible CO release of these heterometallic Rh clusters, in particular by preparing Rh-based photothermal nanomodulator CORMs for medical treatments. [3] Moreover, it could be taken into consideration the possibility of testing these compounds as biomarker sensors, for instance by adsorbing them onto monolayer graphene. [4]

In the end, we started a collaboration with a catalysis group of our department with the aim of testing our heterometallic clusters as active phases in new catalysts. The first tests were carried out to compare the activity of the neutral $Rh_4(CO)_{12}$ (previously tested in other reactions) with the one of a conventional Rh IWI catalyst in the steam reforming of methane at low temperature. $Rh_4(CO)_{12}$ was firstly deposited on $Ce_{0.5}Zr_{0.5}O_2$ and later just on ZrO_2. On the first support the cluster was less sensitive to deactivation if not treated with H_2, but the best results were overall obtained with the Rh IWI catalyst. On the contrary, by changing support into ZrO_2 the $Rh_4(CO)_{12}$ not treated with H_2 and the Rh IWI presented comparable results, including a non-relevant deactivation. Moreover, in these conditions the starting methane conversion was higher by exploiting the Rh cluster catalyst.

1 K. M. Mackay, B. K. Nicholson, W. T. Robinson, A. W. Sims, *Chem. Commun.* **1984**, 1276.

2 K. M. Mackay, C. C. Tan, *J. Chem. Res.* **1982**, *229*, 2301.

3 M. J. Tan, H.-C. Pan, H. R. Tan, J. W. Chai, Q. F. Lim, T. I. Wong, X. Zhou, Z.-Y. Hong, L.-D. Liao, K. V. Kong, *Adv. Healthc. Mater.* **2018**, *7*, 1701113.

4 D. Lin, C.-Y. Tseng, Q. F. Lim, M. J. Tan, K. V. Kong, *J. Mater. Chem. B* **2018**, 2536.

CHAPTER X

Experimental Section

All reactions and sample manipulations were carried out using standard Schlenk techniques under nitrogen, carbon monoxide or hydrogen atmospheres.

IR spectra were recorded on a Perkin Elmer SpectrumOne interferometer in CaF_2 cells with 0.1 mm thickness.

^{1}H and $^{31}P\{^{1}H\}$ NMR measurements were performed on a Varian Mercury Plus 400 MHz instrument. The proton chemical shift was referenced to the non-deuterated aliquot of the solvent, whereas the phosphorous chemical shifts were referenced to external H_3PO_4 (85% in D_2O).

Positive/negative-ion mass spectra were recorded in CH_3CN solutions on a Waters Micromass ZQ 4000 by using electrospray (ES) ionization. Experimental conditions: 2.56 kV ES-probe voltage, 10 V cone potential, 250 L h^{-1} flow of N_2 spray-gas, incoming-solution flow 20 μL min^{-1}.

ESR spectra have been recorded on a Bruker ESP 300E spectrometer.

The diffraction experiments were carried out on a Bruker APEX II diffractometer equipped with either a CCD (in some cases) or a CMOS detector (in others) using Mo–Kα radiation in both cases. Data were corrected for Lorentz polarization and absorption effects (empirical absorption correction SADABS). Structures were solved by direct methods and refined by full-matrix least-squares based on all data using F_2. Hydrogen atoms were fixed at calculated positions and refined by a riding model. All non-hydrogen atoms were refined with anisotropic displacement parameters. Structure drawings were performed with SCHAKAL99. [1]

[1] E. Keller, *SCHAKAL99* University of Freiburg: Germany, 1999.

X.I. Reagents (Chapter II)

Synthesis of $Rh_4(CO)_{12}$

4.20 g of NaCl and 4.0 g of Cu were added to a water solution of $RhCl_3$ (5 g in 1 L) contained in a 2 L round bottom flask saturated with carbon monoxide. CO was added as required during about 8 h of stirring to maintain at atmospheric pressure. A 1 M solution of disodium citrate (10 mL) was added to the mixture which was stirred for a further 12 h. The solid was filtered off, washed with water, dried in vacuum and extracted with methylene chloride.

Synthesis of $[Rh_7(CO)_{16}][NEt_4]_3$

A methanol solution KOH (4.50 g, 80 mmol) was added to a suspension of $Rh_4(CO)_{12}$ (2.0 g, 2.7 mmol) in the same solvent under carbon monoxide and stirring. After 16 hours the green solution was filtered, precipitated with $[NEt_4]Br$ in water, washed with further water and dried in vacuum. The solid was then extracted in acetonitrile.

X.II. Rhodium-Bismuth system (Chapter III)

Synthesis of $[Rh_{12}Bi(CO)_{27}]^{3-}$

An acetonitrile suspension of $BiCl_3$ (0.39 mmol) was slowly added to a solution of $[Rh_7(CO)_{16}][NEt_4]_3$ (0.51 mmol) in the same solvent, under N_2 atmosphere, and in a 0.75:1 molar ratio, respectively. After ~6 h the resulting brown solution was dried under vacuum, and the solid washed with water (10 mL), ethanol (10 mL), and THF (20 mL). The residue was extracted with ~20 mL of acetonitrile, and di-isopropyl ether was layered on top, to obtain black crystals of $[Rh_{12}Bi(CO)_{27}][NEt_4]_3$ (yield ≈ 70% based on Rh). The product with both $[NEt_4]^+$ and $[NMe_4]^+$ counterions, is soluble in acetone and acetonitrile and stable, but not soluble, in water. Its IR spectrum recorded in CH_3CN shows ν_{CO} absorptions at 1992(s), 1857(m), 1829(m), and 1774(sh) cm^{-1}. ESI-MS analysis shows characteristic signals at 705, 855, 1095, 1146, and 1240 m/z (accompanied by

satellite signals due to CO losses), attributable to the $[Rh_{12}Bi(CO)_{24}]^{3-}$, $\{[Rh_{12}Bi(CO)_{26}][NEt_4]_3\}^{3-}$, $\{[Rh_{12}Bi(CO)_{22}][NEt_4]\}^{2-}$, $\{[Rh_{12}Bi(CO)_{21}][NEt_4]_2\}^{2-}$, and $\{[Rh_{12}Bi(CO)_{23}][NEt_4]_3\}^{2-}$ ions, respectively.

Synthesis of $[(Rh_{12}Bi(CO)_{26})_2Bi]^{5-}$ and $[Rh_{14}Bi_3(CO)_{27}]^{3-}$

To an acetonitrile solution of $[Rh_{12}Bi(CO)_{27}][NEt_4]_3$ under CO (or N_2) atmosphere (15 mL), an acetonitrile suspension of $BiCl_3$ was added in the same solvent (8 mL), reaching a 1:1 molar ratio. After ~4 h the brown mother solution was dried under vacuum and dissolved in 10 mL of N,N-dimethylformamide (DMF). A water solution of $[NMe_4]Br$ was added to it (30 mL) to perform the cation exchange. After the metathesis the suspension was filtered and washed with water (10 mL), ethanol (10 mL), and THF. The dimeric cluster $[(Rh_{12}Bi(CO)_{26})_2Bi]^{5-}$ was extracted in acetone, and, by layering hexane on the solution, black crystals of $[(Rh_{12}Bi(CO)_{26})_2Bi][NEt_4][NMe_4]_4 \cdot 4(CH_3)_2CO$ were obtained (yield ≈ 20% based on Rh). The residue was dried in vacuum and extracted in acetonitrile, and black crystals of $[Rh_{14}Bi_3(CO)_{27}][NMe_4]_3 \cdot 3CH_3CN$ were obtained, by layering di-isopropyl ether onto the acetonitrile solution (yield ≈ 15% based on Rh). Both of these clusters are well-soluble in acetonitrile and DMF (the former is also soluble in acetone), and are both stable in water. Their IR spectra recorded in CH_3CN show ν_{CO} absorptions at 1991(s), 1865(ms), and 1828(m) cm^{-1} for the dimer; 1989(s), 1896(s) and 1863(ms) cm^{-1} for $[Rh_{14}Bi_3(CO)_{27}]^{3-}$. ESI-MS analysis of $[(Rh_{12}Bi(CO)_{26})_2Bi]^{5-}$ shows signals at 1190, 1095, and 1072 m/z (accompanied by satellite ones due to CO losses) attributable to the $\{[Rh_{12}Bi(CO)_{26}]Bi\}^{2-}$, $\{[Rh_{12}Bi(CO)_{22}][NEt_4]\}^{2-}$, and $[Rh_{12}Bi(CO)_{25}]^{2-}$ ions. ESI-MS analysis of $[Rh_{14}Bi_3(CO)_{27}]^{3-}$ presents main signals at 1566, 1341, 1072, 922, and 851 m/z, due to the $\{[Rh_{14}Bi_3(CO)_{26}][NEt_4]_2[NMe_4]\}^{2-}$, $[Rh_{14}Bi_3(CO)_{22}]^{2-}$, $\{[Rh_{14}Bi_3(CO)_{27}][NEt_4]_3\}^{3-}$, $[Rh_{14}Bi_3(CO)_{25}]^{3-}$, and $[Rh_{14}Bi_2(CO)_{25}]^{3-}$ ions, respectively.

Synthesis of $[Rh_{17}Bi_3(CO)_{33}]^{4-}$

An acetonitrile suspension of $BiCl_3$ (8 mL) was added to a solution of $[Rh_{12}Bi(CO)_{27}][NEt_4]_3$ in the same solvent (15 mL), under either CO or N_2 atmosphere, reaching a 1.5:1 molar ratio, respectively. After ~5 h the brown mother solution was dried under vacuum, and the solid was washed with water (10 mL), methanol (10 mL), and THF. $[Rh_{17}Bi_3(CO)_{33}]^{4-}$ was extracted in acetone, and black crystals of $[Rh_{17}Bi_3(CO)_{33}][NEt_4]_4$ were obtained by layering hexane onto the acetone solution (yield ≈ 30% based on Rh). The product is well-soluble in acetone, acetonitrile, and DMF and stable in water. Its IR spectrum presents ν_{CO} absorptions in CH_3CN at 2002(sh), 1996(s), 1990(sh), 1872(ms), and 1870 (ms) cm^{-1}. ESI-MS analysis results of $[Rh_{17}Bi_3(CO)_{33}][NEt_4]_4$ show characteristic signals at 1673, 1566, 1134, and 1091 m/z, assigned to the $\{[Rh_{17}Bi_3(CO)_{30}][NEt_4]\}^{2-}$, $[Rh_{17}Bi_3(CO)_{27}]^{2-}$, $\{[Rh_{17}Bi_3(CO)_{32}][NEt_4]\}^{3-}$ and $[Rh_{17}Bi_3(CO)_{32}]^{3-}$ ions, respectively.

X.III. Rhodium-Germanium system (Chapter IV)

Synthesis of $[Rh_{13}Ge(CO)_{25}]^{3-}$

An acetonitrile solution of $GeBr_2$ (0.18 g, 0.78 mmol) was slowly added to a solution of $[Rh_7(CO)_{16}][NEt_4]_3$ (1.00 g, 0.65 mmol) in the same solvent, under N_2 atmosphere, and in a 1.2:1 molar ratio, respectively. After 2 hours, the resulting brown solution was dried under vacuum and the solid washed with water (100 mL), ethanol (300 mL) and THF (40 mL). The residue was extracted with 30 mL of acetone and hexane was layered on top, to afford black crystals of $[Rh_{13}Ge(CO)_{25}][NEt_4]_3 \cdot [NEt_4]Br$ (yield around 77% based on Rh). $[Rh_{13}Ge(CO)_{25}][NEt_4]_3$ is soluble in acetone, acetonitrile and DMF and stable, but poorly soluble, in water. Its IR spectrum recorded in CH_3CN shows ν_{CO} absorptions at 1987(vs), 1885(mw) and 1834(ms) cm^{-1}. ESI-MS analysis results of $[Rh_{13}Ge(CO)_{25}][NEt_4]_3$ show characteristic signals at 1106, 1056 and 694 m/z, assigned to the $\{[Rh_{13}Ge(CO)_{24}][NEt_4]\}^{2-}$, $[Rh_{13}Ge(CO)_{25}]^{2-}$ and $[Rh_{13}Ge(CO)_{24}]^{3-}$ ions, respectively.

Synthesis of $[Rh_{12}Ge(CO)_{27}]^{4-}$

An acetonitrile solution of $[Rh_{13}Ge(CO)_{25}][NEt_4]_3$ (0.425 g, 0.17 mmol) was put under CO atmosphere. After 12 hours, the IR frequencies of the solution changed from 1987(vs), 1884(w) and 1834(ms) cm^{-1} to 1997(vs), 1989(s), 1850(sh), 1823(ms) and 1756(sh) cm^{-1}. Without further work-up, di-isopropyl ether was layered on top and black crystals of $[Rh_{12}Ge(CO)_{27}][NEt_4]_4 \cdot 2CH_3CN$ were obtained. $[Rh_{12}Ge(CO)_{27}][NEt_4]_4$ is soluble in acetonitrile and DMF and stable, but not soluble in water. Its IR spectrum recorded in CH_3CN slightly differs from the one recorded at the end of the reaction and shows ν_{CO} absorptions at 1997(vs), 1989(vs), 1795(ms) and 1751(mbr) cm^{-1}. ESI-MS analysis results of $[Rh_{12}Ge(CO)_{27}][NEt_4]_4$ show characteristic signals at 1163, 1097 and 1019 m/z, assigned to the $\{[Rh_{12}Ge(CO)_{26}][NEt_4]_2\}^{2-}$, $\{[Rh_{12}Ge(CO)_{27}][NEt_4]\}^{2-}$ and $[Rh_{12}Ge(CO)_{26}]^{2-}$ ions, respectively.

Synthesis of $[Rh_{14}Ge_2(CO)_{30}]^{2-}$

An acetonitrile solution of $GeBr_2$ (0.08 g, 0.33 mmol) was slowly added to a solution of $[Rh_{13}Ge(CO)_{25}][NEt_4]_3$ (0.675 g, 0.27 mmol) in the same solvent, under N_2 atmosphere, and in a 1.2:1 molar ratio, respectively. After 3 hours the resulting brown solution was dried under vacuum and the solid washed with water (100 mL), ethanol (100 mL) and THF (30 mL). The residue was extracted with 20 mL of acetone, hexane was layered on top and after a few days black crystals of $[Rh_{14}Ge_2(CO)_{30}][NEt_4]_2$ were obtained (yield around 50% based on Rh). $[Rh_{14}Ge_2(CO)_{30}][NEt_4]_2$ is soluble in acetone, acetonitrile and DMF and stable, but poorly soluble, in water. The IR spectrum, recorded in CH_3CN, displays main peaks at 2012(vs) and 1837(ms) cm^{-1}. ESI-MS analysis results of $[Rh_{14}Ge_2(CO)_{30}][NEt_4]_2$ show characteristic signal at 1185 assigned to the $[Rh_{14}Ge_2(CO)_{28}]^{2-}$ ion.

Synthesis of $[Rh_{23}Ge_3(CO)_{41}]^{5-}$

An acetonitrile solution of $GeBr_2$ (0.148 g, 0.64 mmol) was slowly added to a solution of $[Rh_7(CO)_{16}][NEt_4]_3$ (0.830 g, 0.53 mmol) in the same solvent, under CO atmosphere, and in a 1.2:1 molar ratio, respectively. After 4 hours the resulting brown solution was dried under vacuum and the solid washed with water (100 mL), ethanol (100 mL), THF (30 mL) and acetone (40 mL). The residue was extracted with 20 mL of acetonitrile, di-isopropyl ether was layered on top and after a few days black crystals of $[Rh_{23}Ge_3(CO)_{41}][NEt_4]_5$ were obtained (very low yield). $[Rh_{23}Ge_3(CO)_{41}][NEt_4]_5$ is soluble in acetonitrile and DMF and stable, but not soluble, in water. Its IR spectrum in CH_3CN shows peaks at 1991(s) and 1800(ms) cm^{-1}. ESI-MS analysis results of $[Rh_{23}Ge_3(CO)_{41}][NEt_4]_5$ show characteristic signal at 1199 m/z, assigned to the $[Rh_{23}Ge_3(CO)_{36}]^{3-}$ ion.

X.IV. Rhodium-Antimony system (Chapter V)

Synthesis of $[Rh_{11}Sb(CO)_{26}]^{2-}$ and $[Rh_{12}Sb(CO)_{27}]^{3-}$

An acetonitrile solution of $SbCl_3$ (0.104 g, 0.46 mmol) was slowly added to a solution of $[Rh_7(CO)_{16}][NEt_4]_3$ (0.950 g, 0.61 mmol) in the same solvent, under CO atmosphere, and in a 0.75:1 molar ratio, respectively. After 3 hours the resulting brown solution was dried under vacuum and the solid washed with water (120 mL) and ethanol (100 mL). $[Rh_{11}Sb(CO)_{26}]^{2-}$ was extracted in THF (10 mL) and by layering hexane on the solution, black crystals of $[Rh_{11}Sb(CO)_{26}][NEt_4]_2$ (yield ≈ 15% based on Rh) were obtained. The residue was dried in vacuum and extracted in acetone (20 mL), and black crystals of $[Rh_{12}Sb(CO)_{27}][NEt_4]_3$ (yield ≈ 70% based on Rh) were obtained by layering hexane on the solution.

Both of these clusters are well-soluble in acetone, acetonitrile and DMF (the former is also soluble in THF), and are both stable in water. Their IR spectra recorded in CH_3CN show ν_{CO} absorptions at 2033(vs), 1869(mw), and 1813(mw) cm^{-1} for $[Rh_{11}Sb(CO)_{26}]^{2-}$; 2021(sh), 2013(vs) and 1826(m) cm^{-1} for $[Rh_{12}Sb(CO)_{27}]^{3-}$. ESI-MS analysis results of $[Rh_{11}Sb(CO)_{26}][NEt_4]_2$ show characteristic signal at 963 m/z, assigned to the $[Rh_{11}Sb(CO)_{24}]^{2-}$ ion. ESI-MS

analysis results of $[Rh_{12}Sb(CO)_{27}][NEt_4]_3$ show characteristic signals at 1159, 1093, 1028 and 704 m/z, assigned to the $\{[Rh_{12}Sb(CO)_{25}][NEt_4]_2\}^{2-}$, $\{[Rh_{12}Sb(CO)_{25}][NEt_4]\}^{2-}$, $[Rh_{12}Sb(CO)_{25}]^{2-}$ and $[Rh_{12}Sb(CO)_{27}]^{3-}$ ions, respectively.

Synthesis of $[Rh_{20}Sb_3(CO)_{36}]^{3-}$

An acetonitrile solution of $SbCl_3$ (0.118 g, 0.52 mmol) was slowly added to a solution of $[Rh_7(CO)_{16}][NEt_4]_3$ (0.700 g, 0.45 mmol) in the same solvent, under CO atmosphere, and in a 1.15:1 molar ratio, respectively. After 4 hours the resulting brown solution was dried under vacuum and the solid washed with water (150 mL), ethanol (150 mL) and THF (50 mL). $[Rh_{20}Sb_3(CO)_{36}]^{3-}$ was extracted in acetone (30 mL) and black crystals of $[Rh_{20}Sb_3(CO)_{36}][NEt_4]_3$ (yield ≈ 85% based on Rh) were obtained by layering hexane on the solution. $[Rh_{20}Sb_3(CO)_{36}][NEt_4]_3$ is soluble in acetone, acetonitrile and DMF and stable, but not soluble, in water. Its IR spectrum recorded in CH_3CN shows ν_{CO} absorptions at 2030(vs) and 1833(ms) cm^{-1}. ESI-MS analysis results of $[Rh_{20}Sb_3(CO)_{36}][NEt_4]_3$ show characteristic signals at 1782, 1135, m/z, assigned to the $\{[Rh_{20}Sb_3(CO)_{36}][NEt_4]\}^{2-}$and $[Rh_{20}Sb_3(CO)_{35}]^{3-}$ ions, respectively.

Synthesis of $[Rh_{24}Sb_4(CO)_{44}]^{n-}$ and $[Rh_{21}Sb_2(CO)_{38+x}]^{5-}$

An acetonitrile solution of $SbCl_3$ (0.145 g, 0.64 mmol) was slowly added to a solution of $[Rh_7(CO)_{16}][NEt_4]_3$ (1.420 g, 0.91 mmol) in the same solvent, under N_2 atmosphere, and in a 0.70:1 molar ratio, respectively. After 3 hours the resulting brown solution was dried under vacuum and the solid washed with water (150 mL), ethanol (100 mL) and THF (40 mL). $[Rh_{24}Sb_4(CO)_{44}]^{x-}$ was extracted in acetone (30 mL) with impurities of $[Rh_{21}Sb_2(CO)_{38+x}]^{5-}$ and by layering hexane on the solution, black crystals of $[Rh_{24}Sb_4(CO)_{44}][NEt_4]_x$ (very low yield) were obtained. The residue was dried in vacuum and extracted in acetonitrile (20 mL), and black crystals of $[Rh_{21}Sb_2(CO)_{38+x}][NEt_4]_5$ (yield ≈ 40% based on Rh) were obtained by layering di-isopropyl ether on the solution.

Both of these clusters are soluble in acetone (the latter only sparingly soluble), acetonitrile and DMF and stable, but not soluble, in water. Their IR spectra recorded in CH_3CN show ν_{CO} absorptions at 1993(vs), and 1806(mw) cm^{-1} for $[Rh_{24}Sb_4(CO)_{44}]^{n-}$; 1995(vs), 1954(w) and 1805(ms) cm^{-1} for $[Rh_{21}Sb_2(CO)_{38+x}]^{5-}$ with more CO; 1987(sh), 1981(s) and 1857(ms) cm^{-1} for $[Rh_{21}Sb_2(CO)_{38+x}]^{5-}$ with less CO. ESI-MS analysis results of $[Rh_{21}Sb_2(CO)_{38+x}][NMe_3Bz]$ show characteristic signals at 1795, 1197 and 1138 m/z, assigned to the $\{[Rh_{21}Sb_2(CO)_{37}][NMe_3Bz]\}^{2-}$, $\{[Rh_{21}Sb_2(CO)_{37}][NMe_3Bz]\}^{3-}$ and $[Rh_{21}Sb_2(CO)_{36}]^{3-}$ ions, respectively.

Synthesis of $[Rh_{12}Sb(CO)_{24}]^{4-}$ and $[Rh_{21}Sb_2(CO)_{38+x}]^{5-}$

An acetone solution of $SbCl_3$ (0.059 g, 0.257 mmol) was slowly added to a solution of $[Rh_7(CO)_{16}][NEt_4]_3$ (0.500 g, 0.321 mmol) in the same solvent, under N_2 atmosphere, and in a 0.80:1 molar ratio, respectively. After 3 hours the resulting brown solution, separated from the insoluble residue, was dried under vacuum and washed with water (60 mL), ethanol (150 mL) and THF (50 mL). $[Rh_{12}Sb(CO)_{24}]^{4-}$ was extracted with about 20 mL of acetone but transferred to acetonitrile, where it crystallized by layering on di-isopropyl ether. After a few days, black crystals of $[Rh_{12}Sb(CO)_{24}][NEt_4]_4 \cdot 2CH_3CN$ formed (yield ≈ 22% based on Rh).

The insoluble residue that had precipitated during the reaction was dried in vacuum and extracted in acetonitrile (20 mL), and black crystals of $[Rh_{21}Sb_2(CO)_{38+x}][NEt_4]_5$ (yield ≈ 35% based on Rh) were obtained by layering di-isopropyl ether on the solution. $[Rh_{12}Sb(CO)_{24}]^{4-}$ is well soluble in acetone, acetonitrile and dimethylformamide. Its IR spectrum presents ν_{CO} in CH_3CN: 1992(vs), 1805 (ms) cm^{-1}.

Synthesis of $[(Rh_{12}Sb_2(CO)_{25})_2Rh(CO)_2PPh_3]^{7-}$

The cluster $[Rh_{12}Sb(CO)_{27}][NEt_4]_3$ was prepared as described before and put in acetonitrile, then precipitated with an aqueous solution of $[NEt_4]Br$ in order to eliminate the residual acidity. A sample of such $[Rh_{12}Sb(CO)_{27}][NEt_4]_3$ (0.280 g, 0.112 mmol) was dissolved in acetonitrile and a second solution of PPh_3 (0.024 g,

0.090 mmol) in the same solvent was slowly added to the former, under CO, in a 1:0.8 molar ratio. After a few hours the resulting mother solution was filtered and di-isopropyl ether was layered on top, allowing to obtain $[(Rh_{12}Sb_2(CO)_{25})_2Rh(CO)_2PPh_3][NEt_4]_7 \cdot CH_3CN$ in a crystalline form. (yield ≈ 43% based on Rh). The compound is well soluble in acetone, acetonitrile and dymethylformamide. Its IR spectrum presents ν_{CO} in CH_3CN: 2022(sh), 1998(vs), 1806(ms), 1767(m) cm^{-1}. $^{31}P\{^1H\}$ NMR (CD_3CN, 298 K) δ_P (ppm): 29.9 (d, $^1J_{Rh-P}$ = 128 Hz).

Synthesis of $[Rh_{10}Sb(CO)_{21}PPh_3]^{3-}$

The cluster $[Rh_{12}Sb(CO)_{27}][NEt_4]_3$ was prepared as described before and put in acetonitrile, then precipitated with an aqueous solution of $[NEt_4]Br$ in order to eliminate the residual acidity. A sample of such $[Rh_{12}Sb(CO)_{27}][NEt_4]_3$ (0.260 g, 0.104 mmol) was dissolved in acetonitrile and a second solution of PPh_3 (0.022 g, 0.083 mmol) in the same solvent was slowly added to the former, under N_2, in a 1:0.8 molar ratio. After a few hours the resulting mother solution was filtered and di-isopropyl ether was layered on top, allowing to obtain $[Rh_{10}Sb(CO)_{21}PPh_3][NEt_4]_3 \cdot CH_3CN$ in a crystalline form (yield ≈ 30% based on Rh). The compound is well soluble in acetone, acetonitrile and dymethylformamide. Its IR spectrum presents ν_{CO} in CH_3CN: 1991 (vs), 1981(sh), 1844(m), 1805(m) and 1762(ms) cm^{-1}. $^{31}P\{^1H\}$ NMR (CD_3CN, 298 K) δ_P (ppm): 33.38 (m, $^1J_{Rh-P}$ = 249 Hz and $^2J_{Rh-P}$ = 5 Hz).

Synthesis of $Rh_4(CO)_4(PPh_3)_4(H_2O)_2$

The cluster $[Rh_{12}Sb(CO)_{27}][NEt_4]_3$ was prepared as described before. A sample of such cluster (0.300 g, 0.120 mmol) was dissolved in acetonitrile and a second solution of PPh_3 (0.096 g, 0.360 mmol) in the same solvent was slowly added to the former, under N_2, in a 1:3 molar ratio. The resulting solution was then heated at reflux for 90 minutes and di-isopropyl ether was layered on top, leading to the formation of a solution and an amorphous solid which were separately treated.

The solution, dried under vacuum, washed with water and dissolved into CH_2Cl_2 was then layered on with hexane, giving crystals of $Rh_4(CO)_4(PPh_3)_4(H_2O)_2$ (very low yield). The compound is well soluble in CH_2Cl_2 and hexane. Its IR spectrum presents ν_{CO} in CH_2Cl_2: 1979(m) and 1918(vs) cm^{-1}.

X.V. Rhodium-Gold system (Chapter VI)

Synthesis of $[Rh_{20}Au_2(CO)_{42}]^{6-}$

An acetonitrile solution of $[AuCl_4][NMe_3Bz]$ (0.138 g, 0.282 mmol) was slowly added to a solution of $[Rh_7(CO)_{16}][NEt_4]_3$ (0.440 g, 0.282 mmol) in the same solvent, under CO atmosphere, and in a 1:1 molar ratio, respectively. After 24 hours the resulting brown solution was dried under vacuum and the solid washed with water, EtOH, THF and acetone. $[Rh_{20}Au_2(CO)_{42}][NEt_4]_6$ was then extracted in acetonitrile (15 mL) and crystallized by layering di-isopropyl ether on top of the solution (yield ≈ 20% based on Rh). This species is soluble in acetonitrile and DMF and stable, but not soluble, in water. Its IR spectrum presents ν_{CO} absorptions in CH_3CN at 1989(vs) and 1843(ms) cm^{-1}.

Synthesis of $[Rh_{16}Au_6(CO)_{36}]^{6-}$

A DMF solution of $[AuCl_4][NMe_3Bz]$ (0.141 g, 0.29 mmol) was slowly added to a solution of $[Rh_7(CO)_{16}][NEt_4]_3$ (0.600 g, 0.39 mmol) in the same solvent, under CO atmosphere, and in a 0.75:1 molar ratio, respectively. After 24 hours the resulting brown solution was precipitated by adding a water solution of $[NEt_4]Br$, and the dried solid washed with water and THF. $[Rh_{16}Au_6(CO)_{36}]^{6-}$ was then extracted in acetone (25 mL) and after having been transferred into acetonitrile, crystallized as $[Rh_{16}Au_6(CO)_{36}][NEt_4]_6 \cdot 2CH_3CN$ by layering di-isopropyl ether on top of the solution (yield ≈ 30% based on Rh). This species is soluble in acetone, acetonitrile and DMF and stable, but not soluble, in water. Its IR spectrum presents ν_{CO} absorptions in CH_3CN at 2001(s) and 1805(ms) cm^{-1}.

The ESI-MS analysis showed that the cluster is not stable in the experimental conditions and heavily breaks. Only two signals at 1285 and 1241 m/z could be

attributed to the $\{[Rh_{16}Au_6(CO)_{32}][NEt_4]\}^{3-}$ and $\{[Rh_{16}Au_6(CO)_{32}]\}^{3-}$ ions, respectively.

Synthesis of $[Rh_{18}Au(CO)_{33}]^{3-}$

An acetone solution of $[Rh_{16}Au_6(CO)_{36}][NEt_4]_6$ (0.15 g, 0.032 mmol) was put under N_2 atmosphere. After 24 hours, the IR frequencies of the solution changed from 2001(s) and 1805(ms) cm^{-1} to 1996(vs), 1853(sh) and 1822(ms) cm^{-1}. Without further work-up, di-isopropyl ether was layered on top and black crystals of $[Rh_{18}Au(CO)_{33}][NEt_4]_3 \cdot 2CH_3CN$ were obtained (yield ≈ 50% based on Rh). $[Rh_{18}Au(CO)_{33}][NEt_4]_3$ is soluble in acetone, acetonitrile and DMF and stable, but non soluble in water. Its IR spectrum recorded in CH_3CN shows ν_{CO} absorptions at 2019(vs), 1994(ms), 1960(sh) and 1819(ms) cm^{-1}.

Synthesis of $[HRh_9(CO)_{20}]^{2-}$

An acetone solution of $[Rh_{16}Au_6(CO)_{36}][NEt_4]_6$ (0.16 g, 0.034 mmol) was put under H_2 atmosphere. After 24 hours, the IR frequencies of the solution changed from 2001(s) and 1805(ms) cm^{-1} to 1988(vs), 1960(sh) and 1825(m) cm^{-1}. Di-isopropyl ether was directly layered on top and black crystals of $[HRh_9(CO)_{20}][NEt_4]_2 \cdot$were obtained (yield ≈ 90% based on Rh). $[HRh_9(CO)_{20}][NEt_4]_2$ is soluble in acetone, acetonitrile and DMF and stable, but non soluble in water. Its IR spectrum recorded in CH_3CN shows ν_{CO} absorptions at 1988(s), 1967(ms), 1964(m) and 1825(mw) cm^{-1}.

Synthesis of $[Rh_{22}(CO)_{37}]^{n-}$

A DMF solution of $[AuBr_4][NEt_4]$ (0.166 g, 0.257 mmol) was slowly added to a solution of $[Rh_7(CO)_{16}][NEt_4]_3$ (0.400 g, 0.257 mmol) in the same solvent, under CO atmosphere, and in a 1:1 molar ratio, respectively. After 48 hours the resulting brown solution was precipitated by adding a water solution of $[NEt_4]Br$, and the dried solid washed with water, EtOH and THF. $[Rh_{22}(CO)_{37}]^{n-}$ was extracted in acetone (15 mL), transferred to acetonitrile and crystallized as $[Rh_{22}(CO)_{37}][NEt_4]_n$

(yield ≈ 45% based on Rh) by layering di-isopropyl ether on top of the solution. This species is soluble in acetone, acetonitrile and DMF and stable, but not soluble, in water. Its IR spectrum presents ν_{CO} absorptions in CH_3CN at 2012(vs), 1959(w), 1857(sh), 1842(w) and 1810(w) cm^{-1}.